Biogeochemical cycling of mercury in the atmosphere-ocean-land system: Global and regional modeling

Yanxu Zhang

A dissertation
submitted in partial fulfillment of the
requirements for the degree of

Doctor of Philosophy

University of Washington
2013

Reading Committee:

Lyatt Jaeglé, Chair

Daniel A. Jaffe

LuAnne Thompson

Program Authorized to Offer Degree:
Atmospheric Sciences

University of Washington

Abstract

Biogeochemical cycling of mercury in the atmosphere-ocean-land system: Global and regional modeling

Yanxu Zhang

Chair of the Supervisory Committee:
Professor Lyatt Jaeglé
Atmospheric Sciences

Mercury (Hg) is a ubiquitous trace metal in the environment originating from both natural and anthropogenic sources. It is a pollutant of concern because of the adverse human health effects caused by the consumption of fish and seafood containing methylmercury, which is a neurotoxin. Through development of two transport and chemistry models in the atmosphere and ocean, this dissertation investigates the regional Hg atmospheric transport and wet deposition over North America, and the global ocean Hg cycle as well its perturbation by anthropogenic Hg emissions.

Chapter 2 develops a new nested-grid Hg simulation over North America with a 1/2° latitude by 2/3° longitude horizontal resolution employing the GEOS-Chem global chemical transport model. The nested model shows generally improved skill at capturing the high spatial and temporal variability of a variety of observations including wet deposition fluxes, surface concentrations and aircraft measurements of atmospheric Hg. We find that a hypothesized sub-grid rapid in-plume reduction of reactive to elemental Hg improves the model-observation comparison. The nested model suggests that North American anthropogenic emissions account

for 10-22% of Hg wet deposition flux over the U.S., depending on whether the in-plume reduction process is included or not.

Chapter 3 examines the trends in Hg precipitation concentrations at 47 Mercury Deposition Network (MDN) sites over the United States during 2004 – 2010. We run the model with constant anthropogenic emissions and subtract the model results from the observations in order to remove the influence of meteorological fluctuations. We find significant decreasing trends in the Northeast U.S. (-4.3±2.2% yr^{-1}) and in the Midwest (-2.5±1.6% yr^{-1}), but weaker trends over the Southeast (-0.63±2.5% yr^{-1}) and West (+0.33±7.7% yr^{-1}). Sensitivity simulation with the nested-grid Hg simulation shows that the combination of domestic emission reductions and decreasing background concentrations explains the observed trends over Northeast and Midwest, with domestic emission reductions accounting for 51-33% of the decreasing trends.

Chapter 4 implements Hg biogeochemistry in a global 3D offline ocean tracer model, OFFTRAC, and investigate the natural Hg cycle, prior to any anthropogenic input. This model simulates the transformations among different Hg species, and links them to carbon dynamics in the ocean. In the deep ocean, a region which is not expected to be significantly influenced by anthropogenic emissions, the modeled total Hg concentrations (Hg^T, 1.1±0.3 pM) are consistent with observations (1.4±0.9 pM). High concentrations in the mixed layer are modeled at Southern Ocean, coastal regions, closed and shallow water body, western Equatorial Pacific Ocean. The modeled Hg^T concentrations in the deep old North Pacific waters are a factor of two higher than in the younger the deep North Atlantic because of the longer time to accumulate Hg sinking from the surface. The modeled fraction of elemental Hg (Hg^0_{aq}) is also higher in aged deep waters because of the slow accumulation of Hg^0_{aq} generated by reduction of oxidized Hg in subsurface waters.

Chapter 5 focuses on the perturbation of legacy anthropogenic Hg emissions (1450 – 2008) on oceanic Hg cycle. We couple the OFFTRAC-Hg simulation developed in Chapter 4 with the GEOS-Chem atmospheric Hg simulation. According to the model, the total Hg mass in the global ocean has increased from 1150 Mmol in 1450 to a present-day value of 1640 Mmol. The modeled anthropogenic Hg concentrations peak at a depth of 400-500 m. The model result shows that approximately 43% (210 Mmol) of the anthropogenic Hg resides at depths below the mixed layer and shallower than 1000 m, 55% (270 Mmol) at depths deeper than 1000 m, while only approximately 2% (10 Mmol) in the mixed layer. The model also suggests that sinking with particulate organic carbon is the major pathway for the anthropogenic Hg to penetrate into the deep ocean. The modeled anthropogenic Hg concentrations are higher over the east tropical Pacific Ocean, the east tropical Atlantic Ocean, tropical Indian, west coast of continents, and high-latitude North Pacific and Atlantic Oceans, while being lower over centers of mid-latitude gyres and the Arctic Ocean.

TABLE OF CONTENTS

Page

List of Figures

List of Tables

Table Number Page

ACKNOWLEDGMENTS

Foremost, I would like to give my warmest thank to my advisor, Professor Lyatt Jaeglé, not only for her continuous support and guidance throughout the years, but also for her patience, encouragement and care about my success in my future careers. My sincere thanks also goes to my committee members, LuAnne Thompson, Steven Emerson, Daniel Jaffe, Robert Wood, Joel Thornton, and Paul Quay, for their helpful discussions and insightful suggestions. Their feedbacks have greatly improved my research and this dissertation. I would also give my thanks to my group members, Maurizio Di Pierro, Yurong Luan and Viral Shah, for their joyful companionship. I also want to thank my collaborators: Chris Holmes, Helen Amos, Anne Soerensen, Andrew Shao, David Trossman, Aaron van Donkelaar, Randall Martin, and David Streets. I also want to express my gratitude to the operators and experimentalists who made those observations used to constrain my models in this dissertation. Finally, I want to thank my wife, Lily and my son, Ethan, for their love, support and inspiration.

Chapter 1

INTRODUCTION

Mercury (Hg) is a ubiquitous and persistent trace metal, which cycles among the atmosphere, ocean, and land over different time scales ranging from days to centuries. Hg can be emitted by both anthropogenic and natural sources. These emissions occur mainly in the elemental form, which is slowly transformed to the oxidized form and removed from the atmosphere via deposition. When deposited to ocean, Hg undergoes methylation in near-shore sediments and within the open ocean water column. The resulting methylmercury (MeHg) is a neurotoxin that bioaccumulates in the food chain. Human exposure occurs mainly via marine fish and seafood consumption.

1.1 General Physicochemical properties of Hg

Hg is a transition metal with atomic number 80 and a completely filled electron configuration in the outer subshells ($4f^{14}5d^{10}6s^2$). This configuration results in a low melting point (234.32 K) for Hg, which is thus the only metal that is liquid under standard conditions for temperature and pressure. Hg has a relatively high vapor pressure (~1 Pa at 315 K). Hg has oxidation states of IV, II, I and 0, with stable states of 0 (Hg^0) and II (Hg^{II}). A unique property of Hg is the formation of amalgams with gold, silver and many other metals.

1.2 Motivation

Hg is treated as an environmental pollutant because of the concern regarding its toxicity. Although potential health risks caused by exposure to other forms of Hg can occur, the major health risk is from the exposure to MeHg (Merger et al., 2007). This is largely because of the affinity of MeHg to protein and the tight combination with muscle tissue after being digested. This leads to MeHg being bioaccumulated and biomagnified through the trophic levels in the food web (Morel et al., 1998). As a result, the MeHg concentrations in fish could be 10^6 times higher than in surrounding waters (AMAP, 2011). The concentrations also vary by several orders of magnitudes across species at different trophic levels (Merger et al., 2007). Human exposure to MeHg is mainly via the consumption of fish and seafood (e.g. Sunderland 2007, Kim and Lee, 2010). Other sources include the consumption of rice (e.g. Horvat et al., 2003; Zhang et al., 2010), Hg vapor from dental amalgams, occupational exposure (e.g. dental offices and Hg mining) and from artisanal gold and silver mining operations (Merger et al., 2007 and references therein). The health effect of MeHg exposure includes neurodevelopmental delays in children, immune system suppression, and compromised cardiovascular health in adults (Clarkson and Magos, 2006; Mergler et al. 2007). Integrative analysis of current available epidemiologic data reveals that a 0.18 (95% confidence interval: 0.009-0.378) intelligence quotient (IQ) points decrease would occur for each part per million increase of maternal hair Hg (Axelrad et al., 2007). Trasande et al. (2005) found that this IQ loss integrates over the entire lifetime of the children, which leads to a loss in productivity of US$8.7 billion annually (2000 dollars) in the US. Because of the severe health effect, Hg pollution is being actively regulated for both emission and exposure at national and inter-governmental levels. For example, the World Health Organization established a tolerable intake of 1.6 μg/kg bodyweight per week for MeHg (JECFA, 2004). The USEPA developed a series of fish consumption advisories based on the types of fish (http://www.epa.gov/hg/advisories.htm). There are now ongoing international negotiations to achieve a global legally-binding agreement for Hg emission reductions (UNEP, 2012).

1.3 Anthropogenic Hg emissions

The main anthropogenic Hg emission sources include coal combustion, metal production and mining, cement production and waste incineration (Streets et al., 2009; Pacyna et al., 2010). Global anthropogenic Hg emissions to the atmosphere in 2005 are estimated to be 1921 (range: 1230-2890) Mg (AMAP/UNEP, 2008). Figure 1.1 shows the contributions from individual sources and the spatial distribution of anthropogenic emissions. The largest anthropogenic Hg emissions occur during combustion of fossil fuels for power and heating with a contribution of 46% to global anthropogenic emissions. Metal production results in a total contribution of 33%. Other sources such as cement production and waste incineration contribute the remaining ~20%. The spatial distribution of anthropogenic Hg emissions generally follows that of energy consumption and industrial activity, with larger contribution from Asia (65%), North America (8.3%) and Europe (7.9%). South America contributes about 7.3% mainly from artisanal and small-scale gold mining, quite different from other regions of the world.

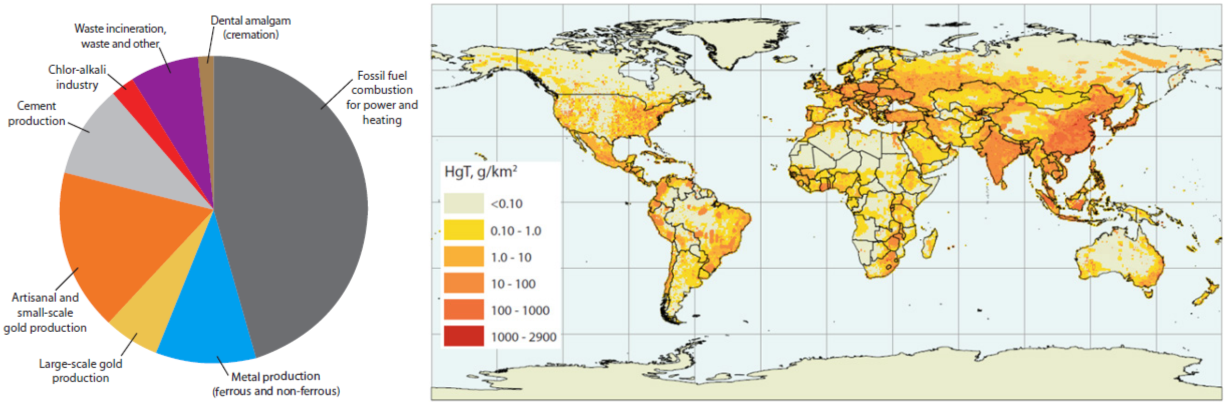

Figure 1.1: Global source contribution (left) and spatial distribution (right) to the anthropogenic emissions of Hg to air in 2005 (AMAP 2011). Reprinted with the permission of the AMAP/UNEP.

Anthropogenic releases of Hg to the environment date back to the early history of human civilization through the production of energy and use of Hg amalgams in gold and silver extraction. This precious metal extraction technique was uses by Phoenicians and Carthaginians as early as 2,700 BC, and was widely used by the Romans around 50 AD (Lacerda, 1997). While large-scale use of Hg in gold and silver mining stopped in the early 20th century, Hg amalgamation is still in use in many artisanal and small-scale gold mining areas today (Lacerda, 1997). Streets et al. (2011) estimated that the all-time release of Hg to the atmosphere from human activities amounted to 350 Gg with around 40% emitted before 1850 and 60% emitted after 1850. Figure 1.2 shows the evolution of global total anthropogenic Hg emissions since 1850. The anthropogenic Hg emissions peaked in 1890 due to gold/silver rush over North America and mercury mining over Europe with global Hg emissions of 2,600 Mg, about one third higher than the present-day emissions. The Hg emissions decreased significantly after this peak because of the phasing out amalgam technique in favor of cyanidation extraction. Starting in 1950, anthropogenic Hg emissions started to increase again as a result of coal combustion and artisanal gold mining.

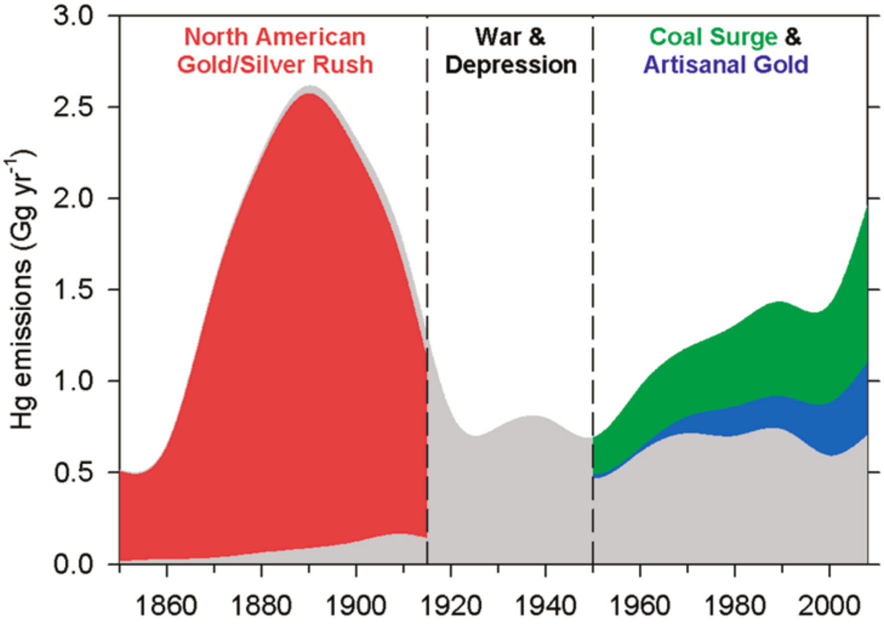

Figure 1.2: Historical anthropogenic Hg emissions during 1850 – 2008. Reprinted with permission from Streets et al., 2011. Copyright 2011 American Chemical Society.

1.4 Mercury biogeochemical cycle

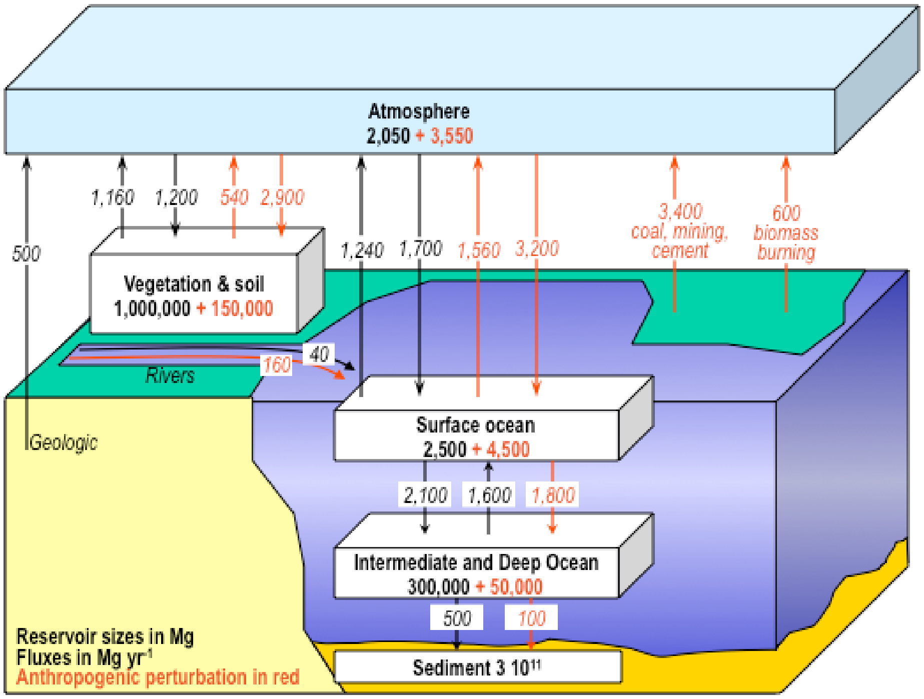

Figure 1.3: Global Hg cycle in the atmosphere-ocean-land system. Reservoir sizes are in units of Tg, while fluxes are in Tg/yr. The black arrows and numbers indicated the pre-industrial Hg budget, while the anthropogenic perturbation is shown in red. Numbers are from the GEOS-Chem pre-industrial and present-day simulations of Selin et al. (2008).

The GEOS-Chem atmosphere-ocean-soil simulation of the Hg biogeochemical cycle in the contemporary global environment is summarized in Figure 1.3 (Selin et al., 2008). In addition to anthropogenic source, Hg is also released to the atmosphere from natural sources including biomass burning, volcanic eruptions, as well as re-emissions from soil and ocean (Mason, 2009). Currently, direct anthropogenic emissions account for about 1/3 of total emissions to the atmosphere (Pacyna et al., 2010), while the ocean and land re-emissions are estimated to account for approximately 1/3 each with large uncertainties based on evasion fluxes as reported in the literature (e.g. Mason and Fitzgerald 1993; Laurier et al., 2004; Linderberg et al., 2004; Gustin and Lindberg 2005). After being released to the atmosphere, Hg can enter the land and ocean reservoirs via deposition in the form of Hg^{II} (e.g. Bullock et al., 2009; Weiss-Penzias et al., 2011) and/or air-surface exchange in the form of Hg^0 (e.g. Mason and Sheu 2001). Once deposited some of the Hg can reduced back to Hg^0 (Amyot et al., 1997; Mason et al., 1995; Zhang et al., 2001), which because of its low vapor pressure can be reemitted to the atmosphere. In this way, Hg keeps cycling among different environmental media for millennia after release to the atmosphere before eventually returning to the sediment reservoir (Young et al., 1973). Over geologic time scales, the geogenic source (mainly volcanoes: e.g. Nriagu and Becker, 2003; Pyle and Mather, 2003) balances the sedimentation process happening in the ocean bottom. As a result, the current atmospheric Hg burden is the result of not only present-day emissions, but also recycled legacy Hg released in prior decades and centuries.

Figure 1.3 also shows the modeled human perturbation to the Hg cycle (numbers in red). The biogeochemical cycling of anthropogenic Hg has led to the increase in ocean and soil emissions by ~100% and ~50% respectively. Thus, the overall effect of anthropogenic activity has been to increase Hg in the atmosphere and surface ocean by nearly a factor of 3, while the larger soil and intermediate/deep oceans reservoirs have each increased by ~15%. Large uncertainties are associated with these enhancement factors (Selin et al., 2008). One important reason lies on the lack of direct measurements of historical level of Hg in the environment, other than the Hg accumulation rate archived in lake sediments, ice cores and peat bogs. These records have indicated an approximately 3-fold increase in atmospheric Hg deposition since the Industrial Revolution (e.g. Fitzgerald et al., 2005).

1.5 Hg chemistry in the atmosphere

Hg in the atmosphere exists in three operationally defined forms: gaseous elemental Hg (GEM or Hg^0), reactive gaseous or gaseous oxidized Hg (RGM or GOM, consisting of $HgBr_2$, $HgCl_2$, HgO, $Hg(OH)_2$, etc.) and particulate-bound Hg (PBM or Hg^P). Figure 1.4 illustrates the atmospheric transport and chemistry of these species. Anthropogenic emissions of Hg occur in the form of Hg^0, as well as GOM and PBM (Pacyna et al., 2010). Natural sources occur exclusively as Hg^0 (Mason 2009). Reactive Hg is partitioned in the gaseous (GOM) or particulate (PBM) phases, depending on temperature and local levels of particulates in the atmosphere (Rutter and Schauer, 2007a; b). Both GOM and PBM are rapidly removed from the atmosphere by wet and dry deposition, with a lifetime of several days in the atmosphere. In contrast, Hg^0 has a much longer lifetime in the atmosphere (6-12 months) and can thus be transported on global scales (Lindberg et al., 2007). This leads to relatively uniform atmospheric concentrations of Hg^0 (e.g. Kellerhals et al., 2003; Wangberg et al., 2007; Wang et al., 2007). Therefore, Hg is treated as both a global and local pollutant (AMAP/UNEP, 2008).

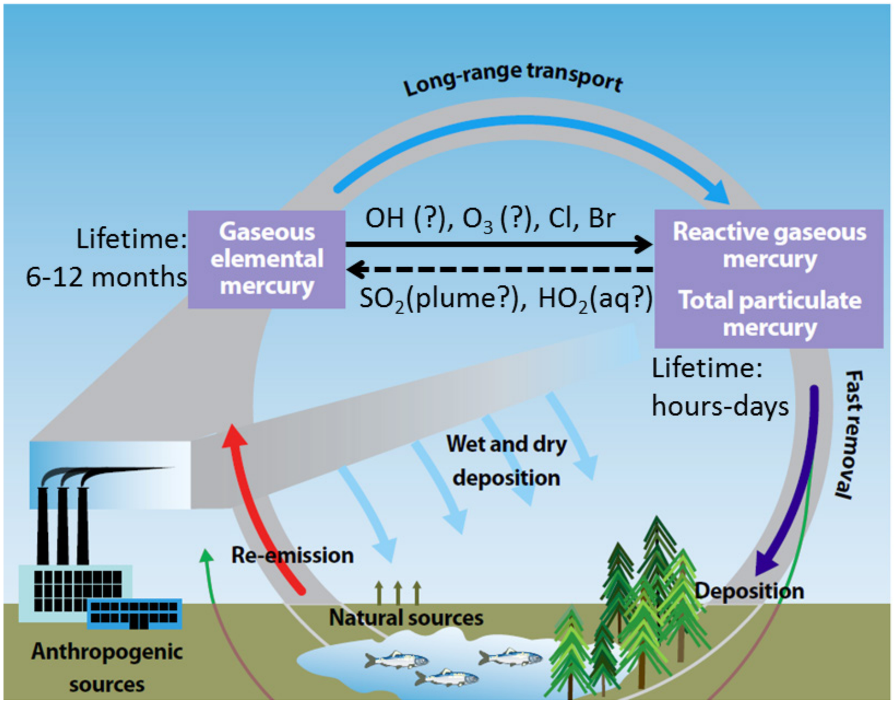

Figure 1.4: Atmospheric transport and chemistry of Hg species in the atmosphere from "The global atmospheric mercury assessment: sources, emissions and transport", by UNEP-Chemicals, copyright 2008 United Nations. Reprinted with the permission of the United Nations.

As the principal form of Hg (> 98%; Gustin and Jaffe 2010) present in the atmosphere, Hg^0 is slowly oxidized to Hg^{II} by different oxidants. The main oxidants reacting with Hg^0 are not well known and the kinetic rates for many reactions are poorly constrained (e.g., Hynes et al., 2009), probably because of the extremely low concentrations of Hg^{II} in the atmosphere (~10's of pg sm^{-3}, even much lower for individual speciated Hg) and the subsequent large measuring uncertainty (Gustin and Jaffe, 2010). Possible mechanisms include the oxidation by gaseous hydroxyl radicals (OH), gaseous and aqueous ozone (O_3), NO_3 radical as well as halogens (Cl, Br, BrO) (Hynes et al., 2009). Initially, OH and O_3 were assumed to be the major oxidants in most global Hg models (e.g. Selin et al., 2007; Lin and Tao 2003) because of the rapid rates of oxidation measured in the laboratory (Sommar et al., 2001; Pal and Ariya, 2004a; b; Hall, 1995). However, later analysis demonstrated that oxidation by O_3 and OH might be too slow under atmospheric conditions as a result of the rapid thermal dissociation of intermediates HgOH and HgO (Goodsite et al., 2004; Calvert and Lindberg 2005; Hynes et al., 2009 and references therein). Observations in Polar Regions (e.g. Steffen et al., 2008), ab-inition calculations (e.g. Goodsite et al., 2004), as well as global model calculations (Holmes et al., 2006; 2010) have shown that the reaction between Hg^0 and Br atom could be fast enough to be the predominant global sink of Hg^0.

Most models also include aqueous reduction of Hg^{II} to Hg^0 in cloud droplets (e.g., Lin and Tao 2003; Selin et al., 2007), but there are no direct laboratory measurements for this reaction. In the plumes of large point sources such as coal-fired power plants, the measured Hg^{II} fraction is lower than that measured near the stack, despite the total Hg concentrations being essentially conserved (e.g. Weiss-Penzias et al., 2011). This suggests a rapid *in situ* reduction of Hg^{II} to Hg^0 in the plume (Edgerton et al., 2006; ter Schure et al., 2011). The mechanisms associated with reduction are still uncertain; one possibility is reaction with the high concentrations of SO_2 from coal combustion (Edgerton et al., 2006).

Surface observations show that global background concentrations of total Hg are 1.5 - 1.7 ng/m^3 in the Northern Hemisphere and 1.1-1.3 ng/m^3 in the Southern Hemisphere (Lindberg et al., 2007; Ebinghaus et al., 2009; and references to many other studies). The measured concentrations are much higher in urban areas and polluted regions near to major anthropogenic sources such as mining (e.g. 4.4±2.7 ng/m3, Baltimore, Sheu et al., 2002; 9.8±4.0 ng/m3, Mexico City, Ebinghaus et al., 2009; 0.1-5 µg/m3 at Almaden, Spain, Ferrara et al., 1998). The spatial coverage of the land-based measurements remains relatively sparse (Ebinghaus et al., 2009), and it is only over the last decade that observation networks have been developed in North America and Europe such as the Canadian Atmospheric Mercury Measurement Network (CAMNet), Atmospheric Mercury Measurement Network (AMNet), Mercury Deposition Network (MDN), Mercury Species Over Europe (MOE); as well as independent measurements with much less spatial coverage over other regions. Cruise measurements of atmospheric Hg remain sporadic and have been conducted over the Arctic, Atlantic, Pacific, Southern Oceans, Baltic and North Seas and the Mediterranean (Sprovieri et al., 2009). The measurement over the polar regions including both the Arctic and Antarctic mainly focus on the atmospheric mercury depletion events (AMDEs) as well as the role of snow and ice surfaces in the Hg cycle (Dommergue et al., 2009). In early measurements, only the Hg^0 or TGM (total gaseous mercury, defined as the sum of Hg^0 and RGM) were measured (e.g. CAMNet). Since the 2000s, the development of automated instruments (TEKRAN, Ebinghaus et al., 2009) has allowed the measurement of RGM and PBM. The RGM and PBM levels at remote and background regions are on the order of several pg/m^3 (e.g. RGM: 5±5 pg/m3 and PBM: 6±7 pg/m^3 at Point Petre, Han et al., 2004; RGM: 2-3 pg/m^3 at rural Michigan, Lyman and Keeler, 2005), while elevated levels were observed over high elevation sites (e.g. 50 pg/m^3 for RGM and 4.4 pg/m^3 for RGM and PBM, respectively, at Mount Bachelor, Swartzendruber et al., 2006) as well as urban and polluted regions (e.g. 21 pg/m^3 for RGM and 39 pg/m^3 at Baltimore in 1998, Sheu et al., 2002).

1.6 Hg chemistry in the ocean

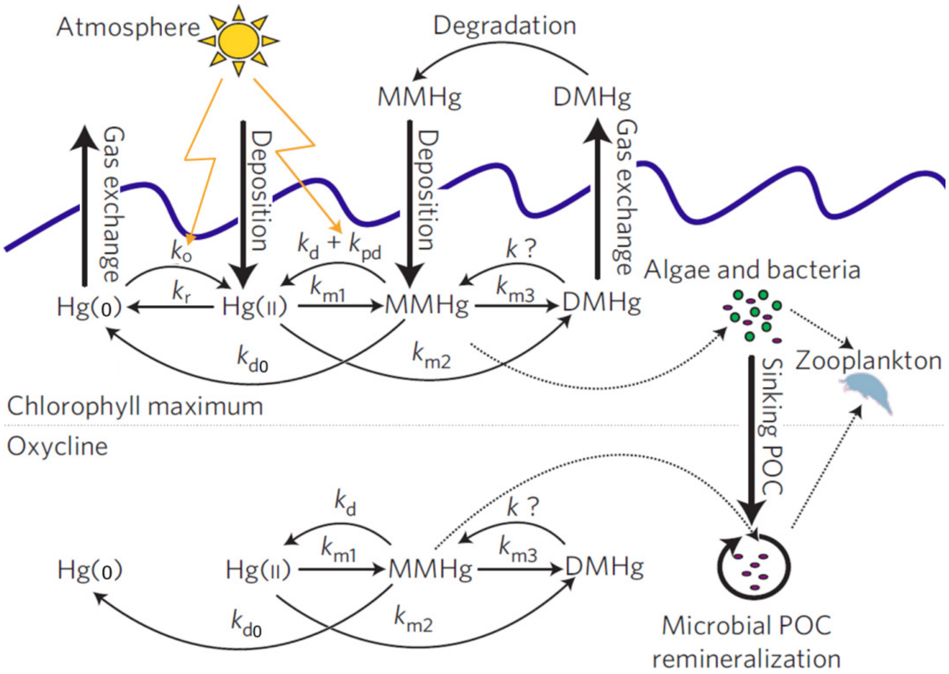

Figure 1.5: Conceptual model of methylmercury (MeHg) chemistry in marine waters. The various methylation and demethylation processes are represented by black arrows with corresponding reaction coefficients along with associated photochemical and biological processes: k_o: photo-chemical oxidation of Hg^0_{aq} to Hg^{II}_{aq}; k_r: photo-chemical and biological reduction of Hg^{II}_{aq} to Hg^0_{aq}, the biological pathway is associated with the production process of phytoplankton, which only exists in the euphotic zone; k_{m1}, k_{m2}, k_{m3}: methylation process facilitated by organic matter remineralization; k_d, k_{d0}, k_{pd}, k: demethylation process facilitated either by photo or microbiological activities. Adapted by permission from Macmillan Publishers Ltd: Nature Geosciences Lehnherr et al., 2011, copyright 2011.

The ocean contains 50 times more Hg than the atmosphere (Mason et al., 1994). Air-sea exchange is an important source for Hg to the atmosphere (Figure 1.3). Furthermore, once in the ocean inorganic Hg species are transformed to toxic methylmercury (MeHg) species (Fitzgerald et al., 2007; Mason et al., 2012). As seen in Figure 1.2, anthropogenic Hg emissions increase and decrease on timescale of decades to centuries. The timescales of ocean response to atmospheric input vary with depth, ranging from days to months in the surface ocean, decades to century in the intermediate ocean, and centuries to millenniums in the deep ocean. Thus while the surface ocean will equilibrate rapidly with atmospheric Hg composition, the intermediate and deep ocean concentrations will respond with a lag time of decades to centuries (Sunderland and Mason, 2007; Strode et al., 2010). As a result of the long memory of the ocean, the ocean re-emission flux not only reflects the strength of current level of anthropogenic emissions, but also the legacy of past anthropogenic emissions. Therefore, ocean re-emission fluxes and atmospheric deposition fluxes will not respond immediately to changes in anthropogenic emissions. For example, the modeling study of Amos et al. (2013) shows that if anthropogenic Hg emissions are kept constant at their present day value, global Hg deposition will continue to increase, and at least a 50% decrease in primary anthropogenic Hg emissions is required to maintain the Hg deposition to present-day levels by 2050.

Within the ocean, Hg cycles among elemental (Hg^0_{aq}), divalent inorganic (Hg^{II}_{aq}), methyl (MMHg), dimethyl (DMHg), and particulate bound (Hg^P_{aq}) mercury (Mason and Fitzgerald, 1993). Figure 1.5 highlights some of the main pathways interconverting these Hg species in the ocean. Based on previous Hg budget studies (Mason and Sheu 2002; Lamborg et al., 2002; Sunderland and Mason 2007; Mason et al., 2012; Amos et al., 2013), atmospheric wet and dry deposition in the form of Hg^{II} is the most important source of Hg to the ocean (10-29 Mmol/yr). Other sources include riverine input of Hg^{II} at ocean margin (1-2.9 Mmol/yr) and atmospheric deposition of MMHg (0.05-0.15 Mmol/yr), but are much smaller. A large fraction of the Hg^{II}_{aq} in the surface ocean is reduced back to Hg^0_{aq} via biological and photochemical processes (Mason et al., 1995; Amyot et al., 1997; Rolfhus and Fitzgerald, 2001), which leads to a sea-air evasion flux because of the low solubility of Hg^0_{aq}. This Hg^0 evasion flux is the major pathway of Hg leaving the ocean (10-15 Mmol/yr). A fraction of Hg^{II}_{aq} and MMHg can be absorbed onto suspended particulate matter to form Hg^{P}_{aq} (Mason and Fitzgerald, 1993; Mason et al., 1998), which can then sink to the deep ocean along with the exported particulate organic carbon (POC) pool (Mason et al., 1994). When reaching the ocean floor, the sinking Hg undergoes sedimentation, which is another pathway for Hg to leave the ocean water (1-2 Mmol/yr). In subsurface waters, MeHg species and related methylation and demethylation processes play a center role for Hg chemistry. As a substrate for microbial activity, i.e. remineralization, the sinking POC facilitates water column methylation of Hg^{II}_{aq} and the formation of MMHg and DMHg (Sunderland et al., 2009). In the water column, certain enzymes (e.g. encoded by the *mer* operon) can demethylate MeHg back to inorganic Hg (Schaefer et al., 2004; Rio Segade et al., 2010). There are two types of demethylation: oxidative and reductive pathways (Rio Segade et al., 2010). The former is much faster and forms Hg^{II}_{aq}, while the latter forms Hg^{0}_{aq} (Lehnherr et al., 2011). Because of the fast demethylation and particle scavenging, MMHg has a short lifetime (2-5 days) and would only travel 20-200 km before 90% is demethylated (Lehnherr et al., 2011).

Measurements of Hg concentrations in the ocean started 30 years ago, and, while they still remain relatively sparse, the coverage of data has been increased in recent years, especially because of the on-going GEOTRACES program (e.g. Sunderland et al., 2009; Cossa et al., 2011). Figure 1.6 summarizes the locations of cruises in the ocean where water column profiles with speciation measurements for Hg have been made. These observations will provide new constraints for ocean Hg models. Aqueous Hg measurements are reported as dissolved gaseous (DGM), reactive (Hg_R), particulate (Hg^{P}_{aq}), methylated (MeHg) or total mercury. Reactive Hg is defined as Hg that can be reduced by $SnCl_2$, including Hg^{0}_{aq} and Hg^{II}_{aq}, as well as inorganic Hg ions and kinetically facile organic complexes (Lamborg et al., 2003). DGM includes Hg^{0}_{aq} and DMHg, both of which are volatile. The measured MeHg accounts for both MMHg and DMHg.

The particulate Hg is measured by filter method, while the total Hg includes all the Hg species mentioned above. Although not displaying a "nutrient-type" profile (e.g., N, P, Si), the total Hg concentrations in surface water can be modestly depleted compared with deeper depths due to particle scavenging. In addition, total Hg concentration peaks are frequently observed within or just above the thermocline region in the water column. This is close to the behavior of nutrients because Hg is bioactive, i.e. association with soft tissue (dead organic material) remineralization in subsurface waters (Fitzgerald et al., 2007; Mason et al., 2012). Other alternative type of profiles are also observed, such as "surface-enrichment" and "conservative" profiles, which are caused by the atmospheric deposition enhancement at the surface (Gill and Bruland, 1987).

Based on the rather limited observations in different ocean basins, as summarized in Mason et al. (2012), the mean total Hg concentrations in the deep (below 1,500 m) far offshores water masses are typically 1.0-2.3 pM, with most reported surface water (mixed layer) total Hg concentrations are 0.3-1.7 pM, and 1.1-2.9 pM in subsurface waters (below mixed layer but above the permanent thermocline). Significant horizontal gradient exist for the total Hg concentrations over the entire water column, with higher values over North Atlantic (2.1±0.8 pM), medium values over Equatorial Atlantic (1.7±0.7 pM), Equatorial Pacific (1-2 pM), and Southern Ocean (0.6-2.8 pM), and lower values over North Pacific (1.0±0.5 pM) (Mason et al., 2012 and references therein). The Hg^{II}_{aq} is particle-reactive and subject to scavenging at depth with higher concentrations over deep ocean (Fitzgerald et al., 2007). Observations over North Atlantic, Equatorial Pacific and Southern Ocean indicate that Hg_R often accounts for 30-35% of the total Hg, with varied fraction (20-80%) as Hg^{II}_{aq} (Mason et al., 1993; Mason et al., 1998; Cossa et al., 2011). The concentrations of Hg^0_{aq} are lower near the ocean's surface because of the depletion by evasion to the atmosphere. Highest concentrations of Hg^0_{aq} are often observed at intermediate depths (~1,000 m), suggesting production of Hg^{0}_{aq} from in situ reduction of Hg^{II}_{aq}. Deep ocean concentrations of Hg^{0}_{aq} generally decrease or remain nearly unchanged with depth (e.g. Mason et al., 1998). The Hg^{P}_{aq} are only measured over the surface ocean with low concentrations (35±20 fM) (Mason et al., 1998). Observations of MeHg are much sparser than for inorganic species. Typical methylmercury concentrations range between 100 and 200 fM, accounting for ~10% of the total Hg concentrations (Mason et al., 2012). The MeHg concentrations are low in open ocean surface waters because of its rapid photo-dissociation, and reach a maximum at intermediate depths especially with low oxygen concentrations. The MeHg concentrations are low and relatively constant in deeper waters (> 1,000 m) (Mason et al., 2012). This type of distribution is indicative of *in situ* production, which is associated with the remineralization of sinking organic matters and peaks in intermediate waters (< 1,000 m) (Martin et al., 1987; Sunderland et al., 2009).

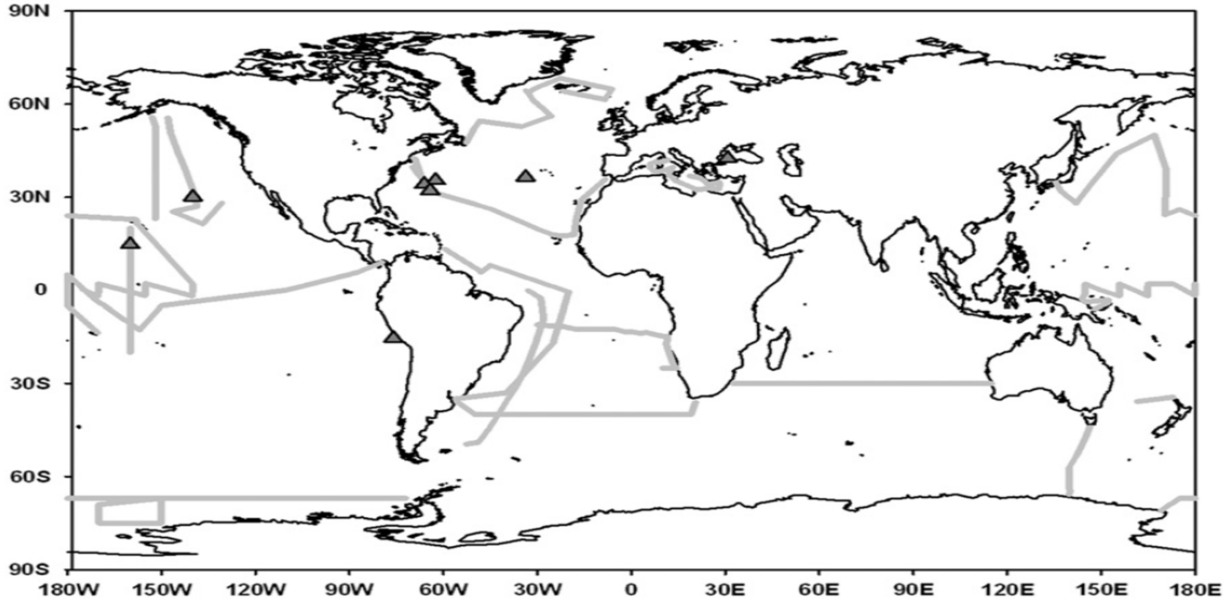

Figure 1.6: Tracks of cruises in the ocean where water column profiles Hg speciation measurements have been made. Triangles indicate cruises indicate cruises where profiles were not measured at all the sites or stations. Reprinted from Environmental Research, 119, Mason et al., Mercury biogeochemical cycling in the ocean and policy implications, 101-117, Copyright 2012, with permission from Elsevier.

1.7 Thesis work

Although our knowledge of the biogeochemical cycling of Hg has greatly improved over the past decade, large gaps still remain and continue to confound our ability to constrain the global Hg budget (e.g. Lindberg et al., 2007; Pirrone and Mason, 2009). Especially, there is on-going debate about the kinetics of atmospheric Hg oxidation and reduction reactions (e.g. Holmes et al., 2009; 2010; Subir et al., 2011). The atmosphere is poorly sampled spatially, especially for speciated Hg concentrations. Trends in wet deposition and atmospheric concentrations remain difficult to constrain given the scarcity of long-term measurements (e.g. Temme et al., 2007). Anthropogenic impacts on oceanic Hg are poorly understood and observed spatial patterns and temporal trends are not fully explained (Fitzgerald et al., 2007).

This dissertation addresses four objectives:

1) Constrain the origin, chemical transformation and deposition of Hg over North America;
2) Understand and attribute the recent trends of Hg wet deposition over North America;
3) Understand the ocean's role in the biogeochemical cycling of anthropogenic Hg; and
4) Evaluate the human perturbation from anthropogenic Hg emissions to the ocean Hg cycle.

This work uses the GEOS-Chem global atmosphere-ocean-land mercury simulation. In order to address the first two objectives, I have developed a new high-resolution (1/2° latitude×2/3° longitude) nested-grid Hg simulation over North America embedded within the global low resolution (4° latitude×5° longitude) GEOS-Chem simulation. For the latter two objectives, I have implemented Hg biogeochemistry in the 3D offline ocean tracer model OFFTRAC, and coupled it to GEOS-Chem. These four objectives span different scales in time (from natural conditions ~pre-1450, pre-industrial ~ 1850, to present-day) and space (global to regional scales) over multiple media (atmosphere, ocean, and land). This is necessary because:

1) I need to take into account the full evolution of Hg cycle in a time-dependent fashion because of the ubiquitous recycling of Hg on long and short timescales; and

2) I need to critically assess assumptions about physical and chemical processes in the GEOS-Chem Hg model via systematic comparisons to observations focusing over North America, where the Hg observations are the most condensed over the globe.

Chapter 2 ("*Nested-grid simulation of mercury over North America*", published in Atmospheric Chemistry and Physics, Zhang et al., 2012) develops a high-resolution nested-grid Hg simulation employing GEOS-Chem and closely compares the model results with observations over North America. Building on the nested-grid model and findings from Chapter 2, in Chapter 3 (*"Decreases in mercury wet deposition over the United States during 2004 – 2010: Roles of domestic and global background emission reductions",* submitted to Atmospheric Chemistry and Physics) I evaluate recent observed trends of Hg wet deposition over North America, and examine the relative roles of domestic emission reductions and declines in global background concentrations. Chapter 4 ("*Natural biogeochemical cycle of mercury in a global three-dimensional ocean tracer model",* in preparation for Global Biogeochemical Cycles) develops the first global 3-D oceanic transport and chemistry model for Hg and examines the natural marine Hg cycle. Using this model, Chapter 5 ("*Anthropogenic mercury in a coupled global three-dimensional atmosphere-ocean tracer model*", in preparation for Global Biogeochemical Cycles) estimates the human perturbation to the oceanic Hg cycle and analyzes the main mechanisms and pathways controlling this process. Chapter 6 discusses the major uncertainties associated with the Hg biogeochemical cycling. Conclusions and summary are presented in Chapter 7.

Chapter 2

NESTED-GRID SIMULATION OF MERCURY OVER NORTH AMERICA

2.1 Introduction

Mercury (Hg) is a ubiquitous trace metal in the atmosphere and is emitted by both natural (Mason, 2009) and anthropogenic sources such as coal combustion, waste incineration and gold mining (Streets et al., 2009; Pacyna et al., 2010; Pirrone et al., 2009). Anthropogenic emissions of Hg occur in the long-lived elemental form (Hg(0)), but also as short-lived oxidized mercury (Hg(II)) and particulate-bound mercury (Hg(P)). Both Hg(II) and Hg(P) are rapidly removed by wet and dry deposition near source regions, while Hg(0) can be transported on global scales. Hg(0) is then deposited over remote areas via dry deposition of Hg(0) itself or through oxidation to Hg(II), followed by its subsequent deposition (Lindberg et al., 2007). Once in aquatic ecosystems, Hg may be converted to the neurotoxin methylmercury, which can bioaccumulate in the food chain (Morel et al., 1998). Human exposure occurs via consumption of fish and seafood (Mergler et al., 2007; Sunderland, 2007). Because of its adverse effects on human health and the environment, Hg pollution is being actively regulated at national levels and there are now ongoing international negotiations to achieve a global legally-binding agreement for Hg emission reductions (UNEP, 2012).

A number of global Hg models have been developed to interpret observations, test chemical mechanisms and constrain the global Hg budget (e.g. GISS-CTM: Shia et al., 1999;

GEOS-Chem: Selin et al., 2007; GRAHM: Dastoor and Larocque, 2004). However, these models often have coarse horizontal resolution (~200 – 1000 km) and thus lack the resolution needed for detailed evaluation at the regional scale. Regional models have higher resolution over a limited domain, which is necessary to resolve the observed high spatial variability in Hg deposition (Keeler et al., 2006; Dvonch et al., 2005). A disadvantage of these models is their sensitivity to assumed initial and lateral boundary conditions. One way to solve this issue is to use a global model to provide initial and boundary conditions in a multi-scale modeling approach (Bash, 2010; 9; Lin and Tao, 2003; Pan et al., 2007; Seigneur et al., 2001; Vijayaraghavan et al., 2008). A significant problem with this approach, however, is that the regional and global models often use different assumptions about Hg emissions, chemistry, deposition, and meteorology. Use of different global models to define boundary conditions leads to large variations in regional patterns of atmospheric Hg concentrations, as well as wet and dry deposition (Bullock et al., 2008; Bullock et al., 2009; Pongprueksa et al., 2008).

In this chapter, we describe the development of a new nested North American Hg simulation with higher resolution (1/2° latitude by 2/3° longitude) in the GEOS-Chem model. This North American window is imbedded in a lower resolution (4°×5°) global GEOS-Chem simulation. Chemistry, deposition, emissions, and meteorology are self-consistent between the nested and global domains. The horizontal resolution of the nested-grid domain (~50 km) is comparable to that used in many regional scale Hg models (for example, most published work with CMAQ uses 36 km), however the vertical resolution is much higher (surface to 10 hPa: 14 vertical levels in CMAQ versus 40 levels in GEOS-Chem).

The aims of this chapter are to 1) evaluate the GEOS-Chem nested-grid Hg simulation by comparisons to observations of wet deposition and atmospheric concentrations over North

America; 2) examine the impact of resolution (4°×5° versus 1/2°×2/3°) and partitioning of anthropogenic North American emissions on model predictions; 3) assess the origin of wet deposition over the U.S. in the nested-grid GEOS-Chem model and quantify the relative impacts of domestic versus global emissions on deposition.

2.2 Model description

2.2.1 GEOS-Chem global Hg simulation

GEOS-Chem is a global chemical transport model (Bey et al., 2001), which is driven by assimilated meteorological observations from the NASA Goddard Earth Observing System (GEOS). The most recent meteorological fields (GEOS-5) have a spatial resolution of 1/2° latitude by 2/3° longitude, with 72 hybrid eta levels from the surface to 0.01 hPa. The lowest 2 km are resolved with 13 layers. For input to the GEOS-Chem global simulation, these fields are degraded horizontally to 4°×5° and vertically to 47 levels due to computational limitations. We use GEOS-Chem version v9-01-02 in this chapter (http://acmg.seas.harvard.edu/geos/).

The GEOS-Chem atmospheric Hg simulation is described and evaluated in Selin et al. (2007), with recent updates in Hg chemistry and deposition by Holmes et al. (2010) and Amos et al. (2011). The model includes two atmospheric mercury species: elemental Hg (Hg(0)) and divalent Hg (Hg(II)). Anthropogenic Hg emissions are from the Global Emission Inventory Activity (GEIA) 2005 inventory of Pacyna et al. (2010), with a native spatial resolution of 0.5°×0.5°. This inventory provides anthropogenic emissions for Hg(0), Hg(II), and Hg(P). We combine both Hg(II) and Hg(P) emissions into our single Hg(II) tracer. Over the U.S. and Canada the GEIA anthropogenic inventory is overwritten with more recent regional inventories (see Section 2.2). The resulting global anthropogenic emissions are 1,900 Mg/a. Natural sources account for a total of 6,600 Mg/a, including 4,900 Mg/a (3,000 Mg/a net evasion) from air-sea exchange (Strode et al., 2007; Soerensen et al., 2010a), 1,400 Mg/a from land (Selin et al., 2008; Amos et al., 2012), 220 Mg/a from open fire biomass burning in 2008-2009 (Global Fire Emission Database version 2, assuming a Hg/CO emission ratio of 100 nmol/mol as suggested by Holmes et al., 2010), and 140 Mg/a from snow re-emissions (Holmes et al., 2010).

Considerable uncertainty remains on the Hg(0) oxidation mechanisms and their kinetics (Gårdfeldt et al., 2001; Calvert and Lindberg, 2005; Si and Ariya, 2008). In the original GEOS-Chem simulation, Selin et al. (2007) assumed OH and O_3 to be the main oxidants for Hg(0). They also included aqueous-phase photochemical reduction of Hg(II), proportional to OH concentrations and scaled to match constraints on Hg lifetime and seasonal variation. However, work by Calvert and Lindberg (2005) and Hynes et al. (2009) suggest that the oxidation of Hg(0) by OH and O_3 is too slow to be significant in the atmosphere. Therefore, Holmes et al. (2006; 2010) updated GEOS-Chem to use Br atoms as the sole oxidant for Hg(0), with kinetic parameters from Donohoue et al. (2006), Goodsite et al. (2004) and Balabanov et al. (2005). They found that Hg + Br chemistry, like the previous Hg + OH/O_3 chemistry, can reproduce most mercury observations, with some improved prediction of the interhemispheric gradient in total gaseous mercury (TGM) concentrations and the TGM concentrations in polar regions. Holmes et al. (2010) included aqueous-phase photochemical reduction of Hg(II), scaled to NO_2 photolysis. We follow the Holmes et al. (2010) chemical mechanism in this work.

The global bromine fields are described in Holmes et al. (2010), and are based on 3-D monthly archived Br concentrations from the p-TOMCAT model in the troposphere (Yang et al., 2005) and from NASA's Global Modeling Initiative model in the stratosphere (Strahan et al., 2007). The resulting BrO column concentrations are consistent with satellite observations (Richter et al., 2002; Sioris et al., 2006). Over polar regions, elevated concentrations of Br atoms can be produced by refreezing of open leads during spring (Simpson et al., 2007), leading to so-called bromine explosion events and rapid depletion of Hg(0) (Steffen et al., 2008). This process is parameterized in GEOS-Chem by assuming 5 ppt BrO in the polar boundary layer during springtime over areas with sea ice, sunlight, stable conditions and temperatures below 268K (Holmes et al., 2010).

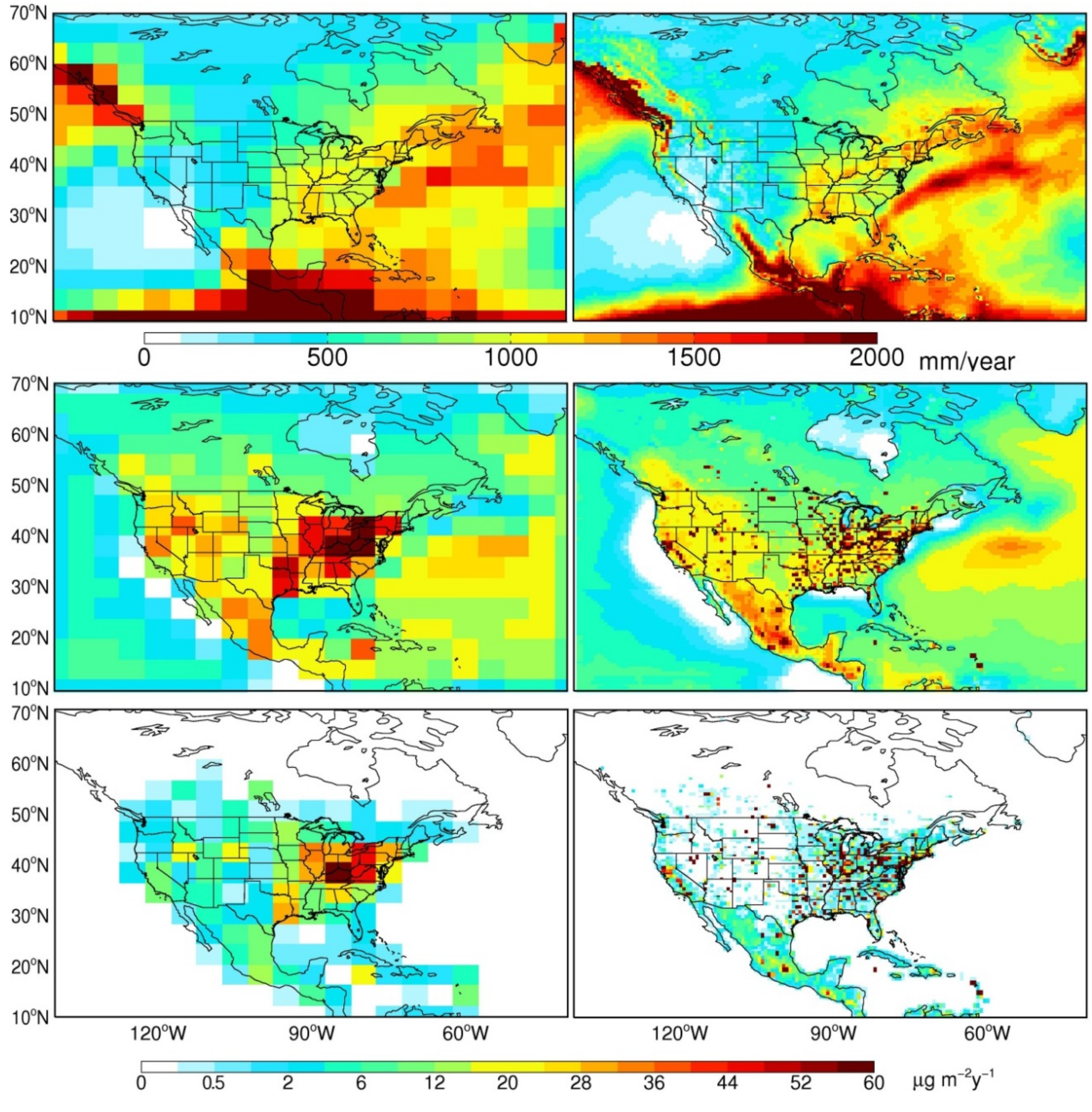

Figure 2.1: Comparison between the global (4°×5°, left column) and nested (1/2°×2/3°, right column) models over the North American domain. Top row: Total surface precipitation in 2008. Middle row: total Hg emissions including natural and anthropogenic sources (IPR simulation). Bottom row: Anthropogenic Hg emissions based on the EPA NEI 2005 inventory for the U.S., the NPRI 2005 inventory for Canada, and the GEIA2005 inventory for Mexico.

We assume that Hg(II) is in equilibrium between gas and particulate phase at all times. The partitioning between these two phases is based on the empirical relationship derived by Amos et al. (2012) and is calculated as a function of temperature and monthly mean fine particulate matter concentrations. This empirical relationship was obtained from long-term observations of gas phase Hg(II) (reactive gaseous mercury, RGM) and particulate-bound Hg(II) (particulate bound mercury, PBM) at five sites over North America (Edgerton et al., 2006; Graydon et al., 2008; Lyman and Gustin, 2009; Rutter and Schauer, 2007, Sigler et al., 2009).

GEOS-Chem simulates wet scavenging of Hg(II) and dry deposition of Hg(0) and Hg(II) following the scheme of Liu et al. (2001) and the resistance-in-series scheme of Wesely (1989), respectively. We assume complete retention of Hg(II) during freezing of supercooled water in mixed-phase clouds, but no scavenging during vapor condensation to cloud ice (Holmes et al., 2010; Wang et al., 2011). Below-cloud scavenging by snow is included only for Hg(II) in the aerosol phase (Holmes et al., 2010; Amos et al., 2012). The loss of Hg(II) via uptake onto sea-salt aerosol and subsequent deposition in the marine boundary layer is also included in this chapter (Holmes et al., 2009; 2010).

2.2.2 Nested-grid Hg simulation

We have implemented a new nested-grid capability with higher resolution in the GEOS-Chem Hg simulation. We use results from the global (4°×5°) Hg simulation as initial and boundary conditions for a nested-grid simulation over the North American domain (defined as 10° – 70°N and 40° – 140°W). The nested model is driven by GEOS-5 meteorological fields at their native horizontal resolution (1/2°×2/3°). Both the nested and global models use the same vertical resolution. This one-way nesting approach was first developed in GEOS-Chem by Wang et al. (2004a; 2004b) to examine CO and NO_x variability over Asia, and has also been applied to understand ozone and aerosol chemistry over North America (Fiore et al., 2005; Li et al., 2005; Park et al., 2006). These simulations used an earlier version of the GEOS fields (GEOS-3) with a native resolution of 1°×1°. More recently, Chen et al. (2009) updated the nested-grid CO simulation over Asia to use the newest GEOS-5 data, allowing for higher resolution. Chen et al. (2009) found that the higher spatial resolution allows for more efficient advection-related ventilation of the lower atmosphere and can better resolve frontal lifting. The nested model can also resolve the variability of emission densities over individual cities.

We first conducted a global 4°×5° resolution simulation (referred to as the global model) for 2004 – 2009, archiving tracer mixing ratios of Hg(0) and Hg(II) at the lateral boundaries of the nested model every 3 hours. The nested model was then run for 2008 – 2009 using these 3-hourly lateral mixing ratios, with an initial spin-up time of one month starting with initial conditions from the global model. Figure 2.1 (top panels) compares the meteorological data driving the global and nested models, using precipitation as an example. The nested model resolves many fine features in the spatial distribution of precipitation which are lost by horizontal averaging at the 4°×5° resolution. In particular, orographic precipitation is identifiable in the mountain ranges along the west coast of North America, the Rocky Mountains and the Appalachian Mountains. In addition, details in precipitation over the Gulf of Mexico and Northwest Atlantic are more clearly apparent.

Anthropogenic Hg emissions in the U.S. were obtained from the 2005 EPA NEI inventory (NEI05, http://www.epa.gov/ttn/chief/eiinformation.html). The NEI05 inventory includes Hg emissions from point, nonpoint (area), and mobile sources within different sectors. We assign the point source Hg emissions into the corresponding model grid box according to geographic location. For nonpoint and mobile sources, the county-specific Hg emissions were distributed into the model grid system with the surrogate data provided by the EPA (http://www.epa.gov/ttn/chief/emch/spatial/newsurrogate.html). Mercury speciation profiles are reported for all coal-fired power plants (CFPPs) individually in the NEI05 inventory. For other sources, we use the source-specific emission profiles reported in the inventory. As in the global model, we merge Hg(II) and Hg(P) emissions into the Hg(II) tracer in the nested model. Over the continental U.S., the 2005 anthropogenic Hg emissions are 111.3 Mg/a (61.5 Mg/a Hg(0), 49.8 Mg/a Hg(II)). Point sources dominate these emissions with 104.7 Mg/a, while nonpoint and mobile sources emit 5.5 Mg/a and 1.1 Mg/a, respectively. CFPPs account for 49% of the total national anthropogenic emissions. For simplicity, we do not take into account the seasonal, weekly, and diurnal variations in Hg anthropogenic emissions reported in the NEI inventory.

Over Canada, we used emissions from the Canadian National Pollutant Release Inventory 2005 (NPRI05, http://www.ec.gc.ca/inrp-npri/). The point sources in the NPRI05 inventory were processed in a similar manner as those in NEI2005, and the area and mobile sources were spatially allocated over the model grid using population as the surrogate. The total Canadian anthropogenic Hg emissions are 6.2 Mg/a (3.8 Mg/a Hg(0), 2.4 Mg/a Hg(II)). Anthropogenic emissions from Mexico in the nested model domain are directly gridded from the GEIA emission inventory, and account for 27.9 Mg/a.

Observations collected at ground-based sites 7-15 km downwind of power plants in the Southeastern U.S. show that Hg(II) accounts for only 8-21% of total Hg (Edgerton et al., 2006; Weiss-Penzias et al., 2011). This is a factor of ~3-5 lower than the Hg(II) fraction measured in CFPPs stacks (40-70% Hg(II)). From airborne measurements downwind of a CFPP, ter Schure et al. (2011) show that reduction occurs in CFPP plumes much faster than in the background atmosphere. Lohman et al. (2006) speculated that this in-plume conversion of Hg(II) to Hg(0) could be due to reduction by SO_2. Vijayaraghavan et al. (2008) incorporated this rapid reduction into a regional Hg model with an explicit treatment of stack plume evolution. They found that this improved model performance for wet deposition in the Northeast U.S. In order to consider this process in this chapter, we modified the CFPPs Hg emission partitioning from the original 56.8% Hg(0) and 43.2% Hg(II) in the NEI and NPRI inventories to 89.2% Hg(0) and 10.8% Hg(II) over the U.S. and Canada. This effectively assumes that 75% of the CFPPs Hg(II) emissions are reduced to Hg(0) in the immediate vicinity of power plants, consistent with the Edgerton et al. (2006) and Weiss-Penzias et al. (2011). The NEI inventory assumes relatively high portions of Hg(II) in the emission profiles for waste incineration (22% Hg(0), 78% Hg(II)). Because of the high SO_2 concentration from stacks of waste incinerator (Psomopoulos et al., 2009; Stevenson 2002), we assume a similar in-plume reduction process happens to this source, and reduce the Hg(II) content from waste incineration emissions by 75%, resulting in a speciation profile of 80.5% Hg(0) and 19.5% Hg(II). We note that no measurements of Hg speciation in waste incinerator plumes have been reported, so this assumption remains speculative.

With these speciation profile changes, the resulting anthropogenic Hg emissions in North America are: 121 Mg/a Hg(0) and 25 Mg/a Hg(II). We will refer to simulations with this inventory as in-plume reduction (IPR) simulations and contrast them to our standard (STD) simulations with the original anthropogenic Hg speciation (87 Mg/a Hg(0), and 59 Mg/a Hg(II) over North America). To have self-consistent global and North American anthropogenic inventories in the IPR simulation, we also modified the Hg(0):Hg(II) speciation profile for fossil fuel combustion in Pacyna et al. (2010) from 50%:50% to 87.5%:12.5%.

Figure 2.1 (bottom panels) shows the spatial distribution of total anthropogenic Hg emissions over North America. These are held constant over the 2008 – 2009 simulation periods. Emissions are highest in coal combustion regions in the Ohio River Valley and eastern Texas. Some individual point sources such as power plants and municipal waste incinerators are distinct in the nested model, whereas they are averaged over much larger regions in the global model.

Within the nested model domain, geogenic emissions (60 Mg/a) and legacy soil emissions (130 Mg/a) are interpolated to finer resolution from the global model. Other emissions are calculated interactively within the nested model using the same algorithms as the global model, including biomass burning (10 Mg/a), oceans (280 Mg/a), soil (35 Mg/a), and snow (12 Mg/a). Figure 2.1 (middle panels) shows the total Hg emission from both anthropogenic and natural sources. Geogenic Hg emissions in the model are a significant source in western North America along a band stretching from southwest Canada to Mexico (Gustin et al., 1997). The modeled re-emissions from soil, snow and ocean generally follow the spatial pattern of anthropogenic emissions. The modeled soil, snow and ocean emissions strengths depend on meteorology, but vary by less than 15% over these two years.

The monthly concentrations of Br, BrO and OH radicals in the nested model are obtained by interpolating fields used in the global model. To evaluate the contribution from North American anthropogenic sources, we conducted a sensitivity simulation with primary anthropogenic Hg emissions from the U.S., Canada and Mexico turned off. We will refer to this simulation as the “background” simulation.

2.3 Model evaluation

We evaluated the nested-grid model against a series of observations in North America including Hg wet deposition from the Mercury Deposition Network (MDN, 2011), near surface Hg concentrations from the Atmospheric Mercury Network (AMNet, 2009) and from the Canadian Atmospheric Mercury Measurement Network (CAMNet, 2011), and tropospheric Hg concentrations observed during the ARCTAS aircraft campaign (Mao et al., 2011). We will also compare the nested model against the global model.

2.3.1 Annual mean Hg wet deposition

Figure 2.2 shows the 2008 – 2009 annual mean Hg wet deposition flux over North America predicted by the global (upper panel) and nested (middle panel) models for the STD simulation. The eastern U.S. is divided as MW (Midwest), NE (Northeast), ORV (Ohio River Valley and Mid-Atlantic), and SE (Southeast) as shown in Figure 2.2. The spatial distribution of modeled wet deposition is the result of the combined variations of anthropogenic Hg(II) emissions, free tropospheric Hg(II) concentrations and precipitation. Although the global model and the nested model have very similar large scale patterns for wet deposition, the nested model resolves more detail (Figure 2.2). In the nested model, high wet deposition fluxes occur along the coastal regions of British Columbia, Washington and Mexico due to orographic precipitation; discrete high wet deposition flux is predicted over the Rocky Mountains following precipitation (Figure 2.1). Higher spatial variability is also predicted by the nested model near point sources over the ORV and SE regions. For instance, the global model shows the highest wet deposition occurring over the grid box covering southern Indiana, Kentucky and southern Ohio. In contrast, the nested model shows elevated wet deposition flux concentrated over eastern Ohio and western Pennsylvania. Furthermore, the nested model displays more detail in land/ocean contrast in coastal regions (e.g. Florida and the western Gulf Coast), with enhanced deposition over land associated with scavenging of local emissions and enhanced precipitation. With this improvement, the nested model is able to reproduce the observed latitudinal pattern for Hg wet deposition over the SE region – the deposition flux increases with lower latitude – a feature which is smoothed out by the coarse global model.

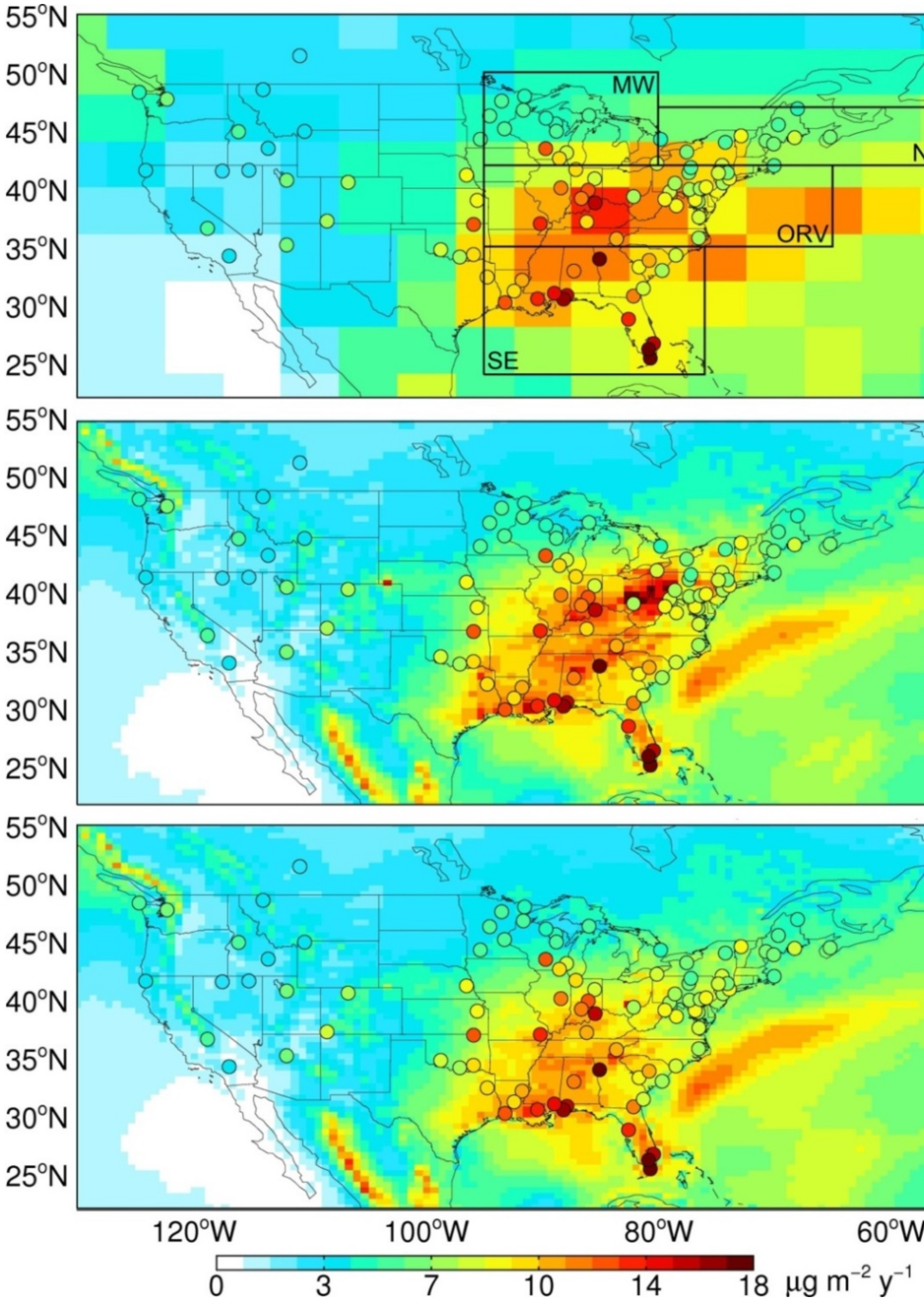

Figure 2.2: Annual mean observed (circle) and simulated (background) Hg wet deposition flux for 2008 – 2009 over North America. Observations are from the Mercury Deposition Network (MDN). The three panels correspond to different GEOS-Chem Hg simulations: global STD model (top), nested STD simulation (middle), nested IPR simulation (bottom). The four regions considered in this chapter are indicated with black boxes in the top panel: Midwest (MW), Northeast (NE), Ohio River Valley (ORV), and Southeast (SE).

Figure 2.2 also displays Hg wet deposition flux measurements from the MDN network (circles). MDN sites collect weekly integrated precipitation samples and report Hg wet deposition flux and the Hg concentration in precipitation (MDN, 2011). Here we use the annual mean wet deposition flux for 2008 – 2009 at MDN sites with at least 75% of annual data availability (95 sites are selected). One issue with the samplers used by MDN is their low snow collection efficiency (Butler et al., 2008; Prestbo and Gay, 2009). Prestbo and Gay (2009) find that the MDN annual collection efficiency of precipitation is 87.1 ± 6.5% at cold weather sites, but is unbiased at warm weather sites (efficiency = 98.8 ± 4.3%). Lynch et al. (2003) summarized the 16 sites in Pennsylvania in 2002 and found the average collection efficiency was 89% in the cold period when snow and/or ice dominate precipitation. We correct for this bias in MDN weekly wet deposition by taking into account the fraction of precipitation falling as snow in the corresponding month and assuming an 89% collection efficiency of snow. The resulting annual wet deposition increases by 2% at sites in the NE and MW regions, with an 11% increase in winter. Wet deposition over the ORV and SE (where snow accounts for 11% and <2% of annual precipitation, respectively) are nearly unaffected. All the MDN observations we show in this chapter are corrected for this snow bias.

The standard nested-grid simulation captures the general spatial pattern of MDN wet deposition, especially the east-west gradient and higher wet deposition flux over the SE region (Figure 2.2). However, the standard model systematically overestimates the observed wet deposition flux over the ORV region. As shown in Table 2.1, the mean normalized model bias is +27% in this region. For all 95 MDN sites, the model displays a -3.4% bias for annual mean wet deposition flux with a spatial correlation coefficient $r = 0.60$ (Figure 2.3, left panel). The sites with the largest positive model bias are in ORV (blue circles), while negative model bias primarily occurs in the SE (orange circles) and the central and western U.S. (denoted as OT, purple circles). Calculated regionally, the correlation coefficients vary drastically, and are largest over the OT region ($r = 0.78$, Figure 2.3), lowest in ORV ($r = 0.17$).

Table 2.1: Comparison of annual wet deposition fluxes (2008–2009) between MDN observations and the nested-grid GEOS-Chem model

Regions[a]	# of sites	Annual precipitation (cm y^{-1})[b]		Annual Hg wet deposition flux (μg m^{-2} y^{-1})		
		MDN	GEOS-5	MDN	GEOS-Chem STD simulation	GEOS-Chem IPR simulation
MW	19	6.2±2.6	5.8±1.7	7.0±4.8	5.9±2.3 (-14%[c])	5.0±2.5 (-27%)
NE	10	9.9±1.7	9.5±1.6	6.8±3.0	6.8±2.4 (+2.6%)	6.0±2.4 (-9.0%)
ORV	29	9.1±1.9	9.3±1.8	9.3±3.6	11±4.5 (+27%)	8.8±3.8 (-2.3%)
SE	20	11±2.9	10±5.2	13±5.3	11±5.4 (-14%)	10±5.2 (-20%)
All sites	95	8.1±1.3	8.1±1.5	8.8±3.6	8.3±3.4 (-3.4%)	7.2±3.2 (-16%)

The model is sampled at the location of the 95 sites selected.

[a] Regions are defined in Figure 2.2.

[b] Mean and standard deviation of monthly averaged values.

[c] The mean normalized bias, defined as the mean of $\frac{\text{model-observation}}{\text{observation}}$ × 100 is indicated in parentheses.

When we change the partitioning of anthropogenic Hg emissions in our IPR simulation (Section 2.2), the simulated Hg wet deposition flux in the ORV region decreases by 22% (Figure 2.2, bottom panel). In particular for Athens, Ohio (OH02) the model bias decreases from 200% to 20% (Figure 2.3). There are several major power plants located near this site that have a total of more than 0.5 Mg/a Hg(II) emission in the corresponding 1/2°×2/3° model grid (accounting for 3% of the total power plant Hg(II) emission of the U.S.). Smaller decreases occur over the NE (-11%), MW (-16%), and SE (-4.5%) regions, and nearly no change in the western and central U.S. due to the smaller Hg contribution from anthropogenic emissions. The IPR simulation leads to improved agreement with MDN observations over the ORV region, with a decrease in the model bias from +27% to -2.3% (Table 1) accompanied by an increase in the correlation coefficient from 0.17 to 0.61 (Figure 2.3). Over the MW, NE and SE regions the correlation coefficients improve, however the mean bias tends to worsen somewhat in the IPR simulation (MW from -14% to -27%; NE from +2.6% to -9.0%; SE from -14% to -20%, Table 2.1). As discussed in Section 2.3.2 some of the low bias in the IPR simulation is associated with seasonal underestimates in precipitation for these regions. The overall correlation coefficient for all the MDN sites increases from r = 0.60 to r = 0.78. For 70% of the MDN sites, IPR model values are within ±25% of observations. Assuming that in-plume reduction occurs in CFPP plumes and does not occur in waste incinerators plumes results in a positive model bias of +7.4% over the ORV region, only partially correcting the STD model overestimate. Vijayaraghavan et al. (2008) conducted a more complex plume-in-grid modeling of the reduction of Hg(II) in CFPP plumes and found a 10-30% reduction in wet deposition over the ORV region, partially correcting their overprediction of wet deposition in that region. Our results are consistent with this previous study.

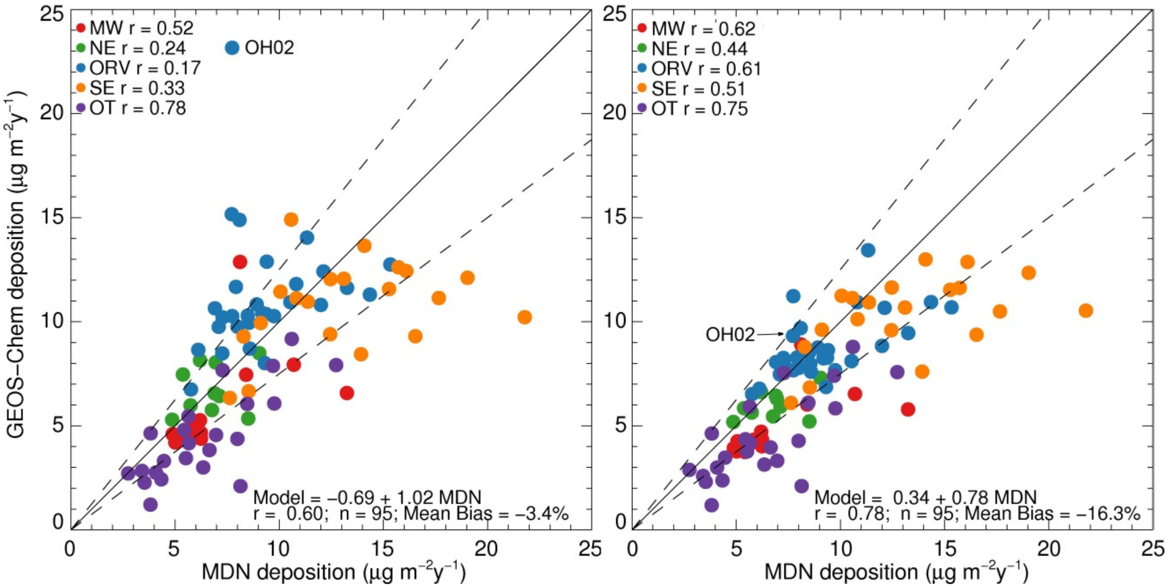

Figure 2.3: Scatter plot of observed and modeled annual mean (2008 – 2009) Hg wet deposition flux. Left panel: standard nested-grid simulation; Right panel: IPR nested-grid simulation. The solid line indicates the 1:1 line, while the dashed lines correspond to ±25%. The points are colored according to their geographic location as defined in Figure 2.2 (OT corresponds to sites west of 95˚W longitude). The correlation coefficient for each region as well as the overall regression statistics are also shown.

2.3.2 Seasonal variations in Hg wet deposition

Figure 2.4 shows the comparison of modeled monthly Hg wet deposition flux and precipitation depth with MDN observations during 2008 – 2009. The observed Hg wet deposition flux has a strong seasonality in the eastern U.S., with a peak during summer and minimum during winter (Figure 2.4, upper panels). The STD simulation generally captures this seasonality. The STD simulation overestimates observed mean Hg wet deposition over the ORV region (red line in Figure 2.4, upper panels) especially in 2009, but this overestimate is largely mitigated in the IPR simulation (green line). The IPR simulation slightly underestimates the Hg wet deposition flux over ORV during 2008, but shows no bias in terms of two-year average (Table 2.1). The GEOS-5 meteorological fields reproduce monthly precipitation observations in both the ORV and NE regions quite well (bottom panels in Figure 2.4; Table 2.1). The low bias of the IPR simulation for the MW region is associated with a 60% underestimate of wet deposition during June and July 2008. This seems to be partially caused by an underestimate in precipitation during this time.

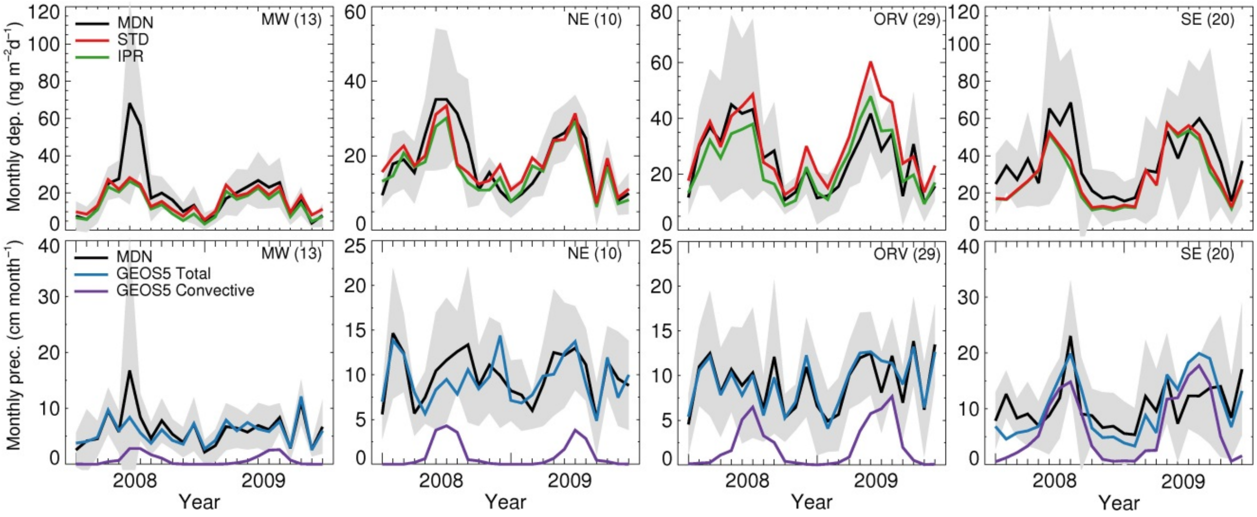

Figure 2.4: Monthly mean variation in Hg wet deposition fluxes (ng m^{-2} d^{-1}) and precipitation (cm $month^{-1}$) during 2008 – 2009 for four regions over the eastern United States. Top row: MDN observations (black line, with shaded area indicating the standard error) are compared to the STD (red line) and the IPR (green line) nested simulations. Bottom row: Surface precipitation observed at MDN sites is compared to total and convective GEOS-5 precipitation.

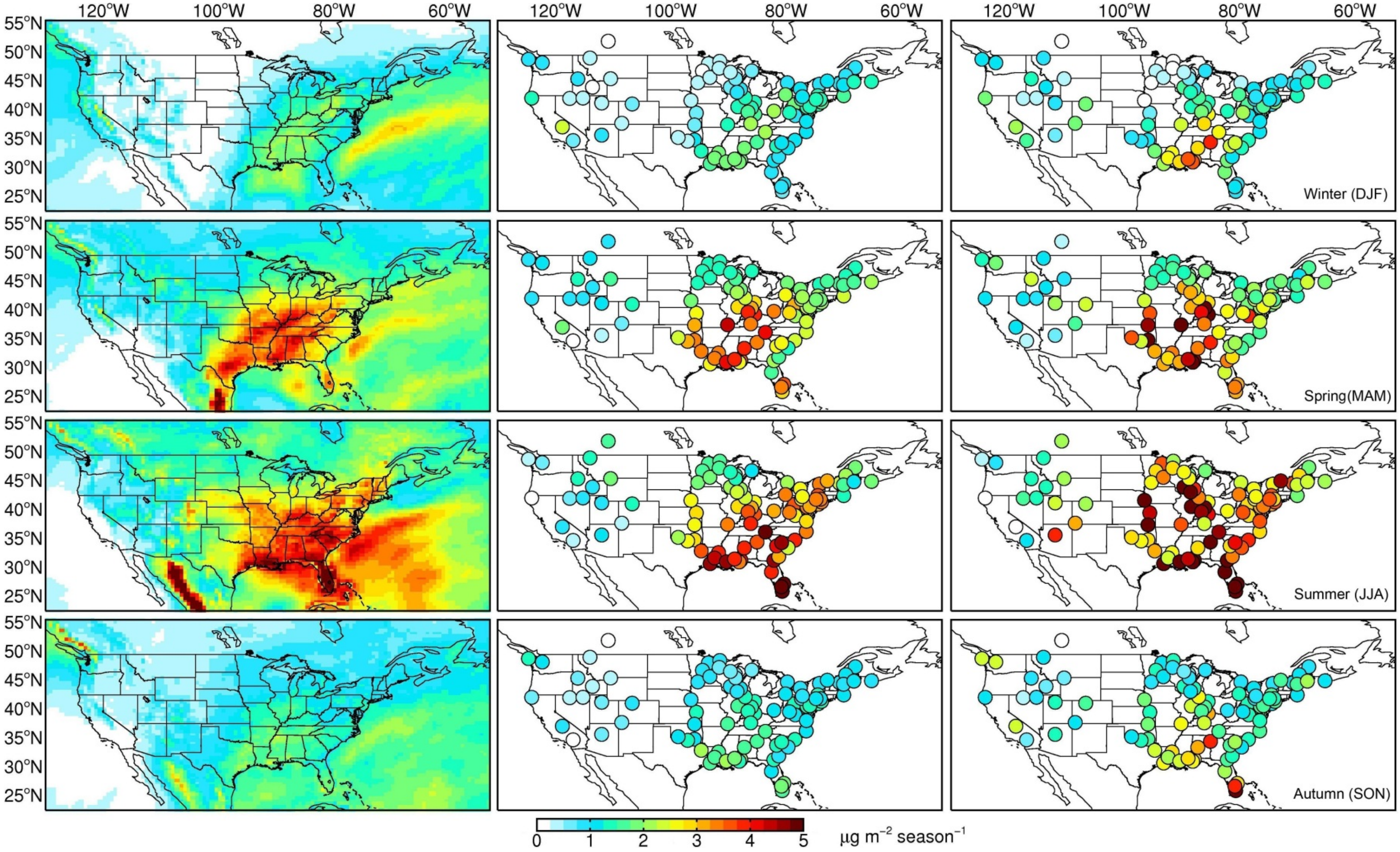

Figure 2.5: Seasonal variations in the Hg wet deposition flux for 2008 – 2009. From top to bottom: winter (DJF), spring (MAM), summer (JJA), and autumn (SON). The first column shows the spatial distribution of the IPR nested-grid model wet deposition; the second column shows the model values extracted at MDN sites; the third column shows the observed wet deposition at MDN sites.

Over the SE, the IPR simulation underestimates MDN observations from August to October. While the model reproduces the high deposition rates observed over Louisiana, Mississippi, and Alabama, it does not reproduce the very high wet deposition rates (10-12 μg m^{-2} $season^{-1}$) observed at sites in Florida (Figure 2.5). During summer, the model meteorological fields capture the observed high precipitation rates observed in the SE in 2008 (15-20 cm $month^{-1}$) due to convective precipitation, but overestimates summer 2009 precipitation. The high wet deposition rates in the SE, especially over Florida, have been attributed to deep convective scavenging from the free troposphere (Guentzel et al., 2001; Selin and Jacob, 2008). Thus the modeled low bias during late summer and autumn over Florida might be due to errors in the height of deep convection or to an underestimate of Hg(II) concentration in the tropical free atmosphere (Holmes et al., 2010).

Figure 2.5 shows the spatial distribution of the Hg wet deposition flux for each season. The IPR nested simulation and MDN observations are plotted separately. In winter (December, January, February (DJF)), the observed wet deposition flux is highest over the SE, in a region extending from Louisiana to Tennessee. Deposition rates increase in spring (March, April, May (MAM)) with high deposition areas extending northward to the MW. During summer (June, July, August (JJA)), wet deposition is very high along the Gulf Coast in a region covering eastern Texas to Florida, and further stretches to the NE. During autumn (September, October, November (SON)), the observed wet deposition decreases again and has similar spatial distribution to that of winter. Generally, the nested model captures the seasonal change in the spatial pattern of wet deposition (Figures 2.5 and 2.6). The spatial correlation coefficient between modeled values and MDN observations varies between r = 0.70 (JJA) and r = 0.77 (MAM). The IPR nested-grid simulation has the greatest predicting capacity over the eastern U.S.

during spring in terms of both low mean bias and correlation coefficient. During summer, the nested model captures the observed maximum high deposition fluxes over the SE, but underestimates MDN observations over the MW, as noted above. The nested model also underestimates the observed high deposition fluxes in SE in autumn and winter.

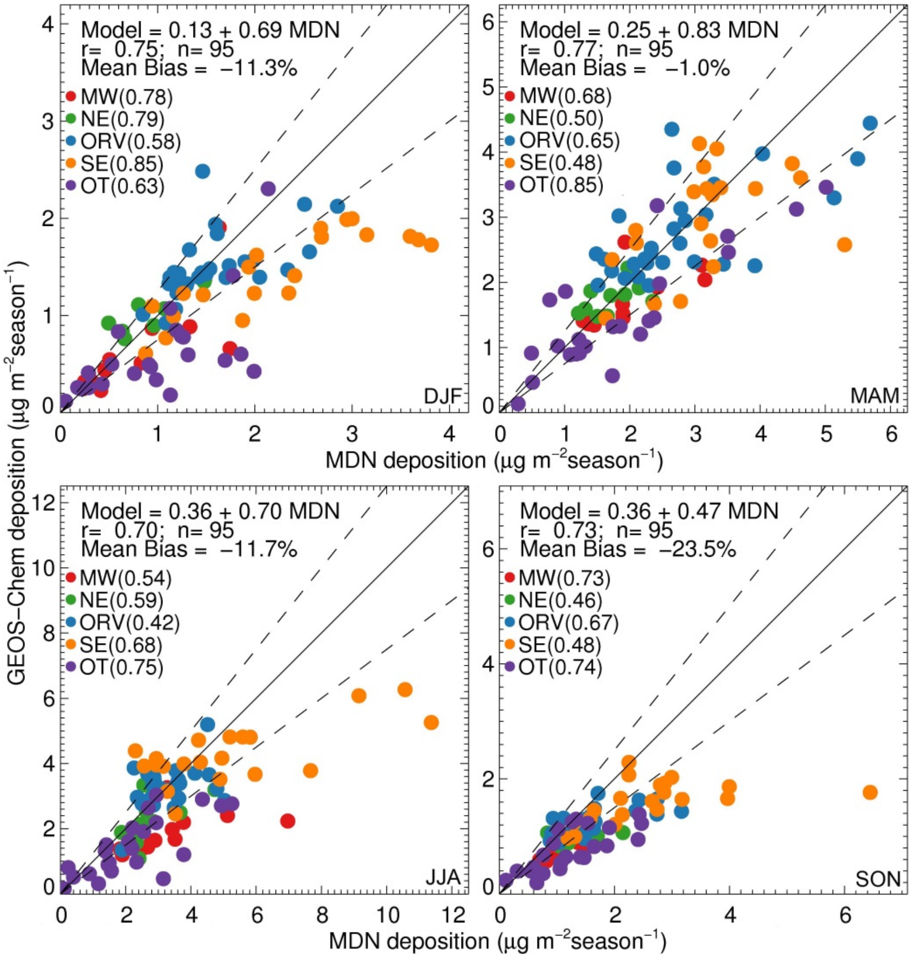

Figure 2.6: Scatter plot of seasonal averaged (2008 – 2009) Hg wet deposition fluxes (μg m^{-2} season^{-1}) between IPR nested-grid simulation (vertical axis) and MDN observations (horizontal axis). Different colors denote sites in different regions as defined in Figure 2.2, while OT corresponds to sites west of 95˚W longitude.

2.3.3 Annual mean surface concentrations of atmospheric Hg

Figure 2.7 shows the annual mean TGM (defined as modeled Hg(0) + gas-phase Hg(II)), reactive gaseous mercury (RGM, gas-phase Hg(II)) and particulate-bound mercury (PBM, particulate-phase Hg(II)) surface concentrations for the IPR Hg simulation in 2008-2009. The global and nested simulations show similar spatial distribution patterns for surface Hg concentrations following natural and anthropogenic Hg emissions. Highest TGM concentrations over the contiguous U.S. are predicted over the ORV region (1.7 – 1.8 ng/m^3), where a large number of power plants and waste incinerators are located. Slightly lower TGM concentrations (1.5 – 1.6 ng/m^3) are modeled in Nevada and Utah where metal ore smelting plants and strong geogenic sources are located (Gustin et al., 1997). Modeled TGM concentrations are lower (1.3 – 1.5 ng/m^3) over the Great Plains region, southern Canada and northern Mexico, corresponding to typical Northern Hemisphere background concentrations (Slemr et al., 2011). The model predicts lower (1.3 – 1.4 ng/m^3) TGM concentrations in the marine boundary layer (MBL) because of faster oxidation of Hg(0) to Hg(II) in the MBL and subsequent deposition. These MBL concentrations are lower than cruise measurements over the Northern Atlantic Ocean (1.7-2.2 ng/m^3) (Soerensen et al., 2010b), probably due to a model underestimate in ocean Hg(0) evasion (Soerensen et al., 2010b).

Compared with TGM, both RGM and PBM display stronger spatial variability due to their much shorter lifetimes. Following the anthropogenic emission pattern, RGM and PBM concentrations are enhanced over the ORV region (10 – 20 pg/m^3), and are lowest in the region stretching across Southern Canada, the Great Plains, southern Canada and northern Mexico. The modeled RGM surface concentrations are highest over the West because of the subsidence of free tropospheric air (Selin and Jacob, 2008). The simulated PBM concentrations are low in this region because of the low particulate matter concentrations.

As expected, the nested model reveals much more spatial variability than the global model, especially near large point sources and over western North America. The average surface RGM and PBM concentrations in the nested model are 40% higher than in the global model.

This is due to the stronger ventilation of surface air in the nested model (Wang et al., 2004a), which more efficiently mixes Hg(II)-rich free tropospheric air down to the surface. The global model averages the sub-grid vertical velocity (Wang et al., 2004a) and suppresses subsidence of Hg(II) from higher altitude, where both the nested and global GEOS-Chem models predicts high Hg(II) concentrations due to faster oxidation of Hg(0) at lower temperatures and lack of removal (Holmes et al., 2006; 2010).

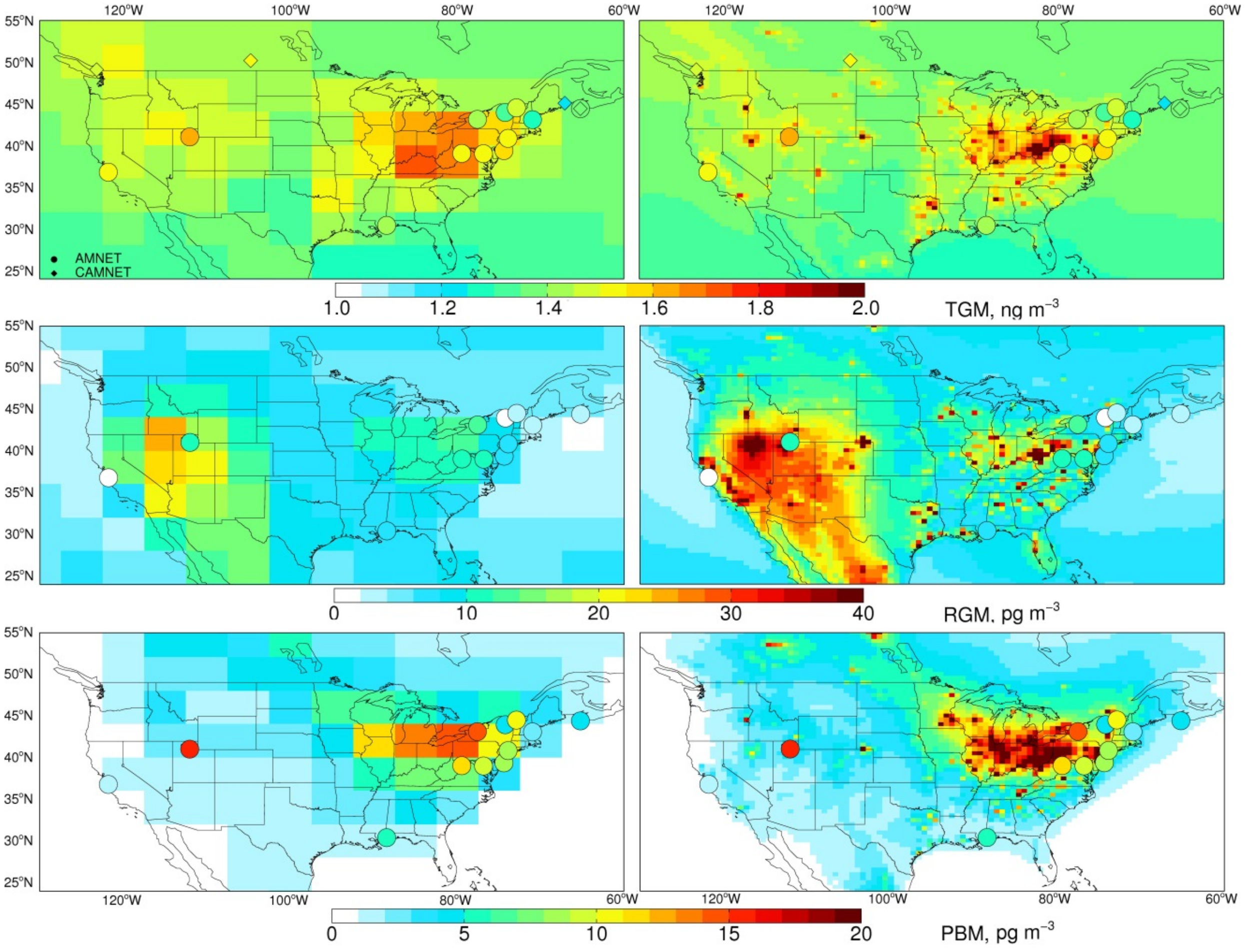

Figure 2.7: Annual mean surface concentrations of TGM (top), RGM (middle) and PBM (bottom) during 2008 – 2009. Results from the global (left column) and nested (right column) IPR simulations are compared to observations from 14 AMNET sites (circles) and 5 CAMNET sites (diamonds). Two pairs of AMNet sites are collocated, so only 12 AMNet sites are identifiable.

We compare the model results to surface concentrations measured at 5 CAMNet sites and 14 AMNet sites (Figures 2.7 and 2.8). CAMNet was established in 1996 and measures TGM across Canada using TEKRAN mercury vapor analyzers (Temme et al., 2007). AMNet is part of the National Atmospheric Deposition Program and currently consists of 20 sites (AMNET, 2009). At these sites, Hg measurements are conducted by TEKRAN instruments, and include Hg(0), RGM and PBM with a 2.5-micrometer impactor and KCl-coated annular denuder (for ionic Hg), thermally-desorbed particulate filter (for PBM), and gold traps (for Hg(0)). To evaluate the model, we have selected 14 AMNet sites which are not influenced by large nearby sources (sites with <2000 kg/a anthropogenic Hg emissions within 100 km).

The nested IPR simulation reproduces the observed TGM annual mean concentrations at the 19 surface sites with no bias (obs.: 1.46 ± 0.11 ng/m^3, IPR model: 1.42 ± 0.11 ng/m^3). Observed PBM concentrations are well-captured by the IPR simulation (obs.: 7.8 ± 4.2 pg/m^3, IPR model: 8.8 ± 6.7 pg/m^3), however the model tends to overestimate observed RGM concentrations by a factor of 2.4 (obs.: 6.2 ± 4.1 pg/m^3, IPR model: 15 ± 9.2 pg/m^3). If we take into account the large variability (±70%) and high uncertainty (30 – 40%) in RGM measurements (Aspmo et al., 2005; Lyman et al., 2007; Gustin and Jaffe, 2010) this degree of agreement is not unreasonable, especially since the model has some success at reproducing the seasonal cycle of RGM observations (see Section 2.3.4).

The nested IPR model shows higher correlation (r = 0.51, 0.64 and 0.46 for TGM, RGM and PBM, respectively) with observations than does the global model (r = 0.43, 0.36 and 0.39, respectively). Indeed, for the NE region, where the number density of AMNet sites is highest, the nested model captures the north-south gradient much better than the global model, such as higher TGM concentrations in the Bronx (NY06, 1.52 ng/m^3) than in upstate New York (NY43 and NY49, 1.42-1.33 ng/m^3).

The STD nested simulation predicts RGM and PBM concentrations that are twice as large as the IPR simulation, leading to a STD simulation overestimate of observations by a factor of 4 for RGM (obs.: 6.2 ± 4.1 pg/m^3, STD model: 26 ± 24 pg/m^3) and 2 for PBM (obs.: 7.8 ± 4.2 pg/m^3, STD model: 16 ± 18 pg/m^3). These concentrations are too high compared with observations even if we assume they have a low measurement bias of up to 30-40% for RGM. This also indicates a high sensitivity of RGM and PBM concentrations to local Hg(II) emissions and shows that the AMNet RGM and PBM observations are consistent with rapid reduction of RGM in CFPP and waste incinerator plumes.

2.3.4 Seasonal variation of surface Hg concentrations

Figure 2.8 compares the seasonal cycle of observed and modeled TGM, RGM and PBM surface concentrations at AMNet and CAMNet sites. The observations at CAMNet sites are averaged over 2004 – 2007 (top four panels). For each AMNet site, the range of years with available observations is indicated in Figure 2.8. The nested model results (STD: red line; IPR: green line) are averaged over 2008 – 2009.

The model closely matches the seasonal cycle of TGM at sites that are farthest from anthropogenic point sources. These include Kejimkujik, Burnt Island, NY20, VT99. At these sites, the seasonal cycle exhibits a summer minimum, which the model attributes to stronger summertime oxidation by Br atoms (Br concentrations peak in summer) and deposition (maximum in precipitation) (Holmes et al., 2010). This seasonal cycle was also reproduced by previous model studies assuming OH/O_3 as Hg(0) oxidants (Bergan and Rodhe, 2001; Selin et al., 2007). In these studies OH and O_3 concentrations also peak in summer. Discrepancies between observations and models seem to occur when sites are affected by local sources (Kellerhals et al., 2003). For example, Chester, New Jersey (NJ32), Rochester, New York (NY43), and Antelope

Island, Utah (UT96). The remote site in Kejimkujik, Nova Scotia shows a TGM maximum in June with a high standard deviation, indicating episodic influence by long range transport and/or fires.

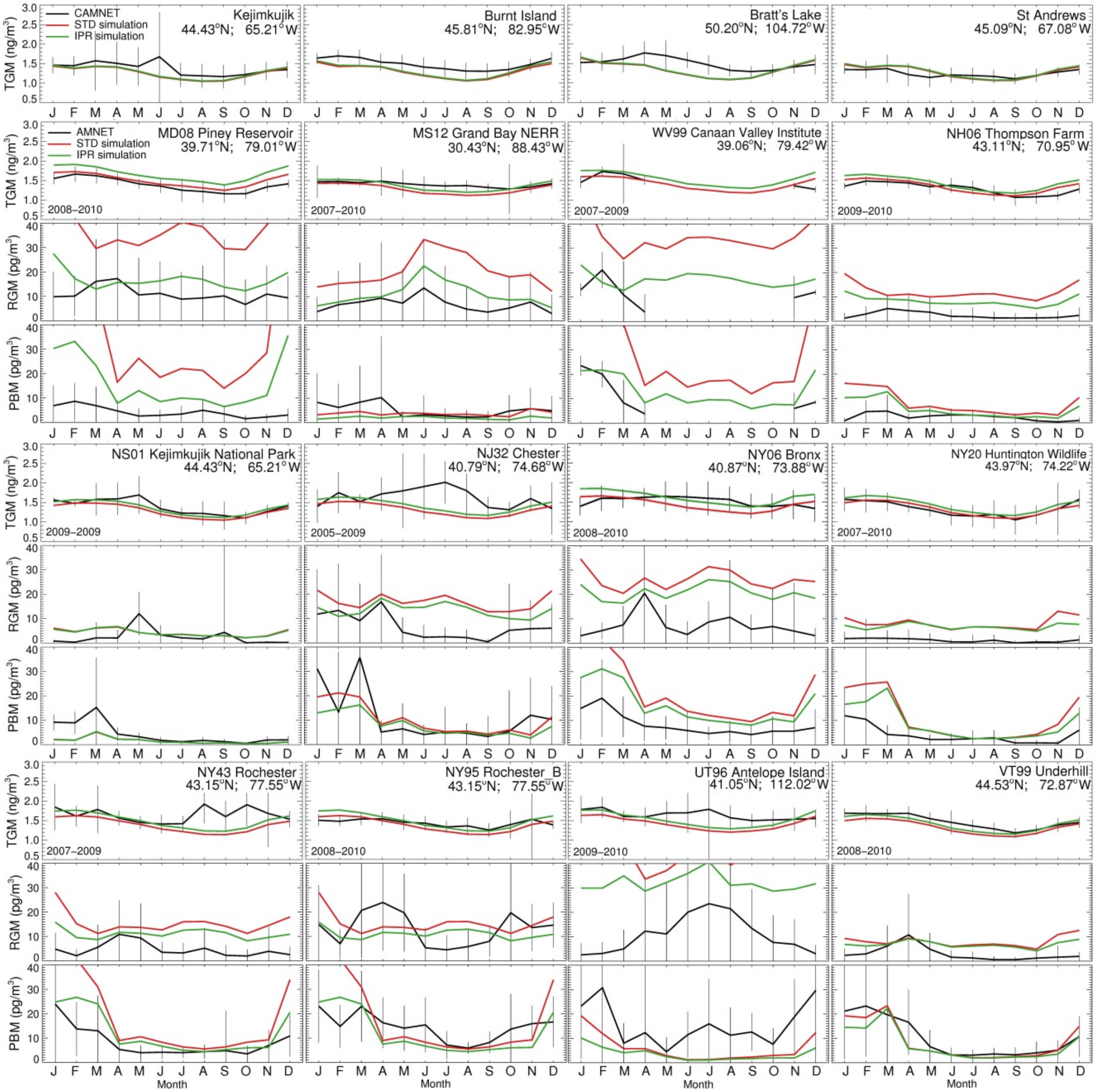

Figure 2.8: Comparison of the monthly mean TGM, RGM and PBM concentrations observed at CAMNet and AMNet sites with the STD (red line) and IPR (green line) nested-grid GEOS-Chem simulations. The CAMNet sites are averaged over 2004 – 2007, while the AMNet sites observations are averaged during 2005 – 2010 when observation are available. The model results are averaged over 2008 – 2009. For the CAMNet sites (the 4 panels in the first row), only TGM observations are available.

The observed seasonal cycle for RGM varies from site to site. Most of the sites have a maximum during spring and a minimum during summer (e.g. MD08, NH06, NJ32, NS01, NY06, NY43, NY95 and VT99), while other sites (e.g. MS12, MS99 and UT96) show a maximum in summer. Similar site-to-site variability in the RGM seasonality was noted by Engle et al. (2010). These variations are likely caused by different combinations of the seasonality for oxidation, deposition, and subsidence of upper troposphere/lower stratospheric (UT/LS) air at these sites (Amos et al., 2012): oxidation is strongest in late spring, wet deposition is strongest during summer, and UT/LS influence maximizes in winter-spring. The IPR simulation captures the summer maximum of RGM at MS12 and UT96. However, it predicts little seasonality at the other sites and does not capture the spring peak observed at most of the sites. The reasons for this are unclear at this point, but could be associated with an underestimate of subsidence of RGM-rich air during spring.

PBM concentrations measured at AMNet sites show a seasonal maximum during the colder months, when Hg(II) would be expected to preferentially partition to aerosols (Rutter and Schauer, 2007; Amos et al., 2012). The IPR simulation captures this seasonality, especially at the sites in New Jersey, New York, and Vermont (NJ32, NY06, NY20, NY43, NY95, and VT99).

2.3.5 Vertical and horizontal variations of TGM over California during ARCTAS

Figure 2.9 shows the vertical distribution of TGM obtained in summer 2008 during the ARCTAS aircraft campaign (Jacob et al., 2010). We focus here on observations collected during flights over California and Nevada (32° – 43°N, 114° – 125°W), out of the Palmdale and Moffett Field (CA) airports. The measurements include Hg(0) and some fraction of Hg(II) due to uncertain inlet loss of Hg(II) (Holmes et al., 2010), so for comparison to the GEOS-Chem nested IPR simulation we show both the Hg(0) and TGM vertical profiles. We exclude episodic biomass burning plumes from the observations: CO > 200 ppb or CH_3CN > 0.25 ppt, following Holmes et al. (2010). The nested IPR simulation is sampled at the same time and altitude as the ARCTAS aircraft observations. The nested simulation reproduces the observed mean TGM concentration below 2 km altitude (1.1 – 1.3 ng/m^3). At 2-5 km altitude, observations show a slight increase to 1.3 ng/m^3, while above 7 km observations decrease to ~ 1 ng/m^3. These features are not captured by the model, which shows a relatively invariant vertical profile. Overall, the nested model shows no significant bias (Hg(0): 1.16 ng/m^3; TGM: 1.25 ng/m^3) compared with observations (1.21 ng/m^3).

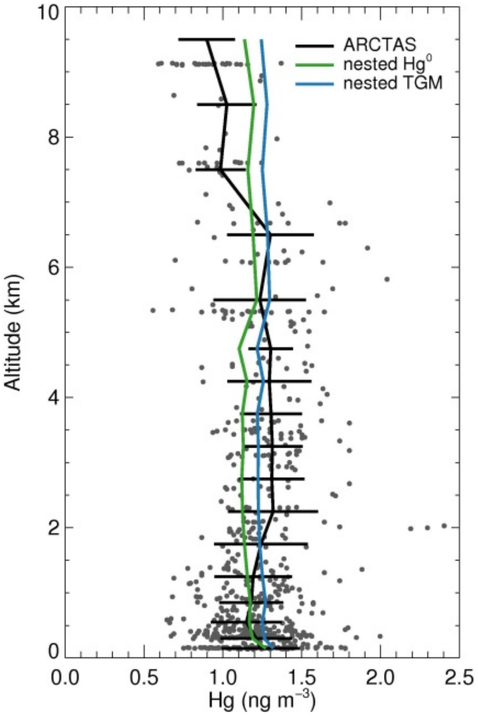

Figure 2.9: Mean vertical profiles (black line) and standard deviations of TGM concentrations measured during the ARCTAS campaign over California and Nevada (32-43ºN; 114-125ºW) during summer 2008. Gray points correspond to individual TGM observations. The modeled vertical profile of Hg(0) from the nested IPR simulation is shown in green, while modeled TGM is in blue. The model is sampled at the time of observations along the flight track.

The spatial distribution of observed TGM concentrations is displayed in Figure 2.10. We show the modeled TGM concentrations from the global and nested IPR simulations for comparison. Because the model shows much smaller variability than the observations, we use different color scales and mainly focus on the relative spatial patterns. Although both the global and nested models have similar level of correlation with ARCTAS observations (*r* = 0.3), the nested model shows larger spatial variability than the global model. The nested model simulates localized enhancements in TGM over fires sampled in northern California (the branch with red color near 30° – 40°N and 122°W in the right panel). It also captures higher TGM concentrations due to anthropogenic emissions in southern California. The global model shows weaker and diluted enhancement of concentrations in these regions. Both the global and nested models miss the observed high concentration in western Nevada, which might be caused by a mix of mining activities and naturally Hg-enriched soils (Lyman and Gustin, 2008).

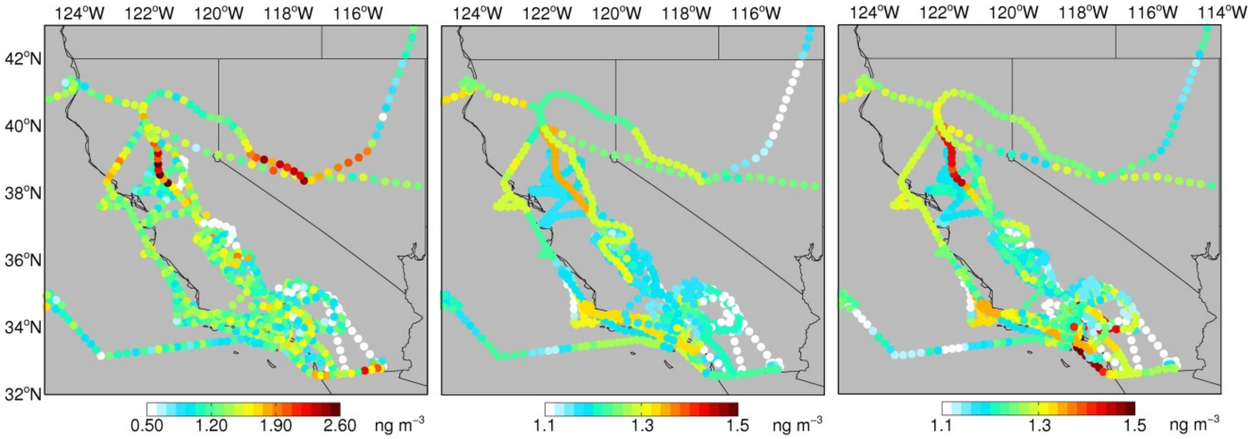

Figure 2.10: Observed TGM concentrations during the ARCTAS aircraft campaign (left). The TGM concentrations predicted by the global (middle) and nested (right) IPR simulations sampled along the flight track are also shown. Note that the observation and model results have different color scales.

2.3.6 Origin of Hg deposition over North America

We conduct a sensitivity simulation where all anthropogenic Hg emissions over the U.S., Canada, and Mexico are turned off to separate the influence on deposition of regional anthropogenic Hg emissions from background emissions.

The two left panels in Figure 2.11 show annual mean wet deposition over North America contributed by background sources (natural sources over North America as well as natural + anthropogenic sources outside of North America) for the STD and IPR simulations. The model shows that these external sources lead to a maximum in wet deposition stretching from southern Texas to the NE, and there is also a maximum over Florida. The IPR simulation predicts slightly higher (5%) background wet deposition compared to the STD simulation. Indeed the IPR simulation assumes a lower fraction of anthropogenic emissions as Hg(II), leading to less local deposition and increased export efficiency of anthropogenic emissions in the form of Hg(0) from regions outside of North America. Following transport on hemispheric scales, this additional background anthropogenic Hg(0) is oxidized to Hg(II) and leads to a small increase in background wet deposition flux over North America.

Table 2.2: Contribution from North American anthropogenic Hg sources to wet and dry deposition (2008-2009)

Regions		GEOS-Chem STD simulation	GEOS-Chem IPR simulation
MW	Wet	31%	15%
	Dry	21%	14%
	Total	**24%**	**14%**
NE	Wet	32%	16%
	Dry	18%	12%
	Total	**23%**	**13%**
ORV	Wet	32%	15%
	Dry	41%	24%
	Total	**39%**	**22%**
SE	Wet	16%	8%
	Dry	25%	16%
	Total	**23%**	**13%**
Contiguous U.S.	Wet	22%	10%
	Dry	20%	13%
	Total	**21%**	**12%**

The contribution from anthropogenic North American Hg emissions is obtained by difference between this background simulation and simulations including anthropogenic emissions (central and right panels in Figure 2.11). As expected, the assumed speciation of anthropogenic Hg emissions greatly affects our results. In the STD simulation, we find that North American anthropogenic sources account for 22% of the Hg wet deposition flux and 20% of the dry deposition flux in the contiguous United States (Table 2.2). The STD model shows that North American anthropogenic sources are responsible for large contributions in the industrial ORV, MW and NE (~30% of wet deposition), with the contributions near the borders between Ohio, Pennsylvania and West Virginia reaching up to 60% (Figure 2.11). The modeled contribution from North America anthropogenic sources decreases gradually away from this region. In our IPR simulation we find that the contribution of anthropogenic North American emissions to wet deposition decreases by a factor of 2 relative to the STD simulation (Table 2.2): 10% of wet deposition and 13% of dry deposition in the contiguous U.S. (compared to 22% and 20% in the STD simulation), reaching a maximum of 15% (wet) and 24% (dry) in the ORV region (compared to 32% and 41% in the STD simulation).

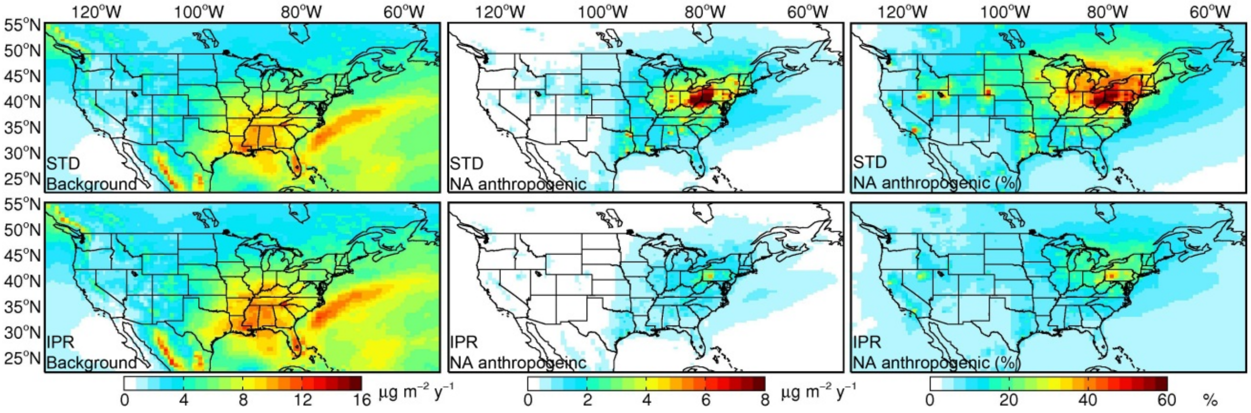

Figure 2.11: Contributions of global background and North American anthropogenic emissions to wet deposition during 2008 – 2009. Top row (STD simulation): Absolute wet deposition fluxes due to global background (left) and North American anthropogenic sources (middle), and the percent contribution by North American anthropogenic sources (right). The bottom three panels are for the IPR simulation.

A similar diagnosis was done by Selin and Jacob (2008) with OH/O_3 as the main oxidants of Hg using GEOS-Chem at a spatial resolution of 4°×5°. They found the North American anthropogenic sources account for 27% and 17% for the wet and dry deposition fluxes over contiguous U.S., respectively. Seigneur et al. (2004) used the regional model TEAM at a resolution of 100 km and found North American emissions contributions to deposition to be 24% (wet) and 43% (dry). The results for wet deposition from both studies are similar to results from our STD simulation which assumes a high fraction of anthropogenic emissions as Hg(II). For example, Selin and Jacob (2008) assume anthropogenic emissions of 55 Mg/a Hg(II) and 23 Mg/a Hg(P) for the year 2000 over North America, similar to our STD emission inventory (59 Mg/a Hg(II)). Seigneur et al. (2004) assume 72 Mg/a Hg(II) and 13 Mg/a Hg(P) (for years 1998-1999). Our IPR simulation assumes significantly lower emissions for Hg(II) (25 Mg/a), leading to a decrease in Hg deposition near point sources, and thus a decrease in their contribution to the deposition flux over the contiguous US. This implies that the domestic contribution diagnosed by this approach is highly sensitive to the large uncertainties associated with anthropogenic Hg emission speciation and in-plume reduction processes. Given the improved agreement of our IPR simulation with observations of wet deposition (Sections 2.3.1 and 2.3.2), RGM and PBM (Section 2.3.4), our 12% estimate of the North American anthropogenic contribution to deposition appears to be most consistent with observations.

Compared to the model results of Selin and Jacob (2008) our results differ in the spatial distribution of background sources' contribution to wet deposition. Selin and Jacob (2008) calculated a maximum wet deposition flux over southern Texas of 18 – 20 $\mu g/m^2$, nearly twice as large as our 10 – 12 $\mu g/m^2$. Compared to Br atom oxidation, the OH/O_3 chemistry shifts wet deposition to tropical regions with elevated OH concentrations (Holmes et al., 2010). Convective precipitation in the GEOS-4 meteorological fields is stronger than in the GEOS-5 fields. In addition, the updates for Hg wet deposition implemented by Wang et al. (2011) and Amos et al. (2012) could also influence the spatial distribution of Hg wet deposition flux.

Many studies have tried to estimate the contribution of local sources to wet deposition, either using surface observations or models. In general, estimates that relied on observations result in higher contributions than estimated by models. Keeler et al. (2006) attributed ~70% of Hg wet deposition at Steubenville, Ohio to coal combustion. In a later study, White et al. (2009) found an enhancement of up to 72% of Hg concentration in precipitation at sites within 1 km of power plants during episodic events, and 42% when averaged over the whole summer season. Similar studies conducted in the Chicago/Gary urban area show that sites less than 100 km apart differed in volume-weighted mean Hg concentration by over 30% (Lin and Pehkonen, 1999). The volume-weighted mean Hg concentration measured in urban sites in Detroit was also 25-35% higher than those measured in a rural site ~60 km east (Gildemiester, 2001). The short lifetimes of Hg(II) lead to strong spatial variance near point sources at a spatial scale of 1 – 10 km, which cannot be captured in our GEOS-Chem nested grid simulation with a ~50 km horizontal resolution. As most of the MDN and AMNet sites used in this chapter are not directly downwind of large point sources, they should represent regional levels of Hg(II) concentrations and wet deposition. Similarly, the GEOS-Chem model results evaluated at those sites should thus be representative over regional scales, but likely underestimate the anthropogenic contribution at very small local scales.

2.4 Conclusions

We have developed a nested Hg simulation in the GEOS-Chem chemical transport model, with a horizontal resolution of 1/2° latitude by 2/3° longitude over North America. Boundary conditions are provided by a global GEOS-Chem Hg simulation at 4°×5° resolution using the same emissions, chemistry, deposition, and meteorological fields as the nested model. We have updated the anthropogenic Hg emission in the U.S. and Canada using the EPA's National Emissions Inventory and the Canadian National Pollutant Release Inventory, both for 2005. The resulting anthropogenic Hg emissions in North America are 87 Mg/a Hg(0) and 59 Mg/a Hg(II). While these inventories assume that a significant fraction of anthropogenic emissions are emitted as Hg(II), observations in power plant plumes suggest a possible quick reduction from Hg(II) to Hg(0) directly downwind. We therefore conduct a sensitivity simulation (IPR) by changing the anthropogenic Hg speciation profile over North America to yield 121 Mg/a Hg(0) and 25 Mg/a Hg(II). We contrast results from this IPR simulation to our standard (STD) simulation.

Relative to the global model, the nested-grid model shows improved skill at capturing the high spatial and temporal variability of Hg wet deposition observed at MDN sites in 2008-2009. However, the STD nested model simulation shows a systematic 27% overestimate in Hg wet deposition over the Ohio River Valley (ORV), a region with high emissions from coal-fired power plants. Changing the speciation of anthropogenic emissions in our IPR simulation reduces this model bias to -2% over the ORV region. The IPR simulation slightly increases the low bias of the nested model compared with MDN observations, but improves the model performance over North America in terms of reproducing the spatial pattern of MDN observations. The IPR simulation also captures the spatial patterns of wet deposition as a function of season, with high wet deposition fluxes concentrated in the SE during spring and extending towards the NE during summer. The IPR simulation shows a 60% underestimate in wet deposition over the MW in the summer of 2008, which is associated with a 50% underestimate in precipitation. While the model reproduces the high deposition rates observed in the SE in Louisiana, Mississippi, and Alabama, it does not reproduce the very high wet deposition rates observed at sites in Florida during summer.

The nested IPR simulation reproduces the observed annual mean and seasonal variations in surface concentrations of TGM, RGM and PBM observed at 5 CAMNet sites and 14 AMNet sites. The nested model reproduces the horizontal variability in observations better than the global model, because it better resolves the influence of local anthropogenic sources. The nested IPR model shows no bias for TGM and PBM, but is a factor of 2.4 too high relative to RGM observations. In contrast, the STD simulation leads to a factor of 4 overestimate in observed RGM and a factor of 2 overestimate in PBM. This may be further evidence for rapid in-plume reduction of RGM. The nested model captures the overall horizontal variability in TGM concentrations observed over California during the ARCTAS campaign, but displays a reduced dynamic range compared to observations.

By conducting a sensitivity simulation without North American anthropogenic Hg emissions, we assess the relative contribution of regional anthropogenic emissions on deposition. Our results are highly sensitive to the assumed speciation of anthropogenic emissions. In the IPR simulation, the North American anthropogenic sources contribute only 10% of the total Hg wet deposition in the US, compared to 22% in the STD simulation. The modeled IPR percent contribution varies from 4% in the western U.S. to 16% in the eastern U.S (32% in the STD simulation). The modeled percent contribution can be as high as 60% near some large point emission sources. The IPR mean modeled contribution of North American anthropogenic emissions to dry deposition is 13% (20% in the STD simulation), increasing to 24% in the Ohio River Valley (41% in the STD simulation). Given the improved agreement with wet deposition, RGM, and PBM observations obtained in the IPR simulation, our lower estimate of North American contribution to deposition (12%) appears to be more robust.

Chapter 3

DECREASES IN MERCURY WET DEPOSITION OVER THE UNITED STATES DURING 2004 – 2010: ROLES OF DOMESTIC AND GLOBAL BACKGROUND EMISSION REDUCTIONS

3.1 Introduction

Mercury (Hg) is listed as a Hazardous Air Pollutant (HAP) by the U.S. Environmental Protection Agency (EPA) because of its neurotoxicity (USEPA, 2012). Atmospheric Hg is emitted in two forms: gaseous elemental Hg (GEM or Hg(0)) and divalent oxidized Hg (Hg(II)), which can partition into both gaseous oxidized Hg (GOM) and particulate-bound Hg (PBM). Hg originates from both natural, mainly in the form of Hg(0), and anthropogenic sources, as Hg(0) and Hg(II) (Mason, 2009; Streets et al., 2011). It is generally assumed that 1/3 of global Hg emissions are natural, 1/3 are anthropogenic, and 1/3 are derived from re-emission of previously deposited anthropogenic Hg (Pirrone et al., 2009; Selin, 2009). Hg(0) has an atmospheric lifetime of several months and can thus be transported on large scales before being deposited or oxidized to Hg(II), while Hg(II) is readily deposited and thus has shorter transport distances (Holmes et al., 2006). Deposition of Hg to water surfaces and the resulting possibility of fish contamination is the main human exposure pathway to Hg in North America (e.g., Clarkson, 2003; Mergler et al., 2007).

The relative contribution of domestic and global emissions to Hg deposition over the United States has been evaluated in several studies (Seigneur et al., 2004; Selin and Jacob, 2008;

Chapter 2 in this thesis). For example, Seigneur et al. (2004) used a multi-scale modeling system and found North American anthropogenic emissions contributions to deposition to be 24% (wet) and 43% (dry). Selin and Jacob (2008) found that North American anthropogenic sources contribute 27% (wet) and 17% (dry) to deposition flux over the U.S. in 2004-2005. To account for the observed small fraction of Hg(II) in plumes downwind of power plants (Edgerton et al., 2006; Weiss-Penzias et al., 2011), Zhang et al. (2012) modified the source profiles of Hg emitted from power plants as well as waste incinerators, and estimated lower contributions of 10% (wet) and 13% (dry) in 2008 – 2009.

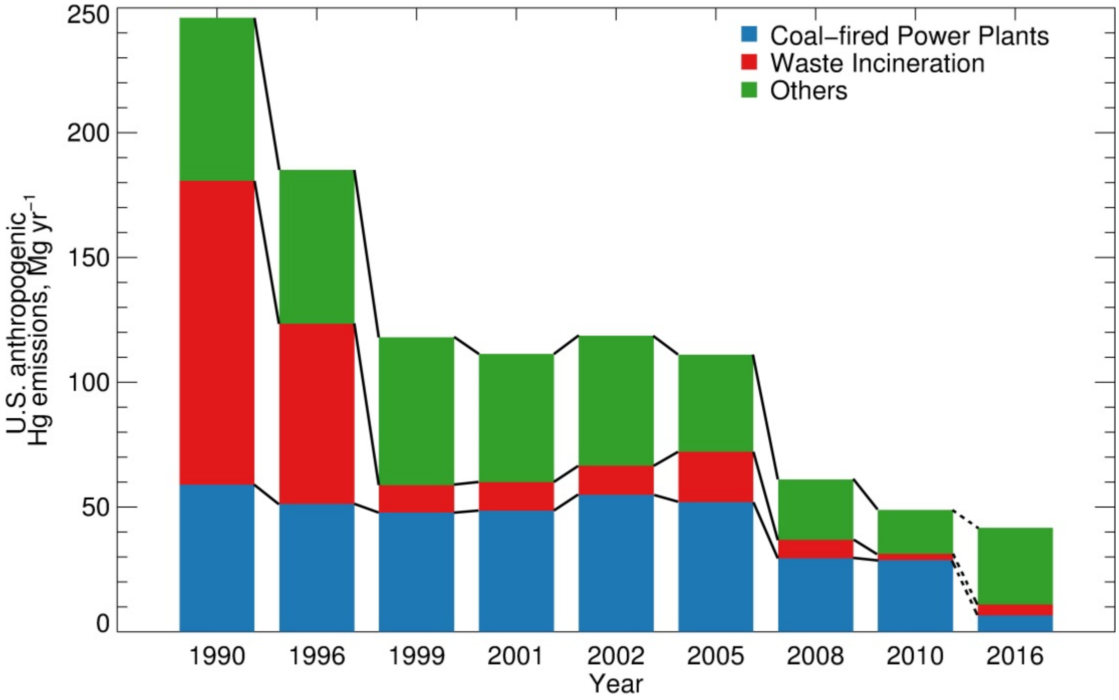

Figure 3.1: Anthropogenic Hg emissions in the U.S. between 1990 and 2010. Hg emissions are lumped into three source categories: coal-fired power plants (CFPPs), waste incineration (including hospital/medical/infectious, municipal, industrial/commercial and hazardous waste incineration and sewage sludge), and others (mainly stone/clay/glass/cement production, chemical production, primary metal production, and metal mining). Emissions for 1990, 1999, 2002, 2005 and 2008 are from the National Emission Inventories (NEI). The 1996 emissions are from the National Toxics Inventories (NTI). The data for 2001 is from US EPA (2005). The CFPP emission for 2010 is based on Information Collection Request (ICR) by the EPA. For 2010, non-CFPP emissions are estimated based on Toxic Release Inventories (TRI) for 2005 and 2010. Emissions for 2016 are projected by the Integrated Planning Model (IPM).

In the United States, the main anthropogenic sources of Hg include coal-fired power plants (CFPP), waste incineration, cement manufacturing, chemical production, primary metal production, and metal mining (Houyoux and Strum, 2011). Figure 3.1 summarizes U.S. Hg anthropogenic emissions for 1990-2010 based on several inventories: the Toxics Release Inventory (TRI, http://www.epa.gov/tri/), the National Toxics Inventory (NTI, http://epa.gov/air/data/netemis.html), and the National Emission Inventory (NEI, http://www.epa.gov/ttn/chief/net/2008inventory.html). We separate emissions into three categories: CFPP, waste incinerators, and "others" (the remaining U.S. anthropogenic source categories). The implementation of the 1990 Solid Waste Combustion Rule (http://www.epa.gov/ttn/atw/129/hg/regs.html) as part of the Clean Air Act has led to the decrease of Hg emissions from medical, municipal, commercial and industrial waste incinerators from 122 Mg yr^{-1} in 1990 to 10.9 Mg yr^{-1} in 1999 (Figure 3.1). Anthropogenic Hg emissions remained nearly constant between 1999 and 2005, with CFPPs accounting for 50% of Hg emissions. In 2005, the EPA issued the Clean Air Mercury Rule to cap and reduce CFPP emissions (http://www.epa.gov/mercuryrule). Although this rule was overturned in 2008, Hg emissions from the CFPP sector are estimated by EPA to have decreased by 43%, from 52 Mg yr^{-1} in 2005 (NEI2005) to 29.5 Mg yr^{-1} in 2008 (NEI2008), and remained constant during 2008-2010 based on the recent release of 2010 Information Collection Request (ICR) estimates by the EPA (http://www.epa.gov/ttn/atw/utility/utilitypg.html). The causes for these large emission reductions are not fully understood, but likely include compliance with state Hg-specific rules, voluntary reductions by utility operators, and co-benefits of Hg reductions from control devices installed for the reduction of other pollutants such as SO_2 and PM (Houyoux and Strum, 2011). Meanwhile, the 2005 Hg emissions from waste incinerator (20 Mg yr^{-1}) and other sectors (39 Mg yr^{-1}) decreased by 2008 to estimated levels of 7 Mg yr^{-1} and 24 Mg yr^{-1}, respectively, because of further regulatory implementation (NEI2008). With the announcement of the Mercury and Air Toxics Standard (MATS) in December 2011 (http://www.epa.gov/mats), Hg emissions from CFPPs are projected to decrease to less than 7 Mg yr^{-1} in 2016 based on the results of Integrated Planning Model (IPM, http://www.epa.gov/airmarkets/progsregs/epa-ipm/index.html; Houyoux and Strum, 2011) simulations. The significant decreases in Hg emissions over the 1990 – 1999 and 2005 – 2010 time periods provide an opportunity to quantitatively evaluate the contribution of anthropogenic emissions to Hg deposition over the U.S.

Table 3.1: Summary of trends in Hg precipitation and atmospheric concentrations from selected studies in the literature.

Reference	Period	Trends (% yr^{-1})			
		Hg concentrations in precipitation over North America			
		Northeast	Midwest	Southeast	West
Butler et al. (2008)	1998-2005	-1.7±0.51[a] *-2.5±2.1*[c]	-3.5±0.74 -3.4±2.2	*0.01±0.71*[b] *-0.33±2.0*[d]	
Prestbo and Gay (2009)	1996-2005	-2.1±0.88	*-1.8±0.28*	*-1.3±0.30*	-1.4±0.42
Risch et al. (2012)	2002-2008	0.84±2.9	-2.0±3.8		
This chapter	2004-2010	-4.3±2.2	*-2.5±1.6*	*-0.63±2.5*	+0.33±7.7
		Atmospheric Hg concentrations			
Temme et al. (2007)	1995-2005	Canada		-1.3±1.9	
Slemr et al. (2011)	1996-2009	Mace Head, Ireland		-1.4	
		Cape Point		-2.7	
Soerensen et al. (2012)	1990-2009	North Atlantic		-2.5±0.54	
		South Atlantic		-1.9±0.91	
Cole et al. (2013)	2000-2009	Arctic		-0.45±0.64	
		Sub-Arctic		-2.1	
		Temperate Canada		-1.9±0.3	

aMean±standard deviation, calculated by random coefficient model with site as a random effect

[b] Not significant, $p = 0.98$

[c] Calculated by averaging individual trend at each site

[d] Less than half of the sites have trends which are significant at $p = 0.10$

Likely as a response to anthropogenic emission reductions, the observed Hg wet deposition flux and Hg concentrations in precipitation at Mercury Deposition Network (MDN) sites over the U.S. have decreased during these periods, although the reported trends vary depending on the study and time period, as summarized in Table 3.1. For example, Butler et al. (2008) find trends ranging from -1.7% yr^{-1} to -3.5% yr^{-1} in Hg concentrations at most sites in the Northeast and Midwest for 1998 – 2005, but found no significant trend over the Southeast. Prestbo and Gay (2009) also report decreasing Hg concentration trends (1 – 2% yr^{-1} during 1996 – 2005), but only at half of the MDN sites, particularly across Pennsylvania and extending up through the Northeast region. Risch et al. (2012) find Hg wet deposition to be unchanged in the Great Lakes region during 2002 – 2008 by evaluating 5 monitoring networks in the USA and Canada. Furthermore, they find that the small decreases in Hg concentrations were offset by increases in precipitation. Gratz et al. (2009) describe how declines in precipitation Hg concentrations at remote sites in the Northeast are linked to local-scale meteorological variability rather than to reductions in emissions. In Florida, trends in Hg wet deposition have been minimal or non-existent, despite large reductions in regional emissions of Hg (Butler et al., 2008; Vijayaraghavan et al., 2011). One issue associated with these different studies is the significant interannual variation of Hg concentration in precipitation and Hg wet deposition flux due to variability in precipitation. Indeed, an increase in precipitation results in an increase in the Hg deposition flux. This is accompanied by a decrease in Hg concentrations in rain due to the dilution of the washout loading (Landis et al., 2002a; Prestbo and Gay, 2009). Thus interannual changes in meteorological conditions, especially precipitation, complicate the interpretation of MDN observations and might mask any trends due to changes in Hg emissions.

Over the last two decades, anthropogenic Hg emissions over East Asia, especially in China, have rapidly increased (Wu et al., 2006; Streets et al., 2011). Streets et al. (2009) estimates that Hg emissions from Asia and Oceania increased from 975 Mg yr^{-1} in 1996 to 1,318

Mg yr^{-1} in 2006, equivalent to an annual increase rate of +3.1% yr^{-1}. Wu et al. (2006) found that anthropogenic Hg emissions from China have increased at an annual average growth rate of 2.9% yr^{-1} during 1995 – 2003 reaching 696 Mg yr^{-1} in 2003. In particular, emissions from CFPPs in China increased from 63 to 100 Mg yr^{-1} with a +5.9% annual growth rate during 1995 – 2003 (Wu et al., 2006), and reached 132 Mg yr^{-1} in 2007 (Tian et al., 2011).

Despite increases in anthropogenic emissions in Asia, there are indications that global background atmospheric Hg concentrations are decreasing (Table 3.1). Temme et al. (2007) evaluated the trend of total gaseous mercury (TGM, defined as the sum of Hg(0) and gas phase Hg(II)) at 11 sites from the Canadian Atmospheric Mercury Network (CAMNet), finding a decreasing trend of -1.3±1.9% yr^{-1} with large site by site variation for the 1996 – 2005 period. Slemr et al. (2011) evaluated long-term observations at stations in the Southern and Northern Hemisphere combined with cruise measurements over the Atlantic Ocean, and found TGM concentrations have decreased by 20-38% between 1996 and 2009. In particular, TGM concentrations at Mace Head, Ireland have decreased from 1.75 ng m^{-3} in 1996-1999 to 1.4 ng m^{-3} in 2009, showing a trend of -0.024±0.005 ng m^{-3} yr^{-1} (equivalent to -1.4% yr^{-1}). Soerensen et al. (2012) analyzed 1977-2010 trends in atmospheric Hg from 21 ship cruises over the North Atlantic (NA) and 15 over the South Atlantic (SA). During the 1990-2009 period, they found a decline of -0.046±0.010 ng m^{-3} yr^{-1} (-2.5% yr^{-1}) over the NA, and a smaller trend of -0.024±0.005 ng m^{-3} yr^{-1} (-1.9% yr^{-1}) over the SA. The causes for this decreasing trend are not fully understood, but might be due to decreasing reemissions from the legacy of historical mercury emissions in soils and ocean (Slemr et al., 2011; Soerensen et al., 2012). In a recent study, Cole et al. (2013) found that the TGM concentration trends at Arctic sites (-0.45% yr^{-1})

are weaker than at sites in the sub-Arctic (-2.1% yr^{-1}) and in temperate Canada (-1.9% yr^{-1}) during 2000-2009.

In this chapter, we will evaluate observations of Hg concentrations in precipitation from MDN sites across the United States for the 2004-2010 period. We will use a Hg simulation in the GEOS-Chem chemical transport model to take into account the influence of variability in precipitation on the detected trends. Our objectives are 1) to evaluate recent variations and trends in Hg wet deposition and precipitation concentration over the United States; 2) to attribute the observed trends to domestic and global background emission changes.

3.2 Observations and model

Wet deposition of Hg has been monitored over the U.S. as part of the National Atmospheric Deposition Program since 1995 (MDN, 2012). The network initially consisted of 17 sites and currently includes more than 100 active sites. MDN sites collect weekly integrated precipitation samples and report Hg wet deposition flux and the Hg concentration in precipitated water/snow. In this chapter, we select MDN sites with at least 75% data coverage each year during the 2004 – 2010 period, resulting in a group of 47 sites (see Figure A1.1 for the locations of these sites). To account for the lower collection efficiency of snow by MDN samplers (Butler et al., 2008; Prestbo and Gay, 2009), we correct the weekly deposition fluxes based on the average snow capture efficiency and the snow fraction over total precipitation as described in Zhang et al. (2012). In our analysis, we use the volume-weighted mean (VWM) Hg concentration in precipitated rain/snow instead of the total Hg wet deposition flux as our analysis variable because it is less sensitive to changes in precipitation (Figure A1.2 and the related text in the appendix).

We use the GEOS-Chem multi-scale nested-grid Hg simulation over North America (Chapter 2). The GEOS-Chem chemical transport model itself is described in Bey et al. (2001). The model is driven by assimilated meteorological fields from the NASA Goddard Earth Observing System (GEOS). We use here GEOS-5 meteorological fields with a horizontal resolution of 1/2° latitude by 2/3° longitude and 72 hybrid eta levels from the surface to 0.01 hPa. The lowest 2000 m are resolved with 13 layers.

The GEOS-Chem global atmospheric Hg simulation is described by Selin et al. (2007), with recent updates in Hg oxidant chemistry by Holmes et al. (2010) and gas-particulate partitioning of Hg(II) by Amos et al. (2012). The model has two atmospheric mercury species: Hg(0) and Hg(II). The Hg chemistry includes Hg(0) oxidation by Br atoms with kinetic parameters from Donohoue et al. (2006), Goodsite et al. (2004) and Balabanov et al. (2005), as well as aqueous-phase photochemical reduction of Hg(II), scaled to NO_2 photolysis (Holmes et al., 2010).

Anthropogenic emissions are from the Global Emission Inventory Activity (GEIA) 2005 inventory of Pacyna et al. (2010). Over the U.S. and Canada, the GEIA emission inventory is overwritten with the 2005 EPA NEI inventory (USEPA, 2012d) and the 2005 Canadian National Pollutant Release Inventory (Environment Canada, 2012). The U.S. and Canadian anthropogenic emission inventories assume a 55%/45% partitioning for Hg(0)/Hg(II), with 56.8%/43.2% for CFPP emissions. However, observations in power plant plumes suggest that most of the Hg(II) emitted is quickly reduced to Hg(0) within a few kilometers downwind (Edgerton et al., 2006; Weiss-Penzias et al., 2011; ter Schure et al., 2011). In Zhang et al. (2012), we demonstrated that using a 83%/17% partitioning for N. American anthropogenic Hg emissions (89%/11% in CFPPs) significantly improves model performance in reproducing observations of Hg wet deposition and atmospheric Hg speciation, especially over the Ohio River Valley region where numerous CFPPs are situated. In this chapter, we use the same anthropogenic Hg partitioning as in Zhang et al. (2012). For global anthropogenic emissions, we assume a partitioning of 87%/13% (89%/11% Hg(0)/Hg(II) from CFPP emissions). Re-emission of Hg(0) from soil and ocean are also considered based on legacy Hg concentrations in these media (Selin et al., 2007; Soerensen et al., 2010a). GEOS-Chem simulates wet scavenging of Hg(II) following the scheme of Liu et al. (2001), with recent updates by Amos et al. (2012) and Wang et al. (2011). The model simulates the dry deposition of Hg(0) and Hg(II) based on the resistance-in-series scheme of Wesely (1989). Loss of Hg(II) via uptake onto sea-salt aerosol in the marine boundary layer is also considered (Holmes et al., 2009; 2010).

The nested-grid model preserves the original resolution of the GEOS-5 meteorological fields (1/2° latitude × 2/3° longitude) over North America (10° – 70°N and 40° – 140°W), and uses results from a global (4°×5°) simulation as initial and boundary conditions with self-consistent chemistry, deposition and meteorology between the nested and global domains. A full evaluation of the nested-grid Hg simulation is given in Zhang et al. (2012). The model reproduces the magnitude of MDN Hg wet deposition over the U.S. with a small negative bias (-16%) and captures the spatial and seasonal cycle of wet deposition quite well. Furthermore, the model shows no bias in its simulation of ground-based and aircraft observations of GEM over the U.S. The model reproduces the seasonal cycle of observed PBM. The model overestimates the GOM observations by a factor of 2, which is not unreasonable given the large variability and uncertainty of GOM measurements.

We run this nested-grid Hg simulation over North America for 2004 – 2010 assuming constant anthropogenic emissions based on the 2005 EPA NEI inventory (“BASE simulation”).

We also conduct three additional sensitivity simulations. In the “US simulation”, we use the 2008 NEI inventory, which shows a 45% decrease in domestic anthropogenic Hg emissions compared to the 2005 NEI inventory. If we assume that US domestic anthropogenic Hg emissions remained nearly unchanged during 2004 – 2005 and 2008 – 2010 (Figure 3.1), this corresponds to a -7.5% yr trend for 2004-2010. TGM concentrations observed at Mace Head, Ireland have decreased from 1.60 ng m^{-3} in 2004 to 1.40 ng m^{-3} in 2010 (Slemr et al., 2011). To reflect this 12% decrease in Northern Hemisphere background TGM concentrations (equivalent to a -2% yr^{-1} trend), we conduct a “NH simulation” in which we apply a uniform 12% decrease in the nested-grid lateral boundary concentrations of Hg(0) and Hg(II). There is evidence that anthropogenic Hg emissions in East Asia have been increasing. Wu et al. (2006) reports a 5.9% yr^{-1} increase in Hg emission from CFPPs between 1995 and 2003. This trend increased to 7.2% yr^{-1} during 2003 – 2007 (Tian et al., 2011). Wu et al. (2006) also find a 4.2% yr^{-1} increase in Hg emission from nonferrous metal smelting. As these two sectors contribute 80-85% to the total Hg emissions in China (Wu et al., 2006), we estimate an overall Hg emission increase trend in China during 2004 – 2010 of 5.4% yr^{-1} and conduct an “EA simulation” with a 32% increase in anthropogenic Hg emissions from East Asia (70 – 150°E, 8 – 45°N). Each of these sensitivity simulations (US, NH and EA) is run for 2008 – 2009, and we compare the results against the BASE simulation. The modeled trend, in % yr^{-1}, is calculated by difference with the BASE simulation ($\frac{simulation - base}{base} \times \frac{100}{6}$).

3.3 Results and Discussion

3.3.1 Seasonal and interannual variability in Hg wet deposition

Figure 3.2 shows the observed monthly MDN VWM Hg concentrations in precipitation (left column) for 2004-2010. We aggregate observations at the 47 MDN sites into four regions:

Northeast (16 sites), Midwest (13 sites), Southeast (13 sites) and West (5 sites). The boundaries of these regions are defined in Figure 3.4. Hg concentrations in precipitation have a summer maximum and wintertime minimum. The summer maximum is larger than the wintertime minimum by a factor of 2-3. This seasonality has been reported in many different studies (Guentzel et al., 2001; Hoyer et al. 1995; Burke et al. 1995; Landis et al., 2002b; Dvonch et al., 2005) and reflects the stronger oxidation of Hg(0) to Hg(II) during summer providing more Hg(II) for scavenging in rain (Holmes et al., 2010; Chapter 2). The GEOS-Chem BASE simulation of VWM Hg concentration is within one standard deviation of MDN observations (Figure 3.2, left panels). The model shows a mean negative bias of -3.0% (Northeast), -15% (Midwest), -6.3% (Southeast) and -36% (West). The model captures the observed seasonal cycle, with correlation coefficients (*r*) of 0.87 (Northeast), 0.75 (Midwest), 0.76 (West). In the Southeast region, we find a lower correlation ($r = 0.34$). The GEOS-5 precipitation (Figure 3.2, right panels) has no bias over the Northeast and Southeast, but shows a small underestimate of MDN precipitation over the Midwest (-17%) and an overestimate over West (+17%). The *r* values for monthly precipitation amount are larger than 0.80 in these regions.

Observed annual VWM Hg concentrations display some interannual variations, with the range ($\equiv \frac{\text{maximum}-\text{minimum}}{\text{mean}}$) varying from 20 to 40%. The coefficients of variance (ratios of standard deviation to the mean) are 12% (Northeast), 8% (Midwest), 5% (Southeast) and 12% (West). The MDN observed precipitation amounts also have significant interannual variability, with coefficients of variance of 5.0% (Northeast), 7% (Midwest), 12% (Southeast) and 20% (West). Although Hg concentrations in different years have similar seasonal patterns, the peak month and degree of seasonality can vary. For example, the West region displays much higher concentrations in August in 2008 and 2010 relative to other years. Over the Midwest, elevated

Hg concentrations are measured during August 2006, 2008 and 2009 because of the relatively lower precipitation amount in these months, while the peak occurs earlier in other years. Lower Hg concentrations are observed during the summer of 2009 compared with multi-year mean in the Northeast and Midwest. The BASE simulation generally captures these features and has *r* values for observed and modeled annual VWM Hg concentrations of 0.54 (Northeast), 0.26 (Midwest), 0.73 (Southeast) and 0.29 (West). However, we find that the model tends to be on the high side of observations for the last three years and on the low side for the first three years, especially in the Northeast and Midwest. As we will show below, this indicates a trend in VWM Hg concentrations not captured by the model with constant anthropogenic emissions.

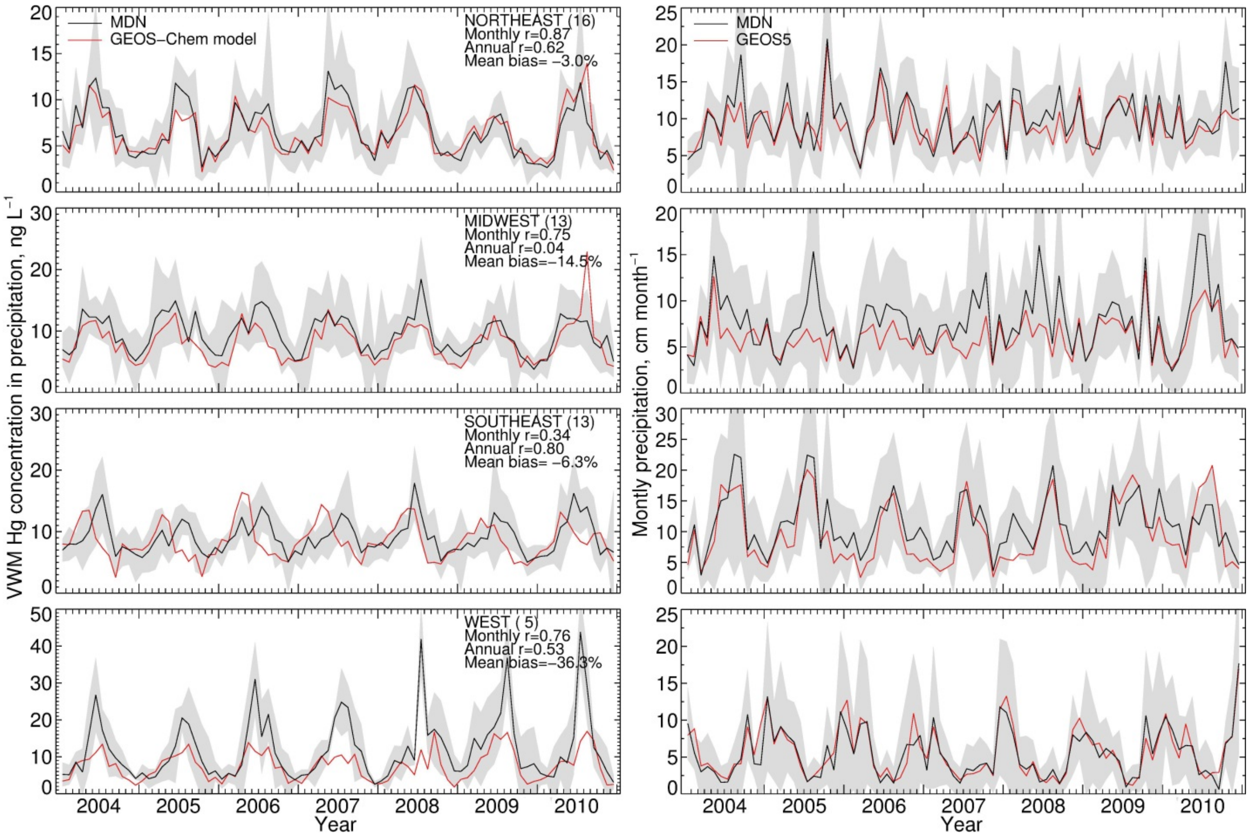

Figure 3.2: Monthly variations in monthly VWM Hg concentrations in precipitation (left column) and precipitation depth (right column) from MDN observations and the GEOS-Chem model BASE simulation (constant anthropogenic emissions) for 2004 – 2010. The grey shaded area shows the one time standard deviation envelope for the MDN observations.

Table 3.2: Regional trends in VWM Hg concentration and precipitation depth

Region	Number of sites	VWM Hg concentrations in precipitation				Precipitation depth (observed)	
		Model subtraction		Direct regression			
		% yr^{-1}	ns[a]	% yr^{-1}	ns	% yr^{-1}	ns
NORTHEAST	16	-4.3±2.2[b]	13	-4.1±2.4	9	+0.25±2.9	3
MIDWEST	13	-2.5±1.6	6	-1.8±1.8	4	+2.2±2.4	2
SOUTHEAST	13	-0.63±2.5	4	+0.51±2.3	3	-0.99±5.1	6
WEST	5	+0.33±7.7	3	+2.3±6.3	3	+3.7±5.0	1

[a] number of sites with significant trends ($p < 0.1$).

3.3.2 Trend in Hg precipitation concentrations for 2004-2010

We calculate the trend in observed monthly VWM Hg concentrations using two methods. In the "direct regression" method, we first remove the seasonal cycle in Hg concentrations by subtracting the mean 2004 – 2010 seasonal cycle at each of the 47 individual MDN sites. We then conduct a least-square linear regression of the resulting time series against month number (n = 84 for 7 years), and the slope of the regression line is the trend in VWM Hg concentrations. We express the calculated slope into a percent trend (in % yr^{-1}) relative to the multi-year mean VWM Hg concentration of each site. The accompanying probability (p) for the slope is calculated based on the t-score of the regression. In a second method ("model subtraction"), we further subtract the deseasonalized modeled time series of VWM Hg concentrations from the observed deseasonalized time series before calculating the trend. We use our BASE simulation with constant anthropogenic emissions. This allows removing the influence of varying meteorological conditions, in particular precipitation, on observed VWM Hg concentrations. We thus expect the variability and trend of the residual after subtraction to be caused by changes in domestic anthropogenic emissions and/or in background Hg concentrations (including changes in natural sources and non-domestic anthropogenic sources).

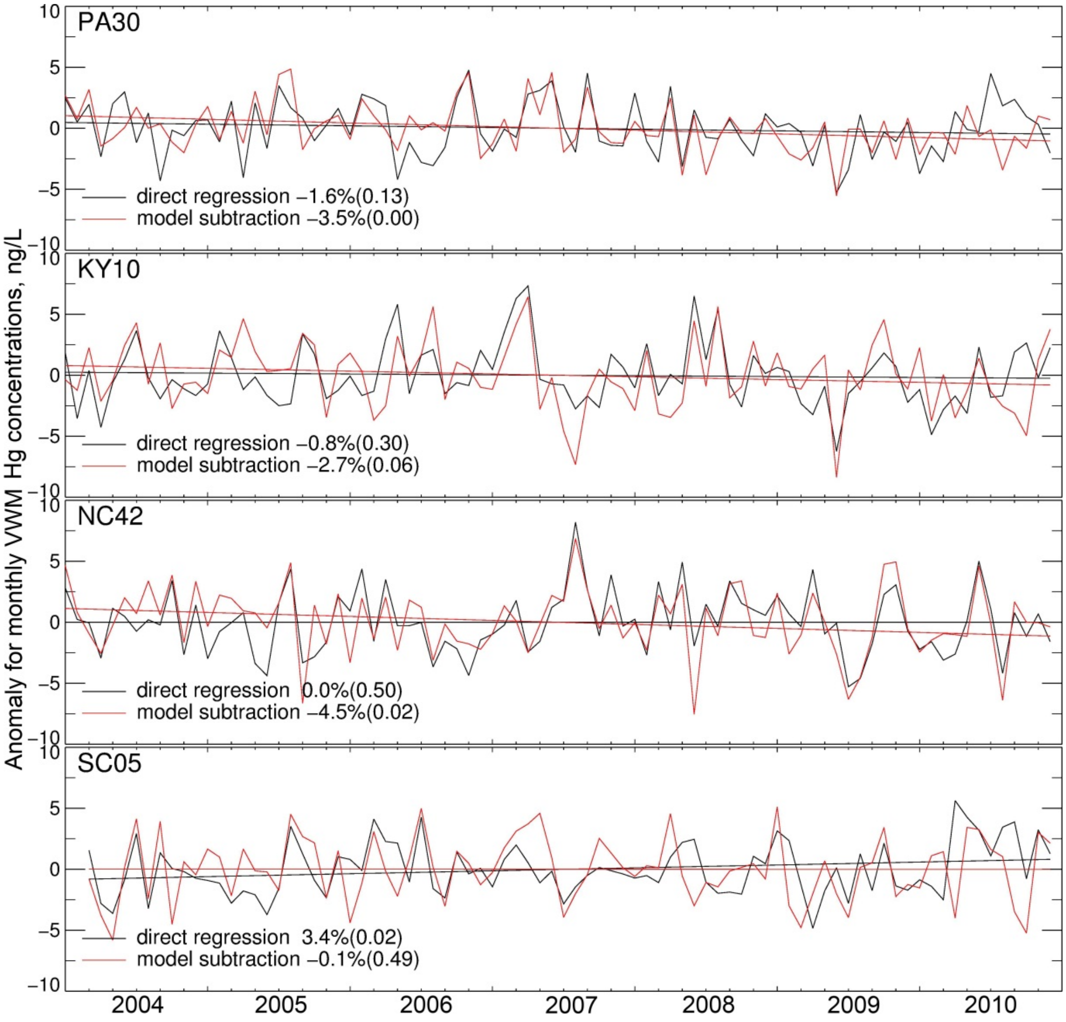

Figure 3.3: Monthly anomalies time series of VWM Hg concentrations in precipitation for the direct regression method (black) and the model subtraction method (red). Four MDN sites are shown, from top to bottom: Erie site, Pennsylvania (PA30); Mammoth Cave National Park-Houchin Meadow, Kentucky (KY10); Pettigrew State Park, North Carolina (NC42) and Cape Romain National Wildlife Refuge, South Carolina (SC05), for the trends, in % yr^{-1}, and *p*-scores (in parenthesis).

Compared to the direct regression method, we find that the model subtraction approach reduces the noise of the Hg concentration time series, because it removes the variability associated with precipitation changes. The number of sites with significant trends ($p < 0.1$) increases from 19 for the direct regression approach to 26 for the model subtraction approach. The values of these trends at individual MDN sites are listed in Table A1.1. This table also includes a comparison to the trends of the Hg concentrations calculated by the direct regression approach, modeled Hg concentrations (BASE simulation), as well as for precipitation. Figure 3.3 shows the deseasonalized time series of VWM Hg concentrations calculated with our two approaches at 4 MDN sites: PA30 on the shore of Lake Erie, in Pennsylvania; KY10 at Mammoth Cave National Park-Houchin Meadow, Kentucky; NC42 at Pettigrew State Park, North Carolina; and SC05 at Cape Romain National Wildlife Refuge, South Carolina (see Figure A1.1 for the location of these sites). At PA30 and KY10, the direct regression method yields trends of -1.64% yr^{-1} and -0.91% yr^{-1}, respectively, which are not significant (p=0.13 and 0.30). In contrast, the model subtraction approach results in stronger (-3.6% yr^{-1} and -2.9% yr^{-1}) and more significant trends ($p<0.01$ and p=0.06). At these sites it appears that changes in local precipitation (-2.1% yr^{-1} and -3.4% yr^{-1}, Table A1.1) yield a positive trend in the VWM Hg concentrations calculated in the BASE model simulation (+2.0% yr^{-1} for both sites). At the NC42 site, the direct regression method yields no trend (0.01% yr^{-1}, p=0.50). However, a strong decrease of precipitation occurred during 2004 – 2010 (-7.1% yr^{-1}, p=0.02). The BASE model thus predicts a significant increasing trend of Hg concentration in precipitation (+4.8% yr^{-1}, $p<0.01$). By subtracting this trend, the model subtraction approach yields a significant negative trend at NC42 (-4.8% yr^{-1}, p=0.02). At SC05, although the direct regression approach yields a significant increasing trend in Hg concentration (+3.5% yr^{-1}, p=0.02), this trend appears to be caused by decreasing precipitation (-2.5% yr^{-1}, p=0.25). By taking this into account, the model subtraction approach results in no trend (-0.07% yr^{-1}, p=0.49). More generally, we find that at 28 sites out of the 47 MDN sites, the model subtraction method increases the absolute value of the trend and for almost all these 28 sites, the p value of the trend is reduced.

Figure 3.4 shows the spatial distribution of the regression trends (model subtraction method) in monthly VWM Hg concentrations for all 47 MDN sites. Sites with a significant trend

($p < 0.1$) are shown as colored circles (26 sites), while sites with insignificant trend are in triangles (21 sites). The fractions of sites with significant trends vary by region: Northeast (13 significant sites out of a total of 16), Midwest (6 out of 13), Southeast (4 out of 13), and West (3 out of 5). The mean trends for the sites in each region are summarized in Table 3.2: -4.3±2.2% yr^{-1} (Northeast), -2.5±1.6% yr^{-1} (Midwest), -0.63±2.5% yr^{-1} (Southeast) and +0.33±7.7% yr^{-1} (West). Over the Northeast, the 13 sites with significant trends display trends ranging from -8% yr^{-1} to -2.4% yr^{-1} (Table A1.1). As the trends in observed VWM Hg concentrations are strong and consistent, and the trend in precipitation is weak and non-significant (+0.25±2.9% yr^{-1}), there is not much difference in the trend calculated with the model subtraction and direct regression methods for this region (Table 3.2). In the Midwest, the 6 significant sites display trends in VWM Hg concentrations ranging from -2.9% yr^{-1} to -4.8% yr^{-1}. On the other hand, only 3 of 13 sites in the Southeast show significant negative trends, and those sites are located near the northern bound of this region. One site in Eastern Texas (Longview, TX 21) displays a significant increasing trend of nearly +5% yr^{-1}. Most of the other sites with non-significant trends show neutral or slightly decreasing trends. Two of 5 sites in the West (CO99 in Colorado and NV02 in Nevada) show significant and strong increasing trends, while the sites in Washington (WA18) and California (CA75) show decreasing trends. The overall trend of all the 47 sites is -2.3±3.5% yr^{-1}, with large spatial variability.

The precipitation shows a general increasing trend during 2004 – 2010 ranging from +0.25% yr^{-1} (Northeast) to +3.7% yr^{-1} (West), except in the Southeast where it decreased (-0.99% yr^{-1}). Although the number of sites with significant trends (12 out of 47) for precipitation depth is few, the average precipitation trends in Northeast, Midwest and West are all positive, which would cause a decrease in Hg concentration even without any change in Hg emissions.

The Hg concentration trends calculated by direct regression approach are thus more difficult to interpret because of the underlying trend in precipitation in these regions. Furthermore, the direct regression approach tends to miss the decreasing trend in Hg concentration if the precipitation trend is also decreasing, which would cause an increasing trend in Hg concentration. For example, the direct regression approach predicts a weak increasing trend of +0.51% yr^{-1} over the Southeast region. Removing the decreasing trend of precipitation with the model subtraction approach brings the calculated trend down to -0.63% yr^{-1}.

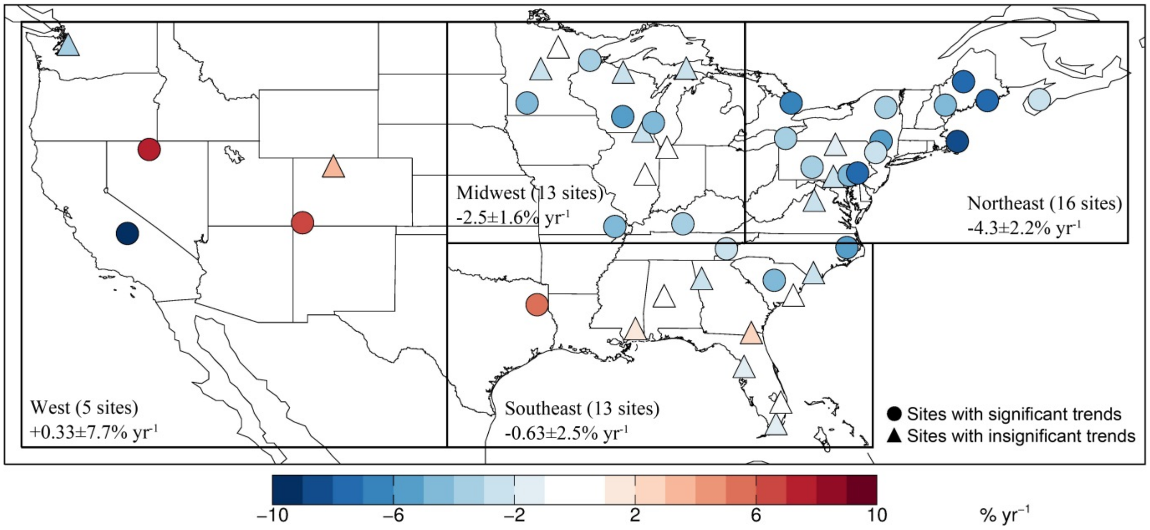

Figure 3.4: Trend in monthly VWM Hg concentrations at 47 MDN sites during 2004 – 2010. Sites with significant trend (p < 0.1) are shown as circles, while sites where the trend is not significant are shown as triangles. The symbols are color-coded based on the magnitude of the trend. We use the results of the model subtraction method to calculate the trends (see details in Section 3.2). The mean trend of all the sites in each region (Northeast, Midwest, Southeast, and West) is also shown.

Over the Northeast, Butler et al. (2008) calculated a trend of -1.7±0.51% yr^{-1} during 1998-2005 by using random coefficient models with site as a random effect. Butler et al. (2008) also calculated the individual trend for each site using a method similar to the direct regression approach used in this chapter, and found an average decreasing trend of -2.5±2.1% yr^{-1} (Table 3.1). Prestbo and Gay (2009) obtained similar trends in the Northeast (-2.1±0.88% yr^{-1}) during

1996-2005 by using a non-parametric statistic method. Compared with these previous studies, our trends over the Northeast for 2004-2010 are stronger (model subtraction approach: -4.3±2.2% yr^{-1}; direct regression: -4.1±2.4% yr^{-1}), this is consistent with the expected significant decrease in domestic anthropogenic emissions since 2005. Over the Midwest, our results (-2.5±1.6% yr^{-1} and -1.8±1.8%yr^{-1} for the two approaches) are comparable to previous studies, which ranged from -1.8% yr^{-1} to -3.5 %yr^{-1} (Table 3.1). Over the Southeast region, we found a weak and non-significant trend (-0.63±2.5% yr^{-1}) in Hg concentration during 2004-2010. Similar results are also obtained by previous studies focusing on the trend before 2005 and extending back for 8 or 10 years (Table 3.1). Prestbo and Gay (2009) argued that the nearly steady Hg concentration in precipitation in this region is because of the steady local emissions after an abrupt emission decrease by the closure or emission controlling of municipal and waste incinerators in the early 1990s. Butler et al. (2008) attributed the steady Hg concentration over Southeast region to the influence of global background Hg, which increased or remained constant during that time period. Butler et al. (2008) also argued that the halogens in the coastal environment in Southeast facilitates more rapid transformation of Hg(0) from global pool to Hg(II), which can enhance Hg wet deposition.

3.3.3 Attribution of observed trends

We examine here whether these observed trends can be explained by changes in emissions from domestic and global sources. Figure 3.5 shows the expected trends in VWM Hg concentrations for the four model simulations (see Section 3.2). The US simulation (Figure 3.5a) suggests a 2-4% yr^{-1} decrease in VWM Hg concentrations near source regions over the Ohio River Valley region. The largest modeled decrease occurs near the borders of Ohio, West Virginia and Pennsylvania (-6% yr^{-1}). In the Southeast and Midwest regions the influence of decreasing domestic emissions is weaker and not as concentrated, with decreases ranging from -1% yr^{-1} to -2% yr^{-1} near point sources. The NH simulation (Figure 3.5b) displays uniform decreases in Hg concentrations across the U.S. (1.7-2.0% yr^{-1}). The decreases are somewhat larger in the West (-2.0±0.02% yr^{-1}), and slightly smaller over the Northeast (-1.7±0.1% yr^{-1}), where domestic emissions are more important. The EA simulation (Figure 3.5d) leads to a broad increase in Hg concentrations ranging from 1% yr^{-1} in the Northwest to 0.5% yr^{-1} in the Ohio River Valley region, with a factor of 2 for the west-to-east gradient. A similar gradient was modeled by Strode et al. (2008) when evaluating the trans-Pacific transport of Asian Hg emissions. They found that the contribution of Asia to the Hg(II) total (dry + wet) deposition over the U.S. ranged from more than 30% in the West to less than 15% in the Northeast. Note that the EA simulation is contained in the envelope of the NH simulation, i.e. the observed atmospheric North Hemispheric background Hg concentration decreases despite of the increase of emission over East Asia (Streets et al., 2011).

Table 3.3: Comparison between observed regional trends in VWM Hg concentrations (model subtraction approach) and three model simulations assuming changing emissions or background conditions.

Region	N	Observed % yr^{-1}	US[a] % yr^{-1}	NH[b] % yr^{-1}	US+NH % yr^{-1}	EA[c] % yr^{-1}
NORTHEAST	16	-4.3±2.2[d]	-1.8±1.1	-1.7±0.1	-3.5±0.93	0.91±0.07
MIDWEST	13	-2.5±1.6	-0.93±0.47	-1.8±0.08	-2.8±0.39	0.98±0.05
SOUTHEAST	13	-0.63±2.5	-0.58±0.39	-1.9±0.06	-2.5±0.33	0.99±0.02
WEST	5	0.33±7.7	+0.42±1.3	-2.0±0.02	-1.5±1.3	1.0±0.02

[a] Simulation assuming a 45% decrease in anthropogenic emissions over the U.S. during 2004-2010.

[b] Simulation assuming a 12% decrease in North Hemisphere background TGM concentrations during 2004-2010.

[c] Simulation assuming a 32% increase in anthropogenic Hg emission from East Asia during 2004-2010.

[d] Mean±standard deviation of trends at MDN sites

Table 3.3 summarizes the results of the three simulations sampled at the locations of MDN sites in each region. The combined US and NH simulations (US+NH, see also Figure 3.5c) seem to explain the magnitude of the observed decreasing trend over the Northeast (obs.: -4.3±2.2% yr^{-1}; model US+NH: -3.5±0.93% yr^{-1}) and Midwest (obs.: -2.5±1.6% yr^{-1}; model US+NH: -2.8%±0.39% yr^{-1}) regions. Over the Northeast decreases in domestic emissions and background concentrations contribute nearly equally to the observed decrease, with 51% of the decrease due to domestic reduction and 49% to background reductions. Over the Midwest, the role of domestic emission reductions is smaller, accounting for 33% of the decreases.

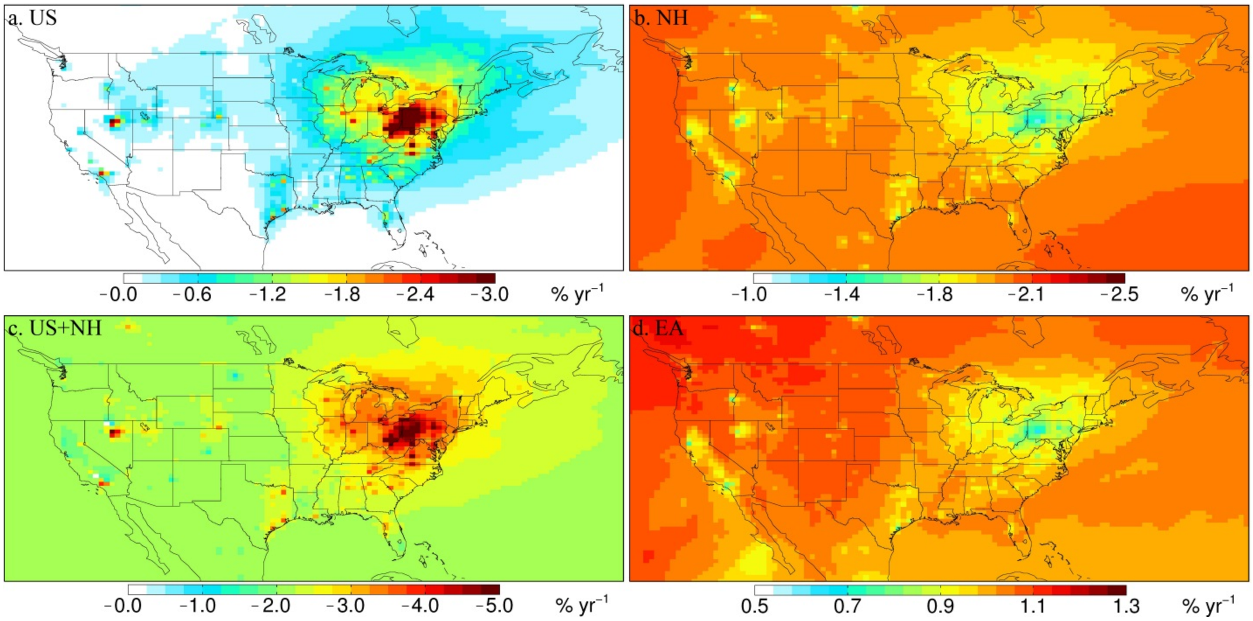

Figure 3.5: Calculated change (in % yr^{-1}) in VWM Hg concentrations over the U.S. for scenarios US, NH and EA, compared with the BASE simulation. a) decreasing trend for US scenario: 45% reduction of Hg emissions from domestic sources; b) decreasing trend for NH scenario: 12% decrease of Hg background atmospheric concentrations; c) the total decreasing trend calculated as the sum of the results of the US and NH scenarios; d) increasing trend for EA scenario: 32% increase in Hg emissions from East Asia.

The US simulation predicts a decreasing trend of -0.58±0.39% yr^{-1} over the Southeast, which is similar to the observed trend (-0.63±2.5% yr^{-1}). However, adding in the contribution from the NH simulation leads to a US+NH decreasing trend of (-2.5±0.33% yr^{-1}), which is a factor of 4 higher than the observed trend. This suggests that atmospheric Hg concentrations over the free troposphere in this region may have remained nearly constant or decreased much more slowly compared to the trend over Mace Head (Table 3.1), which is located at much higher latitude (53°N). Focusing on the three sites with significant trends in the Southeast in North Carolina (NC42), South Carolina (SC19) and Tennessee (TN11), which have the highest latitudes among sites in this region (Figure 3.4), the results from the NH+US scenarios (-2.8±0.26% yr^{-1}) are more in line with observed trends (-3.5±1.5% yr^{-1}). This could indicate a latitudinal dependence of the trend in background concentrations. Our results are consistent with a recent model study by Soerensen et al. (2012). They show that the decreasing trend of surface atmospheric Hg(0) concentrations due to the decrease in subsurface Hg concentrations over the North Atlantic is 2-3 times higher over Mace Head than over the southeast U.S. Thus our assumption of uniformly decreasing background TGM concentrations for the NH scenario overestimates the trend over lower latitudes.

For the West region, although the US+NH scenarios show decreasing trends (-1.5±1.3% yr^{-1}), the observed trend is positive (+0.33±7.7%) with extremely large variations among sites. Our first hypothesis for this increasing trend is that it is caused by the recent increase of East Asian emissions. The EA scenario predicts an increasing trend over the whole U.S. as well as a west-to-east gradient (+1.0±0.02% yr^{-1} in West vs. +0.91±0.07% yr^{-1} in Northeast), but obviously this gradient is not strong enough to explain the observed unique positive trend in the West region. Prestbo and Gay (2009) also failed to detect the influence of Asian emissions after analyzing the Hg deposition flux and concentration data in precipitation observed at the MDN site WA18 located in Seattle, which is thought to be distant from large domestic Hg sources. We find similar results, with a non-significant trend of -0.23% yr^{-1} at WA18 for 2004-2010. We have also evaluated the trend of springtime GEM concentrations observed at the Mount Bachelor Observatory (MBO), Oregon (44°N, 122°W, 2700 m above sea level) during 2005 – 2009 (Jaffe, unpublished data), and found no significant trend. Considering the small number of sites in this region as well as the large spatial variation, the trend at individual sites is likely influenced by local emissions and high variability in precipitation. For example, the site CO99 at Mesa Verde National Park, Colorado near the Four Corners region shows an increasing trend of +6.4% yr^{-1}. A closer look at the weekly deposition flux at this site shows that the strong trend is caused by several strong episodic large deposition events occurring in the summers of 2009 and 2010. Wright and Nydick (2010) evaluated these events by back trajectories and high-resolution dispersion modeling, and found them to be due to transport of local CFPP emissions. Thus, more observations in the West, especially background sites without strong local source influence are needed to evaluate the trend of Hg wet deposition over this region.

3.4 Summary

We calculated 2004-2010 trends in VWM Hg concentrations at 47 Mercury Deposition Network (MDN) sites across the United States. We used the GEOS-Chem nested-grid mercury simulation to take into account the influence of meteorology on observed trends and to assess the role of domestic emission reductions in explaining the trends. The GEOS-Chem model agrees relatively well with the observed VWM Hg concentrations in precipitation, with negative bias of -3.0% (Northeast), -15% (Midwest), -6.3% (Southeast) and -36% (West). The model captures the observed seasonal cycle and interannual variability.

We removed the effect of meteorological changes on VMW Hg concentrations by subtracting results from the GEOS-Chem model simulation with constant anthropogenic emissions. The trend associated with the remaining part is independent from meteorological fluctuations and directly associated with local and/or global background emission changes. We demonstrated that this approach yields more robust and consistent results across different sites than directly calculating the trend from MDN observations. We found regional mean trends for Hg concentrations at MDN sites during 2004 – 2010 of -4.3% yr^{-1} (Northeast), -2.5% yr^{-1} (Midwest), -0.63% yr^{-1} (Southeast) and +0.33% yr^{-1} (West). Over the Northeast, 13 out of 16 sites have significant trends, while over the Midwest 6 out of 13 sites have significant trends. Trends over both regions are thus robust. The trends over the Southeast and West regions are less robust because of the smaller numbers of sites with significant trends: 4 out of 13 in Southeast and 3 out of 5 for the West.

We conducted sensitivity simulations under three separate scenarios: a 45% decrease in domestic emissions (US), a 12% decrease in global boundary condition of atmospheric Hg concentrations (NH) and a 32% increase in East Asian anthropogenic Hg emissions (EA). The US simulation predicts a decrease in VWM Hg concentrations in the Northeast (-1.8±1.1% yr^{-1}), as well as in the Midwest (-0.93±0.47% yr^{-1}) and Southeast (-0.58±0.39% yr^{-1}). The NH scenario displays large decreases in the West (-2.0±0.02% yr^{-1}), and somewhat smaller decreases over Northeast (-1.7±0.1% yr^{-1}). The EA simulation generates a nation-wide increase in Hg wet deposition from more than +1.0% yr^{-1} in the Northwest to approximately +0.5% yr^{-1} in Ohio River Valley region in the Northeast.

The combined US and NH simulations appear to explain most of the observed decreasing trend over the Northeast (model US+NH: -3.5±0.93% yr^{-1}; MDN: -4.3±2.2% yr^{-1}) and Midwest (model US+NH: -2.8±0.39% yr^{-1}; MDN: -2.5±1.6% yr^{-1}). The model predicts that domestic emission reductions account for 51% of the decreasing trend in the Northeast and 33% of the trend in the Midwest. The US simulation predicts a decreasing trend of -0.58±0.39% yr^{-1}over the Southeast, which is similar to the observed trend (-0.63±2.5% yr^{-1}). However, adding the effect of increasing background concentrations (US+NH simulation) overestimates the observed trend by a factor of 4. However, the US+NH simulation reproduces the observed trend at the 3 Southeast sites with significant decreasing trends. These sites are located at the northern edge of the Southeast region. This suggests that the trend in background concentration might have a latitudinal dependence, with weaker decreases at southern latitudes. Our NH simulation might thus be overestimating the changes due to background emissions. For the West region, although the observed trend is positive (+0.33±7.7%), the US+NH scenarios show decreasing trends (-1.5±1.3% yr^{-1}). Considering the small number of sites in this region, more observations, especially background sites away from strong local source influence are needed to evaluate the trend of Hg concentrations in precipitated rain/snow over this region.

By combining our analysis of MDN observations and the GEOS-Chem simulations, we thus find that half of the observed 26% decrease in VWM Hg concentration over the Northeast for 2004-2010 can be explained by reductions in domestic Hg emissions, with the other half due to decreasing background concentrations. Over the Midwest, our model simulation suggests that a third of the observed 15% decrease is explained by domestic emission reductions. Our model results suggest a decreasing contribution of domestic anthropogenic sources to total Hg wet deposition over US: from 10% in 2005 to 5% in 2010. We thus anticipate that further decreases in domestic emissions in response to the 2011 Mercury and Air Toxics Standards, will lead to relatively small decreases in Hg wet deposition overall. Observed decreases over the U.S., however, are likely to be more strongly influenced by changes in background Hg concentrations.

Chapter 4

NATURAL BIOGEOCHEMICAL CYCLE OF MERCURY IN A GLOBAL THREE-DIMENSIONAL OCEAN TRACER MODEL

4.1 Introduction

The ocean plays a central role in the biogeochemical cycling of mercury (Hg). Sea-air exchange is a major source of Hg, accounting for ~1/3 of total emissions to the atmosphere (Lamborg et al., 2002; Mason et al., 2003; Strode et al., 2007; Sunderland and Mason, 2007). As a reservoir of Hg, the ocean is 50 times larger than the atmosphere (Mason et al., 1994). Atmospheric Hg deposition is recognized as the dominant source of Hg to the oceans. It is expected that oceanic concentrations of Hg at the surface ocean have increased by a factor of 2-3 as a result of increasing anthropogenic emissions and depositions (Fitzgerald et al., 2007). When deposited to ocean, Hg undergoes methylation either in near-shore sediments or within the open ocean water column (Hammerschmidt and Fitzgerald, 2004; Sunderland et al., 2009). The resulting methylmercury (MeHg) is a neurotoxin that can bioaccumulate in the food web (Morel et al., 1998). Consumption of marine fish represents the main pathway for human exposure to MeHg, which could cause a variety of adverse health effect including deficits in neurocognitive function in adults and neurodevelopment delays in children (Yokoo et al., 2003; Cohen et al., 2005). Indeed, globally most of the fish and shellfish consumed come from the ocean (Sunderland et al., 2009).

Within the ocean, Hg cycles among elemental (Hg^0_{aq}), divalent inorganic (Hg^{II}_{aq}), methyl (MMHg), dimethyl (DMHg), and particulate bound (Hg^P_{aq}) mercury (Mason and Fitzgerald, 1993). Atmospheric wet and dry deposition is in the form of Hg^{II}, which once in the surface ocean is partially reduced to Hg^0_{aq} via biological and photochemical processes (Mason et al., 1995; Amyot et al., 1997; Rolfhus and Fitzgerald, 2001). Formation of Hg^0_{aq} in the surface ocean leads to a sea-air evasion flux driven by the low solubility Hg^0_{aq}. A fraction of Hg^{II}_{aq} can be absorbed onto suspended particulate matter to form Hg^P_{aq} (Fitzgerald et al., 2007 and references therein), which sinks to the deep ocean along with the particulate organic carbon (POC) pool (Mason et al., 1994). As a substrate for microbial activity, i.e. remineralization process, the sinking POC facilitates water column methylation of Hg^{II}_{aq} to MMHg and/or DMHg (Sunderland et al., 2009; Lehnherr et al., 2011). Once formed, MMHg and DMHg can be demethylated microbiologically in the water column and converted back to Hg^0_{aq} (Schaefer et al., 2004; Fitzgerald et al., 2007; Lehnherr et al., 2011). As a result, observed total Hg concentration profiles often display a transient-type profile, which is atmospherically enhanced at the surface and a minimum in the upper ocean caused by particulate matter scavenging, while the concentrations increase again at depth because of regeneration/remineralization processes (Gill and Bruland, 1987).

The global biogeochemical Hg cycle has been investigated in several studies using a range of box models with increasing complexity. In these models, the number of boxes used to represent the ocean varies from 3 to 14 (Mason et al., 1994; Lamborg et al., 2002b; Mason and Sheu, 2002; Sunderland and Mason 2007; Streets et al., 2011; Amos et al., 2013). Mason et al. (1994) summarized the first global budget for Hg using a 3 box model. This paper synthesized known constraints on the sources and sinks of Hg in the ocean: atmospheric Hg^{II} deposition and

Hg^0 evasion are the major pathways of entering and leaving the ocean; riverine fluxes and deep-sea burial are relatively smaller terms. In the topmost 100 m, Mason et al. (1994) found that the biological reduction of Hg^{II}_{aq} in the surface ocean is a very important process for the global Hg cycle to replenish the Hg^0_{aq} loss via evasion. This paper assumed that atmospheric and surface oceanic Hg concentrations have tripled since preindustrial time (ca. 1850). They proposed that the ocean evasion is fully balanced by atmospheric deposition, and the land is a net sink for anthropogenic Hg emissions. In a later study, Lamborg et al. (2002) divided the ocean vertically into two boxes (surface ocean (~0-100 m) and the permanent thermocline (~100-1000 m)). Their model also took into account of the interhemispheric atmospheric concentrations, and used 6 boxes to represent the atmosphere, the surface and intermediate oceans in both hemispheres (GRIMM model). Lamborg et al. (2002) found a more than factor of 2 lower Hg^0_{aq} evasion flux than previous estimation by Mason et al. (1994), making ocean as a net sink for Hg. Later, Mason and Sheu (2002) considered a 3-box ocean model (mixed layer, upper ocean (50 – 500 m) and deep ocean). They found that *in situ* formation of reactive gaseous mercury (RGM) in the marine boundary layer via oxidation contributes 35% to atmospheric Hg deposition to the ocean. They found that the ocean Hg mass has increased by 9% since 1850, with most of the anthropogenic Hg accumulated in the deep ocean. Sunderland and Mason (2007) developed a 14-box ocean model, taking into account the oceanic Hg transport associated with the Thermohaline circulation. They found that the temporal lag between the atmospheric deposition and deep ocean Hg concentrations varies from decades in the Atlantic Ocean up to centuries in part of the Pacific Ocean. They also found that the deep ocean concentrations have been enriched for 11% since industrial revolution. Recently, Streets et al. (2011) and Amos et al. (2013) introduced three reservoirs for soil to represent the terrestrial carbon pool along with a 3 box ocean model similar to that used by Mason and Sheu (2002). They also run their model since 1450 with a historical emission inventory. These two studies found stronger human perturbations to the ocean than previous studies, with the present-day ocean Hg mass enrichment factor of 2-3 relative to 1450, 135%-176% relative to 1850.

Box models work well to investigate the global biogeochemical Hg cycle and can achieve a reasonably accurate big picture of Hg cycle. However, accumulating observations have shown large regional variability in Hg concentrations in the ocean, and revealed the importance of vertical transport of Hg, including entrainment/detrainment into/out of the mixed layer as well as the particle scavenging over the entire water column (Fitzgerald et al., 2007; Mason et al., 2012 and references therein). This variability and the underlying processes controlling the variability cannot be captured by these simple box models representing the ocean by 2 or 3 boxes in the vertical and 1-6 boxes horizontally. To take into account the variability of ocean Hg concentrations and the regionally varying ocean evasion flux of Hg^0 to the atmosphere, Strode et al. (2007) developed a two-dimensional slab ocean model (Strode et al., 2007) interfaced with the GEOS-Chem atmospheric chemical transport model. The slab ocean model represented the photochemical and biological transformations of Hg^0_{aq} and Hg^{II}_{aq} in the surface ocean and predicted a reasonable Hg^0 evasion flux (Strode et al., 2007), but did not take into account advection within the ocean. Soerensen et al. (2010a) improved this model by assuming basin-scale fixed values for Hg concentrations in intermediate waters. However, this model lacks the ability to represent the dynamic change of Hg concentrations in the intermediate and deep oceans. To solve this drawback, Strode et al. (2010) modeled the vertical advection/diffusion as well as the organic carbon scavenging process in the top 2000 m ocean water with a 1-D column box model with 50 vertical layers. At steady-state under natural conditions (prior to any anthropogenic input), they predicted increasing Hg concentrations with depth due to particle removal. They found that increasing anthropogenic emissions lead Hg concentration peak at ~500 m depth due to remineralization of anthropogenic Hg bound to sinking organic particles. One shortcoming of this study is the lack of regional variability for factors such as atmospheric Hg deposition, sinking flux of organic particles, as well as ocean circulation etc.

In this chapter, we present a new state-of-the-science three-dimensional offline ocean tracer model for Hg. This model is the first to take into account the 3D transport of Hg in the ocean. It not only better describes the vertical transport of Hg in the water column, which is essential to understand the human perturbation by anthropogenic Hg emissions to the oceanic Hg cycle, but also takes into account the regional variability, which allows us to test our current understanding of the Hg cycling in the ocean by allowing direct comparisons to local observations. In the following, we describe this new model and run a Hg simulation under natural conditions, i.e. without concurrent or legacy anthropogenic Hg emissions (pre-1450) (Section 4.2). In Section 4.3, we evaluate our model results against observations of Hg concentrations in the deep ocean, which are thought to be less perturbed by human emissions. We discuss the natural ocean Hg budget in Section 4.4. The spatial distribution of transport/transformation fluxes as well as Hg concentrations are evaluated in Section 4.5 and 4.6, respectively, and major conclusions are summarized in Section 4.7. In the next chapter (Chapter 5), we will use this model to investigate the human perturbation to the ocean Hg cycle.

4.2 Model description

We have developed a new Hg simulation in the University of Washington three-dimensional offline ocean tracer model (OFFTRAC), which was first described in Deutsch et al. (2006). The world's oceans are resolved on an approximate 1°×1° horizontal grid, with 1/3° latitude resolution near the equator, and 49 vertical isopycnal layers referenced to 2000db ranging from $\sigma_2 = 21.85\text{-}37.90$ kg m^{-3}. The model has two levels of Kraus-Turner type mixed layer (Kraus and Turner, 1967) and two buffer layers allowing smooth entrainment/detrainment from/to underlying isopycnal surfaces.

The Ocean circulation in the OFFTRAC model is computed with the Hallberg Isopycnal Model (HIM) (Hallberg and Rhines, 1996; Ladd and Thompson, 2001). The HIM model is initialized as a quiescent ocean with climatological mean isopycnal depths, temperature and salinity (Steele et al., 2001). The surface salinity is restored toward climatological mean at a transfer velocity of 50 m day^{-1}. The model is forced at the surface by the normal year climatological Common Ocean Reference Experiment version 2 (CORE-2) (Large and Yeager, 2009). The model is spun up for 650 years to achieve steady-state. We use the monthly physical fields (including mass transports, temperature, salinity, and monthly instantaneous isopycnal thickness) over the last 20 years of the 650-year HIM run to drive OFFTRAC.

The advection in OFFTRAC model is calculated implicitly with 30 iterations. Transport due to unresolved eddies in the mixed layer and buffer layers are modeled using the scheme developed by Gent and McWilliams (1990), while an uniformly 2000 m^2/s diffusivities are applied along the isopycnal layers (Jenkins 1990). The air-sea exchange in the surface mixed layer is calculated using an Euler forward method with a time step of one day. Calculated tracers include dissolved inorganic carbon, phosphorous, nitrogen, chlorofluorocarbons, oxygen and sulfur hexafluoride. With this model, Deutsch et al. (2006) reproduced the patterns of observed variability in O_2 over the North Pacific and attributed the observed decreases in O_2 between 1980s and 1990s to changes in ocean ventilation and circulation. Since that work, the model has been implemented in the global domain (Deutsch et al., 2011) and is being used to investigate carbon uptake in the North Pacific and chlorofluorocarbons and oxygen in the Southern and global Ocean (Trossman et al., 2012; Shao et al., 2013). The OFFTRAC model has a diagnostic to calculate the age of a water mass, defined as the elapsed time since last contact with the atmosphere.

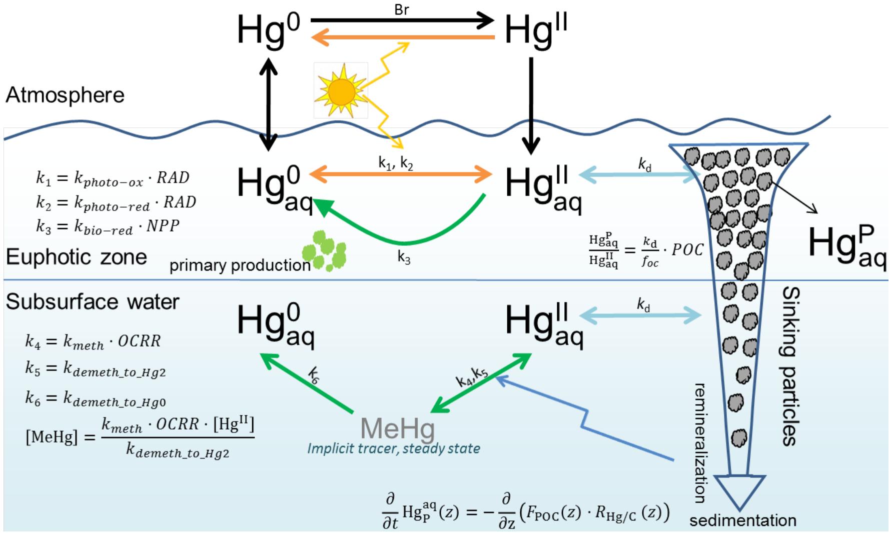

Figure 4.1: Model parameterization of Hg chemistry in the ocean. Black arrow in the atmosphere indicates Hg^0 oxidation to Hg^{II}, while the yellow one indicates photo-reduction. Black arrows across the air-sea interface indicate air-sea exchange of Hg^0 and deposition of Hg^{II} to ocean. The yellow arrows in the euphotic zone indicate photo-oxidation (k_1) and reduction (k_2) between Hg^0_{aq} and Hg^{II}_{aq}, both of which are proportional to the short-wave radiation flux (*RAD*). The green arrow indicates biological reduction of Hg^{II}_{aq} (k_3), which is proportional to net primary production (*NPP*). The green arrows in the subsurface water represent methylation (k_4) and demethylation (k_5, k_6) processes. The methylation of Hg^{II}_{aq} is proportional to organic carbon remineralization rate (*OCRR*). Blue arrows represent the partitioning between Hg^{II}_{aq} and Hg^P_{aq} via a sorption/desorption (k_d). Hg^P_{aq} can be transported downward with sinking particles (*POC*). Yellow broken arrows indicate the reduction of Hg^{II} in atmosphere and the transformations between Hg0aq and HgIIaq are photo-mediated, while blue broken arrow indicates that the methylation in subsurface water is facilitated by the remineralization process. See more details in the text.

Our Hg simulation in OFFTRAC (OFFTRAC-Hg) uses three Hg tracers: dissolved elemental Hg (Hg^0_{aq}), dissolved divalent Hg (Hg^{II}_{aq}), and particle matter associated Hg (Hg^P_{aq}). While there are many more forms of Hg in the oceans, for simplicity we have chosen the Hg^{II}_{aq} tracer to represent all dissolved forms of inorganic and organic Hg complexes including MeHg

(MMHg and DMHg). MeHg is not modeled explicitly, but it is an implicit tracer assumed to be at steady-state in the model (Figure 4.1). The Hg^{P}_{aq} tracer includes both inorganic and organic Hg species bound to particles. We consider the photo- and biogeo-chemical transformations between Hg^{0}_{aq} and Hg^{II}_{aq}, as well as organic particle scavenging and remineralization processes in the water column. These processes are summarized in Figure 4.1 with more details described in the following subsections. We initialize the OFFTRAC-Hg simulation with a clean ocean (i.e. zero Hg concentrations), and spin up the model for 10,000 years using monthly climatological fields of atmospheric Hg^{II} deposition flux and atmospheric Hg^{0} concentrations from the GEOS-Chem natural simulation. We find that after 10,000 years, Hg concentrations in OFFTRAC-Hg reach steady-state.

4.2.1 Surface ocean redox reactions and Hg0 evasion

In the mixed layer, we model the reduction of Hg^{II}_{aq} to Hg^{0}_{aq}, the oxidation of Hg^{0}_{aq} to Hg^{II}_{aq} as well as the Hg^{0} evasion flux following the parameterization of Strode et al. (2007), with updates from Soerensen et al., (2010a). Briefly, both the oxidation and reduction are photochemically and biologically mediated. The photochemical oxidation and reduction first order rate constants (k_1 and k_2 in Figure 4.1) are proportional short-wave radiation at the sea surface attenuated by dissolved organic carbon (DOC) and pigments in the surface ocean water. We use the NASA Goddard Earth Observing System (GEOS-5) climatological monthly mean short wave radiation flux. Climatological annual mean DOC concentrations are from the coupled physical biogeochemical model simulation of Hansell et al. (2009). The chlorophyll concentrations are derived from MODIS satellite data (http://oceancolor.gsfc.nasa.gov). This data is used to calculate pigments concentration in the surface water following Soerensen et al. (2010a). The reduction of Hg^{II}_{aq} to Hg^{0}_{aq} (k_3) is also biologically mediated, and is proportional to the net primary production (NPP) in the surface ocean, which is derived from MODIS satellite data (http://oceancolor.gsfc.nasa.gov). We assume that only 40% of the $\mathrm{Hg^{II}_{aq}}$ is reducible to $\mathrm{Hg^{0}_{aq}}$, following Soerensen et al. (2010a). A first order reaction for the dark oxidation of $\mathrm{Hg^{0}_{aq}}$ in the mixed layer is also considered in this chapter. The $\mathrm{Hg^0}$ evasion flux is calculated based on the concentration gradient across the air-sea interface and the piston velocity, which is a function of wind speed and temperature (Nightingale et al., 2000).

4.2.2 Sorption of Hg^{II}_{aq} to particles

We assume the $\mathrm{Hg^{II}_{aq}}$ and $\mathrm{Hg^{P}_{aq}}$ are in instantaneous equilibrium with each other (Morel et al., 1998). As $\mathrm{Hg^{II}_{aq}}$ species have a high affinity to suspended particles and are associated with organic ligands (Fitzgerald et al., 2007), we assume that the ratio of $\mathrm{Hg^{P}_{aq}}$ to $\mathrm{Hg^{II}_{aq}}$ is proportional to the local levels of particulate organic carbon (*POC*):

$$\frac{\mathrm{Hg^{P}_{aq}}}{\mathrm{Hg^{II}_{aq}}} = \frac{k_{\mathrm{d}}}{f_{oc}} POC \tag{1}$$

where k_d is partition coefficient (L $\mathrm{kg^{-1}}$) and f_{oc} is the fraction of organic carbon in suspended particulate matter. We use $f_{oc} = 10\%$, following Strode et al. (2010). Reported values of k_d range from 10^5 to 10^6 L $\mathrm{kg^{-1}}$ in estuarine and coastal waters (Fitzgerald et al., 2007). Here we adopt a value of 2.9×10^5 L $\mathrm{kg^{-1}}$ in order to reproduce constraints based on observed deep ocean Hg concentrations and Hg sedimentation fluxes.

We use the climatological monthly mean surface ocean POC concentration derived from SeaWiFS ocean color (http://oceancolor.gsfc.nasa.gov). In subsurface waters, POC concentrations are calculated based on a power law following Lam et al. (2011) and Siddall et al. (2005):

$$POC(z) = POC_0 \cdot \left(\frac{z}{z_0}\right)^{-b} \tag{2}$$

where $POC(z)$ is the POC concentration in units of kg L^{-1} at depth z, b is the power law exponent, and POC_0 is the initial POC concentration at reference depth of z_0, which we use the SeaWiFS product at ocean surface. We use $z_0 = 75$ m and $b = 0.9$ following the Ocean Carbon Model Intercomparison Project (OCMIP) protocol (Najjar and Orr 1999).

4.2.3 Particle sinking and sedimentation

The sinking flux of Hg^P_{aq} at each model level at depth z is assumed to be proportional to the exported flux of POC (F_{POC}, mol m^{-2} s^{-1}) and the Hg^P_{aq} to carbon ratio ($R_{Hg/C}$):

$$\frac{\partial}{\partial t}\mathrm{Hg}_{\mathrm{P}}^{\mathrm{aq}}(z) = -\frac{\partial}{\partial \mathrm{z}}\left(F_{\mathrm{POC}}(z) \cdot R_{\mathrm{Hg/C}}(z)\right) \tag{3}$$

with:

$$R_{\mathrm{Hg/C}}(z) = \frac{\mathrm{Hg}_{\mathrm{P}}^{\mathrm{aq}}(z)}{POC(z)} \tag{4}$$

The POC flux at the bottom of the euphotic layer, $F_{POC}(z_0)$, is calculated based on NPP and the ratio of POC export to NPP (the *pe-ratio*, Dunne et al., 2005):

$$F_{\mathrm{POC}}(z_0) = NPP \cdot pe - ratio \tag{5}$$

$$\begin{gathered} pe - ratio = -0.0081T + 0.0806\ln(Chl) + 0.426 \\ 0.04 < pe - ratio < 0.72 \end{gathered} \tag{6}$$

where T is surface atmospheric temperature (°C), and Chl is the surface chlorophyll concentrations (mg Chl m^{-3}). In the subsurface waters, the F_{POC} is calculated as:

$$F_{\mathrm{POC}}(z) = F_{\mathrm{POC}}(z_0) \cdot \left(\frac{z}{z_0}\right)^{-b} \tag{7}$$

we use the same z_0 and b values as in Equation (2).

4.2.4 Reduction of Hg^{II}_{aq} in subsurface water

Based on observations in the low oxygen sub-thermocline region of the Equatorial Pacific Ocean, Mason and Fitzgerald (1993) hypothesized that ionic Hg^{II}_{aq} is converted into DMHg, which then decomposes via MMHg to Hg^0_{aq}. Methylation and demethylation process of Hg^{II}_{aq} in low oxygen subsurface waters thus provide a reduction pathway to Hg^0_{aq} (Fitzgerald et al., 2007). Observations in the Equatorial and South Atlantic Ocean also support this hypothesis (Mason and Sullivan, 1999). Using Hg isotopes, Lehnherr et al. (2011) measured the Hg^{II}_{aq} methylation reaction coefficient to MMHg ($6.8\pm3.9\times10^{-3}$ d^{-1}), MMHg demethylation to Hg^{II}_{aq} ($3.6\pm0.9\times10^{-1}$ d^{-1}) and MMHg demethylation to Hg^0_{aq} (from below detection to 3.6×10^{-4} d^{-1}) in the Arctic Ocean, confirming this hypothesis. Sunderland et al. (2009) found a positive linear relationship between methylated Hg concentrations and organic carbon remineralization rates (*OCRR*) in the subsurface water in the eastern North Pacific Ocean, providing evidence linking POC decomposition rates to bacterial methylation processes. They also observed lower methylated Hg concentrations in deeper water masses resulting from demethylation. We parameterize the net reduction of Hg^{II}_{aq} to Hg^0_{aq} (i.e. $Hg^{II}_{aq} \rightarrow MeHg \rightarrow Hg^0_{aq}$) as a first-order rate constant, $k_{\text{red}}^{\text{methyl/demethyl}}$ (s^{-1}) below 150 m:

$$k_{\text{red}}^{\text{methyl/demethyl}} = \alpha \cdot OCRR \tag{8}$$

where α is a constant (can be calculated as $\frac{\mathrm{k}_{meth}}{k_5} \cdot k_6$) and *OCRR* (mol m^{-3} s^{-1}) is calculated as the vertical gradient of F_{POC}:

$$OCRR = -\frac{\partial}{\partial \mathrm{z}} F_{\text{POC}}(z) \tag{9}$$

The value of the constant, $\alpha = 4\times10^{-6}$, is chosen so as to best reproduce observed profiles of Hg^0_{aq} in subsurface waters and the Hg^0_{aq} evasion flux.

4.2.5 Riverine input

We calculate the riverine input of Hg (F_{riverine}, mol $grid^{-1}$ s^{-1}) at river mouths based on the river runoff (R, $\times10^6$ m^3 s^{-1}) and the nearby average soil Hg concentrations (C_{soil}, ng g^{-1}):

$$F_{\text{riverine}} = \beta \cdot R \cdot C_{\text{soil}} \tag{9}$$

We use the climatological monthly mean freshwater discharge from continents developed by Dai and Trenberth (2002) with a spatial resolution of 1°×1°. We average the soil Hg concentration near the river mouth within a distance of approximately of 500 km based on the soil Hg concentration distribution calculated in the GEOS-Chem land model (see below). We tune the scaling constant ($\beta = 6.7\times10^{-1}$ mol m^{-3} $grid^{-1}$ to obtain a global riverine flux of 0.4 Mmol yr^{-1} under natural conditions, following Amos et al. (2013).

4.2.6 Input from the GEOS-Chem atmosphere-ocean-land Hg simulation

The atmospheric component of our OFFTRAC-Hg simulation is obtained from the GEOS-Chem Hg simulation at 4°×5° horizontal resolution. GEOS-Chem is a global three-dimensional atmospheric chemistry transport model described detailed in Bey et al. (2001). The model is driven by assimilated meteorological fields from the NASA Goddard Earth Observing System (GEOS). The GEOS-Chem Hg simulation (Selin et al., 2007) contains two atmospheric tracers: elemental mercury (Hg^0) and divalent mercury (Hg^{II}). The model assumes that bromine atoms are the only oxidant for Hg^0 and that the reduction of Hg^{II} in the aqueous phase is proportional to the photolysis rate of NO_2 (Holmes et al., 2010). The model also contains surface soil and slab ocean module (Selin et al., 2008; Strode et al., 2007; Soerensen et al., 2010a). In addition to dry/wet deposition, the re-emission of Hg^0 over soil and bi-directional exchange of Hg^0 over ocean surface are considered. As part of this chapter, we conduct a natural GEOS-Chem Hg simulation in which we turn off all the anthropogenic Hg sources. We assume that the only direct source of Hg is from geogenic emissions of 0.5 Mmol yr^{-1} (Mason and Sheu, 2002). This source is distributed according to the locations of Hg mines as an indicator of Hg deposits (Selin et al., 2008 and the reference therein). The global average soil Hg concentrations and intermediate water Hg concentrations for the GEOS-Chem natural simulation are based on the results of

Amos et al. (2013). The spatial distribution of soil Hg concentrations is taken from Selin et al. (2008) which is calculated based on the balance between atmospheric deposition and soil re-emission fluxes, while the Hg concentrations in the intermediate water are assumed to be uniformly distributed. We archive monthly mean atmospheric Hg^0 concentrations and Hg^{II} deposition flux from our GEOS-Chem natural Hg simulation and use them as inputs to our OFFTRAC-Hg simulation.

4.3 Model evaluation

Table 4.1: Summary of cruises with deep ocean total Hg concentration measurements.

Cruise/Station	Ocean	Date	Hg^T concentrations, pM (> 2000 m)[a]		Reference
			Obs.	Model	
IOC 2002 (43t, 48t, and 50t)	West North Pacific	May-Jun 2002	1.2±0.3	1.3±0.06	Laurier et al. (2004)
VERTEX (60t)	East North Pacific	Jul-Aug 1987	1.0±0.2	1.4±0.04	Laurier et al. (2004)
SAFe (57t)	East N. Pacific (30°N, 140°W)	May 2009	1.4±0.2	1.3±0.04	Hammerschmidt and Bowman (2012)
IOC 1993 (22t, 23t, and 24t)	Subarctic N. Atlantic	Aug 1993	1.7±0.4	0.3±0.07	Mason et al. (1998)
BATS (31t)	North Atlantic (31°N, 64°W)	Mar 1999	0.7±0.3	0.6±0.09	Mason et al. (2001)
Knorr IOC 1996 (37t, 38t, and 39t)	Equatorial and S. Atlantic	May-Jun 1996	4.[illegible]±1.0	0.8±0.09	Mason and Sullivan (1999)
SR3 CASO-GEOTRACES	Southern Ocean	Mar-Apr 2008	1.1±0.2	1.0±0.03	Cossa et al. (2011)

[a]Total Hg concentrations at depths below 2000 m (in pM). The mean and standard deviation of observed and modeled values are indicated in separate columns.

We evaluate our simulation against observed Hg concentration profiles and cross sections over different ocean basins obtained over the past two decades. As Hg concentrations in surface and intermediate oceans are believed to have been perturbed by anthropogenic activities (Mason et al., 1994), we will focus our comparison on the deep ocean (depth > 2000 m), where Hg concentrations have not seen much anthropogenic influence (Strode et al., 2010). We also exclude the observations conducted in coastal or near shelf environments, where the influence of human activity may be more prevalent. We have compiled 13 published vertical profiles/sections from 7 individual studies as summarized in Table 4.1. The sampling locations of these observations are shown in Figure 4.2. These observations are from the North Pacific Ocean (Laurier et al., 2004; Hammerschmidt and Bowman 2012), the North Atlantic Ocean (Mason et al., 1998; Mason et al., 2001), the Equatorial and S. Atlantic Ocean (Mason and Sullivan 1999) and the Southern Ocean (Cossa et al., 2011). We sample the model annual mean concentrations (no significant seasonal variation is modeled for Hg concentrations in the deep ocean) at the location of each profile and the results are summarized in Table 4.1 and Figures 4.2- 4.6.

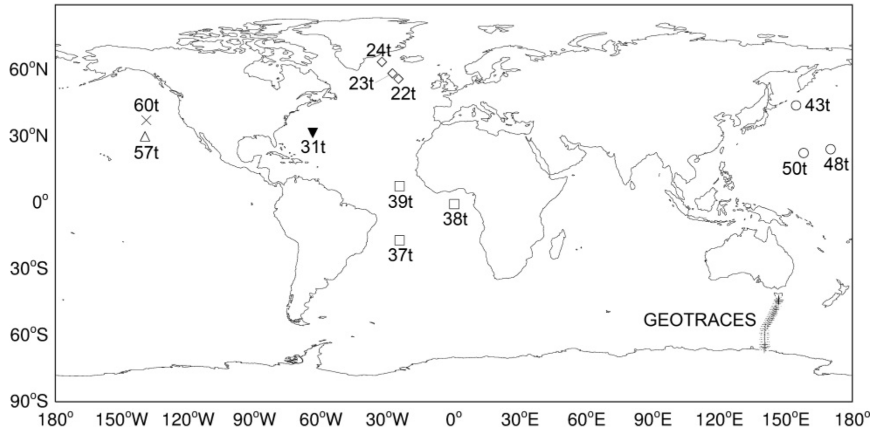

Figure 4.2: Distribution of the location of sites used in this chapter. (○) 2002 IOC; (×) VERTEX; (Δ)SAFe; (▼) BATS; (◊) 1993 IOC; (□) Knorr 1996 IOC; (+) SR3 CASO-GEOTRACES. See Table 4.1 for more detail.

4.3.1 North Pacific Ocean

Laurier et al. (2004) reviewed 20 years of published observations in the North Pacific Ocean and found that Hg concentrations in deep and bottom waters had relatively uniform values (1.0-1.4 pM) among different cruises and studies. In contrast, upper waters displayed large temporal and spatial variability in Hg concentrations. In a more recent study, Hammerschmidt and Bowman (2012) reported similar deep water total Hg concentrations (1.4±0.2 pM) at the SAFe station over the eastern North Pacific. Five profiles of observed Hg concentrations in the North Pacific Ocean are shown in Figure 4.3. The modeled age of water mass is also shown for comparison. Our model captures the mean observed concentration levels (observations: 1.2±0.4 pM; model: 1.3±0.06 pM) in the deeper part of the profile generally well. Our modeled profiles do not display as much variability as the observations, likely because our model is driven by repeating climatological circulation data, missing interannual variations in ocean circulation. Meanwhile, the low resolution in the model cannot resolve the mesoscale eddies which may be likely aliased by these measurements. The modeled bathymetry is also slightly different form the observations because of the coarse resolution and sub-grid variability of ocean depth within model grids.

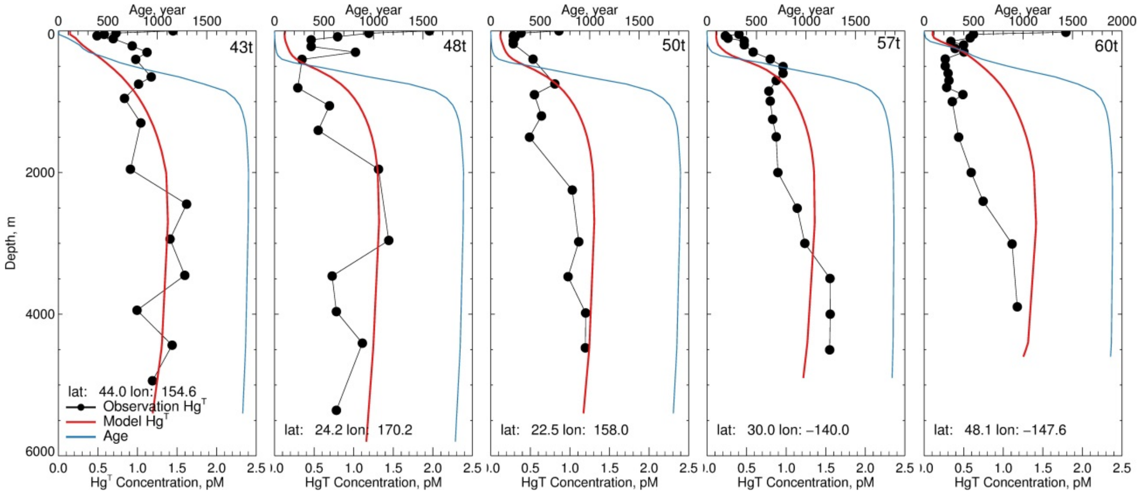

Figure 4.3: North Pacific Ocean profiles of total Hg concentrations. The OFFTRAC-Hg model results (red lines) are compared to observations (black lines with diamonds). The modeled age of water mass is also shown (blue line). The locations of these profiles are shown in Figure 4.2.

4.3.2 North Atlantic Ocean

Figure 4.4 compares four profiles over the North Atlantic Ocean to our model results. Our model reproduces deep ocean total Hg concentrations near Bermuda (profile 31t), with concentration level of around 0.7±0.3 pM (> 2000 m depth) compared to 0.6±0.09 pM for observations. However, the modeled total Hg concentrations are much lower than observations over the Subarctic Atlantic Ocean (profiles 22t, 23t and 24t). The three stations had average total Hg concentration of 1.7±0.4 pM below 2000 m, while the modeled results are 0.3±0.07 pM, a factor of 5-6 lower than observations. As discussed by Mason et al. (1998), newly formed deep water is diagnosed for the deep water for the profile 24t. The subarctic region is one important region for the deep water formation, through which surface Hg can be transported to the deep ocean very quickly (Mason et al., 1998). Further mixing and lateral advection and diffusion enhance the overall Hg concentration over this region. Therefore, the difference between model and observations over this region could be the result deep ocean penetration of anthropogenic Hg influence from both atmospheric deposition and riverine effluent (Soerensen et al., 2010a; 2012; Streets et al., 2011). The anthropogenic influence is not included in our OFFTRAC-Hg simulation. The fact that the lower-latitude BATS station displays much lower observed Hg concentrations (0.7 pM) than the North Atlantic deep ocean formation region (1.7 pM) also demonstrates this point (Table 4.1).

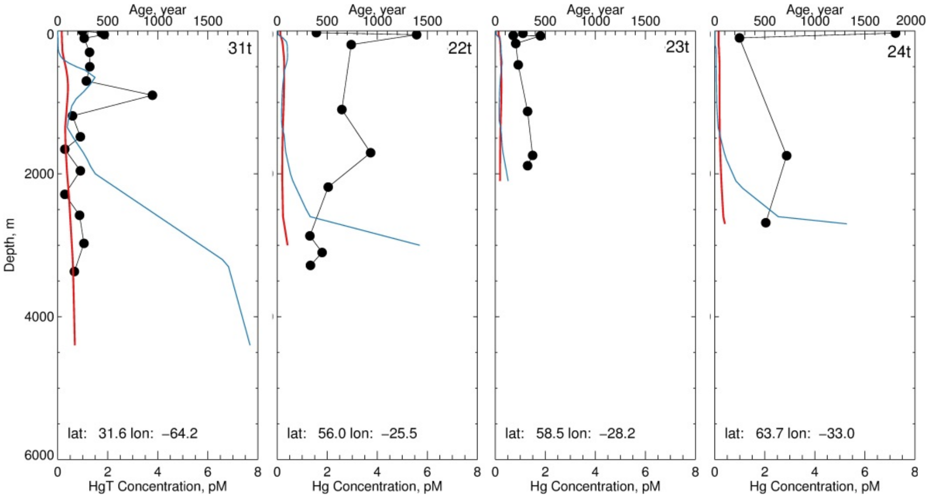

Figure 4.4: Same as Figure 4.3, but for the North Atlantic Ocean.

4.3.3 Equatorial and South Atlantic Ocean

We compare three Equatorial and S. Atlantic Ocean profiles to our model results in Figure 4.5. Total Hg concentrations predicted by the model in the deep ocean (> 2000 m) range from 0.68-

0.81 pM. These values are a factor of 2 lower than observations at station 38t (1.5±0.38 pM), but much lower than observations at the other two stations (37t: 2.9±2.1 pM; 39t: 7.2±4.3 pM). Mason and Sullivan (1999) argued that the high values at the bottom of the profiles could reflect a sediment source of Hg, which is not included in our model.

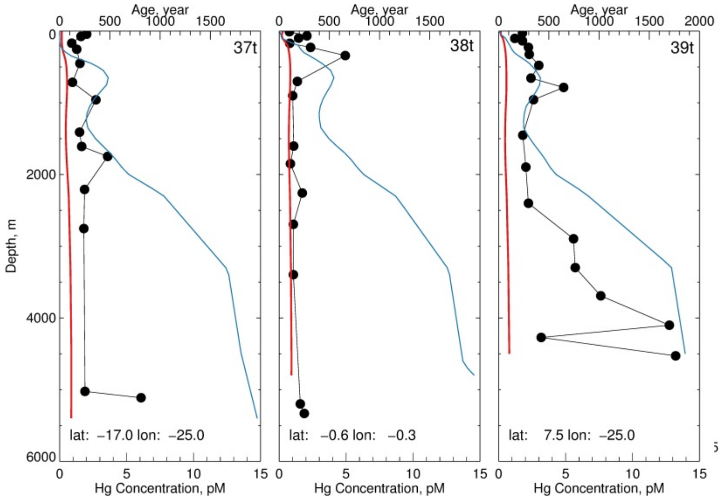

Figure 4.5: Same as Figure 4.3, but for the Equatorial and South Pacific Ocean.

4.3.4 Southern Ocean

Cossa et al. (2011) reported aqueous Hg concentration measurements along a South-to-North section between Antarctica and Australia along the 140°E meridian, as part of the SR3 CASO-GEOTRACES cruise. The distribution of observed total Hg concentrations is displayed in Figure 4.6, along with our model sampled along the cruise track. In the deep ocean north of 55°S, model and observations display similar total Hg concentrations of ~1 pM. South of 55°S, elevated total Hg concentrations are observed in the surface and in deep waters, which Cossa et al. (2011) attributed to the net atmospheric Hg deposition input near the ice edge and subsequent downward transfer during deep water formation in winter months. Similar to the situation in the Subarctic Atlantic Ocean, these high concentrations contain a signature from the present-day anthropogenic perturbation, which is not expected to be captured by our model simulation of the natural Hg cycle.

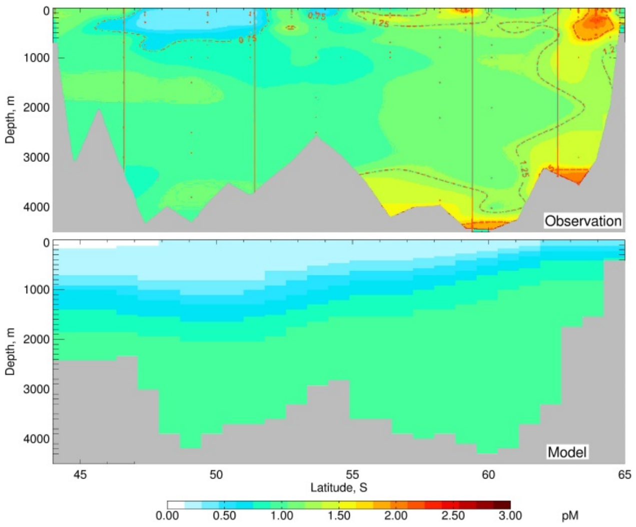

Figure 4.6: Observed (top) and modeled (bottom) total Hg concentrations over the Southern Ocean along a 140°E cross-section during the SR3 CASO-GEOTRACES cruise in April-May 2008 (top panel adapted from Cossa et al., 2011).

In summary, our model predicts Hg concentrations (1.1±0.3 pM) that are consistent with observations in old and deep-water masses (1.4±0.9 pM), which are less influenced by anthropogenic activities, such as the North Pacific Ocean, the mid-latitude and equatorial North Atlantic Ocean as well as sub-polar Southern Ocean. As expected, the model predicts much lower Hg concentrations than observations for younger water masses which reflect the human perturbation. The difference between our natural Hg cycle concentrations and observations in these regions can be used to generate a first-order estimate of the anthropogenic influence in these regions: a factor of ~6 difference for surface ocean concentrations, factors of 3-4 in coastal and near shelf regions (data not shown), factors of 5-6 in deep water formation regions of the North Atlantic, and factors of 1.3-1.4 for the high latitude Southern Ocean. As sediment and related processes are not included in this chapter, our model also tends to underestimate the observed Hg concentrations near the ocean floor, where the sediment could serve as a potential source, especially for methylmercury.

4.4 The natural ocean Hg budget

Figure 4.7 (left) shows the global Hg budget under natural conditions as simulated in OFFTRAC-Hg. We summarize our results by examining 6 reservoirs: the atmosphere, the surface soil and vegetation, the deep mineral reservoir, the mixed layer surface ocean (the depth varies spatially and seasonally, with a global average depth of ~50 m), the intermediate ocean (from the bottom of the mixed layer to a depth of 1000 m, representing the main thermocline), and the deep ocean (below 1000 m, representing the cold, slow-mixing abyssal ocean). The fluxes among all the reservoirs, as well as the Hg mass and mean Hg concentrations are also shown.

The atmosphere receives emissions from a direct geogenic source (0.5 Mmol yr^{-1}) as well as re-emissions from land (1.6 Mmol yr^{-1}) and the ocean (3.8 Mmol yr^{-1}). These inputs are balanced by deposition of Hg to the land (2.0 Mmol yr^{-1}) and ocean surfaces (3.9 Mmol yr^{-1}) (Figure 4.7 left). The surface ocean receives Hg input from the atmosphere (3.9 Mmol yr^{-1}), rivers (0.4 Mmol yr^{-1}) and advection from the intermediate ocean (0.6 Mmol yr^{-1}). Of this total source, 75% of the Hg is loss by evasion to the atmosphere (3.8 Mmol yr^{-1}), while 25% either sinks to the intermediate ocean onto particles (1 Mmol yr^{-1}) or is deposited to coastal and near-shelf sediments (0.1 Mmol yr^{-1}). The mean mixed layer total Hg concentration (0.17 pM) is a factor of ~6 lower that observed present-day concentrations (based on observations summarized in Strode et al., 2007 and Soerensen et al., 2010a). In the intermediate ocean, the main source of Hg is via particle sinking from the surface ocean (1 Mmol yr^{-1}), with a smaller source from upward advection of deep ocean Hg (0.3 Mmol yr^{-1}). This is consistent with previous models

(Strode et al., 2010; Mason et al., 2012; Amos et al., 2013). Loss of Hg from the intermediate ocean occurs via upward transport to the mixed layer (0.6 Mmol yr^{-1}), downward particle sinking flux to the deep ocean (where ocean bathometry is deeper than 1000 m, 0.5 Mmol yr^{-1}) and sedimentation (a depth between 50 m and 1000 m, 0.2 Mmol yr^{-1}). In our model, the only source of Hg to the deep ocean is via particle sinking (0.5 Mmol yr^{-1}), which is subsequently deposited to sediments (0.2 Mmol yr^{-1}) or transported to the intermediate ocean (0.3 Mmol yr^{-1}). The resulting residence times of Hg in the deep ocean (~2,000 years) and intermediate oceans (~100 years) are much longer that in the atmosphere (8 months) and surface oceans (7 months).

Figure 4.7 (right) presents a more detailed view of the marine Hg cycle with speciation information. The total Hg mass in our modeled natural ocean is 1200 Mmol, with 3 Mmol in the surface, 150 Mmol in the intermediate and 1000 Mmol in the deep ocean. In the surface ocean, most of the Hg is in the form of Hg^{II}_{aq} (0.15 pM), with much smaller contributions from Hg^{0}_{aq} (0.014 pM) and Hg^{P}_{aq} (0.014 pM). We find that ~70% of the Hg^{II}_{aq} is reduced to Hg^{0}_{aq} in the mixed layer, with the rest being partitioned onto particles. In the surface ocean, Hg^{0}_{aq} is produced by net reduction of Hg^{II}_{aq} (3.1 Mmol yr^{-1}), with an additional input from upward transport from intermediate waters (0.7 Mmol yr^{-1}). The supersaturation of Hg^{0}_{aq} results in rapid evasion to the atmosphere (3.8 Mmol yr^{-1}). We calculate a mean residence time of Hg^{0}_{aq} in the surface ocean of 22 days. The continuous decreasing POC sinking flux (F_{POC}) with depth due to remineralization (Equation 7) leads to a decrease in the Hg^{P}_{aq} particulate sinking flux with depth (from 1 Mmol yr^{-1} at the bottom of the mixed layer, to 0.5 Mmol yr^{-1} at a depth of 1000 m, and 0.2 Mmol yr^{-1} to the ocean floor deeper than 1000 m). In the intermediate ocean, there is a net desorption of Hg from particles into Hg^{II}_{aq} (0.4 Mmol yr^{-1}), which is then reduced to Hg^{0}_{aq} via methylation/demethylation (0.5 Mmol yr^{-1}). This reduction causes elevated Hg^{0}_{aq} concentrations in the intermediate ocean (0.22 pM), which advects and/or diffuses (0.7 Mmol yr^{-1}) to the surface ocean. Similarly, in the deep ocean the sinking of Hg^{P}_{aq} attached to POC and its remineralization provides a net source of Hg^{II}_{aq} (0.3 Mmol yr^{-1}), which is subsequently either reduced to Hg^{0}_{aq} (0.2 Mmol yr^{-1}) or advected upward (0.1 Mmol yr^{-1}).

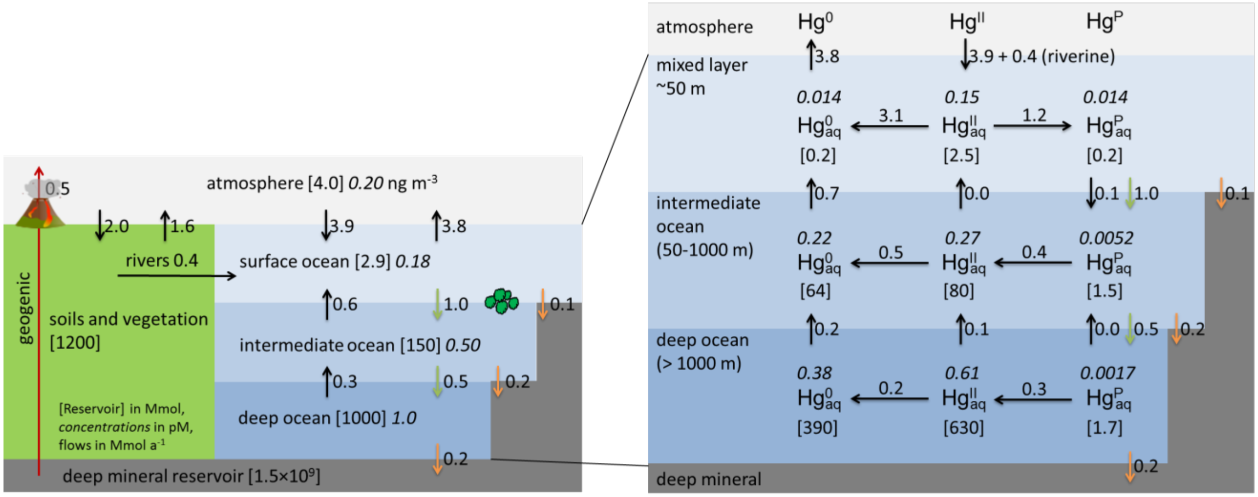

Figure 4.7: Global natural mercury budget in OFFTRAC-Hg. The total Hg mass in each reservoir is indicated in brackets in units of Mmol, while concentrations are shown in italics with units of pM (except for the atmosphere, where we use ng m^{-3}). Next to each arrow, flux is indicated in Mmol a^{-1}. The geogenic source is shown as a red arrow, while the Hg particle sinking and sedimentation fluxes are shown as green and yellow arrows, respectively. The mass of Hg in the soil and deep mineral reservoirs are taken from Amos et al. (2013).

In our model simulation, we find that in the surface ocean, Hg^{0}_{aq} accounts for only ~10% of total Hg, because of its rapid evasion to the atmosphere. However, our model predicts that a significant fraction of Hg is present as Hg^{0}_{aq} in the intermediate ocean (44% of Hg as Hg^{0}_{aq}) and deep ocean (38%) (Figure 4.7 right). This is consistent with observations. For example, Mason and Sullivan (1999) found that Hg^{0}_{aq} accounts for more than 60% of the total Hg concentration at station 38t in the Equatorial Atlantic. At that station, our model predicts that Hg^{0}_{aq} accounts for 48% of total Hg. In the Equatorial Pacific, Mason and Fitzgerald (1993) found increasing concentrations of Hg^{0}_{aq} with depth, reaching values of 0.5 pM and accounting for ~30% of the total Hg concentrations at a depth of several hundred meters, while our model predicts higher fraction (51%). Mason and Sullivan (1999) explained these enhanced Hg^0_{aq} concentrations in deeper waters as the result of methylation of Hg^{II}_{aq} followed by demethylation to Hg^0_{aq}. This process is incorporated in a parameterized form in our model as described in Equation (8) and Figure 4.1. In our model, we find that Hg is transported as Hg^P_{aq} via particle sinking into the intermediate and deep ocean, where it is remineralized to Hg^{II}_{aq} and then reduced to Hg^0_{aq}. Hg^0_{aq} then cycles back to the surface via ocean advection and diffusion. In a sensitivity simulation, we turned off the Hg^{II}_{aq} reduction in sub-surface waters ($k_{\mathrm{red}}^{\mathrm{methyl/demethyl}} = 0$). This leads to very low Hg^0_{aq} concentrations (< 0.01 pM) in the intermediate and deep ocean. Without this reduction pathway, diffusion down from the surface is the only source of Hg^0_{aq} in the deep ocean. It seems that our highly simplified scheme for this production of Hg^0_{aq} in subsurface waters is plausible and is consistent with available observations within a factor of ~2. Hg^P_{aq} accounts about 8% in the surface ocean, but less than 1% in the intermediate and deep ocean, because of the sharp decrease of POC concentrations with depth.

Our estimate for the atmospheric deposition to the ocean (3.9 Mmol yr^{-1}) is approximately a factor of 2 smaller than the previous studies focusing on preindustrial time (ca. 1850, e.g. 8.5 Mmol yr^{-1} by Selin et al. 2008; 6.8 Mmol yr^{-1} by Mason and Sheu 2002), but closer to recent studies which also considered the legacy of the mining activity prior to the industrial revolution (e.g. 2.8 Mmol yr^{-1} by Amos et al., 2013). We find an overall lifetime of Hg in the ocean against sedimentation of 2,600 years, somewhat close to the ocean's overturning time scale, ~1,000 years (Schmittner et al., 2007). This is close to the estimate of 3,000 years by Mason and Sheu (2002), which has similar assumptions for geogenic emission flux and total ocean Hg mass. Our estimate is longer than the 600 years by Selin et al. (2008), which assumes higher geogenic emission (2.5 Mmol yr^{-1}). Our 2,600 year residence time is also longer than the

1,400 years estimated by Amos et al. (2013), even though we assume the same geogenic source. This is probably caused by their assumed stronger ocean vertical mixing. Indeed, they represented the ocean as 3 boxes. The assumption of full mixing in the subsurface and deep ocean is likely to overestimate vertical transport in their model.

Budgets for different ocean basins are tabulated in Table 4.2, which highlights the regional differences in riverine effluent, ocean bathymetry, ocean circulation, as well as primary productivity. For example, unlike the situation for global ocean and other ocean basins, the riverine input and sedimentation are the main source and sink for the Arctic Ocean, respectively, and the ocean evasion is less important because of the large fraction of ice cover. Another significant difference is the fraction of Hg^{II}_{aq} sinking with POC accounting for the total Hg^{II}_{aq} input from atmospheric deposition and riverine effluent in the mixed layer, which is largely dependent on the magnitude of local POC sinking flux. The fractions range from 18% in S. Pacific Ocean, ~22% in North Pacific and Indian Ocean, ~30% in Atlantic Ocean, and ~70% in Arctic and Southern Ocean. We also calculate the lifetime of total Hg in different ocean basins relative to the total sedimentation flux. The lifetime is the shortest (110 years) in the Arctic Ocean because of the shallow depth and thus relatively easy to overturn. This also causes the total Hg concentrations in this ocean basin relatively constant with depth (~0.18 pM). The North Atlantic Ocean basin also has short lifetime regarding to sedimentation (910 years) largely caused by the strong vertical exchange of water mass in the process of deep water formation. The lifetimes in other ocean basins are much longer, ranged between 2,300-4,400 years. These spatial heterogeneities will be discussed in more details in the following sections.

Table 4.2: Natural Hg budgets for different ocean basins

	Arctic	North Atlantic	South Atlantic	North Pacific	South Pacific	Indian	Southern	Global
Mixed layer								
Hg mass[a]	0.09	0.35	0.34	0.46	0.73	0.61	0.37	2.9
Hg conc.[b]	0.18	0.15	0.16	0.14	0.17	0.17	0.34	0.2
Sources								
Atmos. deposit.[c]	0.016	0.44	0.49	0.75	1.2	0.91	0.12	3.9
Riverine input	0.027	0.14	0.071	0.052	0.01	0.063	0	0.4
Upward transport	-0.005	0.054	0.075	0.056	0.16	0.15	0.13	0.6
Horizontal transport	0.001	0.013	0.002	0.004	-0.016	-0.001	-0.013	0
Sinks								
Ocean evasion	0.01	0.48	0.47	0.68	1.1	0.9	0.15	3.8
Particle sinking	0.022	0.13	0.16	0.16	0.21	0.19	0.086	1.0
Sedimentation	0.007	0.037	0.012	0.019	0.012	0.03	0.001	0.1
Intermediate ocean								
Hg mass	1	14	15	43	36	27	8.7	150
Hg conc.	0.18	0.39	0.45	0.65	0.46	0.44	0.71	0.5
Sources								
Particle sinking	0.022	0.13	0.16	0.16	0.21	0.19	0.086	1.0
Upward transport	0	0.04	0.034	0.062	0.062	0.07	0.081	0.3
Horizontal transport	-0.004	-0.013	-0.007	-0.013	0.015	0.012	0.015	0
Sinks								
Upward transport	-0.005	0.054	0.075	0.056	0.16	0.15	0.13	0.6
Particle sinking	0.002	0.066	0.092	0.13	0.12	0.10	0.047	0.5
Sedimentation	0.021	0.037	0.016	0.025	0.008	0.021	0.005	0.2
Deep ocean								
Hg mass	2.1	72	110	320	270	190	57	1000
Hg conc.	0.18	0.6	0.85	1.2	1.1	0.98	0.99	1
Sources								
Particle sinking	0.002	0.066	0.092	0.13	0.12	0.10	0.047	0.5
Horizontal transport	-0.001	-0.005	-0.031	-0.021	-0.01	0.006	0.043	0
Sinks								
Upward transport	0	0.04	0.034	0.062	0.062	0.07	0.081	0.3
Sedimentation	0.001	0.021	0.027	0.048	0.049	0.039	0.009	0.2
Entire column								
Sedimentation	0.029	0.095	0.055	0.092	0.069	0.09	0.015	0.5
Horizontal transport	-0.004	-0.005	-0.04	-0.03	-0.01	0.02	0.05	0
Lifetime[d]	110	910	2300	4000	4400	2400	4400	2600

[a] Mass of Hg in Mmol

[b] Mean concentraions in pM

[c] Fluxes of Hg in Mmol/yr

[d] Lifetime relative to total sedimentation flux in years

Figure 4.8 shows the global average concentration profiles for Hg^{0}_{aq}, Hg^{II}_{aq}, Hg^{P}_{aq} and total Hg in our model simulation. Overall, the model suggests that the total Hg concentrations under natural conditions increase continuously with depth to ~1.1 pM at the deepest ocean floor with higher concentration gradient in the topmost 1,000 m. Most of the Hg is present as Hg^{II}_{aq}, with concentrations increasing with depth because it is particle-reactive: it can be absorbed onto particulate and dead organic matter and be carried downward. A similar profile shape was found by Strode et al. (2010) in their 1D column ocean model, in which total Hg was assumed to be particle reactive. We find that Hg^{0}_{aq} concentrations also increase with depth and achieves maximum at depth of ~1,000 m, reflecting the production from Hg^{II}_{aq} reduction in the subsurface waters. The Hg^{0}_{aq} concentrations keep nearly unchanged below 2,000 m. As Hg^{0}_{aq} is unreactive towards particles, advection and diffusion minimize the vertical concentration gradient. The small enhancement of Hg^{0}_{aq} concentration below 5500 m is due to the North Pacific Ocean basin, which is deeper and has higher Hg^{0}_{aq} concentrations than other ocean basins. The Hg^{P}_{aq} concentrations are much lower and show an exponential decrease following the POC concentrations.

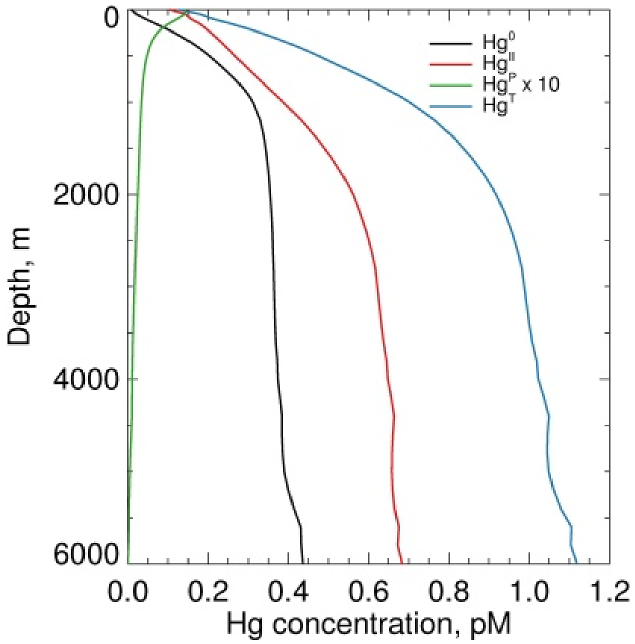

Figure 4.8: Average vertical profiles of Hg concentrations (Hg^{0}_{aq}, Hg^{II}_{aq}, Hg^{P}_{aq}×10 and total Hg_{aq}) over the global ocean in OFFTRAC-Hg.

4.5. Spatial distribution of fluxes

4.5.1 Biological related and chemical reaction fluxes

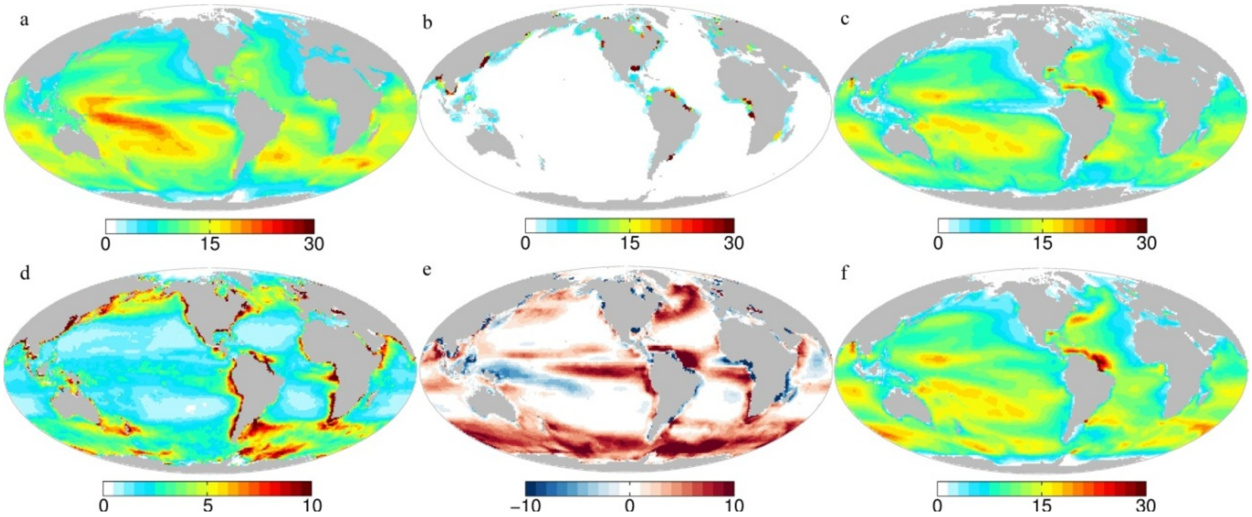

Figure 4.9: Annual mean fluxes for natural simulation (10^{-9} mol m^{-2} s^{-1}): a) atmospheric Hg^{II} deposition flux, b) riverine Hg^{II}_{aq} input flux, c) vertically integrated Hg^{II}_{aq} net reduction rate over the mixed layer, d) Hg^{P}_{aq} sinking flux at the bottom of mixed layer, e) vertical transport flux at the bottom of mixed layer, including advection, diffusion as well as entrainment/detrainment: positive values (red) correspond to upward transport, while negative values (blue) are for downward transport. f) Hg^0 evasion flux from ocean to the atmosphere.

Figure 4.9 shows the spatial distribution of major Hg conversion and transport fluxes, including atmospheric Hg^{II} deposition, riverine Hg^{II} input, Hg^{II}_{aq} reduction in the mixed layer, particle sinking and vertical transport flux across the bottom of mixed layer, and Hg^0_{aq} evasion flux at the ocean surface. Higher deposition fluxes in the southern hemisphere (Figure 4.9a) are due to faster atmospheric oxidation of Hg^0 caused by high Br atom concentrations (due to a larger oceanic source of bromocarbons) combined with faster deposition of Hg onto sea-salt particles (Holmes et al. 2010). The riverine Hg^{II} input flux is confined to the coastal regions near river mouths. The mouths of the largest rivers, including the Mississippi and Columbia in N. America, Amazon and Orinoco in S. America, Yangtze, Amur, Ob and Yenisei in Asia, Congo and Zambezi in Africa are identifiable as red and black spots (panel b). Because of the larger land fraction, the overall riverine Hg^{II} input in the Northern Hemisphere (0.21 Mmol yr^{-1}) is larger than in the Southern Hemisphere (0.17 Mmol yr^{-1}). Hg^{II}_{aq} from both atmospheric deposition and riverine input is reduced photo-chemically and/or biologically to Hg^{0}_{aq} (panel c), with a net global reduction flux of 3.1 Mmol yr^{-1}.

The Hg^{P}_{aq} sinking flux from the mixed layer (1.2 Mmol yr^{-1}) largely follows POC sinking distribution (equation 3), which is higher in regions with enhanced nutrients from either erosion from terrestrial land masses such as high-latitudes N. America and Eurasia, or upwelling from subsurface waters such as equatorial regions, the Southern Ocean, west coasts of continents, as well as along the Gulf Stream and the Kuroshio. Despite the high productivity, the sinking fluxes are generally weaker in the equatorial ocean than other productive regions in high-latitudes because of the higher temperature and subsequently smaller *pe-ratio* (Dunne et al., 2005). Panel e shows the vertical transport flux of Hg at the bottom of the mixed layer. This flux includes advection and diffusion across the bottom of the mixed layer, as well as entrainment and detrainment of Hg-containing water mass into/from the mixed layer resulting from the change of the mixed layer depth. The spatial pattern of the vertical transport flux of Hg is influenced by the physical flow of water and by the vertical concentration gradients of Hg species. Because of higher Hg concentrations in the intermediate waters than in the mixed layer (Figure 4.7), the total Hg vertical advection flux shows an overall upward transport with intensive flux at upwelling regions such as along Gulf Stream, the Equatorial Ocean and Southern Ocean. Evasion of Hg^{0} to the atmosphere (panel f) is controlled by the supersaturation of Hg^{0} concentrations and wind speed. The evasion flux is generally higher in the Southern Hemisphere, reflecting the higher atmospheric Hg^{II} deposition flux and the higher wind speed. The evasion fluxes are generally larger over the Southern Ocean because of the high Hg concentrations there caused by strong vertical mixing (panel e). The evasion is also large along the Gulf Stream due to the stronger entrainment of Hg from subsurface waters (panel e). Regions near the mouths of the Amazon and Orinoco rivers have higher evasion because of the riverine Hg input (panel b). Despite strong upwelling, eastern equatorial Pacific Ocean only show moderate Hg^0 evasion flux because the relatively strong removal of Hg from surface ocean by Hg^P_{aq} sinking.

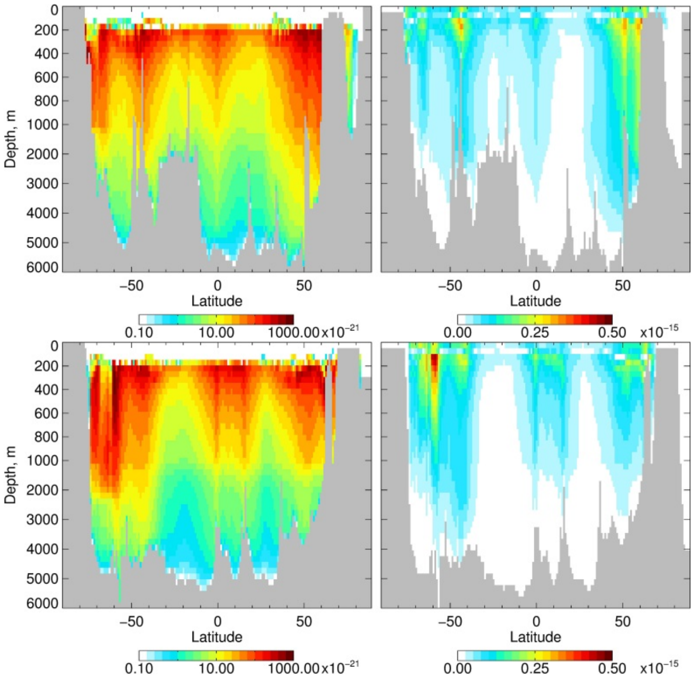

Figure 4.10: Cross section of annual mean Hg^{II}_{aq} reduction rate via methylation/demethylation pathway (left panels, mol m^{-3} s^{-1}) and Hg^P_{aq} sinking fluxes (right, mol m^{-2} s^{-1}) at 180°E (top) and 25°W (bottom).

Figure 4.10 shows two meridional cross sections for the Hg^{II}_{aq} reduction rate (via the methylation/demethylation pathway below the mixed layer) and Hg^P_{aq} sinking flux at 180°E and 25°W, representing the middle of the Pacific and Atlantic Oceans, respectively. As shown in Figure 4.9d, the Hg^{II}_{aq} reduction rate is enhanced over productive high-latitude regions and the tropical regions, where the cross sections indicate stronger reduction rate extending to a depth of ~1,000 m. The reduction rates are much lower at the middle of gyres (~30-40° latitude) in both hemispheres. The Hg^P_{aq} sinking fluxes show similar vertical patterns. They increase from the surface to a depth of ~200 m, resulting from the increase of total Hg concentrations with depth.

Below this depth, the rapidly decreasing POC sinking flux leads to a decrease in the Hg^{P}_{aq} sinking flux with depth.

4.5.2 Physical advection fluxes

Figure 4.11 shows the horizontal advection flux of Hg in the ocean mixed layer, which largely resembles the pattern of near-surface oceanic currents (Stewart 2008). Prevailing easterlies drive persistent westward advection in the tropical regions. One distinct feature is Gulf Stream starting from equatorial Atlantic and extending along the east coast of both N. and S. America to ~40°N. Relatively strong eastward advection is modeled along with the Antarctic Circumpolar Current at ~60°S, resulting from the strong westerlies there. The westward Antarctic Subpolar Current immediately close to the Antarctic can also been seen. Strong eastward advection is also modeled along the Kuroshio in Northern Pacific.

The transport flux integrated over the whole water column between different ocean basins across their contacting interfaces are also shown in Figure 4.11 with bold blue arrows. The directions of these fluxes are influenced by the direction of deep ocean circulations. The North Atlantic Deep Water (NADW) carries 0.01 Mmol yr^{-1} of Hg from Arctic to North Atlantic Ocean, while the oceanic current along the Bering Strait carries 0.004 Mmol yr^{-1} from North Pacific to Atlantic Ocean. There is a flux of 0.15 Mmol yr^{-1} of Hg along the Indonesian through flow as well.

The directions of the transport of Hg also comply well with the Thermohaline Conveyor Belt (TCB, Rahmstorf, 2002). The North Atlantic to South Atlantic Ocean flux is 0.010 Mmol yr^{-1}, while the South Pacific to North Pacific flux is 0.12 Mmol yr^{-1}. Larger transport fluxes are calculated along the Antarctic Circumpolar Current, 0.48, 1.9 and 1.2 Mmol yr^{-1} between the Pacific, Atlantic and Indian Ocean sectors of the Southern Ocean, respectively.

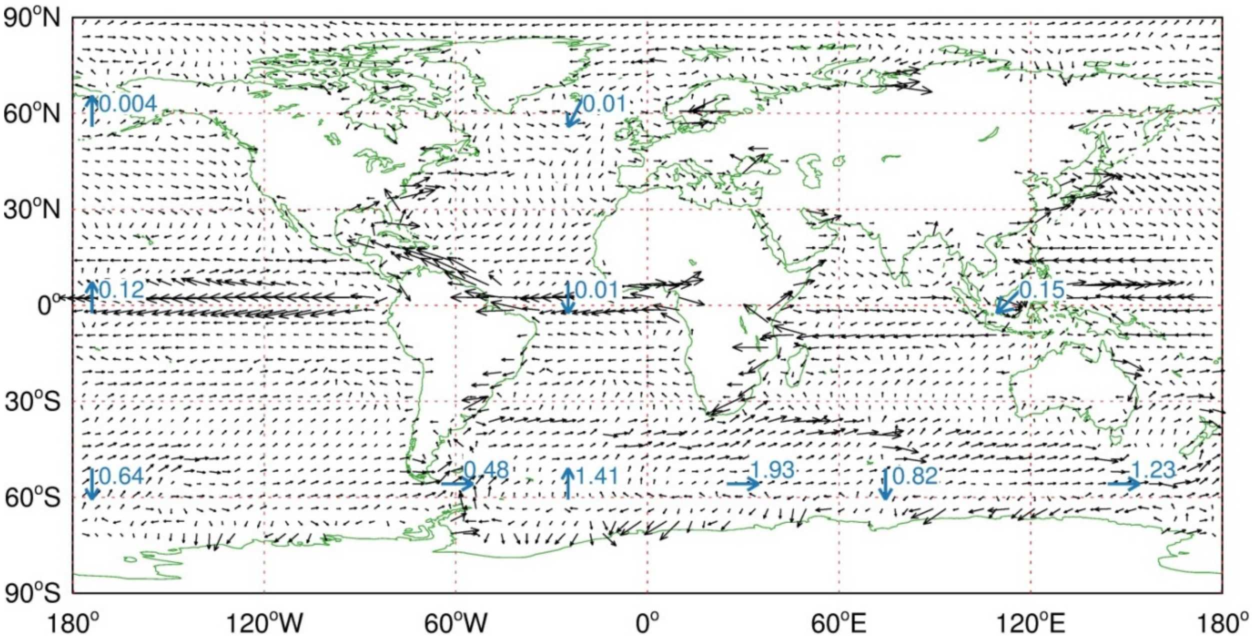

Figure 4.11: Annual mean horizontal advection fluxes of total Hg in the mixed layer. The longest arrow representing 50×10^{-12} mol m^{-2} s^{-1}. The thick blue arrows indicate the vertically integrated transport fluxes along interfaces between ocean basins (Arctic, North Atlantic, South Atlantic, North Pacific, South Pacific, Indian and Southern Ocean, in units of 10^6 mol yr^{-1}).

Another important factor influencing the Hg transport among different ocean basins are the concentration gradients across these interfaces. Opposite-direction transport fluxes relative to the TCB are calculated between the Southern Ocean and the South Pacific, South Atlantic and Indian Oceans. This pattern reflects the horizontal concentration gradient, especially in the deep ocean (i.e. S. Pacific (1.1 pM) → Southern Ocean (0.99 pM) → South Atlantic (0.85 pM) and Indian (0.98 pM)).

Generally, the net horizontal transport flux is a much smaller term (<10%) than the atmospheric deposition input (Table 4.2). The only exception is the Southern Ocean, which gains ~30% of the Hg mass from the adjacent ocean basins (S. Pacific and Indian) because of its large contacting area with other ocean basins.

4.6 Variability in Hg concentrations

4.6.1 Horizontal distribution at different depths

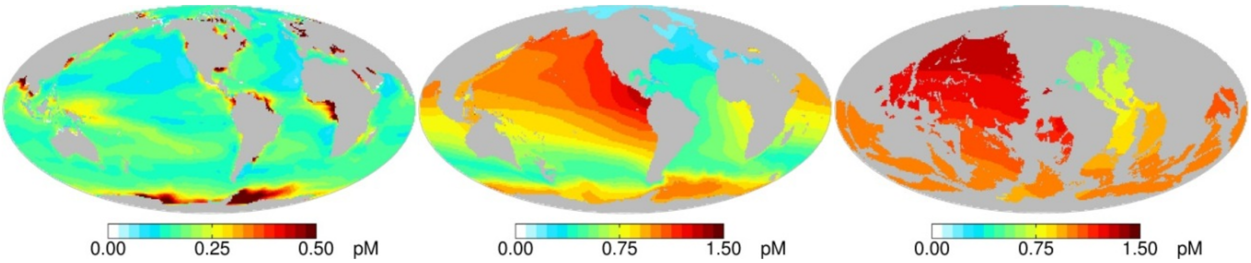

Figure 4.12: Annual mean total Hg concentrations in the mixed layer (left), at 1000 m depth (middle) and 4000 m depth (right). Note: difference scale for the left panel.

The spatial pattern of Hg concentrations is largely controlled by the patterns of fluxes discussed above (Figure 4.9-4.11). Figure 4.12 shows the annual mean total Hg concentrations at the surface, 1000 m and 4000 m, representing the mixed layer, intermediate and deep oceans, respectively. The total Hg concentrations in the surface ocean are generally higher in the S. Hemisphere (0.18 pM) than in the N. Hemisphere (0.15 pM), reflecting the larger atmospheric deposition (Figure 4.9a). Upwelling of enriched subsurface Hg near the circumpolar Antarctic current results in high surface concentrations in that region (Figure 4.9e). The total Hg concentrations near the Weddell Sea can be as high as 0.5 pM, much larger than the global average concentration of 0.17 pM. Coastal regions, as well as closed and shallow water body such as Hudson Bay and Black Sea also show elevated Hg concentrations (> 1 pM) because of the strong riverine input (Figure 4.9b). The relatively small volume of water in these regions compared with open oceans also elevates the concentrations. The western Equatorial Pacific Ocean has a concentration level of ~0.25 pM, because of the strong input via atmospheric deposition and weaker particle scavenging (Figure 4.9d). Over the Arctic Ocean, a large riverine input combined with low evasion leads to the maintenance of intermediate Hg concentration of ~0.15 pM (Figure 4.9f, Table 4.2).

At 1,000 m depth, total Hg concentrations are more uniform, as they are free from the signature of the atmospheric and riverine input. We predict significant interbasin differences, with lower concentrations in the North Atlantic Ocean (0.2-0.4 pM) and the South Atlantic Ocean (0.6-0.7 pM), and higher concentrations over the South Pacific Ocean (~0.8 pM), the Indian Ocean (~0.8 pM) and the North Pacific Ocean (~1 pM). These increasing concentrations follow increasing age of the water masses. Indeed, the age of the water masses calculated within OFFTRAC at 1,000 m depth is ~100 years in the Subarctic North Atlantic Ocean, increasing to 500 years in the South Atlantic Ocean, and is older than 1,000 years in the Indian and S. Pacific Ocean. The oldest water at this depth is predicted at North Pacific with ages greater than 1,600 years (the distribution of the age of water mass in available in the Appendix). In the younger water masses of the North Atlantic Ocean, total Hg concentrations are lower because they have kept the signature of low surface Hg concentrations, while the old waters in the Pacific and Indian Ocean have received continuous input of Hg from particle sinking and remineralization. This leads to higher total Hg concentrations in the Pacific and Indian Ocean compared to the North Atlantic Ocean. However, the largest total Hg concentrations are not predicted at the oldest water at high latitudes in North Pacific, but over the eastern Pacific Ocean, caused by the combination of relatively stronger particle sinking flux from the surface ocean there (Figure 4.9d) and upwelling of Hg from water mass deeper than 1,000 m. Similar upwelling processes also lead to higher total Hg concentrations (0.7-0.8 pM) relative to the age of the water mass over the Southern Ocean. The spatial distribution of Hg in the intermediate depths shows some similarity with that of oxygen because of their common connection with sinking particulate organic matters, especially over the tropical regions. A similar maximum for hypoxic conditions is also observed over the eastern Pacific Ocean and northern Indian Ocean at the thermocline (intermediate waters: below mixed layer to ~1000 m) because of the strong particle sinking flux and induced occurrence of respirations (Deutsch et al., 2011).

At 4,000 m depth, we also find interbasin differences in Hg concentrations, but not as dramatic as at 1,000 m depth. The average total Hg concentrations increase from ~0.6 pM in North Atlantic, ~0.8 pM in S. Atlantic, and ~0.9 pM in Southern Ocean, to ~1.0 pM in S. Pacific and ~1.2 pM in North Pacific. At this depth, water age is more uniform: ~1,800 years in the North Atlantic compared to ~2,000 years in the North Pacific. In addition to this age difference, the lower total Hg concentrations in overlying waters decrease the Hg particle sinking flux from atop over North Atlantic Ocean, which leads to lower Hg penetration to deeper than 4,000 m at this region. Similar pattern of deep ocean concentrations is also observed for some other particle-reactive metals (e.g. Cd, Zn and Ag) (Mason et al., 2012 and references therein).

As the end-product of Hg^{II}_{aq} reduction, we find that the fraction of Hg^{0}_{aq} increases with the age of the water mass along the TCB: increasing from 34% in the North Atlantic to 42% in the North Pacific below 1,000 m. As the water mass ages, more of the Hg^{II}_{aq} can be converted to Hg^{0}_{aq} via methylation/demethylation, thereby increase the fraction of Hg present as Hg^{0}_{aq}. This is supported by observations. Indeed, the observed fraction of Hg^{0}_{aq} (15%) at station 22t and 24t in the Subpolar Atlantic Ocean is much lower than at equatorial Atlantic (60%, Mason and Sullivan, 1999). The modeled fraction of Hg^{0}_{aq} shows similar trend: lowest over North Atlantic (38% at 1,000 m), highest over North Pacific (55% at 1,000 m).

4.6.2 Cross sections of Hg concentrations

We examine the influence of ocean circulation in two meridional cross sections of total Hg concentrations along 180°E and 25°W (Figure 4.13). In these cross sections, the influence of the age of water masses on Hg distribution is even clearer. The deep water formation process over the Subpolar Atlantic is clearly seen over the cross section at 25°W as a tongue with uniformly low Hg concentrations extending from the surface ocean to 3,000 m depth. Hg concentrations in the deep ocean increase from North to South in the Atlantic Ocean, and from South to North in the Pacific Ocean following the increasing of age of water masses along the TCB. In the intermediate ocean, the contours of Hg concentration generally resemble that of density, reflecting the importance of stratification and isopycnal transport (Brown et al., 2002). The Hg-rich water in the deep ocean upwells to the intermediate ocean and forms bulges of high Hg concentrations over the tropical region and the Southern Ocean. Conversely, downwelling over the centers of the gyres at mid-latitudes (~30-40°) causes lower total Hg concentrations in thermocline / intermediate waters.

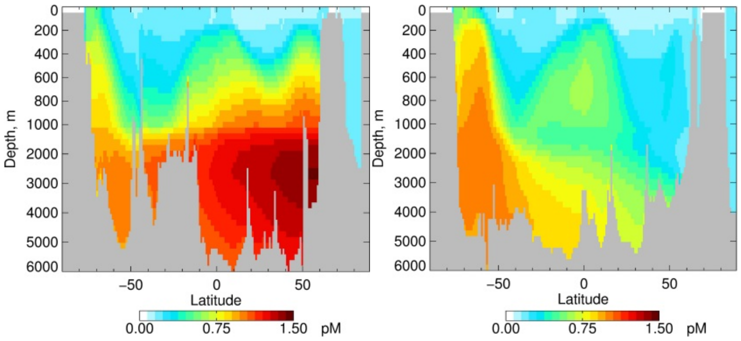

Figure 4.13: Cross section of annual mean total Hg concentrations in the Pacific Ocean at 180°E (left) and Atlantic Ocean at 25°W (right).

4.6.3 Influence of riverine input

As discussed before (Figure 4.12a), our model results show that the spatial distribution of total Hg concentrations in the mixed layer shows a significant fingerprint of influence from riverine input, especially over coastal and near-shelf regions. Figure 4.14 shows the percent contribution to the mixed layer total Hg concentrations caused by riverine Hg input. This is calculated by difference of our natural simulation with a simulation without riverine input. Riverine input contributes more than 60% in coastal regions near large river mouths, but displays much smaller contributions (less than 10%) in open oceans. As discussed in Section 4.4, the riverine input contributes more than 50% of the Hg concentrations for the entire basin in the Arctic Ocean (Table 4.2). This is because the total Hg riverine input to the Arctic accounts for 9% of the global value, while the volume of water over the Arctic Ocean only accounts for 1% of that of the global oceans. The contribution of riverine input could be more important today because of the relatively larger enrichment of Hg in the riverine effluents, compared with atmospheric deposition (Streets et al., 2011), not only for the Arctic Ocean (Outridget et al., 2008; Fisher et al., 2012), but also for other ocean basins such as North Atlantic (e.g. Soerensen et al., 2012).

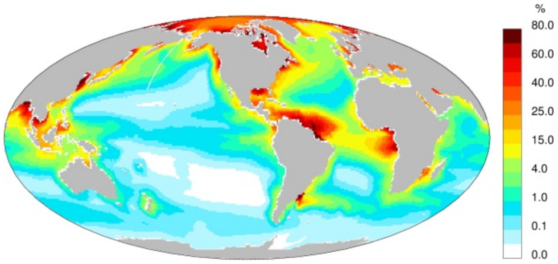

Figure 4.14: Percent contribution to total Hg concentrations in the mixed layer by riverine input of Hg.

4.6.4 Seasonal cycle

Although no significant seasonal variability is predicted for Hg concentrations in the intermediate and deep ocean, the Hg concentrations in the mixed layer show a small seasonal cycle in the both hemispheres, as shown in Figure 4.15. Also shown in this figure are the seasonal cycles of the modeled atmospheric deposition, riverine input, ocean evasion, and particle sinking fluxes from the mixed layer. The Hg concentrations peak during Apr. – Jun. in the North Hemisphere, and Nov. – Feb. in the South Hemisphere. This pattern generally reflects those of the associated fluxes, especially the atmospheric deposition and ocean evasion fluxes. Take the South Hemisphere as an example, the atmospheric deposition peaks (~0.3 Mmol/month) during Oct. – Nov. because of the stronger oxidation of Hg^0 in the austral summer (Holmes et al., 2010). Meanwhile, the ocean evasion flux is the lowest (~0.2 Mmol/month) because of the lower wind speed. In addition, the particle sinking flux is the lowest during this period (0.03-0.04 Mmol/month). Therefore, a net accumulation of Hg (~0.05 Mmol/month) happens in these two months, resulting in a peak concentration of higher than 0.19 pM. Similar condition happens in the boreal summer in the North Hemisphere.

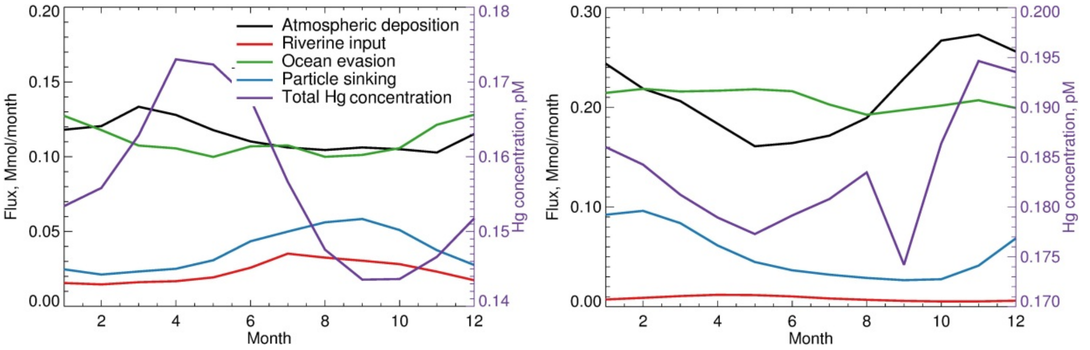

Figure 4.15: Seasonal cycle of the total Hg concentrations in the mixed layer and the associated fluxes in the North Hemisphere (left) and South Hemisphere (right).

4.7 Conclusions

We have implemented Hg biogeochemistry in a state-of-the-art 3D offline ocean tracer model (OFFTRAC). This model simulates the distribution of three Hg species (Hg^0_{aq}, Hg^{II}_{aq} and Hg^P_{aq}), which are diffused and advected in the ocean. Hg^0_{aq} and Hg^{II}_{aq} are interconverted in the surface ocean via parameterized photochemical and biological redox processes. The partitioning between Hg^{II}_{aq} and Hg^P_{aq} depends on the local levels of particulate organic carbon (POC). The sinking of Hg^P_{aq} is parameterized by coupling with the carbon cycle. The reduction of Hg^{II}_{aq} to Hg^0_{aq} in the subsurface water is proportional to the remineralization of POC. OFFTRAC is coupled to a global simulation of the natural atmospheric Hg cycle in the GEOS-Chem chemical transport model. The GEOS-Chem simulation includes a geogenic source of 0.5 Mmol yr^{-1} and predicts the atmospheric deposition flux of Hg^{II} to the ocean (3.9 Mmol yr^{-1}) and atmospheric Hg^0 concentrations (0.2 ng m^{-3}). The riverine input of Hg is calculated based on the climatological monthly mean fresh water discharge from continents to ocean and the average soil concentrations near the river mouth.

We compared the model results against 13 observed Hg concentration profiles/sections over the North Pacific, North Atlantic, Equatorial and S. Atlantic and Southern Ocean. We restricted our comparison to the deep ocean (> 2,000 m), with little anthropogenic influence. Our calculated total Hg concentrations (1.1±0.3 pM) generally agree with the observed concentration (1.4±0.9 pM). In particular, our model results are comparable with observations sampled at North Pacific, mid- and low-latitude deep Atlantic, deep South Atlantic as well as sub-polar deep Southern Ocean, but significantly underestimate observations in deep water formation regions in North Atlantic (by a factor of 5-6) and Antarctic Southern Ocean (by 20-30%). This reflects the penetration of anthropogenic Hg into the ocean, which is not taken into account in our simulation. Compared to present-day surface ocean concentrations, our natural simulation is a factor of 6 too low, suggesting that anthropogenic input has led to a factor of 6 increase in surface Hg concentrations.

The model results show that the total Hg mass in the global ocean is 1200 Mmol, with about 3 Mmol, 150 Mmol and 1000 Mmol in the surface, intermediate and deep ocean, respectively. The corresponding global mean concentrations of total Hg are 0.17 pM, 0.50 pM and 1.0 pM, respectively. Hg^0_{aq} accounts 10% in the surface ocean because of its rapid evasion to the atmosphere. This fraction increases to 44% and 38% in the intermediate and deep ocean, respectively, because of *in situ* production of Hg^0_{aq} in subsurface waters. Hg^P_{aq} accounts 8% in the surface ocean, but is negligible in the intermediate and deep ocean.

We find that the spatial pattern of total Hg concentrations in the mixed layer is influenced by a variety of factors including atmospheric deposition, ocean circulation as well as the organic carbon export. The mixed layer Hg concentrations are highly variable, with generally higher in the S. Hemisphere because of larger atmospheric deposition. High concentration regions are predicted in the Southern Ocean, the western Equatorial Pacific Ocean, coastal regions as well as closed and shallow water bodies. At 1,000 m depth, Hg concentrations increase with the age of water mass because of the continuous input of Hg from remineralization of sinking particles. The Hg concentrations are lower in the youngest water masses of the North Atlantic (0.2-0.4 pM) and South Atlantic (0.6-0.7 pM), and higher over the South Pacific (~0.8 pM), Indian (~0.8 pM) and North Pacific (~1 pM). Upwelling of water with high Hg concentrations also enhances the concentrations in the eastern Equatorial Pacific Ocean and the Southern Ocean. At 4,000 m depth, the horizontal segregation is smaller (a factor of 2 increase between the North Atlantic and North Pacific) than at 1,000 m because of the smaller difference in water mass age. The gradient of Hg concentrations in the water mass atop also helps to shape the gradient at this depth via controlling the Hg particle sinking flux. We also predict that the fraction of Hg present as Hg^0_{aq} in subsurface waters increases with the age of water mass. This is because more of the Hg^{II}_{aq} can be converted to Hg^0_{aq} via methylation/demethylation, thereby increase the fraction of Hg present as Hg^0_{aq} as the water mass ages. This is consistent with the observed fraction of Hg^0_{aq} (15%) in the Subpolar Atlantic Ocean and at equatorial Atlantic (60%).

The model predicts that the riverine input enhances Hg concentrations at surface by a factor of 2-3 near large river mouths and nearby coastal regions, and approximately doubles surface Hg concentration over the Arctic because of the small basin volume. The Hg concentrations in the mixed layer show a mild seasonal cycle with peaks in the late spring and early summer in the both hemispheres. This reflects the seasonal pattern in atmospheric deposition, ocean evasion as well as particle sinking flux from the mixed layer.

Chapter 5

ANTHROPOGENIC MERCURY IN A COUPLED GLOBAL THREE-DIMENSIONAL ATMOSPHERE-OCEAN TRACER MODEL

5.1 Introduction

The marine mercury (Hg) cycle and its anthropogenic perturbation are of particular interest because human exposure to Hg occurs mainly via the consumption of marine fish and seafood containing methylmercury (MeHg) (Sunderland, 2007; Kim et al., 2010). MeHg is a bioaccumulating neurotoxin and can cause a variety of severe health effects including neurodevelopment delays in children and deficits in neurocognitive function in adults (Yokoo et al., 2003; Cohen et al., 2005). Mercury enters the ocean primarily via atmospheric deposition in inorganic forms as either elemental (Hg^0) and divalent (Hg^{II}) mercury. In the surface ocean, Hg^{II} and Hg^0 interconvert via photochemical and biological processes (Fitzgerald et al. 2007; Mason et al., 2012). In surface waters, Hg^{II} can be absorbed onto particulate organic matters. As part of the biological pump, some particular organic matter sinks to the intermediate and deep ocean waters, where remineralization leads to the release of Hg^{II} (Mason and Fitzgerald 1993; Mason et al., 1998). In subsurface waters, microbial methylation and demethylation lead to interconversion of Hg^{II} and MeHg (Sunderland et al., 2009; Lehnherr et al. 2011), with a small fraction of MeHg demethylated to form Hg^0 (Lehnherr et al. 2011). Observations show that total Hg concentrations in the open ocean are typically less than 3 pM (1 pM = 10^{-12} mols/L) with some horizontal gradients: somewhat higher concentrations in the North Atlantic Ocean (2.1±0.8 pM), intermediate values in Equatorial regions in both the Atlantic (1.7±0.7 pM) and Pacific (1-2 pM)

Oceans, as well as the Southern Ocean (0.6-2.8 pM), and lower values in the North Pacific Ocean (1.0±0.5 pM) (Mason et al., 2012 and references therein). Compared to subsurface waters, the total Hg concentrations in the surface ocean are generally < 1 pM because of the depletion from ocean evasion and particle scavenging.

The biogeochemical cycling of anthropogenic Hg emissions has led to the increase of Hg burden in the environment, as recorded in lake sediments (e.g. Fitzgerald et al., 1998; Biester et al., 2007; Lindberg et al., 2007), marine sediments (Young et al., 1973), peat bog cores (Madsen, 1981; Givelet et al., 2003), snow layers (e.g. Loewen et al., 2007), ice cores (Schuster et al., 2002) as well as biological matrices (e.g. Xu et al., 2011; Fain et al., 2009; Vo et al., 2011). These records suggest that the current atmospheric Hg deposition flux has increased to two- to five-fold of the pre-industrial (ca. 1850) levels. Some records extending back to several thousand years ago show even larger present-day enrichment (a factor of ~10) when compared with Hg deposition flux long before 1850 (e.g. Cooke et al., 2009; Elbaz-Poulichet et al., 2011).

Anthropogenic Hg emissions date back to the early history of human civilization through the exploitation of useful material and energy source. Preindustrial Hg emissions were mainly from the volatile loss of Hg^0 during Hg mining and the amalgam extraction of gold and silver using Hg. Hg amalgamation for gold and silver extraction dates back to the Phoenician and Carthaginians civilizations as early as 2,700 BC (Lacerda 1997), and was extensively used in 1550-1880 over Spanish America (Nriagu, 1993), as well as during the North American gold rush in 1860-1910 (Streets et al., 2011). A new gold rush took place in the 1970s, mainly in the third world countries in the southern hemisphere (Lacerda 1997). While Hg amalgamation is no longer used in industrial gold mining, artisanal gold extraction via Hg amalgamation still takes place in Asia, South America and Africa, accounting for 17% of global Hg emissions (AMAP

2011). Other Hg sources involve the production of metals such as copper, zinc, and lead (Streets et al., 2011). Since the industrial resolution, Hg emissions from fossil fuel burning have become the dominant source of Hg, accounting for 46% of present-day emissions (Pacyna et al., 2010). The historical emission inventory of Streets et al. (2011) indicates that cumulative Hg emissions from human activities for all the time are 350 Gg, of which 39% was emitted before 1850. Current global anthropogenic Hg emissions are estimated to be about 2,000 Mg yr^{-1} (Pacyna et al., 2010), as compared with 90 Mg yr^{-1} from natural geogenic sources (Pirrone et al., 2010), 530 Mg yr^{-1} in South and Central America during 1580-1820 (Nriagu 1993), and 2,600 Mg yr^{-1} mainly from North America in 1890 (Streets et al., 2011).

Several modeling studies have examined how anthropogenic Hg emissions have perturbed marine Hg biogeochemical cycle (Mason et al., 1994; Lamborg et al., 2002; Mason and Sheu, 2002; Sunderland and Mason 2007; Selin et al., 2008; Streets et al., 2011; Amos et al., 2013). These studies modeled the oceans as 1-6 boxes in the horizontal and 1-3 boxes in the vertical. Only taking into account the ocean mixed layer (1 box in ocean), Mason et al. (1994) estimated the surface oceanic Hg concentrations have been tripled since preindustrial time (ca. 1850). Lamborg et al. (2002) calculated a 90% increase in the top 100 m of the ocean, a 20% increase in the thermocline (100 – 1000 m) since 1850. Dividing the ocean into 2 boxes (upper ocean: top most 500 m, deep ocean: deep than 500 m), Mason and Sheu (2002) inferred a 9% increase in oceanic Hg mass, with most of the increase happening in the deep ocean. Using an oceanic model with 14 boxes, Sunderland and Mason (2007) predicted that the anthropogenic enrichment is 25% and 11% in the surface and deep oceans, respectively. With a 2-D slab ocean model (vertically two boxes: mixed layer and below), Selin et al. (2008) found the Hg in the ocean mixed layer had increased by 180% since preindustrial time. All these studies have considered the years 1800-1850 as a baseline for Hg emissions. However, as noted above significant anthropogenic emissions occurred prior to that time. This was taken into account in the studies of Streets et al. (2011) and Amos et al. (2013), who extended their simulations back in time to natural conditions, which they defined as 1450 and 2,000 BC, respectively. Both studies modeled the ocean with 3 boxes (surface, subsurface and deep). They calculated the all-time Hg enrichments in the ocean relative to natural conditions as 1.9-2.8, with enrichments of 1.5-2.0 in the deep ocean, 2.7-5.2 in subsurface ocean, and 3.6-6.0 in surface ocean. Their models also estimated that the present-day total marine Hg mass has increased by 35%-76% since pre-industrial time (defined as the year 1850).

The results of these models display significant variations, which are the result of different assumptions on the evolution of anthropogenic Hg emissions as well as on the transport timescales among ocean boxes. A common difficulty faced by these box model studies is the assumption of a uniform deep ocean, which is not well-mixed on timescales representative of the human perturbation ~100-200 years (Siegenthaler and Oeschger, 1978). To examine this issue, Strode et al. (2010) developed a one-dimensional column model with 50 vertical layers, using a vertical diffusion parameter constrained by the distributions of both natural and bomb-produced ^{14}C. They found a 150% enrichment in surface ocean Hg concentrations since 1850, with a 18% increase in the total oceanic Hg burden. They further estimated that anthropogenic Hg is mainly located within the intermediate ocean (57% in 400 – 1,500 m), with only 7% anthropogenic Hg below 1,500 m. While this type of 1D box-diffusion model uses more realistic framework for vertical transport (Joos et al., 1997; Strode et al., 2010), it does not capture any horizontal variability.

In this chapter, we will use a 3D offline ocean tracer model (OFFTRAC) with Hg biochemistry to understand the fate of anthropogenic Hg in the ocean. One novel feature of this chapter is a more complete representation of oceanic circulation and its impact on Hg. The development of this OFFTRAC-Hg model is described in Chapter 4, which also includes results for a simulation of the natural Hg marine cycle. In this chapter, we couple OFFTRAC-Hg with a global simulation of atmospheric Hg in the GEOS-Chem chemical transport model. We conduct a time-dependent global ocean-atmosphere-land simulation over the last 600 years to track the evolution of the anthropogenic Hg perturbation.

5.2 Model description

5.2.1 OFFTRAC Oceanic Chemistry and Transport Model.

OFFTRAC is an offline advection/diffusion ocean tracer model. It uses archived monthly averaged transport fields from the Hallberg Isopycnal Model (HIM) (Hallberg and Rhines, 1996; Ladd and Thompson, 2001). The world's oceans are resolved on an approximate 1° latitude by 1° longitude with 1/3° latitude resolution in the equatorial ocean. The model has 49 isopycnal (constant density) layers containing 2 layers of Kraus-Turner type mixed layer and 2 buffer layers. The HIM model is run for 650 years with climatological forcing at the surface by prescribed atmospheric boundary conditions (CORE-II) (Large and Yeager, 2009), and then integrated further using interannanually varying winds, air temperatures and humidity from the NCEP reanalysis between 1950 and 2006 (Kalnay et al., 1996). The advection and diffusion of tracers are computed using archived monthly averaged circulation fields from the HIM model. OFFTRAC has been used to examine thermocline variability in the North and Topical Pacific Oceans (e.g., Thompson and Ladd, 2004; Thompson and Dawe, 2007), oxygen variability in the ocean (Deutsch et al., 2005, 2006, 2011), chlorofluorocarbons undersaturation over mixed layer

(Shao et al., 2013), formation of mode waters in the North Atlantic and Southern Ocean using chlorofluorocarbon tracer transport simulation (Trossman et al., 2012).

The Hg modeling capability in the OFFTRAC model (OFFTRAC-Hg) was developed and described in Chapter 4. Briefly, the OFFTRAC-Hg model simulates three Hg tracers: dissolved elemental mercury (Hg^{0}_{aq}), dissolved oxidized mercury (Hg^{II}_{aq}), and mercury bound to particulate matter (Hg^{P}_{aq}). We assume that Hg input to the ocean is via atmospheric deposition and riverine effluent input (both in the form of Hg^{II}_{aq}). There is also bidirectional air-sea exchange of Hg^{0}_{aq} with the atmosphere. In the surface ocean, Hg^{0}_{aq} and Hg^{II}_{aq} are in quasi-steady state because of the fast photolytic oxidation and reduction. These reactions are parameterized to be proportional to the incoming short-wave radiation. A biological reduction proportional to net primary production (NPP) and a first-order dark oxidation are also included in the modeled surface ocean. The parameterizations of air-sea exchange and interconversion between Hg^{0}_{aq} and Hg^{II}_{aq} use the expressions described in Soerensen et al. (2010a). Hg^{II}_{aq} and Hg^{P}_{aq} are assumed to be in instantaneous partitioning equilibrium in the water, and the fraction of Hg^{P}_{aq} relative to Hg^{II}_{aq} is proportional to the local levels of particulate organic carbon (POC). The POC concentrations in the surface ocean are derived from satellite retrieving products. The POC sinking fluxes at the bottom of euphotic layer are calculated based on the satellite retrieved NPP data and its export ratio following Dunne et al., (2005). The POC sinking flux decreases exponentially with depth following the Martin curve (Martin et al., 1987). As POC sinks, the particulate-bound Hg^{P}_{aq} also undergoes downward transport until it is remineralized in the sub-surface ocean back to Hg^{II}_{aq} or reaches the ocean floor. Hg^{II}_{aq} is slowly reduced to Hg^{0}_{aq} in the subsurface water, and the reduction rate is assumed to be proportional to the organic carbon remineralization rate, which is calculated based on the vertical gradient of POC sinking fluxes. In the previous chapter, the natural (prior to any anthropogenic input) Hg simulation in OFFTRAC was compared to observed deep ocean concentrations and found reasonable agreement. The model results show that the total Hg mass in the global ocean is 1200 Mmol for natural conditions. The model also predicts significant horizontal segregation for total Hg concentrations in the intermediate and deep ocean, with higher concentrations in North Pacific Ocean (~1 pM at 1,000 m and ~1.2 pM at 4,000 m) than in North Atlantic Ocean (0.2-0.4 pM at 1,000 m and ~0.6 pM at 4,000 m), reflecting the different age of these waters, because the old waters have received continuous input of Hg from particle sinking and remineralization.

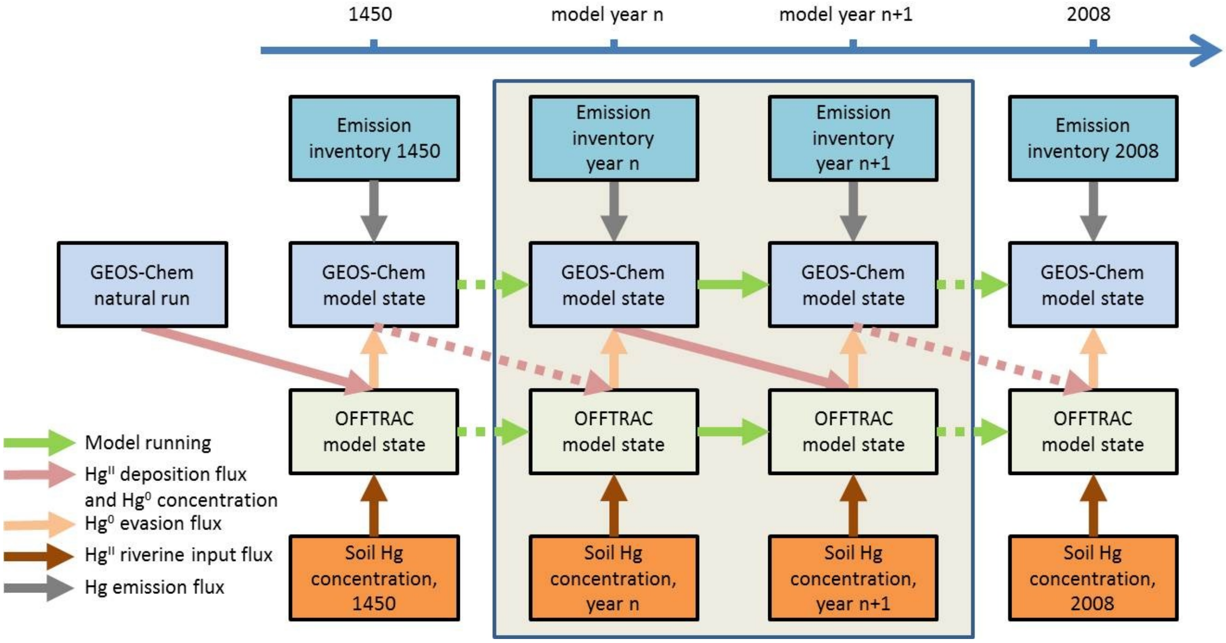

Figure 5.1: Coupling of Hg simulations between GEOS-Chem and OFFTRAC. Green arrows represent the models running forward for one year. Arrows in other colors represent the passing of information from one model to the other. For instance, pink arrows are the atmospheric Hg^{II} deposition fluxes to the ocean surface and the average atmospheric Hg^{0} concentration near ocean surface, while orange arrows are the ocean Hg^{0} evasion flux to the atmosphere.

5.2.2 GEOS-Chem Atmospheric Chemistry and Transport Model

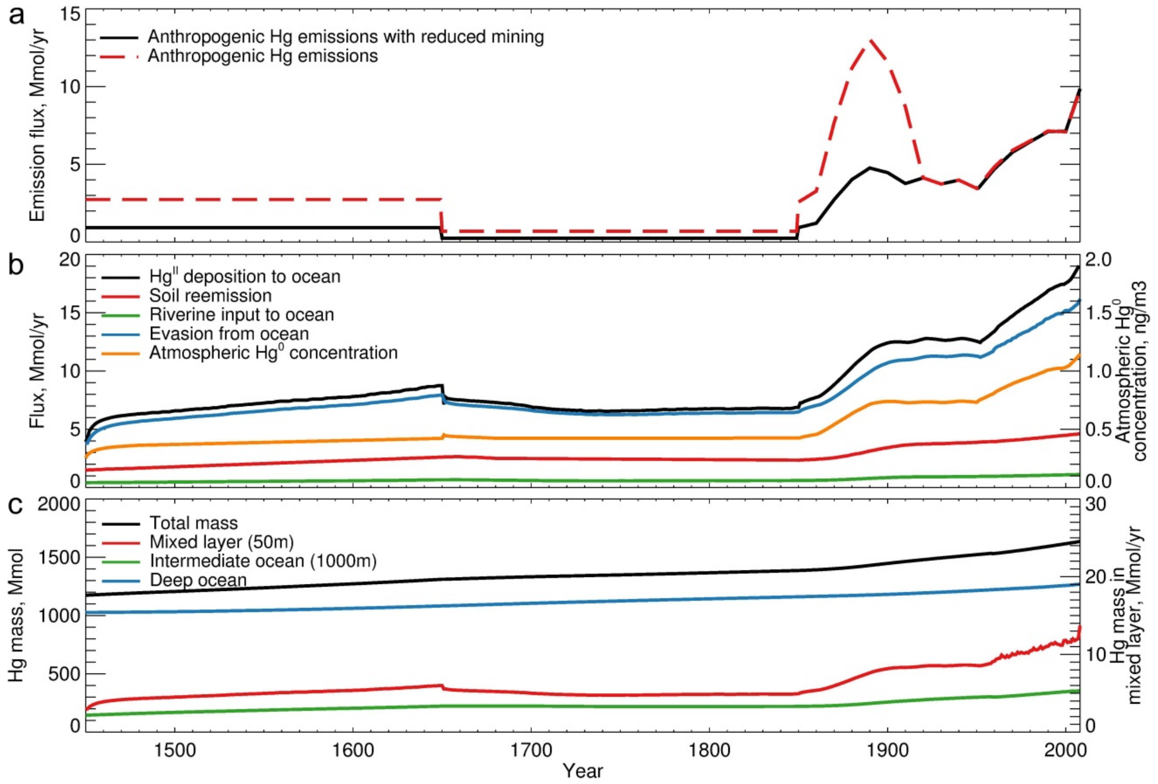

Figure 5.2: Modeled time evolution of a) global anthropogenic Hg emissions in the Streets et al. (2011) inventory (red line) and in the adjusted Streets et al. (2011) inventory, assuming a factor of 3 decrease in mining emissions prior to 1920 (black line); b) atmospheric Hg^{II} deposition flux to ocean, ocean Hg^0 evasion flux, riverine effluent input of Hg^{II} to ocean, and soil Hg^0 re-emission fluxes; and c) total oceanic Hg mass in different depth ranges. The results on panel b-c are for the simulation with anthropogenic emissions with reduced mining.

The Hg cycle in the atmosphere and land reservoirs is simulated by the GEOS-Chem model. The model is driven by assimilated meteorological observations from the NASA Goddard Earth Observing System (GEOS) as described in Bey et al. (2001). In this chapter, we use meteorological fields with a horizontal resolution of 4° latitude by 5° longitude and 47 vertical levels. In our simulation, we use GEOS-5 repeating meteorological fields for the year 2006. The GEOS-Chem atmospheric Hg simulation was described in Selin et al. (2007), with more recent updates in Holmes et al. (2010) and Amos et al. (2012). This model (v9-01-02) simulates two atmospheric Hg tracers: Hg^0 and Hg^{II}. The Hg chemistry in this model includes the oxidation of

Hg^0 by Br atom and the in-cloud reduction of Hg^{II}. Besides the dry and wet deposition of Hg^{II} from the atmosphere, the model also contains a surface soil module with prescribed soil Hg concentration distribution. The soil Hg^0 re-emission is dynamically simulated according to meteorological conditions (Selin et al., 2007).

5.2.3 Coupling between OFFTRAC and GEOS-Chem

Atmospheric transport within GEOS-Chem is calculated with a 60-minute time step, while in OFFTRAC we use a daily time step for the mixed layer and a monthly time step for the rest of the ocean. Coupling between the OFFTRAC-Hg and GEOS-Chem Hg simulations occurs once a year. GEOS-Chem provides to OFFTRAC three variables: atmospheric Hg^0 concentrations, global Hg^{II} deposition fluxes and riverine input, while OFFTRAC provides to GEOS-Chem the Hg^0 evasion flux (Figure 5.1). These variables are all archived on a monthly basis. Riverine flux of Hg from land to ocean is also calculated from the soil Hg concentration distribution around river mouths and the climatological monthly mean fresh water discharge from continents (Dai and Trenberth, 2002).

5.2.4 Historical emission inventory

We first run our coupled OFFTRAC-GEOS-Chem Hg simulation for natural conditions. Once the simulation has reached steady-state (after ~10,000 years), we conduct a time-dependent simulation with increasing anthropogenic emissions using the historical anthropogenic Hg emission inventory developed by Streets et al. (2011) starting from year 1450 until 2008. The Streets et al. (2011) inventory provides global total anthropogenic Hg emission during 1450 – 1850, and detailed decadal Hg emission data for 1850 – 2008 by region (North America, South America, Europe, Former USSR, Africa and Mideast, Asia and Oceania), source type (silver mining, artisanal gold mining, large-scale gold mining, waste incineration, coal combustion, other metal production, etc.) and speciation (Hg^0, Hg^{II} and Hg^P). On a sub-regional basis, we allocate gold/silver/mercury mining based on historical mining locations (Lacerda, 1997) and other anthropogenic emissions are distributed following the present-day geographical distribution within each region (Pacyna et al., 2010). Figure 5.2a shows the time evolution of global anthropogenic Hg emissions. Anthropogenic emissions during 1450 – 1650 are ~2 Mmol/yr due to silver mining in South and Central America, and then decrease to ~1 Mmol/yr during 1650 – 1850.

During 1850 – 1920, Hg emission from gold/silver/mercury mining over North America, Europe and South America increased rapidly, and peaked to a maximum value of 13 Mmol/yr at 1890 assumed in Streets et al. (2011). There is debate in the literature as to the amount of Hg released to the atmosphere during that period. Nriagu (1994) estimated the average annual emission of Hg from gold and silver mining in the United States as 3.9 Mmol/yr during 1850-1900. Strode et al. (2009) estimated a peak global Hg emissions from mining activities of 4.1 Mmol/yr in 1870 based on a comparison of deposition enhancements between lake sediment records and the GEOS-Chem model. There is a large uncertainty associated with the Hg emission factors from amalgamation extraction of silver and gold, especially for the mass ratio of Hg lost during the production as well as the Hg released to the atmosphere (Strode et al., 2009 and references therein). This results in an uncertainty of more than a factor of 5 between the largest and smallest estimates. In a sensitivity simulation, we have decreased the Hg emissions from mining in the Streets inventory by a factor of 3 prior to 1920, which results in a mining-peak Hg emission of ~4.5 Mmol/yr in 1890 (Figure 5.2a). The cumulative total anthropogenic Hg emissions decreases from 1740 Mmol to 950 Mmol, with only 25% emitted before 1850 (compared to 39% in the original Streets et al. (2011) inve3ntory). As shown in Section 5.4, this adjusted emission inventory generates results which are more consistent with historical Hg deposition records in environmental archives. Unless otherwise notes, all the model results in this chapter are for this adjusted emission inventory. Anthropogenic Hg emissions fluctuated around 4 Mmol/yr after the 1930s because of the war associated production and depression. Hg emissions started increasing again in the 1950s because of increasing coal combustion in the Former USSR and Asia, and achieved a global Hg emission of 7.5 Mg/yr, while the Hg emissions from North America and Europe remain unchanged or decreased slightly. Hg emissions then leveled off in the early 1990s because of the breakdown of the Former USSR and stricter emission regulation over North America and Europe, but then started to increase rapidly in the mid-1990s as a result of coal combustion and artisanal gold mining in Asia. Global anthropogenic Hg emissions in 2008 reached 9.5 Mg/yr, with more than two thirds contributed by Asian sources. To calculate the riverine Hg^{II} flux, we used the soil Hg concentration predicted by Streets et al. (2011) which takes into account three terrestrial organic carbon pools. The transport and transformation of Hg among these pools and its exchange with atmosphere were also included in their study.

5.3 Marine Hg budgets

5.3.1 The global Hg budget and its anthropogenic perturbation

Figure 5.3 shows the natural budget of Hg in the ocean-land-atmosphere system along with its present-day anthropogenic perturbation. For the purpose of this figure, we divide the global ocean into three boxes depending on the depth: the mixed layer (the topmost ~50 m), intermediate ocean (bottom of mixed layer to ~1000 m) and deep ocean (below 1000 m). The Hg mass in soil and deep mineral reservoirs are taken from Streets et al. (2011) and Amos et al., (2012), respectively. Our simulation shows that anthropogenic emissions have led to a factor of

5.3 increase in the atmospheric Hg burden (from 4.0 Mmol to 21 Mmol). In the mixed layer ocean, the mass of Hg has increased by a factor of 4.0. The Hg mass in the intermediate and deep ocean increases by 2.4 and 1.2, respectively. The accumulated anthropogenic (950 Mmol) and geogenic (280 Mmol) Hg emissions during 1450-2008 have resulted in the increase of Hg mass in the atmosphere (17 Mmol), soil (320 Mmol) and ocean (490 Mmol), with the remaining 403 Mmol entering deep mineral reservoir via sedimentation.

For the surface ocean, our results are comparable to the studies of Streets et al. (2011) and Amos et al. (2013), who found factors of 3.6-6.0 increase (compared to 4 in our study). However, they report larger increases in the intermediate ocean (factors of 2.7-5.2, compared to 2.4 in our study) and especially in the deep ocean (factors of 1.5-2, compared to 1.2 in our study). We attribute this difference to an overestimate of the vertical mixing of anthropogenic Hg in the box model studies of Streets et al. (2011) and Amos et al. (2013) and the lack of horizontal and vertical transport Anthropogenic emissions have led to a factor of 7.5 increase in the atmospheric deposition flux to land, larger than the factor of 4.8 increase in the deposition to the ocean surface. This is because the anthropogenic sources are located over land, which thus have larger impact for the deposition over the land than the ocean. The riverine effluent input of Hg to the global ocean increases by a factor of 2.8. The sedimentation flux to the ocean floor increases from 0.5 Mmol/yr to 1.37 Mmol/yr (factor of 2.7), but this is a negligible perturbation to Hg in the deep mineral reservoir.

Overall, our results show that the total Hg mass in the global ocean has increased from 1150 Mmol to 1640 Mmol, an increment of 490 Mmol (factor of 1.4 increase) (Figure 5.3). We find that 55% (270 Mmol) of the anthropogenic Hg is in the deep ocean, 43% (210 Mmol) in the intermediate ocean and 2% (8.6 Mmol) in the mixed layer. We find that the penetration of anthropogenic Hg in the ocean's interiors occurs dominantly via particle sinking. Within the ocean, the human perturbations show more complex patterns. At the bottom of ocean mixed layer, anthropogenic Hg emissions have increased the Hg particle sinking flux from 1.0 Mmol/yr to 4.4 Mmol/yr, with an enrichment factor of 4.4. The anthropogenic Hg emissions also decrease the upward physical transport (advection/diffusion and entrainment/detrainment) from 0.6 Mmol/yr to 0.4 Mmol/yr, which results in a net penetration flux of 0.2 Mmol/yr for anthropogenic Hg. Therefore, 94% of anthropogenic Hg penetrates into subsurface ocean waters via particle sinking. Similar condition happens to the interface with 1,000 m depth. The influence of anthropogenic Hg emissions modify the vertical gradient of Hg concentrations, which causes an exact cancellation of the physical upward transport flux at this depth, resulting nearly no net physical transport of dissolved Hg across this interface at present-day. The particle sinking flux across this interface is the only pathway for Hg entering into the deep ocean. Strode et al. (2010) also found that particle sinking was of central importance for the penetration of anthropogenic Hg. By tuning on/off the particle sinking process in their 1-D column model, they found that half of the anthropogenic Hg in the ocean is transported downward by this particle sinking process.

Our simulation started under steady state conditions in 1450. Because the anthropogenic Hg emissions increase more rapidly than mixing timescales of the subsurface ocean, the intermediate and deep oceans are not currently in steady state, with a net Hg increase rate of 2.4 and 1.1 Mmol/yr, respectively. This means that the ocean Hg concentrations would continue to increase at a rate of 0.67%/yr in the intermediate ocean and 0.087%/yr in the deep ocean, respectively, even if present-day anthropogenic Hg emissions stopped increasing.

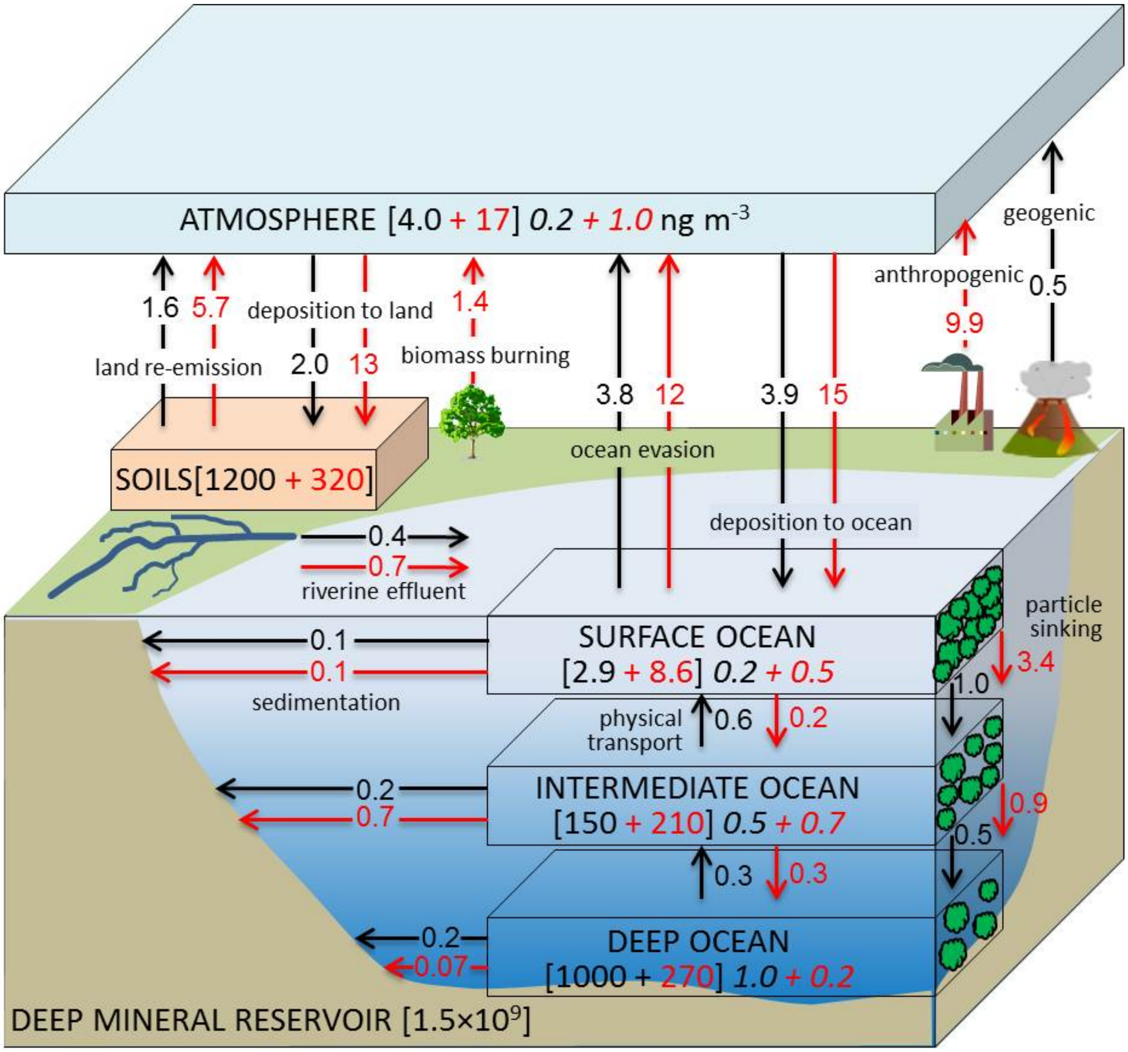

Figure 5.3: Human perturbation to the global Hg cycle via anthropogenic Hg emissions. Fluxes (units of Mmol a^{-1}) are indicated next to arrows, while reservoir sizes are indicated in brackets (units of Mmol), with concentrations in italics (unites of pM in the ocean and ng m^{-3} in the atmosphere). The natural Hg budget is shown with black numbers and arrows, while the human perturbation is shown in red. The Hg particle sinking and sedimentation fluxes are shown as green and orange arrows, respectively.

5.3.2 Temporal evolution

Figure 5.2b shows the 1450-2008 modeled evolution of atmospheric Hg^0 concentration near the surface, atmospheric Hg^{II} deposition to ocean, riverine input to ocean, soil re-emission, and oceanic Hg^0 evasion flux, while figure 5.2c shows the evolution of Hg mass in the ocean. Because of the short lifetime of Hg in the atmosphere (7 months, Figure 5.3) and the mixed layer ocean (7 month, Chapter 4), the Hg mass in these reservoirs have a rapid response and thus their variations follow changing anthropogenic Hg emissions (Figure 5.2c). For the same reasons, the exchange fluxes (Hg^{II} deposition flux to ocean and ocean Hg^0 evasion flux) between these fast-cycling reservoirs also follow anthropogenic emissions. The slower residence times of Hg in soils leads to a much smoother evolution of soil re-emission and riverine input (Streets et al., 2011) (Figure 5.2b). The residence time of Hg in the intermediate ocean is ~120 years and for the deep ocean it is ~2000 years (Chapter 4). Thus, the temporal trends of Hg in these reservoirs are much slower and smoother than in the mixed layer. The trend of Hg mass in the entire ocean generally follows that of the deep ocean, but shows slightly higher accumulation rate after ~1900, because of the faster increasing rate in the intermediate ocean since then.

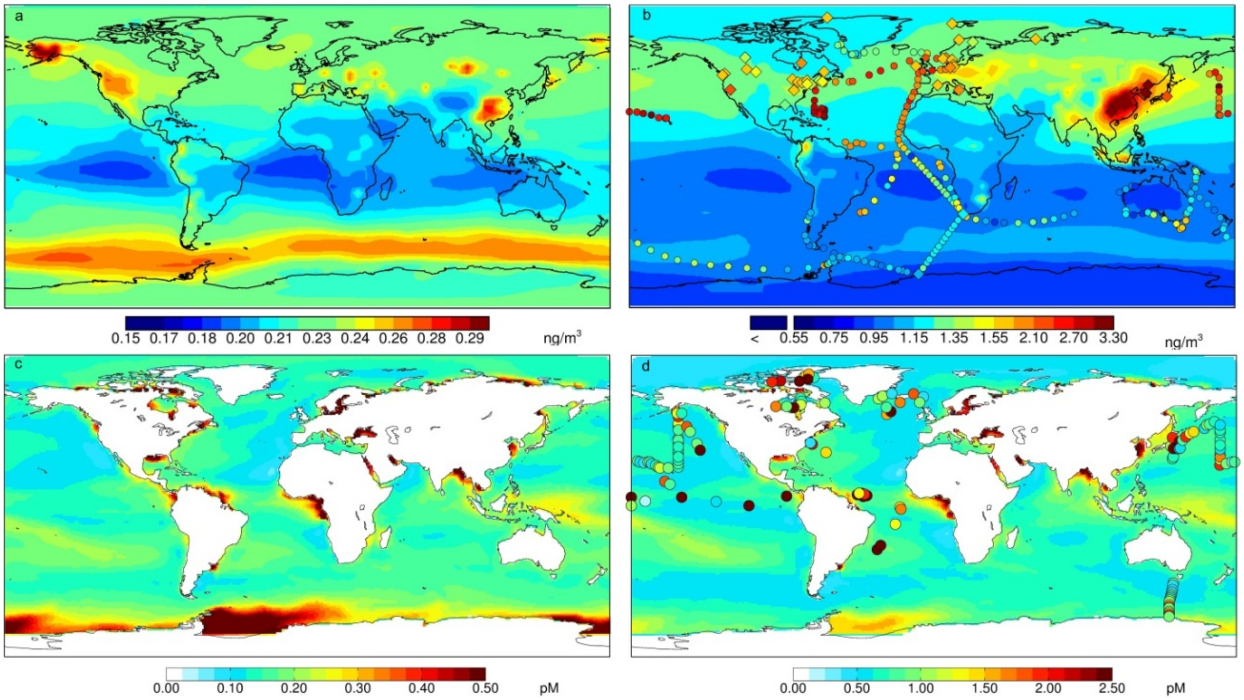

Figure 5.4: Top panels: Modeled surface atmospheric total gaseous mercury (TGM, in ng/m^3) concentrations for a) natural conditions b) present-day conditions. Observed concentrations (2004-2008) are shown as color-coded circles on panel (b). Bottom: Total Hg concentrations (in pM) in the surface ocean for c) natural conditions and d) present-day conditions. Observed concentrations (1984-2010) are shown as color-coded circles on panel (b).

Looking at the present-day burden of anthropogenic Hg in the entire ocean (490 Mmol), we find that 61% (300 Mmol) of the accumulation occurred before 1920, and is thus mostly from mining. The coal surge since 1920 contributes to the remaining 39% (190 Mmol) of the anthropogenic Hg in the ocean. Since 1850, our simulation predicts that the Hg mass in the total ocean has increased by 18%. This estimate is quite close to that by Strode et al. (2010), which also predicts an increase of 18% in Hg mass in the topmost 2000 m based on their one-dimensional column box diffusion model. This result also generally agrees with the result of a 17% increase in total oceanic Hg mass since pre-industrial time by Sunderland and Mason (2007). However, our estimate is higher than the enrichment factor calculated by Mason and Sheu (2002; 9%) and lower than those calculated by Streets et al. (2011; 35%) and Amos et al. (2013; 76%). As discussed above, this variability of anthropogenic perturbation in these box model studies is caused by the different assumptions for the timescale of vertical mixing of anthropogenic Hg.

5.3.3 Horizontal distribution of surface atmospheric and oceanic Hg concentrations

Figure 5.4a and b show the spatial distribution of surface atmospheric total gaseous mercury (TGM = Hg^0+Hg^{II}) concentrations for natural and present-day conditions, while figure 5.5a shows the latitudinal distribution of their zonal averages. For natural conditions, the global mean atmospheric TGM concentration is 0.2 ng/m^3, with small horizontal variations (Figure 5.4a) and no significant interhemispheric gradient (Figure 5.5a). The concentrations are slightly enhanced in regions with strong geogenic sources (Alaska, the Rocky Mountains, and eastern China), where TGM concentrations reach levels of 0.25-0.3 ng/m^3. TGM concentrations are also higher over Southern Ocean (~0.25 ng/m^3), because of the strong ocean Hg^0 evasion in that region caused by the high wind speed and high oceanic Hg concentrations (Chapter 4, Section 4.6.1).

Our present-day simulation has global mean TGM concentrations of 1.2 ng/m^3. The present-day distribution of TGM shows much larger spatial variability with concentrations ranging from 0.5 to 3.5 ng/m^3. The highest concentrations are modeled over regions with strong anthropogenic emissions including East Asia, Western Europe, and North America (Figure 5.4b). Anthropogenic emissions lead to an interhemispheric gradient, with 1.2-1.5 ng/m^3 in the northern hemisphere and 0.9-1.0 ng/m^3 in the southern hemisphere (Figure 5.5a), because most of the anthropogenic Hg emissions are located in the northern hemisphere.

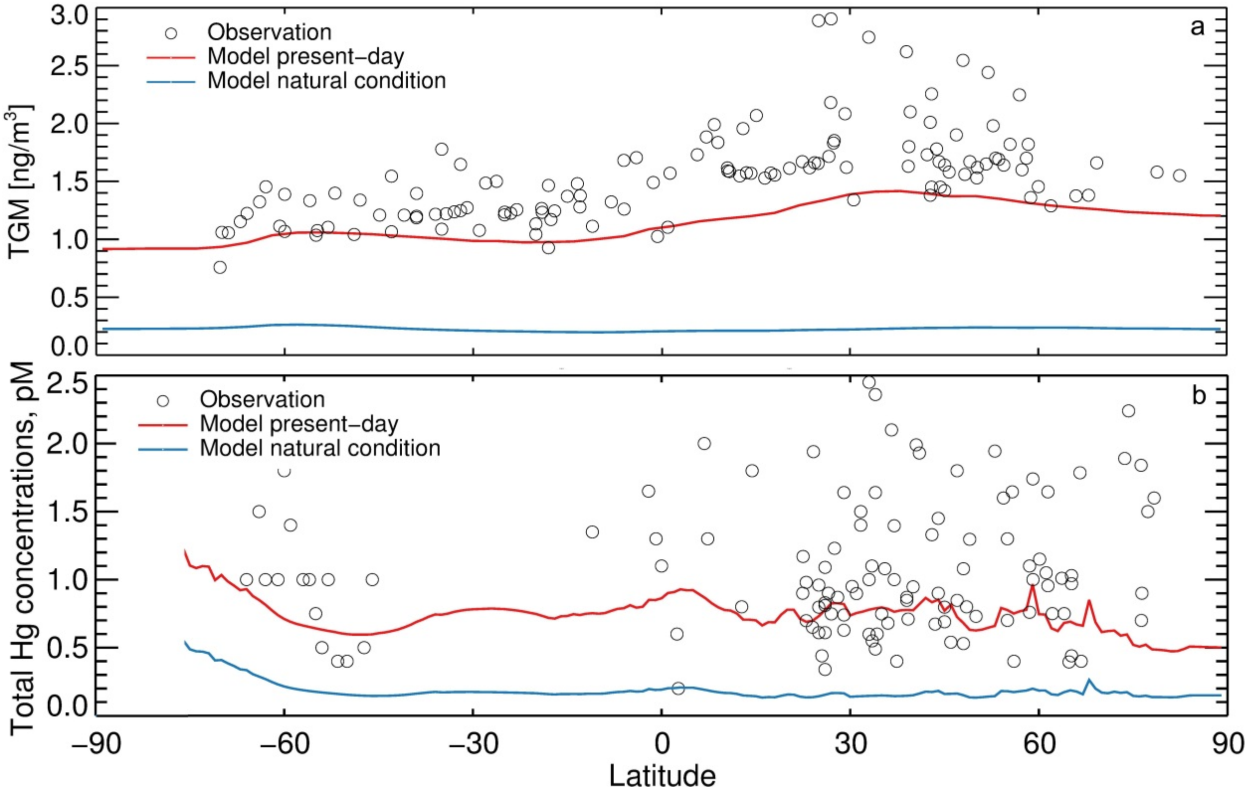

Figure 5.5: Zonal average of a) near-surface atmospheric TGM concentrations and b) total Hg concentrations at ocean surface. Observations are shown as scattering points.

We compare our results to observations taken in the atmospheric marine boundary layer and at terrestrial sites as summarized in previous GEOS-Chem model studies (Selin et al, 2007; Holmes et al., 2010; Soerensen et al., 2010a; 2012). The modeled latitudinal gradient falls at the low edge of the envelope of observations. The horizontal distribution of TGM is similar in both model and observations, with higher concentrations near strong anthropogenic regions. The spatial correlation coefficients between model and observation is high (r^2 = 0.90). At terrestrial sites, the modeled TGM concentrations (1.4±0.4 ng/m^3) are 25% lower than observations (1.9±1.0 ng/m^3). The model also under-predicts the TGM concentrations by cruise measurements over North Atlantic (obs.: 1.9±0.16 ng/m^3; mod.: 1.2±0.02 ng/m^3) and Pacific Oceans (obs.: 2.5±0.4 ng/m^3; mod.: 1.2±0.07 ng/m^3). Previous modeling studies with the GEOS-Chem (e.g. Strode et al., 2007; Holmes et al., 2010) found similar underestimates for the high atmospheric TGM concentrations observed in the Northern Hemisphere marine boundary layer. By increasing the subsurface ocean concentrations, in particular over North Atlantic (1.8-2.0 pM), Soerensen et al. (2010a) achieved better agreement with these cruise observations. However, our model misses this feature. Potential reasons for this include our lower subsurface ocean concentrations (~1.2 pM) over this region, and a possible underestimate of ocean Hg^0 evasion fluxes.

Figure 5.4c and d contrast total aqueous Hg concentrations in the surface ocean for natural and present-day conditions. The latitudinal distribution of zonal average concentrations is shown in Figure 5.5b. At natural conditions, the global average surface total Hg concentrations are 0.17 pM. The surface ocean Hg concentrations are high near the circumpolar Antarctic current in the Ross Sea and Weddell Sea (> 0.5 pM) because of the strong vertical mixing associated with the upwelling of Hg-rich deep water. Coastal regions, as well as closed and shallow water body such as Hudson Bay and Black Sea also show elevated Hg concentrations (> 1 pM) because of the strong influence by riverine input at near-shore/shelf environments. In the natural simulation, surface ocean Hg concentrations are generally higher in the Southern Hemisphere (0.18 pM) compared to the northern hemisphere (0.15 pM), as discussed in Chapter 4. This is because of the stronger atmospheric Hg^{II} deposition over the south hemisphere, which is the dominant pathway for Hg entering the ocean (Chapter 4, Figure 4.9a). No significant latitudinal and inter-hemispheric gradients are modeled for the aqueous total Hg concentrations at natural conditions.

At present-day, the modeled global average total Hg concentrations over surface ocean are 0.72 pM with slightly higher (0.74 pM) over south hemisphere than in north hemisphere (0.71 pM). This is still caused by the higher Hg^{II} deposition flux over the Southern Hemisphere at present-day condition (Holmes et al., 2010), even though the anthropogenic emissions and near-surface atmospheric TGM concentrations are much enhanced over North Hemisphere at present-day. No significant latitudinal and inter-hemispheric gradients are modeled for the aqueous total Hg concentrations at both natural and present-day conditions. The large-scale horizontal spatial pattern of surface ocean Hg concentrations has also not changed too much at present-day compared with that at natural condition, indicating similar controlling factors (e.g. ocean circulation and particle sinking flux).

We compare our present-day model results of surface ocean Hg concentrations to observations spanning the last two decades, as summarized by Soerensen et al., (2010a). Observations display a large variability, with values ranging from less than 0.1 pM to more than 7 pM (Figure 5.4d). Observed median total Hg concentrations are 1.0 pM. The model sampled at the same locations as the observations displays median values that at 33% lower (0.67 pM). When averaged zonally, we find no significant latitudinal trends are associated with the observations, possibly because of the large observed variability. The modeled present-day concentrations fall within the center of envelope for the observations with most density data points (Figure 5.5b), indicating a reasonable agreement between them. Most of the measurements near coastal and shelf regions are significantly higher (> 2 pM) than the corresponding modeled values (~0.5 pM), such as the measurements over the Hudson Bay region and the coastal Canadian Arctic Ocean Archipelago. This could be due to an underestimate of the riverine input Hg flux, especially because we only considered the erosion of Hg from background soils in our model, while the neglected Hg loading at ocean margins from either waste water and industrial sources (Soerensen et al., 2010a; Streets et al., 2011) or snowpack melt water may input more Hg to the ocean waters (Fisher et al., 2012). Furthermore, our low-resolution model does not capture the advection and mixing of Hg near the coastal regions. For the North Atlantic Ocean (obs: 1.0±0.48 pM; mod: 0.68±0.12 pM), North Pacific Ocean (obs: 0.88±0.31 pM; mod.: 0.70±0.11 pM) and Southern Ocean (obs: 1.0±0.44 pM; mod: 0.69±0.12 pM), we find that the model captures observed surface ocean total Hg concentrations reasonably well.

5.4 Comparison against historical archives

We evaluated the coupled historical Hg simulation against proxy records in lake and marine sediments, peat bog cores, and ice cores. Lake sediments are considered to be the most reliable archives for estimating historical Hg accumulation (Biester et al., 2007). Measurements of Hg concentrations in lake sediment cores have been used to reconstruct past atmospheric Hg deposition trends in many regions of the world: North America, South America, Greenland, Europe, Asia, Siberia, and New Zealand (e.g., Landers et al., 1995; Pirrone et al., 1998; Fitzgerald et al., 2005; Lindberg et al., 2007; Jiang et al, 2011). We have compiled 145 profiles reported in the literature (139 lake sediment profiles; 4 peat bog cores, 1 marine sediment cores; and 1 ice cores), with a list of references provided in Appendix). These records can date as far back as 1800.

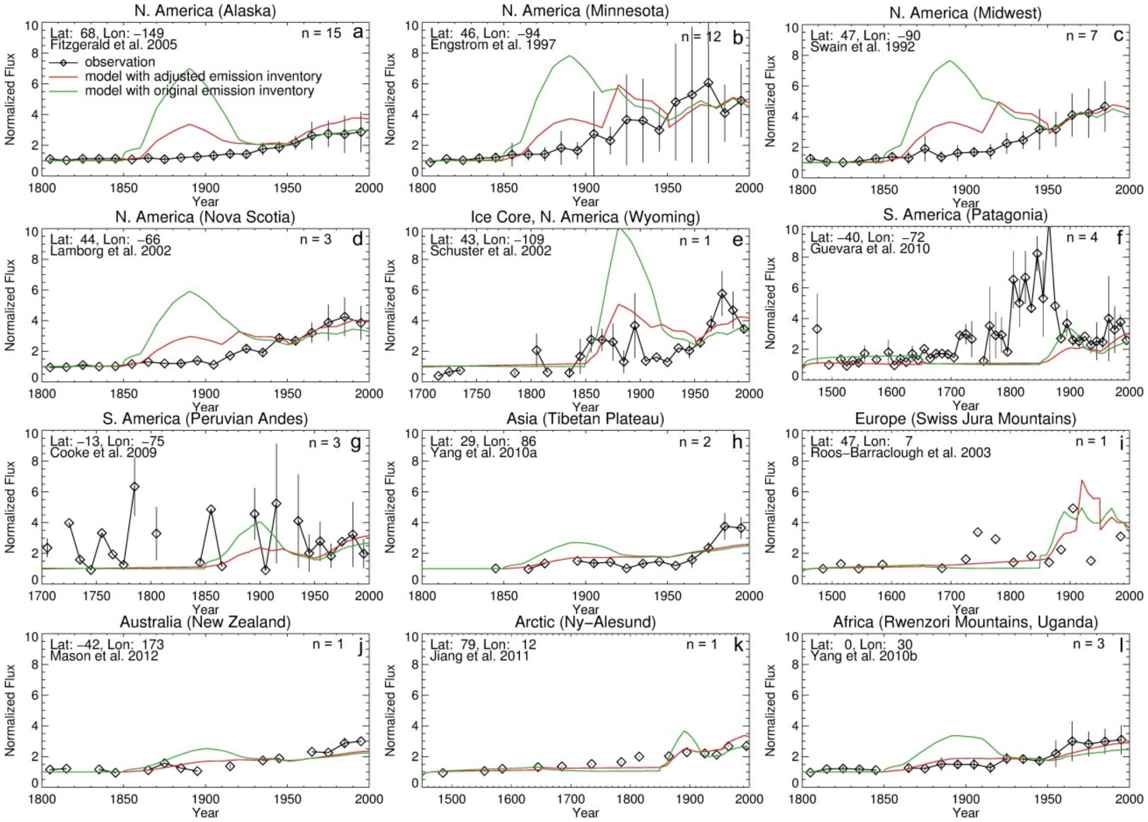

Figure 5.6: Selected lake sediment (panel a-d and f-l) and ice core (panel e) profiles of normalized Hg accumulation fluxes compared against model results. Vertical bars represent the standard deviation of the observations.

Typical examples of these accumulation flux/concentration profiles are shown in Figure 5.6, with comparison to model results. We normalized the Hg accumulation flux rates or concentrations to the levels in the earliest part of the record (observations in 1800 for most of the sites). Multiple profiles sampled at nearby locations are combined and the mean value and standard deviation are shown, because of the large site-by-site variability (up to a factor of 2). This variability reflects the influence of local emission sources at smaller spatial scale, the difference in relative importance of soil Hg input against atmospheric deposition, and/or the different catchment area and region for the riverine input (e.g. Fitzgerald et al., 2005; Engstrom et al., 1997).

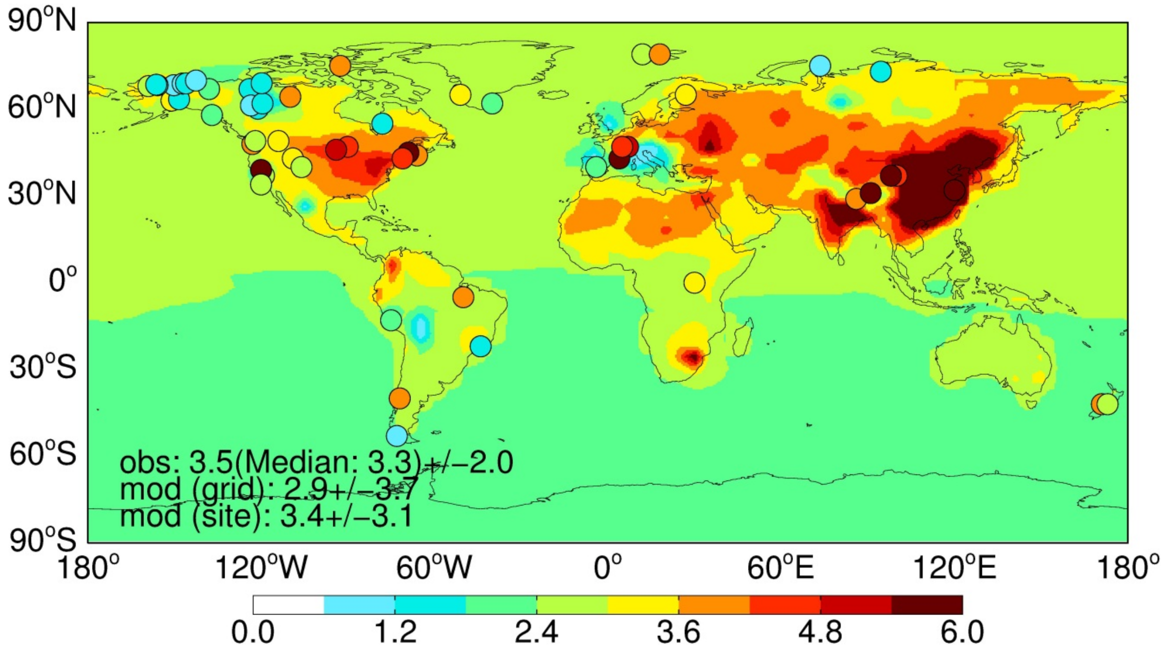

Figure 5.7: Mercury deposition flux enhancement ratio for present-day relative to 1800. The data source of the observations is listed in the Appendix.

Overall the model reproduces the evolution of the observed enhancement in accumulation as recorded in these historical archives, especially for the last 100 years. Larger discrepancies take place in the period between 1850 and 1900, when mining emissions dominated. In that time period, the model result driven by the original emission inventory developed by Streets et al. (2011) largely overestimates the observed enhancement across almost all the sites (green lines) by a factor of ~3. In fact, many observations do not suggest much of an enhancement during this period, for example, the lake sediment profiles obtained over North America, Asia and Arctic (panel a-d, h, and k). Some of these overestimations may be caused by the uncertainties associated with the Hg measurements in these historical archives. However, given the consistency of different sites using different methods, it is likely that there are issues with the estimates of Hg emissions from mining in the inventory we are using. By adjusting the Hg emissions from mining activities (red lines), the model comes closer to observations for most of the sites.

We also examined the ratio of present-day to pre-industrial (year 1800) Hg deposition flux in the model, defined as the enhancement ratios, ER (Figure 5.7). We calculated the same quantities for the historical archives. Both the model and observations suggest a factor of ~3 increase in Hg deposition since 1800. When averaged at all the sites shown in Figure 5.7, observations have ER of 3.5±2.0 (mean ± 1σ), thus a factor of 3.5 increase in Hg deposition at these sites since 1800. Modeled ERs (3.4±3.1) are very close to these observations.

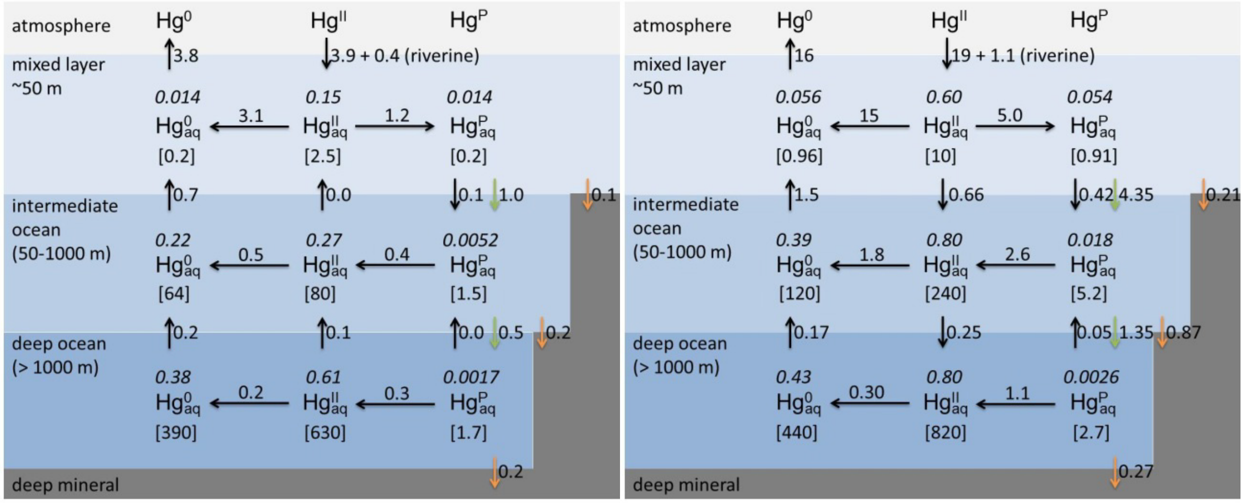

Figure 5.8: Marine Hg budgets for natural (left) and at present-day (right) conditions. Numbers in brackets are Hg stock mass in Mmol, while numbers in italic are Hg concentrations in pM. The numbers along arrows indicate annual flux (Mmol/yr). Particle sinking flux and sedimentation fluxes are shown in green and yellow arrows, respectively.

As shown in Figure 5.7, large spatial variability exists for the ER values with values ranging from 1-2 in remote regions and 5-10 for regions near large anthropogenic source emissions. The ER values can be as high as 8-10 at some lake sediment sites across the Tibetan Plateau (Yang et al., 2010). The average ER values of the 5 sites in China are 6.5±2.2 (obs.) and 7.0±7.2 (mod.), due to the large coal combustion and metal mining emissions of Hg in China (Wu et al., 2006). The model also generally captures the west-east gradient of ER values over the U.S. (obs: 2.9±0.8 (west) and 5.8±2.0 (east); mod: 2.6±0.8 (west) and 3.7±0.6 (east)), which is caused by the enhanced anthropogenic emissions over the eastern U.S., especially over the Ohio

River Valley region. High ER values are also observed at the three western European sites (excluding the Spanish site), with average ER values of 5.1±0.7 and 3.1±0.3 for observation and model, respectively. Remote locations with lower present-day anthropogenic emissions, such as New Zealand, Greenland, Svalbard, Alaska, Western Canada, and Magellanic Moorlands located at the southern end of South America, indicate lower ER values (obs: 2.6±1.0), which are reproduced by the model (2.3±0.3).

Some regions have low ER values because of elevated regional deposition in the 1800s due to mining. For instance, both the observation and model predicts lower ER value (obs: 2.3; mod: 0.8) over an ombrotrophic Spanish mire (Peña da Cadela) site (Biester et al., 2007), due to the historical Hg mining there (Streets et al., 2011). Landers et al. (1998) found relatively low ER values over Alaska and Siberia (1.1-1.2). Some of the difference among these records could be due to the fact that some lake sediments might be affected by strong erosion of Hg from naturally enriched soils, thus minimizing the influence of atmospheric deposition.

5.5 Human Perturbation

5.5.1 Marine Hg budgets

Figure 5.8 shows the budgets of Hg with more detail for the Hg speciation and transformation in the global ocean under natural and at present-day conditions. As discussed in Section 5.3.1, the enrichment factors of total Hg concentrations in the mixed layer, intermediate ocean and deep ocean are 4.2, 2.4 and 1.2, respectively. In the surface ocean, the enrichments for different species are quite uniform (all by a factor of ~4), caused by the fast photo-transformation between Hg^0_{aq} and Hg^{II}_{aq}, as well as instantaneous partition equilibrium between Hg^{II}_{aq} and Hg^P_{aq}. However, the enrichment factors for Hg^{II}_{aq} and Hg^P_{aq} (~3) are larger than that for Hg^0_{aq} (1.8) in the intermediate ocean. Similar condition happens in the deep ocean: 1.3 for Hg^{II}_{aq} and Hg^P_{aq} but only 1.1 for Hg^0_{aq}. This is because the transformation from Hg^{II}_{aq} to Hg^0_{aq} in the intermediate and deep oceans is much slower than in the mixed layer. The long lifetimes of Hg^0_{aq} in the intermediate (~90 years) and deep (~2000 years) oceans relative to this reduction process have make the concentration of Hg^0_{aq} lag behind the change of Hg^{II}_{aq}.

Anthropogenic Hg emissions also significantly perturbed the transformation among different Hg species in the ocean. The Hg^{II}_{aq} reduction fluxes and Hg^P_{aq} sinking/sedimentation fluxes closely track the concentration of Hg^{II}_{aq} and Hg^P_{aq}, respectively, because they are assumed to be first-order processes in the model. The absorption flux of Hg^{II}_{aq} on to POC in the mixed layer (i.e. $Hg^{II}_{aq} \rightarrow Hg^P_{aq}$) is also enriched by a factor of 4.2, proportional to the Hg^{II}_{aq} concentrations in the mixed layer. However, the Hg^P_{aq} releasing flux back to dissolved phase caused by remineralization of POC (i.e. $Hg^P_{aq} \rightarrow Hg^{II}_{aq}$) in the intermediate and deep ocean have higher enrichment factors (6.5 and 3.7, respectively) than the concentration of Hg^P_{aq} itself. This large enhancement is caused by the non-uniformly perturbations in the ocean at different depths. The sinking particles from waters atop are relatively more enriched with Hg than the particles below. Because of the instantaneous partitioning assumption, a larger fraction of Hg (60% and 81% for intermediate and deep ocean, respectively) is released from the sinking particles to the ocean waters than at natural condition (40% and 60%, respectively). The human perturbation to the vertical physical transport fluxes are complex and non-linear, reflecting the change of Hg concentration gradients. For example, the Hg^0_{aq} flux from intermediate ocean to mixed layer is only enhanced by a factor of ~2, roughly reflecting to the change in concentration gradients (0.21 pM at natural condition and 0.33 pM at present-day). The Hg^{II}_{aq} transport flux from deep to intermediate ocean is even reversed in direction, because of the larger enrichment for Hg^{II}_{aq} occurring in the intermediate ocean than deep ocean.

5.5.2 Ocean Hg concentration profiles

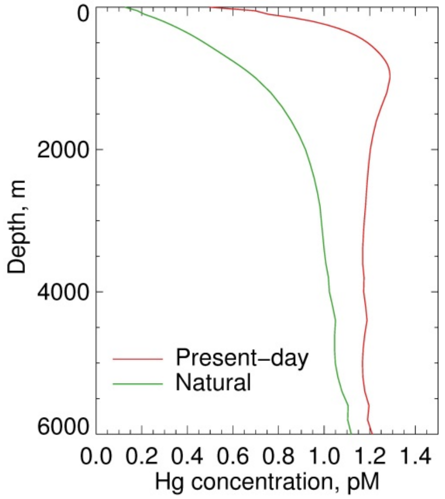

Figure 5.9: Global modeled average marine total Hg concentration profiles for natural (green) and present-day conditions (red).

Figure 5.9 shows the globally averaged profiles of modeled ocean Hg concentrations for natural and present-day conditions. As discussed in Chapter 4 (Figure 4.8), in the natural ocean, the total Hg concentration shows an increasing trend with depth because of the balance between particle scavenging and vertical diffusion (Strode et al., 2010). The present-day profile shows larger concentrations throughout the water column, but with most of the enhancements occurring in the top 2,000 m. The resulting profile at present-day has a maximum (~1.3 pM) at 900-1,000 m, with a peak of anthropogenic Hg (~0.7 pM) at 400-500 m. The absolute change of Hg concentration over the ocean surface (~0.4 pM) is lower due to the low total Hg concentration at ocean surface caused by strong particle removal. Over deep ocean (>1 km), the time scales for mixing with downward surface waters are centuries except the deep water formation regions. In addition, the sinking POC fluxes are mostly remineralized in the top several hundred meters, and thus the Hg transport flux via particle sinking is also extremely low in the deep ocean (Martin et al., 1987). Therefore, the anthropogenic Hg concentration in the deep ocean remains quite low at present-day (0.1-0.2 pM). This present-day profile is quite close to the result predicted by Strode et al.

(2010), demonstrating again that the box diffusion model can capture the vertical transport and distribution of Hg at least in a global average sense.

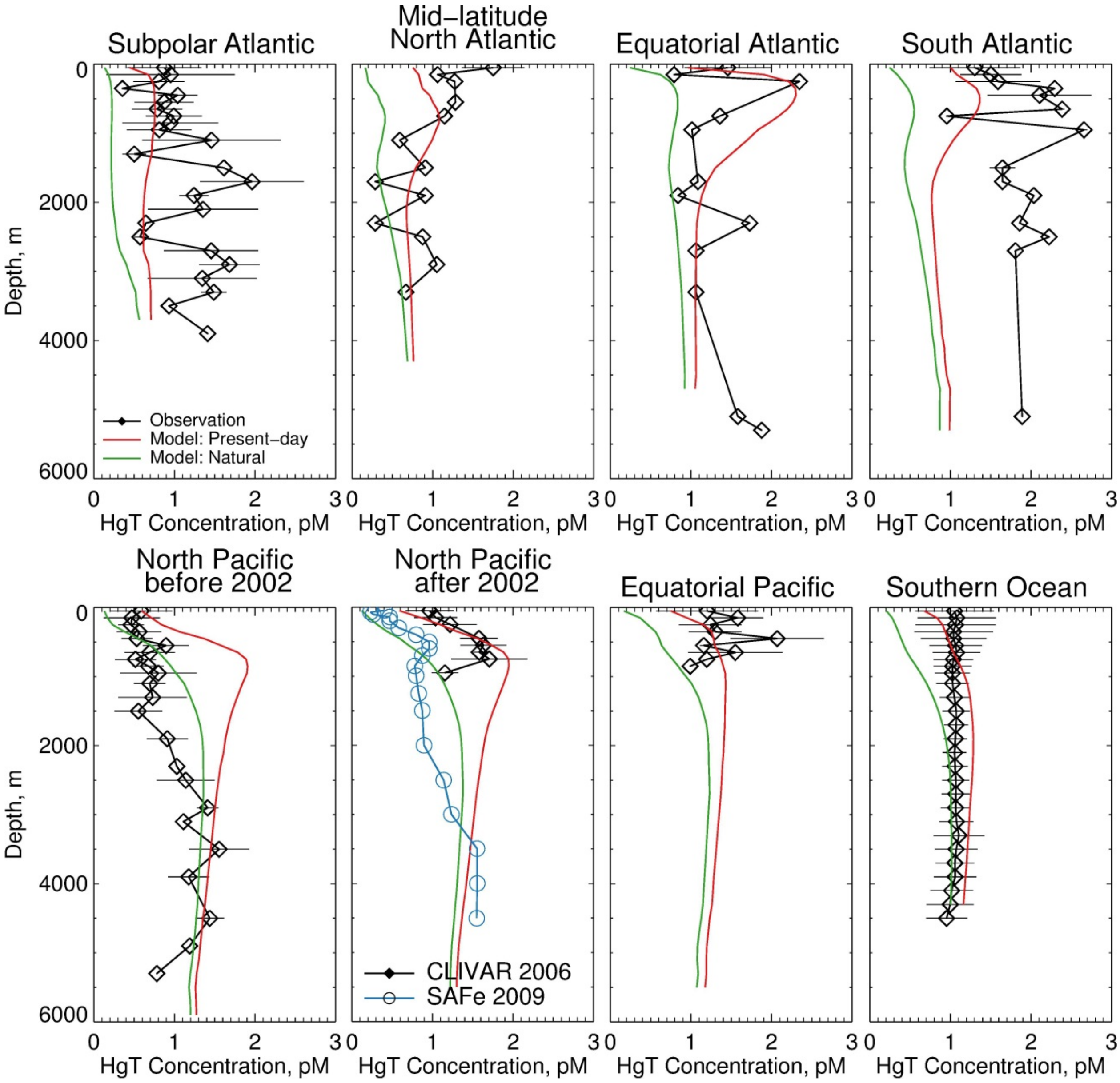

Figure 5.10: Comparison of ocean total Hg concentration profiles against observations over the past 30 years over different ocean basins. Horizontal bars for observations indicate the standard deviation of multiple observations occurring at the same ocean basins.

In Chapter 4, we have summarized the currently available total Hg concentration profiles in different ocean basins and used the deeper part of these profiles to evaluate our oceanic model for natural conditions (the references are listed in the Appendix). We found that the model

(1.1±0.3 pM) generally reproduces the observed (1.4±0.9 pM) Hg concentrations over depth larger than 2 km. In this chapter, we will extend this comparison to the entire profile for present-day conditions. Figure 5.10 shows the comparison of modeled ocean total Hg concentration profiles against selected observations in different ocean basins (Subarctic Atlantic, Mid-latitude North Atlantic, Equatorial Atlantic, South Atlantic, North Pacific, Equatorial Pacific, and the Southern Ocean). We sample the model for the same month, year and location as the observations. Overall, the model (1.3±0.5 pM) reproduces observed (1.3±1.1 pM) Hg concentrations over the intermediate ocean with depth ranging from 100-1000 m. In the next paragraphs, we will examine comparisons for individual regions.

Over the sub-polar North Atlantic (panel a), modeled Hg concentrations do not vary much with depth, reflecting deep water formation and thus rapid vertical mixing in this region (Schmittner et al., 2007). The anthropogenic Hg (the difference between the natural and present-day simulations) remains nearly constant with depth, down to ~3000 m. Observations (Mason et al., 1998) suggest fairly uniform concentrations down to 1000m, but larger variations below. While the model captures the mean observed concentrations above 1000m, below that depth it underestimates observations by a factor of ~2.

In the mid-latitude North Atlantic Ocean (BATS station sampled in 1999, panel b), the observed total Hg concentration profile shows a surface-enhanced pattern: general decreasing trend for total Hg is observed in the topmost ~1500 m, then keeps nearly unchanged below this depth. The model captures the overall shape of the observed profile, but does not reproduce the very high surface concentrations. When compared against the profile at natural time, the human perturbation is the strongest (~0.6 pM) in the top 1000 m. In contrast, we find deeper penetration depths of the anthropogenic perturbation in the Subpolar Atlantic, where it is enhanced by rapid mixing of the anthropogenic mixing by deep water formation.

In the Equatorial Atlantic (panel c), the model reproduces observations quite well, in particular the model captures the 2.5 pM peak at 300-400 m depth with the peak due to anthropogenic Hg. In this region, we find that the anthropogenic Hg enhancement is large (> 1pM) because of the high particle sinking flux. Anthropogenic Hg is taken up by particles as they sink, then at 300-400 m depth the particles are remineralized, releasing Hg as Hg^{II}_{aq}, which is then reduced to Hg^{0}_{aq}. High remineralization rates calculated in the model are supported by the elevated apparent oxygen utilization observed in that region (AOU, ~4.0 ml/L, Mason and Sullivan, 1999).

Over the South Atlantic (panel d), the model is a factor of 2 lower than observations, but does reproduce the shape of the profile. Note that we excluded from the observed profile deep water observations higher than 3 pM in the deep waters, which are likely influenced by a source of Hg from the sediment (Mason and Sullivan, 1999). The reasons for the underestimate are unclear, but we note that observations in this region are factor of 2 or more higher compared to observations in other regions, suggesting unusual conditions for this profile or issues with the measurements.

Observations in the North Pacific Ocean show different profiles depending on location and time. We have thus separated observations before 2002 (2002 IOC and 1987 VERTEX, Laurier et al., 2004, panel e) and observations after 2002 (CLIVAR cruise in March 2006 and at SAFe station in May 2009, which both are in the east part of North Pacific Ocean: Sunderland et al., 2009; Hammerschmidt and Bowman, 2012, panel f). At depths below 3000 m the model agrees with observations, predicting fairly uniform concentrations of ~1.3 pM. For observations prior to 2002 (panel e), the model is a factor of 2 lower than observations at depths of ~50-3000 m. In contrast, the model reproduces observations above 1000 m obtained in the eastern North Pacific Ocean during the CLIVAR 2006 cruise (panel f). Sunderland et al. (2009) argued that the factor of 2 increase in intermediate waters Hg concentrations relative to prior cruises was caused by eastward transport of increasing Asian deposited Hg through ocean currents. However, in observations obtained in 2009 (panel f, SAFe 2009), Hammerschmidt and Bowman (2012) found levels similar to earlier cruises. This variability in observed profiles suggests large interannual and/or seasonal variability for the Hg concentrations and the penetration of anthropogenic Hg over the east North Pacific that is not captured by the model.

In the Equatorial Pacific Ocean, both the model and observation show a peak of total Hg concentrations at intermediate depths (panel g). In the Southern Ocean, observed and model Hg concentrations show uniform concentrations with depths (~1.1 pM). This distribution is similar to what we found over the Subpolar North Atlantic Ocean and reflects rapid vertical mixing in that region.

5.5.3 Horizontal and vertical distribution of anthropogenic Hg in the Ocean

We now examine the vertically integrated column concentrations of Hg in the ocean, contrasting our natural (Figure 5.11a) and present-day simulations (Figure 5.11b). The column concentrations are influenced by variations in both the average Hg concentration levels as well as ocean depths. In the natural simulation, the Arctic and North Atlantic Ocean have the lowest column concentrations because their low Hg concentrations in the intermediate and deep oceans. On the other hand, the North Pacific Ocean displays the highest column concentrations because of its high intermediate and deep ocean concentrations (Chapter 4, Figure 4.12), as well as the largest average ocean depth. As discussed in Chapter 4 (Section 4.6.1), these large concentrations are due to the oldest age for the deep water over this region, which allows accumulation of the Hg falling along with sinking particles from atop. The present-day simulation reflects a similar spatial distribution (Figure 5.11b).

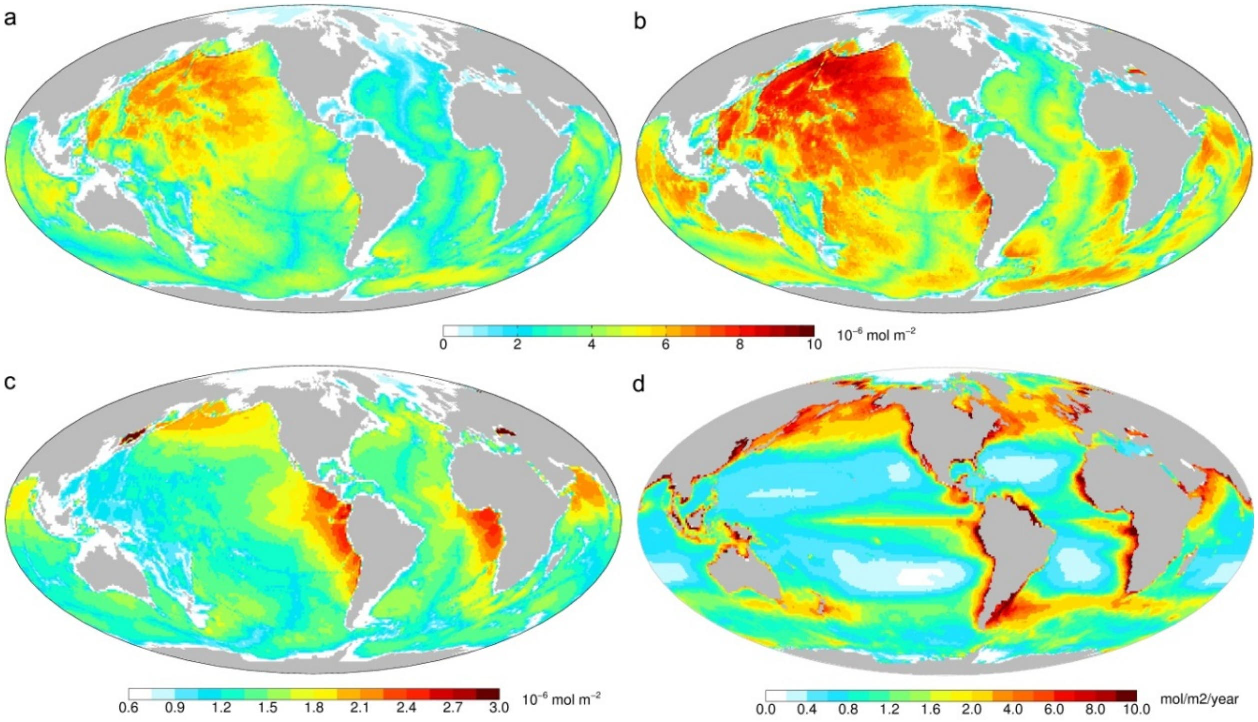

Figure 5.11: a, b) Vertical column concentrations of total Hg under natural condition and at present-day, respectively (×10^{-6} mol m^{-2}); c) The difference between panel a and b, i.e. the anthropogenic Hg (×10^{-6} mol m^{-2}); d) Annual mean particle organic carbon sinking flux used in this chapter (mol m^{-2} yr^{-1}).

We examine the difference in column concentrations between present-day and natural conditions (Figure 5.11c), and find elevated that the column anthropogenic Hg (> 2 µmol/m^{2}) over the east tropical Pacific Ocean and east tropical Atlantic Ocean. The column concentrations are also high over the Arabian Sea (~2 µmol/m^{2}), the high-latitude North Pacific (1.5-2.2 µmol/m^{2}). A small local enhancement is also found in the high-latitude Atlantic Ocean (1.6-1.9 µmol/m^{2}). We find lower anthropogenic column concentrations in the mid-latitude oceans (1-1.3 µmol/m^{2}). The lowest values are for the Arctic Ocean (<0.6 µmol/m^{2}), because of the shallow ocean depth in that region.

As discussed in Section 5.3.1, sinking of Hg attached to POC particles is the dominant way in which anthropogenic Hg penetrates into the subsurface ocean waters. The spatial distribution of anthropogenic Hg that we see in Figure 5.11c is thus directly influenced by the distribution of the POC sinking flux, which we show in Figure 5.11d. The POC sinking fluxes are generally higher in regions with enhanced nutrients from either erosion from terrestrial land masses such as high-latitudes North America and Eurasia or upwelling from deep ocean such as equatorial regions, west coasts of continents, as well as the Southern Ocean. The POC sinking fluxes are generally lower over the centers of gyres. The patterns of anthropogenic Hg are not as sharply defined for the POC sinking flux because of the integrating effect of ocean circulation at depth.

It is useful to contrast the penetration of anthropogenic CO_2 into the ocean to Hg. Anthropogenic CO_2 emissions have increased rapidly since industrial revolution. Penetration of anthropogenic Hg and CO_2 in the oceans is dominated by different penetration pathways. CO_2 is mainly carried downward by physical transport including advection, diffusion and convection. In addition to physical transport, Hg is particle reactive and the anthropogenic fraction can be transported to deep ocean via the biological pump. Sabine et al. (2004) found that about 30% of the anthropogenic CO_2 is located at depths shallower than 200 m, and nearly half at depths above 400 m. They also found that the majority of the anthropogenic CO_2 is confined to the upper ~1000 m. On the other hand, the invasion of anthropogenic Hg is much deeper because of the biological pump, with 55% at deeper than 1000 m (Figure 5.3). The difference in penetration pathways also leads to different horizontal distribution of anthropogenic CO_2 relative to Hg. Anthropogenic CO_2 is found to be higher over deep water formation region in the North Atlantic and mode water formation between 30° and 50° in the south hemisphere (Sabine et al., 2004). In contrast, anthropogenic Hg concentrations are the highest over region with strong POC sinking fluxes including the east tropical Pacific and Atlantic Ocean, the high-latitude North Pacific and Atlantic Ocean, as well as the Arabian Sea.

For other particle-reactive tracer metals which have large human perturbations such as Pb, the comparison with Hg is harder because of the much shorter lifetime of these metals in the atmosphere (e.g. ~1 week for Pb; Liu et al., 2001), which imposes a strong regional fingerprint to the ocean through deposition from the atmosphere (e.g. Henderson and Maifer-Reimer, 2002).

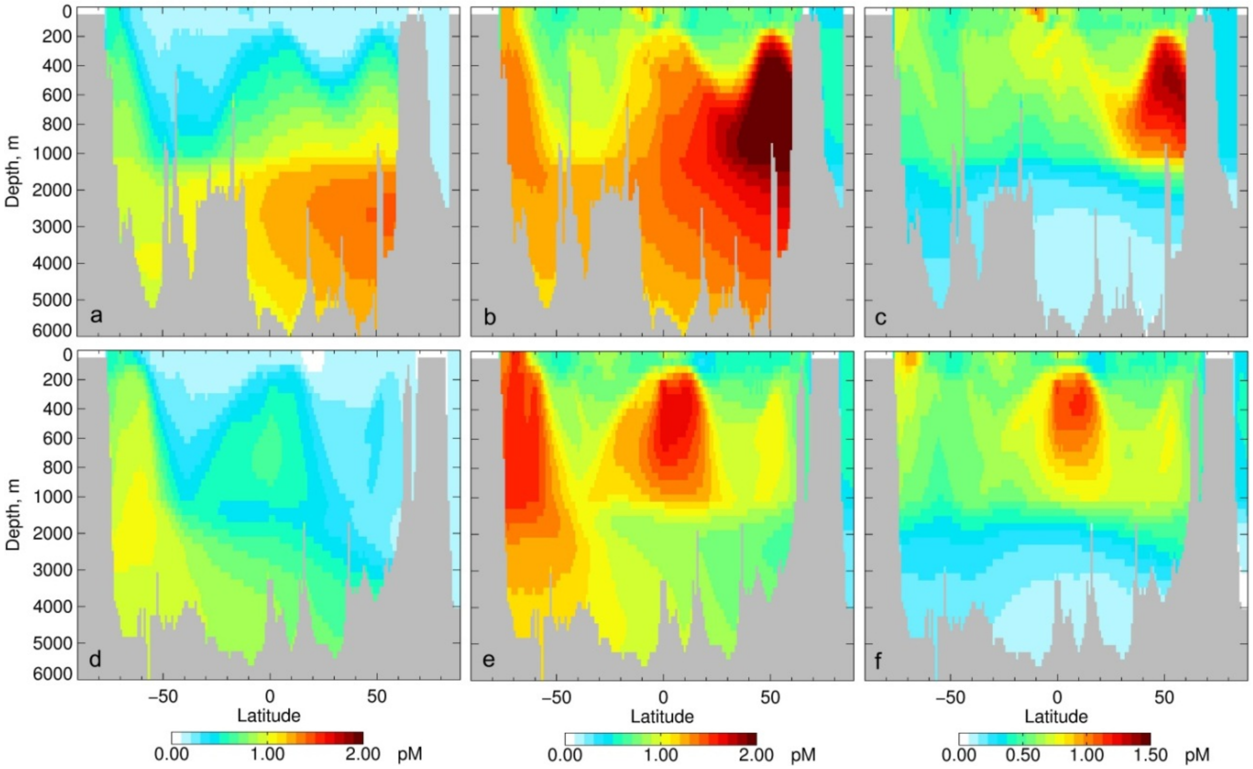

Figure 5.12: Modeled Hg concentration for natural conditions (a and d), present-day conditions (b and e) and their difference (i.e. anthropogenic Hg: c and f) along two representative meridional cross sections in the middle of Pacific (180°E: a, b, and c) and Atlantic (25°W: d, e, and f) Oceans. Note the scale of ocean depth is zoomed in the top 1,000 m and the color scale is different for the anthropogenic Hg concentrations (c and f) from the other four.

Figure 5.12 shows the modeled Hg distributions along meridional cross sections in the Pacific (180°E) and Atlantic (25°W) Oceans in the natural and present-day simulation (Figure 5.12a and b). As discussed in Chapter 4 (Section 4.6.3), the Hg concentrations in the natural simulation along these cross sections increase with depth because of particle scavenging. Deep ocean Hg concentrations increase with the age of waters, reflecting the continuous input of Hg through particle sinking and release of Hg at depth via remineralization. Indeed, concentrations increase from ~0.6 pM in the young deep waters of the North Atlantic Ocean to ~1.2 pM in the older water of the North Pacific Ocean. The vertical distribution of present-day Hg concentrations reflects the added contribution of anthropogenic emissions at depths of 0-2,000m. We see high anthropogenic Hg concentrations in the North Pacific Ocean at 200-1,000 m depth (Figure 5.12c). High anthropogenic Hg concentrations are also found in the tropical regions of Atlantic cross section at 200-800 m (panel f). For the mid-latitudes, where the convergence zones at the centers of gyres are located, the intrusion of low concentration waters at surface extends to a depth of only 200-400 m.

5.6 Conclusions

We have developed a coupled global three-dimensional model system for mercury in both the atmosphere and ocean. In the atmosphere, we modeled the atmospheric transport and chemistry of Hg with the GEOS-Chem Hg model, while in the ocean we used the OFFTRAC-Hg model. We drive this coupled model system with historical anthropogenic Hg emission inventory during 1450-2008. We have decreased the historical Hg emissions from mining activities by a factor of 3 to better match the historical archived Hg accumulation rate in lake sediments and ice cores.

Compared against the natural condition, we find in our simulation that the present-day Hg in the atmosphere and mixed layer ocean have been enriched by a factor of 5.3 and 4.2, respectively. The enrichment factors in the intermediate and deep ocean are much smaller: 2.4 and 1.2, respectively. Overall, we find that the total Hg mass in the global ocean has increased from 1150 Mmol at natural time to 1640 Mmol at present-day, an increment of 490 Mmol with enrichment factor of 1.4. At the bottom of ocean mixed layer, anthropogenic Hg emissions have increased the Hg particle sinking flux from 1.0 Mmol/yr to 4.4 Mmol/yr, with an enrichment factor of 4.4. Therefore, sinking with particles at the bottom of mixed layer is the dominant pathway (94%) for the anthropogenic Hg to penetrate into the subsurface ocean waters.

The perturbation of anthropogenic Hg emissions to the Hg cycle fluctuates depending on the history of anthropogenic emissions. The Hg mass in the mixed layer ocean has similar trend to the total atmospheric Hg emissions. The temporal trend in the intermediate ocean is much smoother than the mixed layer, and shows much broader and flatter fluctuations responding to the change of anthropogenic emissions. We find a very slow penetration of anthropogenic Hg into the deep ocean, and nearly not influenced by the variability of anthropogenic emissions at time scales shorter than approximately a century.

The model generally captures the spatial pattern of direct atmospheric and oceanic observations of Hg concentrations. At terrestrial sites, the modeled atmospheric TGM concentrations (1.4±0.4 ng/m^3) are 25% lower than observations (1.9±1.0 ng/m^3). The model also under-predicts the TGM concentrations by cruise measurements over North Atlantic (obs.: 1.9±0.16 ng/m^3; mod.: 1.2±0.02 ng/m^3) and Pacific Oceans (obs.: 2.5±0.4 ng/m^3; mod.: 1.2±0.07 ng/m^3). The modeled total Hg concentrations at the surface ocean (0.67 pM) are also ~33% lower than observations (~1.0 pM). We also compare our model result to historical archives of changing atmospheric deposition in lake and marine sediments, peat bogs, and ice cores. The model generally captures the increasing trend of Hg accumulation recorded in these different media since 1800. Larger discrepancies take place in the period between 1850 and 1900, when mining emissions dominated. By reducing the Hg emissions from mining activities by a factor of 3, the comparison improves at most of the sites. We thus use the results with this adjusted emission inventory in our analysis. The averaged (±1σ) observed and modeled ER in the samples summarized in this chapter are 3.5±2.0 and 3.4±3.1, respectively.

In the surface ocean, the enrichments of Hg concentrations by human perturbation for different species are quite uniform (by a factor of ~4). However, the enrichment factors for Hg^{II}_{aq} and Hg^{P}_{aq} (~3) are larger than that for Hg^{0}_{aq} (1.8) in the intermediate ocean. Similar condition happens in the deep ocean: 1.3 for Hg^{II}_{aq} and Hg^{P}_{aq} but only 1.1 for Hg^{0}_{aq}. The absorption flux of Hg^{II}_{aq} on to POC in the mixed layer (i.e. $Hg^{II}_{aq} \rightarrow Hg^{P}_{aq}$) is enriched by a factor of 4.2, proportional to the Hg^{II}_{aq} concentrations in the mixed layer. However, the Hg^{P}_{aq} releasing flux back to dissolved phase caused by remineralization of POC (i.e. $Hg^{P}_{aq} \rightarrow Hg^{II}_{aq}$) in the intermediate and deep ocean have higher enrichment factors (6.5 and 3.7, respectively) than the concentration of Hg^{P}_{aq} itself. This is caused by the non-uniformly perturbations in the ocean at different depths, which facilitates the transport of anthropogenic Hg from the surface ocean to the subsurface ocean by sinking POC.

The modeled oceanic profiles of aqueous Hg in our present-day simulation display a maximum at intermediate depth (900-1,000 m), as a result of the penetration of anthropogenic Hg which peaks at 400-500 m (~0.7 pM). The anthropogenic influence below 3000 m is quite low (< 0.2 pM). The absolute change of Hg concentration over the ocean surface is also lower (~0.4 pM). Overall, the model (1.1±0.3 pM) reproduces the observed (1.4±0.9 pM) marine Hg concentrations over at depths greater than 2000 m. One area of discrepancy is in the North Atlantic, where the model is factor of two lower than observations. In the mid-latitude North Atlantic Ocean, the observed total Hg concentration profile shows a surface-enhanced pattern: general decreasing trend for total Hg is observed in the topmost ~1500 m, then keeps nearly unchanged below this depth. Our model captures this pattern very well. The anthropogenic signal

(> 1 pM) is even stronger over the Equatorial Atlantic at a depth of 300-400 m, as suggested by both the model and observations. Over South Atlantic, the observed total Hg concentrations peak at ~1000 m (~2.5 pM). Over the North Pacific Ocean, the model captures some profiles, while overestimating others by a factor of 2. The reason for the differences among observed profiles and between observations and model are unclear. The model reproduces the total Hg concentrations observed in the surface and intermediate waters over the Equatorial Pacific Ocean, and in particular the model captures the observed subsurface peak in Hg concentrations (at ~500-800 m). Our simulation indicates that this subsurface peak is due to the accumulated anthropogenic Hg perturbation. Both the modeled and observed Hg concentration profile at Southern Ocean shows "transient-type" distribution, with nearly constant concentration level with depth. These have indicated to be caused by accumulated anthropogenic Hg perturbation when compared with the model results for natural conditions.

The oceanic total Hg column concentrations are the highest (> 2 μmol/m^2) over the east tropical Pacific Ocean, and the east tropical Atlantic Ocean. These high concentration regions also extend poleward to mid-to-high latitudes along west coast of continents. The column concentrations are also high over the tropical Indian (~2 μmol/m^2), high-latitude Pacific (1.5-2.2 μmol/m^2), and high-latitude Atlantic (1.6-1.9 μmol/m^2) Oceans. The mid-latitude ocean has medium level of column concentration of 1-1.3 μmol/m^2. The column concentrations are the lowest over Arctic, with values less than 0.6 μmol/m^2. This spatial pattern is controlled by the supply of anthropogenic Hg via sinking particulate organic carbon (POC). The vertical distribution of anthropogenic Hg varies at different regions, depending on the ocean circulation and the strength of POC sinking fluxes. The high anthropogenic Hg concentrations over high-latitude N. Pacific extend to a depth range of 200-1000 m. Similar high anthropogenic Hg concentrations are also identifiable in the tropical regions of Atlantic cross section, with slightly shallower depth (200-800 m). At mid-latitudes, where the convergence zones at the centers of gyres are located, the intrusion of low concentration waters at surface to a depth of 200-400 m.

Chapter 6

Uncertainties in Hg biogeochemical cycling

In this Chapter, I discuss some of the significant uncertainties in our understanding of the biogeochemical cycling of Hg. I address separately uncertainties associated to Hg emissions to the atmosphere (Section 6.1), Hg redox chemistry in the atmosphere (Section 6.2), atmospheric dry and wet deposition of Hg (Section 6.3), speciated Hg measurements in the atmosphere (Section 6.4), Hg biogeochemistry in the ocean (Section 6.5), low resolution of the oceanic transport model (Section 6.6), Hg measurements in the ocean (Section 6.7), and Hg measurements in lake sediments (Section 6.8).

6.1 Hg emissions to the atmosphere

6.1.1 Direct anthropogenic emissions

Direct anthropogenic emissions of Hg remain uncertain. In this thesis, we used the GEIA (2005) inventory. According to the UNEP review (2008), the global total anthropogenic Hg emissions range from 1220 Mg/a to 2900 Mg/a with a best estimate of 1930 Mg/a. This uncertainty range is equivalent to 63%-150% of the best estimate. This uncertainty is mainly due to fossil fuel combustion for power and heating (595-1160 Mg/a), artisanal and small-scale gold production (225-475 Mg/a), metal production (excluding gold) (125-275 Mg/a), and cement production (115-265 Mg/a). Although waste incineration (125 Mg/a) is a minor source, accounting for 6.5% of global emissions, it has a large uncertainty with values ranging from 50 to 475 Mg/a, because of the large variability of emission factors (Pacyna et al., 2010).

A more recent analysis of anthropogenic Hg emissions for the year 2005 was presented in UNEP (2013). In this report, Hg emissions from artisanal and small-scale gold mining has increased from 350 Mg/a in GEIA 2005 inventory to 710 Mg/a in this updated inventory, partially because of the inclusion of contribution from China, which was missing from the GEIA 2005 inventory. Furthermore, Hg emissions from coal consumption for domestic and residential use in 2005 has been estimated to be approximately 70 Mg/a, much lower than the previous estimate of 450 Mg/a (UNEP 2008) due to better information on coal consumption in this sector. Although global anthropogenic Hg emissions have not changed significantly in this new report (1910 Mg), individual source contributions have changed: artisanal and small-scale gold production (37% in UNEP 2013 vs 18% in GEIA 2005), fossil fuel burning (24% in UNEP 2013 vs 46% in GEIA 2005).

6.1.2 Ocean reemission

Observational Hg ocean evasion fluxes have large variability. For example, the average evasion flux is 1.9±1.3 nmol/m^2/day over the North Atlantic Ocean (Mason et al., 1998), 0.14-0.94 nmol/m^2/day over Mediterranean (Mason 2009). The global estimates of Hg evasion flux from ocean are extrapolated from a limited number of measurements in different ocean basins to the global scale (Mason and Sheu, 2002; Selin et al., 2008; Strode et al., 2007; Sunderland and Mason, 2007; Soerensen et al., 2010; Streets et al., 2011; Amos et al., 2013), therefore these estimates are subject to large uncertainties. Mason (2009) estimated the 90% confidence interval of global Hg evasion flux from ocean as 782-5282 Mg/a, with the best value of 2682 Mg/a. In this thesis, we have developed our model based on the parameterization for air-sea exchange and surface ocean chemistry of Hg by Soerensen et al. (2010), which has been tuned to match the above-mentioned global estimate of Hg^0 evasion flux and results in a global flux of 2950 Mg/a. Thus the calculated evasion flux by our model should have similar uncertainties with theirs.

6.1.3 Land reemission

In this section, land reemissions include the evasion of Hg from top soils and terrestrial ecosystem, volcanoes/geothermal and biomass burning. The Hg evasion flux varies among different types of ecosystems with a global total Hg evasion flux of 1650 (863-3806) Mg/a (Mason, 2009). Volcanic emissions of Hg are estimated to be 90 Mg/a, with large uncertainties (60-600 Mg/a), probably because of the difficulty to get accurate emission measurements under the extreme conditions (Mason, 2009). Our simulation under natural conditions is quite sensitive to the magnitude of this emissions source because the geogenic source is the sole direct emission source to the atmosphere, which decides the Hg burden in different environmental reservoirs under natural conditions, including the ocean. Global Hg emission from biomass burning is estimated to be 675±240 Mg/a during 1997-2006 with significant interannual variability (Friedli et al. 2009). The emissions are mainly contributed by tropical and boreal Asia (355 Mg/a), followed by Africa (141 Mg/a) and South America (108 Mg/a). Other estimates show similar ranges of emissions with 930 (510-1140) Mg/a and 590 (380-1330) Mg/a using Hg/CO and Hg/CO_2 ratios, respectively (Brunke et al., 2001).

6.2 Hg chemistry in the atmosphere

6.2.1 Hg atmospheric oxidation mechanisms

The predictions of the atmospheric transport and chemistry model used in this thesis are largely limited by the accuracy of our current understanding of the Hg chemistry underlying this model. Field observations of atmospheric mercury depletion events (AMDE) in polar regions and the Dead Sea (e.g. Lindberg et al. 2002; Peleg et al., 2007) and elevated levels of RGM in the upper troposphere (e.g. Landis et al., 2005; Swartzendruber et al., 2006) have suggested relatively rapid transformation of Hg^0 to RGM facilitated by gas phase chemistry. Although these AMDEs have been connected with halogen chemistry, the oxidation in the upper troposphere carries not enough chemical signatures to suggest specified oxidants from possible oxidants including OH, ozone and Br atoms (Hynes et al., 2009).

Ab-initio calculations have demonstrated that oxidation by O_3 and OH is likely to be too slow under atmospheric conditions because of the rapid thermal dissociation of intermediates HgOH and HgO (Goodsite et al., 2004; Calvert and Lindberg 2005; Hynes et al., 2009 and references therein). Concentrations of Cl atom are much lower than Br atoms in the atmosphere, which makes reaction of Hg^0 with Cl atoms likely unimportant oxidants in global scale, except in the marine boundary layer (Hynes et al., 2009). The reactions of Hg^0 with BrO and NO_3 are sufficiently endoergic and therefore can be dismissed (Raofie and Ariya, 2004; Sommar et al., 1997; Hynes et al., 2009). Laboratory measured and ab-initio calculated coefficients for the reaction between Hg^0 and Br atom (Ariya et al., 2002; Spicer et al., 2002; Donohoue et al., 2006; Khalizov et al., 2003; Goodsite et al., 2004; Shepler et al., 2007), as well as modeling studies (Holmes et al., 2006) have indicated that this reaction is a major, and possibly dominant, global sink for Hg^0. However, large uncertainties still exist for this hypothesis, including the concentration of Br atom in the middle and upper troposphere due to the paucity of observations, as well as the fate of the intermediate product HgBr because of the lack of kinetic data. Overall, Hynes et al. (2009) have suggested a range between 3×10^{-13} and 1×10^{-12} molecule cm^{-3} s^{-1} for the Hg^0 + Br reaction rate, corresponding to a factor of ~3 difference between the maximum and minimum rates.

6.2.2 Br atom concentrations

In this thesis, we have used the result of *p*-TOMCAT model for the Br atom concentrations in the troposphere following Holmes et al. (2010). This model incorporates a detailed bromine chemistry scheme that contains both gas phase reactions and heterogeneous reaction on aerosols and cloud droplets. Bromine emissions, including bromocarbon photo-oxidation and from sea-salt bromine, are considered (Yang et al., 2005). The model results have been evaluated against balloon profiles of BrO at Kiruna (68°N, 21°E; Fizenberger et al., 2000). The model results still have large discrepancy with observations especially over the middle and upper troposphere: a factor of 2-3 lower during summer at 4-6 km, and strong overestimation during winter just below the tropopause. When comparing with GOME-2 tropospheric BrO column concentrations, the model results have a 30-40% underestimation depending on the latitudes (Parrella et al., 2012).

6.2.3 Reduction in cloud droplets

A series of reduction reactions for Hg^{II} in aqueous phase have been studied, including the reaction with SO_3^{2-} and HO_2 (Munthe et al. 1991; Pehkonen and Lin, 1998). However, these reactions have been demonstrated to be too slow to be important in the atmospheric aqueous phase (van Loon et al., 2000; Pehkonen and Lin, 1998; Hynes et al., 2009). Although most models have included aqueous reduction of Hg^{II} to Hg^0 in cloud droplets (e.g., Lin and Tao 2003; Selin et al., 2007), there is no direct field evidence for the occurrence of this reaction. The rate of this reaction serves as a tunable parameter in the model used in this thesis, and it could also be removed if a lower oxidation rate and/or lower Br atom concentrations are assumed (Seigneur et al., 2006; Holmes et al., 2010). Thus, direct measurements of Hg^{II} concentrations in cloud droplets would be needed to confirm the occurrence or lack of occurrence of this reduction reaction.

6.2.4 Reduction in pollution plumes

As discussed in Chapter 2 of this thesis, observations downwind of power plants have been used to assess the reduction rate of Hg^{II} to Hg^0 (Edgerton et al., 2006; Lohman et al., 2006). In these studies, measurements of speciated Hg concentrations in the plumes are compared against the speciated concentrations at the stack predicted by emission models such as the EPRI-ICR model (Electricity Power Research Institute – Information Collection Request; EPRI, 2000). The EPRI-ICR model uses total Hg content in coal, chloride, heat content and other characteristics to predict the total and speciated Hg emissions (Edgerton et al., 2006). This model was developed based on the coal analysis data and stack test data using the Ontario Hydro method, which has significant uncertainty because of its complexity and the dependence of the results on the skill of the operators (Sun et al., 2003). Total Hg emission estimates for individual coal-fired power plant have an uncertainty of 20-40%, with much larger uncertainty for Hg speciation (EPRI, 2000).

6.3 Deposition of Hg

The GEOS-Chem model includes dry deposition of Hg^0, Hg^{II} and Hg^P following the resistance-in-series scheme developed by Wesely (1989), Hg^0 air-sea gas exchange following Nightingale et al. (2000), Hg^{II} loss to sea salt following Holmes et al. (2010), as well as the wet deposition of Hg^{II} and Hg^P following the scheme of Liu et al. (2001), with update by Wang et al. (2011) and Amos et al. (2012).

Sensitivity simulations modifying the deposition velocity has shown that this plays a non-negligible role in determining the atmospheric lifetime of Hg^0 as well as its concentrations (Seigneur et al., 2006). The dry deposition velocity of Hg^0 over land ranges from 0.01 cm/s to 0.1 cm/s, depending on the surface type and roughness height, as summarized by Zhang et al. (2009)

and references therein (e.g. Lindberg and Stratton, 1998; Xu et al., 1999; Poissant et al., 2004; Lindberg et al., 2004). Two approaches have been employed to measure this flux: dynamic field chambers and micrometeorological measurements. The former method suffers from interferences of chamber, while the latter requires uniform surface with a homogeneous mass as well as simultaneous measurements of many meteorological variables (Gustin and Jaffe, 2010). Similar to the measurement of Hg^0 reemission flux from vegetation/soils, the dry deposition fluxes are derived from short-term or small-scale experiments. Large uncertainties are introduced in the process of extrapolating these measurements to an annual flux and scaled them on to global scale (Mason, 2009).

There is no standard method to measure Hg dry deposition. So far, a surrogate surface approach has been used in several studies (Lyman et al., 2009 and references therein). This method may not adequately represent the variability and heterogeneity of natural surfaces, since is employs a uniform surface. Second, this method has only been applied in a very limited number of sites, which makes it ever harder to use these measurements to constrain any global and regional models including ours. Indeed, a better understanding of this flux is essential to the overall lifetime of Hg in the atmosphere.

The parameterization for the transfer velocity across the air-sea interface can explain 80% of the total variance in the observed data set, with a range of uncertainty on the order of 20-40% (Nightingale et al., 2000). Similar to that over land, the measurement of dry deposition flux (or air-sea exchange) of Hg^0 over water surface by flux chambers is also subject to the disruption of sampling instrument to the local environment. The small number of direct measurements of Hg^0 deposition fluxes over marine systems also severely limits our understanding of this process (Gustin and Jaffe, 2010).

The understanding and measurement of Hg wet deposition fluxes may have the least uncertainties compared with other deposition fluxes. This is largely because of the relatively more straightforward collection of precipitation/snow samples and relatively small analytical bias (Wetherbee, 2011). In addition, the large spatial coverage especially over North America by the Mercury Deposition Network (MDN) and Europe by the Mercury species over Europe (MOE) and relatively high temporal resolution (weekly sampling) contribute to reduce the associated uncertainties. However, one big knowledge gap occurs over the ocean, where the wet deposition flux of Hg has been measured only over few cruises (e.g. Laurier et al., 2003). Based on sensitivity simulations conducted by Holmes et al. (2010), the spatial patterns of modeled Hg wet deposition flux over the ocean in the south hemisphere vary drastically by assuming different oxidants of Hg^0 in the atmosphere (OH/O_3 or Br atom), yet we lack observations to confirm this.

6.4 Speciated Hg measurements in the atmosphere

Although the measurements of Hg^0 or TGM have relatively small uncertainty (10-20% for 2σ), as illustrated by collocated manual collection systems in the field and automated instruments, the uncertainty in RGM measurement is much greater (30-40%) (Aspmo et al., 2005; Lyman et al., 2007). One major source of uncertainty for the RGM measurement is the collection efficiency of the KCl-coated annular denuder, which is currently the primary method used. This method appears to suffer from interferences with atmospheric ozone and/or other oxidants (Gustin and Jaffe, 2010). Sampling artifacts are also associated with PBM collection by the filter method (Gustin and Jaffe, 2010; Lyman et al., 2010).

6.5 Oceanic Hg biogeochemistry

6.5.1 Redox chemistry in surface waters

The redox reaction coefficients in the surface ocean in this study are derived from the measurements of dual isotope addition to Chesapeake Bay seawater by Whalin et al. (2007), as applied by Soerensen et al. (2010). The photo-oxidation, photo-reduction and biotic reduction rate coefficients have been measured simultaneously. Soerensen et al (2010) further derived a linear parameterization scheme based on these measured rates and related variables including shortwave solar radiation and net primary productivity. One big uncertainty associated with this parameterization scheme is the extrapolating of this one-time single-site measurement to a full year on global scale. In addition, non-linearity may also happen in the parameterization process. However, the magnitudes of these uncertainties are difficult to estimate.

Another source of uncertainty for Hg redox chemistry in surface ocean waters is the reducible fraction of the dissolved Hg^{II} pool. This fraction depends on the chemical speciation of Hg^{II} in the seawater, especially the fraction of the stable chloride complexes, which are abundant and more resistant to reduction under high salinity conditions (Whalin et al., 2007). The reducible fraction of dissolved Hg^{II} varies between 40% and 60% of total Hg^{II} (Soerensen et al., 2010 and references therein). We have used a value of 40%, corresponding to the lower end value. This fraction influences the ratio of Hg^0 and Hg^{II} concentrations in the surface ocean. Adopting the high end reducible fraction (i.e. 60%) will cause a ~50% increase in Hg^0 concentrations and a 5% decrease in Hg^{II} concentrations in the surface ocean. The higher Hg^0 concentrations lead to an enhanced Hg^0 ocean evasion flux to the atmosphere, as well as a lower Hg^P particulate sinking flux to the subsurface ocean. Thus using this higher value would lead to reducing the penetration of anthropogenic Hg in the ocean.

6.5.2 Hg partitioning onto oceanic particles

As discussed in Section 5.3.1, we found that particle sinking is the most important penetration pathway for anthropogenic Hg into the ocean. This process is represented with a partitioning coefficient of Hg^{II}_{aq} onto sinking organic particles, K_d. By running sensitivity studies using 1-D column model, Strode et al. (2010) found that the amount of anthropogenic Hg in the ocean is not very sensitive to this parameter, as increasing K_d leads to a decrease in the Hg^{P}_{aq} concentration at surface, which partially cancels the effect of K_d on the Hg^{P}_{aq} sinking flux with particles. They found a doubling of the (K_d) leads to a 40% increase of anthropogenic Hg burden in the ocean, while a factor of 2 decrease in K_d causes a 20% decrease in the anthropogenic Hg burden. The actual K_d value could vary for an order of magnitude (10^5-10^6 L kg^{-1}) based on available observations as summarized in Soerensen et al. (2010a), implying large influences on the amount of the anthropogenic Hg. In our model simulations, we use $K_\mathrm{d} = 2.9\times10^5$ L kg^{-1}. This value was varied iteratively so as to best match the present-day ocean Hg^0 evasion flux and the deep ocean Hg concentrations. An additional constraint for the K_d value comes from the Hg sedimentation flux under natural conditions, which has to be balanced by geogenic Hg sources (Mason and Sheu 2002). We found that for ±50% variations in K_d lead to a ±10-20% variation in the amount of anthropogenic Hg in the ocean calculated with our ocean model.

6.5.3 Remineralization depth and its spatial variability

The remineralization depth of sinking organic particles controls the vertical profile of Hg and the penetration depth of anthropogenic Hg. The remineralization depth is represented by the Martin curve (Martin et al., 1987): $F(\mathrm{z})=F(\mathrm{z_c})\times(\mathrm{z}/\mathrm{z_c})^{-b}$, where $F(\mathrm{z})$ is the downward flux of particulate organic carbon at a depth z, $\mathrm{z_c}$ is the base of the euphotic zone, and the exponent b is an empirical parameter with global average value ranging between 0.9 and 1.0 (Kwon et al., 2009).

We chose *b* = 0.9 in this chapter following the OCMIP protocol, which is at the lowest bound of this range. Higher *b* value leads to shorter remineralization depth, and thus a shallower penetration of anthropogenic Hg^{II}_{aq} absorbed by the sinking carbon into deeper part of the ocean. The $F(100\text{ m} \mid b{=}0.9)$ value is 3% higher than $F(100\text{ m} \mid b{=}1.0)$ value, and the difference increases to 30% at 1000 m. This suggests that by assigning a value of 1.0 to the exponent *b* will result in a 30% decrease for the amount of anthropogenic Hg below 1000 m. This is equivalent to a decrease of ~80 Mmol or by 16% for anthropogenic Hg in the global ocean.

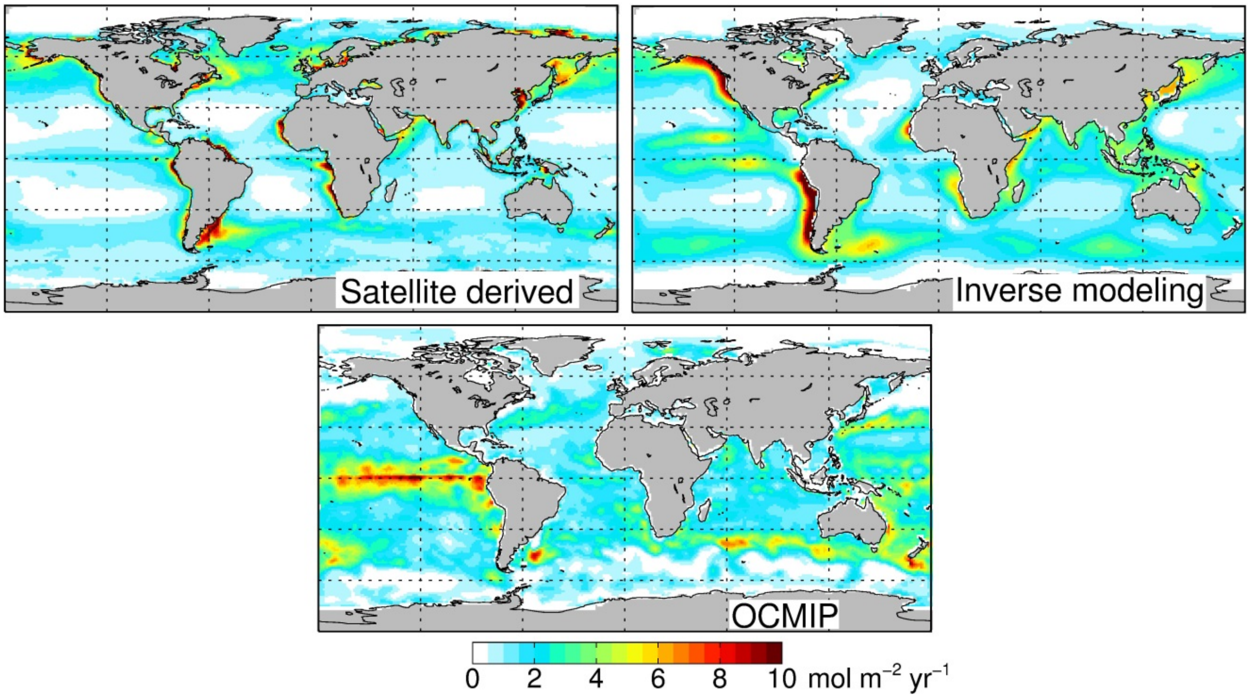

Figure 6.1: Annual mean sinking particulate organic carbon fluxes (mol m^{-2} yr^{-1}) out of the euphotic zone of global ocean derived from satellite derived approach, inverse modeling approach and Ocean Carbon Model Intercomparison Protocal (OCMIP).

6.5.4 Reduction of Hg in subsurface waters

The reduction of Hg^{II}_{aq} to Hg^{0}_{aq} in the intermediate waters involves complex methylation and demethylation process. A higher reduction rate could increase the fraction of Hg^{0}_{aq} in the water column, which escapes from the ocean through air-sea exchange. This would decrease the penetration of anthropogenic Hg. However, the uncertainties associated with these processes are expected to be very large and hard to evaluate because of the scarcity of field observations of these reaction coefficients. In this chapter, we have assumed a reaction pathway of Hg^{II}_{aq} → MeHg → Hg^{0}_{aq} with an overall first order reduction coefficient proportional to the organic carbon remineralization rate (OCRR) (Sunderland et al., 2009; Lehnherr et al., 2011; see more detail in Chapter 4). We have chosen the scaling factor for this first order coefficient so as to reproduce the observed fraction of Hg^{0}_{aq} over total Hg concentrations in the subsurface waters, and the modeled Hg^{0}_{aq} fraction generally agrees with very limited observations within a factor of 2 (Chapter 4).

6.5.5 Spatial variability of sinking particulate organic carbon fluxes

The global total sinking flux of organic carbon out of the euphotic zone is estimated to be approximately 10 GtC/yr (Emerson and Hedges, 2008), but large uncertainties remain in terms of the spatial distribution of this flux. Figure 6.1 shows the spatial pattern of annual mean sinking particulate organic carbon fluxes out of the euphotic zone of global ocean derived from various approaches, including a satellite derived approach based on satellite retrieved Net Primary Productivity and regressed particulate organic carbon export ratio following Dunne et al. (2005), an inverse modeling approach by Schlitzer (2002), and the OCMIP approach based on phosphorous surplus compared with observed concentrations (Najjar and Orr 1999). The satellite approach predicts that a high sinking POC flux at higher latitudes in the North Pacific and North Atlantic Oceans, as well as along the west coasts of continents. It also displays intermediate values in the tropical and mid-to-high latitudes of the South Atlantic, South Pacific and Indian Oceans. Compared to the satellite approach, the inverse modeling approach predicts a stronger sinking flux along the west coasts of North and South America as well as in the tropical Pacific Ocean (excluding the equatorial regions). The OCMIP approach predicts the highest sinking flux over the equatorial Pacific Ocean and close to zero fluxes over the high latitude North Pacific Ocean.

In this study, we have adopted the result of the satellite derived approach because of its relatively stronger constraints by direct observations of particulate organic carbon sinking fluxes incorporated in the empirical and mechanistic models developed by Dunne et al. (2005). As discussed in Chapters 4 and 5, sinking with particle organic carbon is the major pathway for the penetration of anthropogenic Hg to the subsurface and deep oceans. This conclusion also holds if we run our OFFTRAC-HG model with sinking POC fluxes from the other two approaches. However, the spatial distribution of the anthropogenic Hg in the ocean is very sensitive to the spatial pattern of sinking particulate organic carbon (POC) fluxes. Indeed, more observations of the POC sinking fluxes are needed to better constrain the spatial pattern of this variable.

6.6 Low resolution oceanic transport model

The relatively low resolution of the OFFTRAC-HG model (1°×1° for most the regions except the equatorial ocean (1/3° latitude ×1° longitude) and the Arctic Ocean (resolution varies but generally lower than 1°×1°) makes it difficult to capture mesoscale eddies and ocean flow and mixing near the coastal/shelf regions. These small-scale features would only be captured at a much higher spatial resolution (e.g. on the order of 0.1°×0.1°). This low resolution means that the model is not able to capture variability in observations that are obtained in eddies or near coastal regions.

6.7 Ocean Hg measurements

The "ultraclean" sample preparation, collection and handling techniques were developed in the 1970s (Patterson and Settle, 1976). Since then, the measurements of total Hg and speciated Hg concentrations in the ocean water have been accurate with a relative percent difference between analytical duplicates of approximately 10% (Cossa et al. 2011; Sunderland et al., 2009; Hammerschmidt and Bowman 2012; Laurier et al., 2004). However, Hg measurements in ocean waters remain very sparse, especially in terms of the vertical profile of Hg concentrations. There are also some concerns about the validity and accuracy for the early measurements (Mason et al., 2012).

6.8 Lake Sediment Hg

In this study, we have used the Hg accumulation rate in lake sediments as a proxy to evaluate historical Hg deposition fluxes. There are several underlying assumptions:

i) The Hg mass in the lake is at steady state or quasi-steady state. Atmospheric dry and wet deposition is the major source of Hg for the studied lakes, i.e. the amount of Hg that comes from erosion of catchment soils is much smaller and negligible compared to the atmospheric deposition fluxes. Sedimentation is the major sink of Hg in lake waters, i.e. the fraction of deposited Hg that is released back to the atmosphere is negligible or remains constant. Therefore, the sedimentation flux reflects the level of atmospheric Hg input.

ii) The Hg content is conserved in the lake sediment for centuries to thousand years. This assumes that post-deposition and diagenetic processes do not disturb the Hg content in sediments.

iii) When using Hg concentrations instead of Hg accumulation rates, a further assumption is that the accumulation rate of sediment is constant with time.

Although the first assumption holds for most of the studied lakes adopted in this study, there are still some outliers. For example, Landers et al. (1995) found very high present-day deposition rates (20-40 $\mu g/m^2/yr$) over 5 lakes over Alaska, which could be indicative of a large input from local soil catchments instead of atmospheric deposition. Indeed, Landers et al. (1995) also point out that the watershed of one (Feniak Lake) contains serpentine, which is a mineral rich in metals. Fitzgerald et al. (1998) has argued that the second assumption can be tested by looking at the historical distribution of other metals such as Fe, Mn, Cu, Zn, Pb and Cd. Furthermore, lake sediment profiles with simultaneous Hg accumulation rates and Hg concentrations measurements (e.g. Fitzgerald et al., 2005) have shown that Hg concentrations and Hg accumulation rates are not always correlated, and the enrichment of Hg concentrations are generally smaller than Hg accumulation rate. That means the third assumption may be problematic, and large uncertainties are associated with the Hg concentration profile in lake sediments.

Overall, we find large site-by-site variability (up to a factor of 2) when we compare lake sediment cores obtained within ~200 km, reflecting the cumulative impact of uncertainties.

Chapter 7

SUMMARY AND RECOMMENDATIONS FOR FUTURE WORK

In this dissertation, I have developed two new mercury models: a nested-grid high resolution chemical transport model and 3D offline ocean tracer model. I have evaluated these models against observations and used these new tools to investigate: (1) the regional transport and wet deposition of Hg over North America, and (2) the global ocean Hg cycle and its perturbation by anthropogenic emissions.

Summary of Results

I have developed a new high-resolution (1/2° latitude×2/3° longitude) nested-grid Hg simulation over North America embedded within the global low resolution (4° latitude×5° longitude) GEOS-Chem simulation. Compared to the global model, the nested GEOS-Chem model shows improved skill at capturing the high spatial and temporal variability of Hg wet deposition over North America observed by the Mercury Deposition Network (MDN) in 2008 – 2009. The nested simulation resolves features such as higher deposition due to orographic precipitation, land/ocean contrast and predicts more efficient convective rain scavenging of Hg over the southeast United States. Although the inclusion of in-plume reduction (IPR) process in emissions from power plants and waste incinerators slightly increase the low bias of model, it leads to a decrease in the model bias from +27% to -2.3% over the Ohio River Valley region and improves the agreement with observations in terms of spatial patterns. The nested simulation generally reproduces the seasonal cycle in surface concentrations of speciated Hg from the Atmospheric Mercury Network (AMNet) and Canadian Atmospheric Mercury Network (CAMNet). The nested model shows improved skill at capturing the horizontal variability of Hg observed over California during the ARCTAS aircraft campaign. The nested model suggests that North American anthropogenic emissions account for 10-22% of Hg wet deposition flux over the U.S., depending on whether including the in-plume reduction process or not.

I use the nested model to investigate whether domestic emission reductions in Hg emissions have led to changes in MDN observations of Hg wet deposition over the United States for 2004-2010. I find significant decreasing trends in Hg wet deposition in the Northeast U.S (-4.3±2.2% yr^{-1}) and in the Midwest (-2.5±1.6% yr^{-1}), but weaker trends over the Southeast (-0.63±2.5% yr^{-1}) and West (+0.33±7.7% yr^{-1}). By running sensitivity simulations with the nested-grid GEOS-Chem model, I find that the combination of domestic emission reductions and decreasing background concentrations explains the observed trends over Northeast and Midwest, with domestic emission reductions accounting for 51-33% of the observed trend. Over the Southeast, domestic emission reductions can explain all of the observed decreasing trend; however, when I include the added effect of background Hg concentration declines the modeled trend overestimates observations by a factor of four. This could indicate potential issues with the assumption of uniformly decreasing background Hg concentrations and suggests a latitudinal dependence in background concentration changes.

I have developed the first global 3-D oceanic transport and chemistry model for Hg within the OFFTRAC model framework (OFFTRAC-Hg). I first conducted a simulation of the natural marine Hg cycle without any anthropogenic perturbations (prior to ~1450). Marine Hg concentrations in the deep ocean calculated with the OFFTRAC-Hg model are in reasonable agreement with observations (Obs: 1.4±0.9 pM; Mod: 1.1±0.3 pM). The model results for the natural simulation show that the total Hg mass in the global ocean is 1,200 Mmol, with about 3

Mmol, 150 Mmol and 1,000 Mmol in the surface, intermediate and deep ocean, respectively. The corresponding global mean concentrations of total Hg are 0.17 pM, 0.50 pM and 1.0 pM, respectively. Hg^{0}_{aq} accounts 10% in the surface ocean, but accounts 44% and 38% in the intermediate and deep ocean, respectively. Hg^{P}_{aq} accounts 8% in the surface ocean, but is negligible in the intermediate and deep ocean. High Hg concentrations in the mixed layer are modeled in the Southern Ocean, coastal regions, closed and shallow water bodies, and western Equatorial Pacific Ocean. The modeled Hg^{II}_{aq} concentration in the deep North Pacific is approximately twice of that of the deep North Atlantic because of the accumulated source from particles removing Hg from the surface waters, then sinking in the subsurface ocean where they remineralize and release Hg. The fraction of Hg^{0}_{aq} increases with the age of water mass because of the continuous production via reduction from Hg^{II}_{aq}: the average fraction in the deep waters are 34%, 34%, 35%, 39%, and 42% in the N. Atlantic, S. Atlantic, Southern Ocean, S. Pacific and N. Pacific, respectively.

I then conducted a time-dependent coupled GEOS-Chem and OFFTRAC model simulation from 1450 to 2008, with historic anthropogenic emissions of Hg. The model generally captures the increasing trend of Hg accumulation recorded in the lake sediment cores since ~1800. The model reproduces modern in situ observations of atmospheric Hg and of surface ocean Hg concentrations, with a -30-40% negative bias. The present-day model simulation displays a peak in marine Hg concentrations at intermediate depth (50-1,000 m), reflecting anthropogenic Hg. Indeed, I find that sinking of particles at the bottom of mixed layer and release back to subsurface ocean waters is the dominant pathway for the penetration anthropogenic Hg, accounting for 94% of the transport of anthropogenic Hg. The remaining Hg is transported in sinking waters. Below 3000 m, Hg concentrations show smaller anthropogenic influence (0.1-0.2 pM). The model generally captures the ocean Hg profiles observed in North and Equatorial Atlantic, Equatorial Pacific and Southern Ocean, with some discrepancies in Subarctic Atlantic, South Atlantic and North Pacific. By differencing between the present-day and natural simulation I examined the influence of anthropogenic emissions. During 1450-2008, 950 Mmol of anthropogenic Hg was emissions along with 280 Mmol geogenic Hg emissions. I find that 40% of this anthropogenic Hg accumulates in the Ocean, 26% in soils and 1.4% in the atmosphere. The remaining 33% of Hg is loss via sedimentation to deep mineral reservoir. Overall, the total Hg mass in the global ocean has increased from 1150 Mmol at natural time to 1640 Mmol at present-day, an increment of 490 Mmol. Hg concentrations in the ocean's mixed layer have been increased by a factor of 4.2, while in the intermediate and deep ocean they have been enriched by factors of 2.4 and 1.2, respectively.

Recommendations for future work

Large uncertainties are associated with the speciation, chemistry, emissions of Hg as well as the interplay of Hg across different environmental media. In particular, our poor knowledge of atmospheric oxidation (and reduction) mechanisms of Hg, as well as the lack of information on the specific forms of oxidized Hg present in the atmosphere, severely limits our understanding. Speciated Hg measurements, such as those planned for the upcoming Nitrogen, Oxidants, Mercury and Aerosols Distributions, Sources & Sinks (NOMADSS) aircraft campaign, are extremely helpful to answer these questions. One potential usage for the nested Hg model developed in this thesis is to help to make plans for aircraft flight tracks by conducting multi-year hindcast simulations over the United States. The model could also be adapted to use forecast meteorological fields in order to provide Hg predictions for flight planning in the field. The relatively high spatial resolution also makes this model a proper framework for the evaluation of aircraft observations. It can be done by a high-resolution model-observation-comparison along the flight track and/or running sensitivity simulations with different assumption for Hg chemistry schemes.

Another unresolved issue is that despite the increase of global anthropogenic Hg emissions over the last two decades global mercury concentrations have been decreasing in the atmosphere by 20-38% during the last two decades (Temme et al., 2007; Slemr et al., 2011; Soerensen et al., 2012; Cole et al., 2013). There is also some limited evidence that Hg concentrations in the surface and intermediate ocean have been decreasing by a factor of 5-10 over North Atlantic Ocean since 1979 (Mason et al., 2012; Soerensen et al., 2012 and references therein). One hypothesis explaining changes in Hg concentrations is that re-emissions of Hg from soil and/or ocean might be decreasing due to global change (e.g. change in ocean circulation and ventilation, Slemr et al., 2011). Another hypothesis is that the atmospheric oxidation of Hg might be increasing. The third hypothesis involves the historical Hg emission to the ocean margins via riverine input and/or waste water discharge (Streets et al., 2011; Soerensen et al., 2012). The coupled 3D atmosphere-ocean model that I have developed as part of this thesis could be used to test some of these possibilities. Specifically, the enhanced oceanic modeling capability developed in this thesis can be used to fully explore the fate of Hg inputs to ocean margins from wastewater, industry and rivers along with their broader implications for the global Hg cycle. In particular, this model system can be used to test whether the historical inputs of Hg at the ocean margins is sufficient to explain observed changes in subsurface ocean concentrations and associated trends in atmospheric Hg over the last several decades.

Another potential future application of the coupled 3D ocean-atmosphere Hg model is to add the chemistry of methylmercury in the ocean. Methylmercury is important not only because it is the toxic form of Hg which bioaccumulates in the aquatic food change, causing adverse health effect, but also because it is an intermediate controlling the transport and fate of other Hg species in the ocean. As more laboratory and field measurements of the chemistry of methylmercury become available, it will be possible to develop a parameterization for the biological methylation and demethylation processes in the water column. This new 3D ocean simulation of methylmercury could then be used to examine bioaccumulation of Hg in seafood and thus to estimate the human exposure to Hg via seafood consumption.

BIBLIOGRAPHY

AMAP (2011), AMAP Assessment 2011: Mercury in the Arctic. Arctic Monitoring and Assessment Programme (AMAP), Oslo, Norway. xiv + 193 pp.

AMAP/UNEP (2008), Technical Background Report to the Global Atmospheric Mercury Assessment. 159 pp. Arctic Monitoring and Assessment Programme / UNEP Chemicals Branch.

AMNet (2009), NADP's Atmospheric Mercury Network: Moving toward Total Mercury Deposition, National Atmospheric Deposition Program, Illinois State Water Survey, Champaign, IL (http://nadp.sws.uiuc.edu/amn/).

Amos, H. M., et al., (2012), Gas-particle partitioning of atmospheric Hg(II) and its effect on global mercury deposition, Atmospheric Chemistry and Physics, 12, 591-603, 10.5194/acp-12-591-2012.

Amos, H. M., D. J. Jacob, D. G. Streets, and E. M. Sunderland (2013), Legacy of all-time anthropogenic emissions on the global mercury cycle, submitting to Global Biogeochemical Cycles.

Amyot, M., G. A. Gill, and F. M. M. Morel (1997), Production and loss of dissolved gaseous mercury in coastal seawater. Environ. Sci. Technol. 31 (12): 3606–3611.

Amyot M., et al., (2004), Formation and evasion of dissolved gaseous mercury in large enclosures amended with $^{200}HgCl_2$, Atmospheric Environment, 38, 4279-4289.

Andren, M. O. and J. O. Nriagu (1979), The global cycle of mercury, in Biogeochemistry of Mercury in the Environment, edited by J. O. Nriagu, Elsevier, Amsterdam.

Archer, D. et al. (2009), Atmospheric lifetime of fossil fuel carbon dioxide, Annual Review of Earth and Planetary Sciences, 37: 117–134, doi:10.1146/annurev.earth.031208.100206.

Ariya, P. A., A. Khalizov, and A. Gidas (2002), Reactions of gaseous mercury with atomic and molecular halogens: kinetics, product studies, and atmospheric implications, J. Phys. Chem. A. 106: 7310-7320.

Aspmo, K., et al. (2005), Measurements of atmospheric mercury species during an international study of mercury depletion events at Ny-Alesund, Svalbard, spring 2003. How reproducible are our present methods?, Atmos. Environ., 39, 7607-7619.

Axelrad, D. A., D. C. Bellinger, L. M. Ryan, and T. J. Woodrff (2007), Dose–Response Relationship of Prenatal Mercury Exposure and IQ: An Integrative Analysis of Epidemiologic Data, Environ. Health. Perspect., 115, 609-615.

Balabanov, N. B., B. C. Shepler, and K. A. Peterson (2005), Accurate global potential energy surface and reaction dynamics for the ground state of HgBr2, Journal of Physical Chemistry A, 109, 8765-8773.

Bash, J. O. (2010), Description and initial simulation of a dynamic bidirectional air-surface exchange model for mercury in Community Multiscale Air Quality (CMAQ) model, J. Geophy. Res., 115, D0635, doi:10.1029/2009JD012834.

Bergan, T., and H. Rodhe (2001), Oxidation of elemental mercury in the atmosphere; Constraints imposed by global scale modelling, J. Atmos. Chem., 40, 191-212.

Bey, I., et al. (2001), Global modeling of tropospheric chemistry with assimilated meteorology: Model description and evaluation, J. Geophys. Res., 106, 23073-23095.

Biester, H., R. Bindler, A. Martinez-Cortizas and D. R. Engstrom (2007), Modeling the past atmospheric deposition of mercury using natural archives. Environmental science & technology 41(14): 4851-4860.

Brown, E., A. Colling, D. Park, J. Philips, D. Rothery, and J. Wright (2002), Ocean Circulation, edited by G. Bearmann, Butterworth-Heinemann, Oxford.

Brunke, E. G., C. Labuschagne, F. Slemr (2001), Gaseous Hg emissions from a fire in the Cape Peninsula, South Africa, during January 2000. Geophysical Research Letters 28(8): 1483-6.

Bullock, O. R., et al. (2008), The North American Mercury Model Intercomparison Study (NAMMIS): Study description and model-to-model comparisons, J. Geophys. Res., 113, D17310, 10.1029/2008JD009803.

Bullock, O. R., et al. (2009), An analysis of simulated wet deposition of mercury from the North American Mercury Model Intercomparison Study, J. Geophys. Res., 114, D08301,10.1029/2008jd011224.

Butler, T. J., M. D. Cohen, F. M. Vermeylen, G. E. Likens, D. Schmeltz, and R. S. Artz (2008), Regional precipitation mercury trends in the eastern USA, 1998–2005: Declines in the Northeast and Midwest, no trend in the Southeast, Atmospheric Environment, 42, 1582-1592, 10.1016/j.atmosenv.2007.10.084.

Calvert, J. G., and S. E. Lindberg (2005), Mechanisms of mercury removal by O_3 and OH in the atmosphere, Atmos. Environ., 39, 3355-3367.

CAMNet (2011), Canadian Atmospheric Mercury Measurement Network, Environment Canada, http://www.msc.ec.gc.ca/arqp/camnet_e.cfm, accessed 10/24/2011.

Chen, D., Y. Wang, M. B. McElroy, K. He, R. M. Yantosca, and P. Le Sager (2009), Regional CO pollution and export in China simulated by the high-resolution nested-grid GEOS-Chem model, Atmos. Chem. Phys., 9, 3825-3839.

Clarkson, T. W. (2002), The three modern faces of mercury, Environ. Health Perspect., 110, 11-23.

Clarkson, T. W., and L. Magos (2006), The toxicology of mercury and its chemical compounds. Critical Review of Toxicology, 36, 609-662.

Cohen, J. T., D. C. Bellinger, and B. A. Shaywitz (2005), A quantitative analysis of prenatal methyl mercury exposure and cognitive development, Am. J. Prev. Med., 29(4), 353-365.

Cole, A. S., A. Steffen, K. A. Pfaffhuber, T. Berg, M. Pilote, L. Poissant, R. Tordon and H. Hung (2013), Ten-year trends of atmospheric mercury in the high Arctic compared to Canadian sub-Arctic and mid-latitude sites, Atmospheric Chemistry and Physics 13(3): 1535-1545.

Cooke, C. A., P. H. Balcom, H. Biester and A. P. Wolfe (2009). Over three millennia of mercury pollution in the Peruvian Andes. Proc Natl Acad Sci USA 106: 8830-8834.

Cossa, D., J. M. marin, K. Takayanagi, and J. Sanjuan (1997), The distribution and cycling of mercury species in the western Mediterranean. Deap-Sea Research II, 44, 721-740.

Cossa, D., M.-H. Cotte-Krief, R. P. Mason, and J. Bretaudeau-Sanjuan (2004), Total mercury in the water column near the shelf edge of the European continental margin, Marine Chemistry, 90, 21-29.

Cossa, D., et al. (2011), Mercury in the Southern Ocean, Geochimica et Cosmochimica Acta, 75, 4037-4052.

Craig, P. J., U. K. Brinkman, and F. E. Brinkman (1986), Occurrence and pathways of organometallic compounds in the environment-general considerations. In Organometallic Compounds in the EnVironment: Principles and Reactions; Craig, P. J., Ed.; Wiley: New York.

Dai, A., and K. E. Trenberth (2002), Estimates of Freshwater Discharge from Continents: Latitudinal and Seasonal Variations, Journal of Hydrometeorology, 3, 660-687.

Dalziel, J. A. (1992), Reactive mercury on the Scotian Shelf and in the adjacent northwest Atlantic Ocean, Marine Chemistry, 37, 171-178.

Dastoor, A., and Y. Larocque (2004), Global circulation of atmospheric mercury: a modelling study, Atmos. Environ., 38, 147-161.

Deutsch, C., S. Emerson, and L. Thompson (2005), Fingerprints of climate change in North Pacific oxygen Geophys. Res. Let., Vol. 32, No. 16, L16604.

Deutsch, C., S. Emerson, and L. Thompson (2006), Physical-biological interactions in North Pacific oxygen variability, J. Geophys. Res., 111, C09S90, doi:10.1029/2005JC003179.

Deutsch, C., H. Brix, T. Ito, H. Frenzei, and L. Thompson (2011), Climate-forced variability of ocean hypoxia, Science, 333, 336, doi: 10.1126/science.1202422.

Dommergue, A., C. P. Ferrari, M. Amyot, S. Brooks, F. Sprovieri, and A. Steffen (2009), Spatial coverage and temporal trends of atmospheric mercury measurements in polar regions, in: Mercury Fate and Transport in the Global Atmosphere, edited by: Pirrone, N. and R. P. Mason, chap. 10, Springer.

Donohoue, D. L., D. Bauer, B. Cossairt, and A. J. Hynes (2006), Temperature and pressure dependent rate coefficients for the reaction of Hg with Br and the reaction of Br with Br: A pulsed laser photolysis-pulsed laser induced fluorescence study, Journal of Physical Chemistry A, 110, 6623-6632.

Dunne, J. P., R. A. Armstrong, A. Gnanadesikan, and J. L. Sarmiento (2005), Empirical and mechanistic models for the particle export ratio, Global Biogeochem. Cycles, 19, GB4026, doi:10.1029/2004GB002390.

Dvonch, J. T., G. J. Keeler, and F. J. Marsik (2005), The influence of meteorological conditions on the wet deposition of mercury in southern Florida, J. Appl. Meteorol., 44, 1421–1435.

Ebinghaus R., et al. (2009), Spatial coverage and temporal trends of land-based atmospheric mercury measurement in the Northern and Southern Hemispheres, in: Mercury Fate and Transport in the Global Atmosphere, edited by: Pirrone, N. and R. P. Mason, chap. 9, Springer.

Edgerton, E. S., B. E. Hartsell, and J. J. Jansen (2006), Mercury speciation in coal-fired power plant plumes observed at three surface sites in the southeastern US, Environmental Science & Technology, 40, 4563-4570.

Emerson, S. R., and J. I. Hedges (2008), Chemical Oceanography and the Marine Carbon Cycle, 468 pp., Cambridge Univ. Press, Cambridge, U. K, doi:10.1017/CBO9780511793202.

Elbaz-Poulichet, F., L. Dezileau, R. Freydier, D. Cossa and P. Sabatier (2011), A 3500-year record of Hg and Pb contamination in a mediterranean sedimentary archive (the Pierre Blanche Lagoon, France). Environ Sci Technol 45: 8642-8647.

Engle, M. A., et al. (2010), Comparison of atmospheric mercury speciation and deposition at nine sites across central and eastern North America, J. Geophys. Res., 115, 13, D18306, 10.1029/2010jd014064.

Engstrom, D. R. and E. B. Swain (1997). Recent declines in atmospheric mercury deposition in the upper Midwest. Environmental science & technology 31: 960-967.

Environment Canada (2012), National Pollutant Release Inventory, http://www.ec.gc.ca/inrp-npri/, access: Jun. 04, 2012.

EPRI (2000), An assessment of mercury emissions from U.S. coal-fired power plants; EPRI report no. 1000608; Electric Power Research Institute: Palo Alto, CA.

Fain, X., et al. (2009), Polar firn air reveals large-scale impact of anthropogenic mercury emissions during the 1970s. Proc. Nat. Acad. Sci. U.S.A. 106, 16114–16119.

Ferrara, R., et al. (1998), Atmospheric mercury concentrations and fluxes in the Almaden district (Spain) – a model-based analysis. Atmospheric Environment 32, 3897-3904(8).

Fisher, J. A., D. J. Jacob, A. L. Soerensen, H. M. Amos, A. Steffen, and E. M. Sunderland (2012), Riverine source of Arctic Ocean mercury inferred from atmospheric observations. Nature Geosci. 5, doi: 10.1038/ngeo1478.

Fitzenberger, R., H. Bosch, C. Camy-Peyret, M. P. Chipperfield, H. Harder, U. Platt, B.-M. Sinnhuber, T. Wagner, and K. Pfeilsticker (2000), First profile measurements of tropospheric BrO, Geophys. Res. Lett., 27, 2921– 2924.

Fiore, A. M., et al. (2005), Evaluating the contribution of changes in isoprene emissions to surface ozone trends over the eastern United States, J. Geophys. Res., 110, D12303 10.1029/2004JD005485.

Fitzgerald, W. F., D. R. Engstrom, R. P. Mason and E. A. Nater (1998), The case for atmospheric mercury contamination in remote areas. Environmental science & technology 32: 1-7.

Fitzgerald, W. F., D. R. Engstrom, C. H. Lamborg, C. M. Tseng, P. H. Balcom and C. R. Hammerschmidt (2005), Modern and historic atmospheric mercury fluxes in northern Alaska: Global sources and Arctic depletion. Environmental science & technology 39: 557-568.

Fitzgerald, W. F., C. H. Lamborg, and C. R. Hammerschmidt (2007), Marine biogeochemical cycling of mercury, Chem. Rev. 107, 641-662.

Friedli, H. R., A. F. Arellano, Jr., S. Cinnirella, N. Pirrone (2009), Mercury emissions from global biomass burning: spatial and temporal distribution, in: Mercury Fate and Transport in the Global Atmosphere, edited by: Pirrone, N. and R. P. Mason, chap. 8, Springer.

Gordfeldt, K., J. Sommar, D. Stromberg, and X. Feng (2001), Oxidation of atomic mercury by hydroxyl radicals and photoinduced decomposition of methylmercury in the aqueous phase, Atmos. Environ., 35, 3039-3047.

Gebbie, G., and P. Huybers (2012), The Mean Age of Ocean Waters Inferred from Radiocarbon Observations: Sensitivity to Surface Sources and Accounting for Mixing Histories. J. Phys. Oceanogr., 42, 291–305.

Gent, P. R., and J. C. McWilliams (1990), Isopycnal mixing in ocean circulation models, Journal of Physical Oceanography, 20(1), 150-155.

Gildemiester, A. E. (2001), Urban atmospheric mercury, Ph. D., University of Michigan, Ann Arbor.

Gill, G. A., and K. W. Bruland (1987), Mercury in the Northeast Pacific, Eos, Trans. AGU , 68, 1763.

Givelet, N., F. Roos-Barraclough, and W.Shotyk (2003), Predominant anthropogenic sources and rates of atmospheric mercury accumulation in southern Ontario recorded by peat cores from three bogs: Comparison with natural background values (past 8000 years). J. Environ. Monit., 5, 935–949.

Gnanadesikan, A., J. P. Dunne, R. M. Key, K. Matsumoto, J. L. Sarmiento, R. D. Slater, and P. S. Swathi (2004), Oceanic ventilation and biogeochemical cycling: Understanding the physical mechanisms that produce realistic distributions of tracers and productivity, Global Biogeochem. Cycles, 18, GB4010, doi:10.1029/2003GB002097.

Goodsite, M. E., J. M. C. Plane, and H. Skov (2004), A theoretical study of the oxidation of Hg-0 to HgBr2 in the troposphere, Environmental Science & Technology, 38, 1772-1776.

Gratz, L. E., G. J. Keeler, and E. K. Miller (2009), Long-term relationships between mercury wet deposition and meteorology, Atmospheric Environment, 43, 6218-6229, 10.1016/j.atmosenv.2009.08.040.

Graydon, J. A., et al. (2008), Long-term wet and dry deposition of total and methyl mercury in the remote boreal ecoregion of Canada, Environ. Sci. Technol., 42, 8345–8351, doi:10.1021/es801056j.

Gruber, N. (1998), Anthropogenic CO_2 in the Atlantic Ocean, Global Biogeochem. Cycles, 12(1), 165–191, doi:10.1029/97GB03658.

Guentzel, J. L., W. M. Landing, G. A. Gill, and C. D. Pollman (2001), Processes influencing rainfall deposition of mercury in Florida: The FAMS Project (1992–1996), Environ. Sci. Technol., 35, 863–873.

Guevara, S. R., M. Meili, A. Rizzo, R. Daga and M. Arribere (2010). Sediment records of highly variable mercury inputs to mountain lakes in Patagonia during the past millennium. Atmospheric Chemistry and Physics 10: 3443-3453.

Gustin, M. S., G. E. Taylor Jr., and R. A. Maxey (1997), Effect of temperature and air movement on the flux of elemental mercury from substrate to the atmosphere, J. Geophys. Res., 102, 3891– 3898.

Gustin, M. and S. Lindberg (2005), Terrestrial mercury fluxes: is the net exchange up, down or neither? in: Dynamics of mercury pollution on regional and global scales, edited by: Pieeone, N. and K. R. Mahaffey, Springer, New York, pp. 241-259.

Gustin, M., and D. A. Jaffe (2010), Reducing the uncertainty in measurement and understanding of mercury in the atmosphere, Environ. Sci. Technol., 44, 2222-2227.

Hall, B. (1995), The gas phase oxidation of elemental mercury by ozone, Water Air Soil Pollut., 80, 301– 315.

Hallberg, R., and P. Rhines (1996), Buoyancy-driven circulation in an ocean basin with isopycnals intersecting the sloping boundary, J. Phys. Oceanogr., 26, 913–940.

Hammerschmidt, C. R., and W. F. Fitzgerald (2004), Geochemical controls on the production and distribution of methylmercury in near-shore marine sediments, Environ. Sci. Technol., 38, 1487 – 1495, doi:10.1021/es034528q.

Hammerschmidt, C. R. (2005), The biogeochemical cycling of methylmercury in coastal marine sediments, Dissertations Collection for University of Connecticut. Paper AAI3180209. http://digitalcommons.uconn.edu/dissertations/AAI3180209.

Hammerschmidt, C. R. and K. L. Bowman (2012), Vertical methylmercury distribution in the subtropical North pacific Ocean, Marine Chemistry, 132-133, 77-82.

Hansell D. A., C. A. Carlson, D. J. Repeta, and R. Schlitzer (2009), Dissolved organic matter in the ocean: a controversy stimulates new insights, Oceanography, 22, 202-211.

Henderson, G. M. and E. Maier-Reimer (2002). Advection and removal of Pb-210 and stable Pb isotopes in the oceans: A general circulation model study. Geochimica et Cosmochimica Acta 66: 257-272.

Holmes, C. D., D. J. Jacob, and X. Yang (2006), Global lifetime of elemental mercury against oxidation by atomic bromine in the free troposphere, Geophysical Research Letters, 33, L20808, 10.1029/2006gl027176.

Holmes, C. D., D. J. Jacob, R. P. Mason, and D. A. Jaffe (2009), Sources and deposition of reactive gaseous mercury in the marine atmosphere, Atmospheric Environment, 43, 2278-2285, 10.1016/j.atmosenv.2009.01.051.

Holmes, C. D., et al. (2010), Global atmospheric model for mercury including oxidation by bromine atoms, Atmospheric Chemistry and Physics, 10, 12037-12057, 10.5194/acp-10-12037-2010.

Han, Y.-J., et al. (2004), Atmospheric gaseous mercury concentrations in New York State: Relationships with meteorological data and other pollutants, Atmospheric Environment 38, 6432-6446.

Horvat, M., et al., (2003), Total mercury methylmercury and selenium in mercury polluted areas in the province Guizhou, China. Sci. Total Environ., 304, 231–256.

Houyoux, M., and M. Strum (2011), Memorandum: Emissions Overview: Hazardous Air Pollutants in Support of the Final Mercury and Air Toxics Standard.

Hoyer, M., J. Burke, and G. J. Keeler (1995), Atmospheric sources, transport and deposition of mercury in Michigan: two years if event precipitation, Water Air Soil Pollut., 80, 199–208.

Huston, M., and S. Wolverton (2009), The global distribution of net primary production: resolving the paradox, Ecological Monographs, 79, 343-377.

Hynes, A., D. Donohoue, M. Goodsite, I. Hedgecock, N. Pirrone, and R. Mason (2009), Our current understanding of major chemical and physical processes affecting mercury dynamics in the atmosphere and at air-water/terrestrial interfaces, in: Mercury Fate and Transport in the Global Atmosphere, edited by: Pirrone, N. and R. P. Mason, chap. 14, Springer.

Jacob, D.J., et al. (2010), The Arctic Research of the Composition of the Troposphere from Aircraft and Satellites (ARCTAS) mission: design, execution, and first results, Atmos. Chem. Phys., 10, 5191–5212.Jenkins, W. J. (1990), Determination of isopycnal diffusivity in the Sargasso Sea, J. Phys. Oceanogr., 21, 1058– 1061.

JECFA, (2004), Methylmercury. In: Safety evaluation of certain food additives and contaminants. Report of the 61st Joint FAO/WHO Expert Committee on Food Additives. Geneva, World Health Organization, International Programme on Chemical Safety. WHO Technical Report Series 922 pp 132-139. http://whqlibdoc.who.int/trs/WHO_TRS_922.pdf.

Jiang, S., Liu, X., Chen, Q. (2011), Distribution of total mercury and methylmercury in lake sediments in Arctic Ny-Alesund, Chemosphere, 83, 1108-1116.

Joos, F., M. Bruno, R. Fink, U. Siegenthaler, T. F. Stocker, C. Le Quéré, and J. Sarmiento (1996), An efficient and accurate representation of complex oceanic and biospheric models of anthropogenic carbon intake, Tellus, Ser. B, 48(3), 397–417, doi:10.1034/j.1600-0889.1996.t01-2-00006.x.

Parrella, J. P., et al., (2012), Tropospheric bromine chemistry: implications for present and pre-industrial ozone and mercury, Atmos. Chem. Phys. 12, 6723-6740.

Kalnay et al. (1996), The NCEP/NCAR 40-year reanalysis project, Bull. Amer. Meteor. Soc., 77, 437-470,.

Keeler, G. J., M. S. Landis, G. A. Norris, E. M. Christianson, and J. T. Dvonch (2006), Sources of mercury wet deposition in eastern Ohio, USA, Environ. Sci. Technol., 40, 5874-5881.

Kellerhals, M., et al. (2003), Temporal and spatial variability of total gaseous mercury in Canada: results from the Canadian Atmospheric Mercury Measurement Network (CAMNet), Atmos. Environ., 37, 1003-1011.

Khalizov, A. F., B. Viswanathan, P. Larregaray, and P. A. Ariya (2003), A theoretical study on the reactions of Hg with halogens: atmospheric implications, J. Phys. Chem. A., 107, 6360-6365.

Kim, N. S., and B. K. Lee (2010), Blood total mercury and fish consumption in the Korean general population in KNHANES III, 2005, Sci. Total Environ., 408, 4841-4847.

Kwon, E. Y., F. Primeau and J. L. Sarmiento (2009). The impact of remineralization depth on the air-sea carbon balance. nature geoscience 2: 630-635.

Kraus, E. B., and J. S. Turner (1967), A one-dimensional model of the seasonal thermocline II. The general theory and its consequences, Tellus, 19, 98-106.

Lacerda, L. D. (1997), Global mercury emissions from gold and silver mining, Water, Air & Soil Pollut., 97, 209-221.

Ladd, C., and L. Thompson (2001), Water mass formation in an isopycnal model of the North Pacific, J. Phys. Oceanogr., 31, 1517–1537.

Lam, P. J., S. C. Doney, and J. K. B. Bishop (2011), The dynamic ocean biological pump: Insights from a global compilation of particulate organic carbon, CaCO3, and opal concentration profiles from the mesopelagic, Global Biogeochem. Cycles, 25, GB3009, doi:10.1029/2010GB003868.

Lamborg, C. H., W. F. Fitzgerald, A. W. H. Damman, J. M. Benoit, P. H. Balcom, and D. R. Engstrom (2002a), Modern and historic atmospheric mercury fluxes in both hemispheres:

Global and regional mercury cycling implications, Global Biogeochem. Cycles, 16, 1104, doi:10.1029/2001GB001847.

Lamborg, C. H., W. F. Fitzgerald, J. O'Donnel, and T. Torgersen (2002b), A non-steady-state compartmental model of global-scale mercury biogeochemistry with interhemispheric atmospheric gradients, Geochem. Cosmo. Acta, 66, 1105-1118.

Lamborg, C. H., C.-M. Tseng, W. F. Fitzgerald, P. H. Balcom, and C. R. Hammerschidt (2003), Determination of the mercury complexation characteristics of dissolved organic matter in natural waters with ''Reducible Hg'' titrations, Environ. Sci. Technol., 37, 3316–3322.

Landers, D. H., et al. (1998). Using lake sediment mercury flux ratios to evaluate the regional and continental dimensions of mercury deposition in arctic and boreal ecosystems. Atmospheric Environment 32(5): 919-928.

Landers, D. H., J. Ford, C. Gubala, M. Monetti, B. K. Lasorsa, and J. Martinson (1995), Mercury in vegetation and lake sediments from the U.S. Arctic, Water Air & Soil Pollut., 80: 591-601.

Landis, M. S., A. F. Vette, and G. J. Keeler (2002a), Atmospheric mercury in the Lake Michigan Basin: influence of the Chicago/Gary urban area, Environ. Sci. Technol., 36, 4508-4517.

Landis, M. S. and G. J. Keeler (2002b), Atmospheric Mercury Deposition to Lake Michigan during the Lake Michigan Mass Balance Study, Environ. Sci. Technol., 36, 4518–4524.

Landis M. S., et al. (2005), The Monitoring and Modeling of Hg Species in Support of Local, Regional and Global Modeling, in: Dynamics of mercury pollution on regional and global scales: Atmospheric processes and human exposures around the world, edited by: Pirrone, N., and K. R. Mahaffey, Springer Science and Business Media, Inc.

Large, W. G., and S. G. Yeager (2009), The global climatology of an interannually varying air-sea flux data set, Climate Dynamics, 33(2-3), 341-364, doi:10.1007/s00382-008-0441-3.

Laurer, F. J. G., R. P. Mason, L. Whalin, S. Kato (2003), Reactive gaseous mercury formation in the north pacific ocean's marine boundary layer: a potential role of halogen chemistry. Journal of Geophysical Research 108(D17), 4529.

Laurier, F. J. G., R. P. Mason, G. A. Gill and L. Whalin (2004). Mercury distributions in the North Pacific Ocean - 20 years of observations. Marine Chemistry 90: 3-19.

Lehnherr, I., V. L. St. Louis, H. Hintelmann, and J. L. Kirk (2011), Methylation of inorganic mercury in polar marine waters, Nature Geosci., 4, DOI: 10.1038/NGEO1134.

Li, Q. B., et al. (2005), North American pollution outflow and the trapping of convectively lifted pollution by upper-level anticyclone, J. Geophys. Res., 110, D10301 10.1029/2004JD005039.

Lin, C. J., and S. O. Pehkonen (1999), The chemistry of atmospheric mercury: a review, Atmos. Environ., 33, 2067-2079.

Lin, X., and Y. Tao (2003), A numerical modeling study on regional mercury budget for eastern North America, Atmos. Chem. Phys., 3, 535-548.

Lindberg, S. E., and W. J. Stratton (1998), Atmospheric mercury speciation: Concentrations and behavior of reactive gaseous mercury in ambient air, Environ. Sci. Technol., 32, 49–57.

Lindberg, S. E., et al. (2002), Dynamic oxidation of gaseous mercury in the Arctic troposphere at polar sunrise. Environmental Science and Technology 36: 1245-1256.

Lindberg, S. E., D. Porcella, E. Prestbo, H. Friedli, and L. Radke (2004), The problem with mercury: Too many sources, not enough sinks, RMZ Mater. Geoenviron., 51, 1172– 1176.

Lindberg, S., et al. (2007). A synthesis of progress and uncertainties in attributing the sources of mercury in deposition. Ambio 36: 19-32.

Liu, H., D. Jacob, I. Bey, and R. M. Yantosca (2001), Constraints from Pb210 and Be7 on wet deposition and transport in a global three-dimensional chemical tracer model driven by assimilated meteorological fields, J. Geophys. Res., 106, 12109-12128.

Loewen, M., S. Kang, D. Armstrong, Q. Zhang, G., Tomy, F. Wang, (2007), Atmospheric transport of mercury to the Tibetan Plateau. Environ. Sci. Technol., 41, 7632–7638.

Lohman, K., C. Seigneur, E. Edgerton, and J. Jansen (2006), Modeling mercury in power plant plumes, Environ. Sci. Technol., 40, 3848-3854.

Lynch, J. A., K. S. Horner, and J. W. Grimm (2003), Atmospheric deposition: spatial and temporal variations in Pennsylvania 2002, Penn State Institutes of the Environment, The Pennsylvania State University, University Park, PA.

Lyman, S. N., M. S. Gustin, E. M. Prestbo, and F. J. Marsik (2007), Estimation of dry deposition of atmospheric mercury in Nevada by direct and indirect methods, Environ. Sci. Technol., 41, 1970-1976.

Lyman, S. N., and M. S. Gustin (2008), Speciation of atmospheric mercury at two sites in northern Nevada, USA, Atmos. Environ., 42, 927–939.

Lyman, S. N., and M. S. Gustin (2009), Determinants of atmospheric mercury concentrations in Reno, Nevada, USA, Sci. Total Environ., 408, 431–438, doi:10.1016/j.scitotenv.2009.09.045.

Lyman, S., M. Gustin, E. Prestbo, P. Kilner, E. Edgerton, B. Hartsell (2009), Testing and application of surrogate surfaces for understanding potential gaseous oxidized mercury dry deposition. Environ. Sci. Technol. 43: 6235–6241.

Lyman, S. N., D. A. Jaffe, and M. S. Gustin (2010), Release of mercury halides from KCl denuders in the presence of ozone, Atmospheric Chemistry and Physics 10(17): 8197-8204.

Lyman, S. N., and D. Jaffe (2011), Formation and fate of oxidized mercury in the upper troposphere and lower stratosphere, Nature geoscience, doi: 10.1038/ngeo1353.

Lyman, S. N., and G. J. Keeler (2005), Artifacts associated with the measurement of particulate mercury in an urban environment: the influence of elevated ozone concentrations, Atmos. Environ., 39, 3081-3088.

Madsen, P. P. (1981), Peat bog records of atmospheric mercury deposition. Nature, 293, 127–130.

Mao, H., R. W. Talbot, B. C. Sive, S. Youn Kim, D. R. Blake, and A. J. Weinheimer (2011), Arctic mercury depletion and its quantitative link with halogens, J. Atmos. Chem., 65, 145-170.

Martin, J. H., G. A. Knauer, D. M. Karl, and W. W. Broenkow (1987), VERTEX: Carbon cycling in the northeast Pacific. Deep-Sea Res. 34, 267-285.

Mason, R. P. and W. F. Fitzgerald (1990), Alkylmercury species in the equatorial Pacific, Nature, 347, 457-459.

Mason, R. P. and W. F. Fitzgerald (1993), The distribution and biogeochemical cycling of mercury in the equatorial Pacific Ocean, Deep-Sea Research, 40, 1897-1924.

Mason, R. P., W. F. Fitzgerald, and F. M. M. Morel (1994), The biogeochemical cycling of elemental mercury: anthropogenic influences, Geochemica et Cosmochimica Acta, 58, 3191 – 3198.

Mason, R. P., F. M. M. Morel, and H. F. Hemond (1995), The role of microorganisms in elemental mercury formation in natural waters. Water, Air, Soil Pollut. 80: 775–787.

Mason, R., K. Rolfhus, and W. Fitzgerald (1998), Mercury in the North Atlantic, Marine Chemistry, 61, 37-53.

Mason, R. P., and K. A. Sullivan (1999). The distribution and speciation of mercury in the South and equatorial Atlantic. Deep-Sea Research Part II-Topical Studies in Oceanography 46: 937-956.

Mason, R. P., N. M. Lawson, and G. R. Sheu (2001), Mercury in the Atlantic Ocean: factors controlling air-sea exchange of mercury and its distribution in the upper waters. Deep-Sea Research II, 48, 2829-2853.

Mason, R. P., and G. R. Sheu (2002), Role of the ocean in the global mercury cycle, Global Biogeochem. Cycles, 16, 1093, doi:10.1029/2001GB001440.

Mason, R. P., F. J. G. Laurier, L. Whalin, and G. R. Sheu (2003), The role of ocean-atmosphere exchange in the global mercury cycle, Journal De Physique Iv, 107, 835-838.

Mason, R. A. (2009), Mercury emissions from natural processes and their importance in the global mercury cycle, in: Mercury Fate and Transport in the Global Atmosphere, edited by: Pirrone, N. and R. P. Mason, chap. 7, Springer.

Mason, R. P., et al. (2012), Mercury biogeochemical cycling in the ocean and policy implications. Environ Res., 119, 101-117.

McKinley, G. A., M. J. Follows, and J. Marshall (2004), Mechanisms of air-sea CO2 flux variability in the equatorial Pacific and the North Atlantic, Global Biogeochem. Cycles, 18, GB2011, doi:10.1029/2003GB002179.

MDN (2011), National Atmospheric Deposition Program, Mercury Deposition Network Information. http://nadp.sws.uiuc.edu/mdn/ (accessed 10.24.2011).

Mergler, D., et al. (2007), Methylmercury exposure and health effects in humans: A worldwide concern, Ambio, 36, 3–11.

Morel, F. M. M., A. M. L. Kraepiel, and M. Amyot (1998), The Chemical Cycle and Bioaccumulation of Mercury, Annu. Rev. Ecol. Syst., 29, 543-566.

Munthe, J. (1992), The aqueous oxidation of elemental mercury by ozone, Atmos. Environ. 26A: 1461-1468.

NADP's Atmospheric Mercury Network (2009), Moving toward Total Mercury Deposition, National Atmospheric Deposition Program, Illinois State Water Survey : http://nadp.sws.uiuc.edu/amn/.

Najjar, R., and J. C. Orr (1999), Biotic how-to, technical report, 15 pp., Lab. des Sci. du Clim. et de l'Environ./Comm. a`l'Energie Atom., Gif-sur-Yvette, France.

National Atmospheric Deposition Program (2012), Mercury Deposition Network Information: http://nadp.sws.uiuc.edu/mdn/, access: Apr. 18, 2012.

Nazhat, N. B., and K.-D. Asmus (1973), Reduction of mercuric chloride by hydrated electrons and reducing radicals in aqueous solutions. Formation and reactions of HgCl, J. Phys. Chem., 77, 614-620.

Nightingale, P. D., et al. (2000), In situ evaluation of air-sea gas exchange parameterizations using novel conservative and volatile tracers, Global Biogeochem. Cycles, 14, 373– 387.

Nriagu, J. O. (1993), Legacy of mercury pollution. Nature, 363, 589.

Nriagu J., and C. Becker (2003), Volcanic emissions of mercury to the atmosphere: global and regional inventories. Sci. Tot. Env., 304: 3-12.

Outridge, P., R. Macdonald, F. Wang, G. Stern, and A. Dastoor (2008), A mass balance inventory of mercury in the Arctic Ocean. Environ. Chem. 5, 89-111.

Pacyna, E. G., et al. (2010), Global emission of mercury to the atmosphere from anthropogenic sources in 2005 and projections to 2020, Atmospheric Environment, 44, 2487-2499, 10.1016/j.atmosenv.2009.06.009.

Pal, B., and P. A. Ariya (2004a), Gas-phase HO-initiated reactions of elemental mercury: Kinetics and product studies, and atmospheric implications, Environ. Sci. Technol., 38(21), 5555–5566.

Pal, B., and P. A. Ariya (2004b), Studies of ozone initiated reactions of gaseous mercury: Kinetics, product studies, and atmospheric implications, Phys. Chem. Chem. Phys., 6, 572–579.

Pan, L., et al. (2007), Top-down estimate of mercury emissions in China using four-dimensional variational data assimilation, Atmos. Environ., 41, 2804-2819.

Park, R. J., D. J. Jacob, N. Kumar, and R. M. Yantosca (2006), Regional visibility statistics in the United States: Natural and transboundary pollution influences, and implications for the Regional Haze Rule, Atmos. Environ., 40, 5405-5423.

Parrella, J. P., et al. (2012), Tropospheric bromine chemistry: implications for present and pre-industrial ozone and mercury. Atmos. Chem. Phys. 12: 6723-6740.

Pan, L. et al. (2006), Regional distribution and emissions of mercury in east Asia: A modeling analysis of Asian Pacific Regional Aerosol Characterization Experiment (ACE-Asia) observations. Journal of Geophysical Research: Atmospheres 111(D7): D07109.

Patterson, C. C., and D. M. Settle (1976), The reduction of orders of magnitude errors in lead analyses of biological material and natural waters by evaluating and controlling the extent and sources of industrial lead contamination introduced during sample collection, handling and analysis. In Accuracy in Trace Analysis: Sampling, Sample Handling, and Analysis; LaFleur, P. D., Ed.; U.S. National Bureau of Standards Special Publication 422; Washington, DC, 1976.

Pehkonen, S. O., and C. J. Lin (1998), Aquesous photochemistry of mercury with organic acids, Journal of Air and Water Management Association 48: 144-150.

Peleg, M., V. Matveev, E. Tas, and M. Luria (2007), Mercury Depletion Events in the Troposphere in Mid-Latitudes at the Dead Sea, Israel, Environ. Sci. Technol. 41: 7280–7285.

Pirrone, N., and R. Mason (2009), Mercury fate and transport in the global atmosphere: Emissions, measurements and models, DOI:10.1007/978-0-387-93958-2, N. Pirrone and R. Mason (eds), Springer, 636 p.

Pirrone, N., et al. (2010). Global mercury emissions to the atmosphere from anthropogenic and natural sources. Atmospheric Chemistry and Physics 10(13): 5951-5964.

Poissant, L., M. Pilote, X. Xu, H. Zhang, and C. Beauvais (2004), Atmospheric mercury speciation and deposition in the Bay St. Franc¸ois wetlands, J. Geophys. Res., 109, D11301, doi: 10.1029/2003JD004364.

Pongprueksa, P., et al. (2008), Scientific uncertainties in atmospheric mercury models III: Boundary and initial conditions, model grid resolution, and Hg(II) reduction mechanism, Atmospheric Environment, 42, 1828 – 1845.

Prestbo, E. M., and D. A. Gay (2009), Wet deposition of mercury in the US and Canada, 1996-2005: Results and analysis of the NADP mercury deposition network (MDN), Atmospheric Environment, 43, 4223-4233.

Psomopoulos, C. S., A. Bourka, and N. J. Themelis (2009), Waste-to-energy: A review of the status and benefits in USA, Waste Management, 29, 1718-1724.

Pyle, D. M., and T. A. Mather (2003), The importance of volcanic emissions for the global atmospheric mercury cycle. Atmos. Environ. 37: 5115-5124.

Rahmstorf, S. (2002), Ocean circulation and climate during the past 120,000 years. Nature 419, 207–214.

Raufie, F., and P. A. Ariya (2003), Kinetics and products study of the reaction of BrO radicals with gaseous mercury, J. Phys. IV, p. 1119.

Redfield, A.C. (1934), On the proportions of organic derivations in sea water and their relation to the composition of plankton. In James Johnstone Memorial Volume. (ed. Daniel R.J.). University Press of Liverpool, pp. 177–192.

Richter, A., F. Wittrock, A. Ladstatter-Weissenmayer, and J. Burrows (2002), GOME measurements of stratospheric and tropospheric BrO, Adv. Space Res., 29, 1667–1672.

Rio Seagade, S., T. Dias, and E. Ramalhosa (2010), Mercury methylation versus demethylation: main processes involved, in: *Methylmercury: formation, sources and health effects*, edited by: A. P. Clampet, Nova Science Publishers, Inc.

Risch, M. R., et al. (2012), Spatial patterns and temporal trends in mercury concentrations, precipitation depths, and mercury wet deposition in the North American Great Lakes region, 2002-2008, Environ. Pollut., 161, 261-271, 10.1016/j.envpol.2011.05.030.

Rolfhus, K.R., and W.F. Fitzgerald (2001), The evasion and spatial/temporal distribution of mercury species in Long Island Sound, CT-NY, Geochimica et Cosmochimica Acta. 65(3): 407-418.

Rutter, A. P., and J. J. Schauer (2007a), The effect of temperature on the gas-particle partitioning of reactive mercury in atmospheric aerosols, Atmos. Environ., 41, 8647-8657.

Rutter, A. P. and J. J. Schauer (2007b), The impact of aerosol composition on the particle to gas partitioning of reactive mercury. Environmental Science and Technology 41: 3934-3939.

Sabine, C. L., et al. (2004), The oceanic sink for anthropogenic CO2. Science 305: 367-371.

Schaefer, J. K., et al. (2004), Role of the Bacterial Organomercury Lyase (MerB) in Controlling Methylmercury Accumulation in Mercury-Contaminated Natural Waters, Environ. Sci. Technol., 38, 4304-4311.

Schlitzer, R. (2002), Carbon export in the Southern Ocean: Results from inverse modeling and comparison with satellite-based estimates, Deep Sea Res., Part II, 49, 1623–1644.

Schmittner, A., J. C. H. Chiang, and S. R. Hemming (2007), Introduction: The ocean's meridional overturning circulation, Geophysical Monograph Series 173, doi: 10.1029/173GM02.

Schuster, P. F., et al. (2002). Atmospheric mercury deposition during the last 270 years: A glacial ice core record of natural and anthropogenic sources. Environmental science & technology 36: 2303-2310.

Seigneur, C., P. Karamchandani, K. Lohman, K. Vijayaraghavan, and R. L. Shia (2001), Multiscale modeling of the atmospheric fate and transport of mercury, J. Geophys. Res., 106, 27795-27809.

Seigneur, C., K. Vijayaraghavan, K. Lohman, P. Karamchandani, and C. Scott (2004), Global source attribution for mercury deposition in the United States, Environmental Science & Technology, 38, 555-569.

Seigneur, C., K. Vijayaraghavan, and K. Lohman (2006). Atmospheric mercury chemistry: Sensitivity of global model simulations to chemical reactions, Journal of Geophysical Research 111(D22): D22306.

Selin, N. E., et al. (2007), Chemical cycling and deposition of atmospheric mercury: Global constraints from observations, Journal of Geophysical Research, 112, D02308, 10.1029/2006jd007450.

Selin, N. E., and D. J. Jacob (2008), Seasonal and spatial patterns of mercury wet deposition in the United States: Constraints on the contribution from North American anthropogenic sources, Atmospheric Environment, 42, 5193-5204, 10.1016/j.atmosenv.2008.02.069.

Selin, N. E., D. J. Jacob, R. M. Yantosca, S. Strode, L. Jaegle, and E. M. Sunderland (2008), Global 3-D land-oceanatmosphere model for mercury: Present-day versus preindustrial cycles and anthropogenic enrichment factors for deposition, Global Biogeochem. Cycles, 22, GB2011, doi:10.1029/2007GB003040.

Selin, N. E. (2009), Global biogeochemical cycling of mercury: a review, Annu. Rev. Environ. Resourc., 34, 43–63.

Shao, A. E., S. Mecking, L. Thompson, and R. E. Sonnerup (2013), mixed layer saturations of CFC-11, CFC-12, and SF6 in a global isopycnal model, submitted to Journal of Geophysical Research-Oceans.

Shepler, B. C., N. B. Balabanov, and K. A. Peterson (2007), Hg+Br HgHr recombination and collision-induced dissociation dynamics, J. Chem. Phys. 127, 164304.

Sheu, G. R., R. P. Mason, and N. M. Lawson (2002), Speciation and distribution of atmospheric mercury over the northern Chesapeake Bay, ACS Symposium Series 806, pp. 223-242.

Shia, R. L., C. Seigneur, P. Pai, M. Ko, and N. D. Sze (1999), Global simulation of atmospheric mercury concentrations and deposition fluxes, J. Geophys. Res., 104, 23747-23760.

Si, L., and P. A. Ariya (2008), Reduction of oxidized mercury species by dicarboxylic acids (C-2-C-4): Kinetic and product studies, Environ. Sci. Technol., 42, 5150-5155.

Siddall, M., et al. (2005), 231Pa/ 230Th fractionation by ocean transport, biogenic particle flux and particle type, Earth and Planetary Science letters, 237, 135-155.

Siegenthaler, U., and H. Oeschger (1978), Predicting future atmospheric carbon dioxide levels, Science, 199(4327), 388–395, doi:10.1126/science. 199.4327.388.

Sigler, J. M., H. Mao, and R. Talbot (2009), Gaseous elemental and reactive mercury in southern New Hampshire, Atmos. Chem. Phys., 9, 1929–1942, doi:10.5194/acp-9-1929-2009.

Simpson, W. R., et al. (2007), First-year sea-ice contact predicts bromine monoxide (BrO) levels at Barrow, Alaska better than potential frost flower contact, Atmos. Chem. Phys., 7, 621-627.

Sioris, C. E., et al. (2006), Latitudinal and vertical distribution of bromine monoxide in the lower stratosphere from Scanning Imaging Absorption Spectrometer for Atmospheric Chartography limb scattering measurements, J. Geophys. Res., 111, D14301, doi:10.1029/2005JD006479.

Slemr, F., E. G. Brunke, R. Ebinghaus and J. Kuss (2011). Worldwide trend of atmospheric mercury since 1995. Atmospheric Chemistry and Physics 11: 4779-4787.

Smith-Downey, N. V., E. M. Sunderland, and D. J. Jacob (2010), Anthropogenic impacts on global storage and emissions of mercury from terrestrial soils: Insights from a new global model, J. Geophys. Res., 115, doi: 10.1029/2009jg001124.

Soerensen, A. L., et al. (2010a), An Improved Global Model for Air-Sea Exchange of Mercury: High Concentrations over the North Atlantic, Environmental science & technology, 44, 8574-8580, 10.1021/es102032g.

Soerensen, A. L., H. Skov, D. J. Jacob, B. T. Soerensen, and M. S. Johnson (2010b), Global concentrations of gaseous elemental mercury and reactive gaseous mercury in the marine boundatry layer, Environ. Sci. Technol., 44, 7425-7430.

Soerensen, A. L., et al. (2012). Multi-decadal decline of mercury in the North Atlantic atmosphere explained by changing subsurface seawater concentrations. Geophysical Research Letters, 39, L21810, doi: 10.1029/2012GL053736.

Sommar, J., K. Ga°rdfeldt, D. Stro¨mberg, and X. Feng (2001), A kinetic study of the gas-phase reaction between the hydroxyl radical and atomic mercury, Atmos. Environ., 35, 3049–3054.

Spicer, C. W. et al. (2002), Kinetics of gas-phase elemental mercury reaction with halogen species, ozone and nitrate radical under atmospheric conditions: Tallahassee, FL, Florida Department of Environmental Protection.

Sprovieri, F., N. Pirrone, R. P. Mason, and M. Andersson (2009), Spatial coverage and temporal trends of over-water, air-surface exchange, surface and deep sea water mercury measurements, in: Mercury Fate and Transport in the Global Atmosphere, edited by: Pirrone, N. and R. P. Mason, chap. 11, Springer.

Steffen, A., et al. (2008), A synthesis of atmospheric mercury depletion event chemistry in the atmosphere and snow, Atmos. Chem. Phys., 8, 1445-1482.

Steele, M., R. Morley, and W. Ermold (2001), PHC: A global ocean hydrography with a high-quality Arctic Ocean, Journal of Climate, 14(9), 2079-2087.

Stevenson, W. (2002), Emissions from large MWC units at MACT compliance. Memorandum to Docket A-90-45, US EPA, Research Triangle Park, NC.

Stewart, R. H. (2008), Introduction to physical oceanography, Texas A & M University.

Strahan, S. E., B. N. Duncan, and P. Hoor (2007), Observationally derived transport diagnostics for the lowermost stratosphere and their application to the GMI chemistry and transport model, Atmos. Chem. Phys., 7, 2435–2445.

Streets, D. G., Q. Zhang, and Y. Wu (2009), Projections of Global Mercury Emissions in 2050, Environmental Science & Technology, 43, 2983-2988.

Streets, D. G., M. K. Devane, Z. Lu, T. C. Bond, E. M. Sunderland, and D. J. Jacob (2011), All-time releases of mercury to the atmosphere from human activities, Environ. Sci. Technol. 45, 10485-91.

Strode, S., et al. (2007), Air-sea exchange in the global mercury cycle, Glob. Biogeochem. Cycl., 21, doi:10.1029/2006GB002766.

Strode, S. A., et al. (2008), Trans-Pacific transport of mercury, J. Geophys. Res., 113, D15305, doi:10.1029/2007JD009428.

Strode, S., L. Jaegle, and N. E. Selin (2009), Impact of mercury emissions from historical gold and silver mining: global modeling, Atmos. Environ., 43, 2012-2017.

Strode, S., L. Jaeglé, and S. Emerson (2010), Vertical transport of anthropogenic mercury in the ocean, Global Biogeochemical Cycles, 24, GB4014, doi:10.1029/2009GB003728.

Sun, J. Q., K. S. Uhrich, R. L. Schulz (2003), Evaluation of mercury stability in Ontario Hydro method solutions for mercury speciation in flue gas generated from coal-fired stationary sources. Am. Chem. Soc., Div. Fuel Chem. 48: 774-6.

Sunderland, E. M. (2007), Mercury exposure from domestic and imported estuarine and marine fish in the US seafood market, Environ. Health Perspect., 115, 235-242.

Sunderland, E., and R. Mason (2007), Human impacts on open ocean mercury concentrations, Glob. Biogeochem. Cycl., 21, GB4022, doi:10.1029/2006GB002876.

Sunderland, E. M., D. P. Krabbenhoft, J. W. Moreau, S. A. Strode, and W. M. Landing (2009), Mercury sources, distribution, and bioavailability in the North Pacific Ocean: Insights from data and models, Glob. Biogeochem. Cycl., 23, GB2010, doi:10.1029/2008GB003425.

Swartzendruber P. C., et al. (2006), Observations of reactive gaseous mercury in the free-troposphere at the Mt. Bachelor Observatory, J. Geophysic. R. 111(D24), D24301.

Temme, C., et al. (2007), Trend, seasonal and multivariate analysis study of total gaseous mercury data from the Canadian atmospheric mercury measurement network (CAMNet), Atmospheric Environment, 41, 5423-5441, 10.1016/j.atmosenv.2007.02.021.

ter Schure, A., et al. (2011), An integrated approach to assess elevated mercury wet deposition and concentrations in the southeastern United States, 10th International Conference on Mercury as Global Pollutant, Halifax, Nova Scotia, Canada.

Thompson, L, and C. Ladd (2004), The Response of the North Pacific Ocean to Decadal Variability in Atmospheric Forcing: Wind Versus Buoyancy Forcing, J. Phys. Oceanogr., 34, 1373-1389.

Thompson, L, and J. T. Dawe (2007), Propagation of wind and buoyancy forced density anomalies in the North Pacific: dependence on ocean model resolution. Ocean Model. 16, 277-284.

Tian, H., Y. Wang, Z. Xue, Y. Qu, F. Chai, and J. Hao (2011), Atmospheric emissions estimation of Hg, As, and Se from coal-fired power plants in China, 2007, Sci Total Environ, 409, 3078-3081, 10.1016/j.scitotenv.2011.04.039.

Trasande L., P. J. Landrigan, and C. Schechter (2005), Public health and economic consequences of methyl mercury toxicity to the developing brain, Environ. Health Perspect., 113, 590-596.

Trossman, D. S., L. Thompson, S. Mecking, and M. J. Warner (2012), On the Formation, Ventilation, and Erosion of Mode Waters in the North Atlantic and Southern Oceans. Journal of Geophysical Research-Oceans, 117, C09026, doi:10.1029/2012JC008090.

UNEP (2008), The global atmospheric mercury assessment: sources, emissions and transport, UNEP-Chemicals, Geneva, Switzerland.

UNEP (2012), United Nations Environment Programme. http://www.unep.org/hazardoussubstances/Mercury/Negotiations/tabid/3320/Default.aspx (accessed 06/05/2012).

UNEP (2013), Global mercury assessment 2013: sources, emissions, releases and environmental transport, UNEP Chemicals Branch, Geneva, Switzerland.

USEPA (2005), Emissions Inventory And Emissions Processing For The Clean Air Mercury Rule (CAMR), U.S. Environmental Protection Agency, Office of Air Quality Planning and Standards Emissions, Monitoring and Analysis Division, Research Triangle park, NC.

USEPA (2012), Original list of hazardous air pollutants, http://www.epa.gov/ttn/atw/188polls.html, access: Apr. 18, 2012.

Vijayaraghavan, K., P. Karamchandani, C. Seigneur, R. Balmori, and S. Y. Chen (2008), Plume-in-grid modeling of atmospheric mercury, J. Geophys. Res., 113, D24305, 10.1029/2008jd010580.

Vijayaraghavan, K., T. Stoeckenius, L. Ma, G. Yarwood, R. Morris, and L. Levin (2011), Analysis Of Temporal Trends In Mercury Emissions And Deposition In Florida, 10th International Conference on Mercury as Global Pollutant, Halifax, Nova Scotia, Canada.

Vo, A. T. E., M. S. Bank, J. P. Shine, S. V. Edwards (2011), Temporal increase in organic mercury in an endangered pelagic seabird assessed by century-old museum specimens. Proc. Natl. Acad. Sci 108, 7466–7471.

Wang, Q., et al. (2011), Sources of carbonaceous aerosols and deposited black carbon in the Arctic in winter-spring: implications for radiative forcing, Atmospheric Chemistry and Physics, 11, 12453-12473, 10.5194/acp-11-12453-2011.

Wang, Y. X., M. B. McElroy, D. J. Jacob, and R. M. Yantosca (2004a), A nested grid formulation for chemical transport over Asia: Applications to CO, J. Geophys. Res., 109, D22307, 10.1029/2004jd005237.

Wang, Y. X., M. B. McElroy, T. Wang, and P. I. Palmer (2004b), Asian emissions of CO and NOx: Constraints from aircraft and Chinese station data, J. Geophys. Res., 109, D24304, 10.1029/2004JD005250.

Wang, Z., Z. Chen, N. Duan, X. Zhang (2007), Gaseous elemental mercury concentration in atmosphere at urban and remote sites in China, Journal of Environmental Sciences 19(2): 176-180

Wangberg, I., et al. (2007), Trends in air concentration and deposition of mercury in the coastal environment of the North Sea Area. Atmospheric Environment 41:2612-2619.

Weiss-Penzias, P. S., M. S. Gustin, and S. N. Lyman (2011), Sources of gaseous oxidized mercury and mercury dry deposition at two southeastern U.S. sites, Atmospheric Environment, 45, 4569-4579, 10.1016/j.atmosenv.2011.05.069.

Wesely, M. L. (1989), Parameterization of surface resistances to gaseous dry deposition in regional-scale numerical-models, Atmospheric Environment, 23, 1293-1304.

Wetherbee, G. A. (2011), U.S. Geological Survey, Branch of Quality Systems, written communication, May 2011.

Whalin, L. E. Kim, and R. Mason (2007), Factors influencing the oxidation, reduction, methylation and demethylation of mercury species in coastal waters. Mar. Chem. 107: 278–294.

White, E. M., G. J. Keeler, and M. S. Landis (2009), Spatial variability of mercury wet deposition in eastern Ohio: summertime meteorological case study analysis of local source influences, Environ. Sci. Technol., 43, 4946-4953.

Wright, W. G., and K. Nydick (2010), Sources of Atmospheric Mercury Concentrations and Wet Deposition at Mesa Verde National Park, Southwestern Colorado, 2002-08, Mountain Studies Institute, Silverton, CO.

Wu, Y. H., X. Z. Jiang, E. F. Liu, S. C. Yao, Y. X. Zhu and Z. B. Sun (2008), The enrichment characteristics of mercury in the sediments of Dongjiu and Xijiu, Taihu lake catchment, in the past century. Science in China Series D-Earth Sciences 51: 848-854.

Wu, Y., S. Wang, D. G. Streets, J. Hao, M. Chan, and J. Jiang (2006), Trends in Anthropogenic Mercury Emissions in China from 1995 to 2003, Environmental science & technology, 40, 5312-5318.

Xu, X., X. Yang, D. R. Miller, J. J. Reible, and R. J. Carey (1999), Formulation of bi-directional atmosphere-surface exchanges of elemental mercury—Some implication of mixed-layer dynamics, Atmos. Environ., 33, 4345– 4355.

Xu, L.-Q., et al. (2011), A 700-year record of mercury in avian eggshells of Guangjin Island, South China Sea. Environ. Pollut. 159, 889–896.

Yang, H. D., et al. (2010), Historical reconstruction of mercury pollution across the tibetan plateau using lake sediments. Environmental science & technology 44: 2918-2924.

Yang, H. D., D. R. Engstrom, and N. L. Rose (2010a), Recent Changes in Atmospheric Mercury Deposition Recorded in the Sediments of Remote Equatorial Lakes in the Rwenzori Mountains, Uganda. Environmental science & technology 44: 6570-6575.

Yang, H., et al. (2010b), Historical Reconstruction of mercury pollution across the Tibetan Plateau using lake sediments, Environ. Sci. Technol., 44, 2918-2924.

Yang, X., et al. (2005), Tropospheric bromine chemistry and its impacts on ozone: A model study, J. Geophys. Res., 110, D23311, doi:10.1029/2005JD006244.

Yokoo, E. M., J. G. Valente, L. Grattan, S. L. Schmidt, I. Platt, and E. K. Silbergeld (2003), Low level methylmercury exposure affects neuropsychological function in adults, Environmental Health: A Global Access Science Source, 2(8), 10.1186/1476-069X-2-8.

Young, D. R., J. N. Johnson, A. Soutar, and J. D. Isaacs (1973), Mercury concentrations in dated varved marine sediments collected off Southern California. Nature 244, 273–275.

Zhang, H., S. Lindberg, F. Marsik, and G. Keeler (2001), Mercury air/surface exchange kinetics of background soils of the Tahquamenon River watershed in the Michigan Upper Peninsula, Water Air Soil Poll. 126: 151–169.

Zhang, L., L. P. Wright, and P. Blanchard (2009), A review of current knowledge concerning dry deposition of atmospheric mercury. Atmospheric Environment 43: 5853-5864.

Zhang, H., X. Feng, T. Larssen, G. Qiu, and R. D. Vogt (2010), In inland china, rice, rather than fish, is the major pathway for methylmercury exposure, Environ Health Perspect., 118: 1183-1188, doi:10.1289/ehp.1001915.

Zhang, H., X. Feng, T. Larssen, G. Qiu, and R. Vogt (2010), In inland China, rice, rather than fish, is the major pathway for methylmercury exposure, Environ. Health Perspect. 118(9): 1183-1188.

Zhang, Y., et al. (2012), Nested-grid simulation of mercury over North America, Atmospheric Chemistry and Physics, 12, 6095-6111.

Appendix A

APPENDIX FOR CHAPTER 3

Table A1.1: Comparison of the regression results for Hg wet deposition between direct regression approach and regression after model value subtraction approach.

Region	Site	VWM Hg concentration trend						Precipitation trend[b]	
		Model subtraction		Direct regression		Model[a]			
		% yr^{-1}	*p*	% yr^{-1}	*p*	% yr^{-1}	*P*	% yr^{-1}	*p*
Northeast	MA01	**-7.95**[c]	<0.01	**-9.00**	<0.01	-1.43	0.26	2.50	0.17
	ME02	**-4.02**	0.01	**-5.35**	<0.01	-1.31	0.21	3.54	0.12
	ME09	**-7.26**	<0.01	**-4.94**	0.01	2.37	0.20	**5.24**	0.01
	ME98	**-7.19**	<0.01	**-7.97**	<0.01	-0.78	0.34	-0.44	0.44
	NS01	**-2.40**	0.06	**-2.90**	0.06	-0.50	0.39	3.41	0.08
	NY20	**-3.19**	0.04	**-3.16**	0.04	0.03	0.49	-0.62	0.40
	NY68	**-5.09**	<0.01	**-5.25**	<0.01	0.12	0.47	0.05	0.49
	ON07	**-5.87**	0.01	**-4.49**	0.01	1.53	0.17	3.08	0.10
	PA00	-1.64	0.23	-1.26	0.29	0.38	0.40	-1.73	0.25
	PA13	**-2.96**	0.06	**-2.50**	0.05	0.36	0.41	-1.23	0.30
	PA30	**-3.60**	<0.01	-1.64	0.13	**1.95**	0.06	-2.07	0.17
	PA47	**-4.43**	<0.01	**-4.24**	0.02	0.19	0.45	-0.86	0.37
	PA60	**-7.38**	<0.01	**-6.83**	0.01	0.61	0.34	2.19	0.21
	PA72	**-2.35**	0.07	**-2.64**	0.10	-0.30	0.41	0.63	0.41
	PA90	-1.07	0.23	-0.13	0.47	0.94	0.24	**-4.84**	0.02
	VA28	-2.52	0.17	-2.58	0.13	-0.19	0.46	-4.81	0.15
	Subtotal	-4.3±2.2[d]		-4.1±2.4		0.24±1.1		0.25±2.9	
Midwest	IL11	-0.48	0.41	-0.79	0.34	-0.30	0.42	2.03	0.27
	IN34	0.11	0.47	0.53	0.37	0.31	0.42	2.96	0.20
	KY10	**-2.93**	0.06	-0.91	0.30	2.02	0.11	-3.38	0.22
	MI48	-2.10	0.17	-0.32	0.44	1.79	0.10	0.70	0.42
	MN16	-0.08	0.49	-0.07	0.49	-0.03	0.49	0.88	0.38
	MN23	-2.40	0.13	-1.03	0.31	1.30	0.15	**4.59**	0.07
	MN27	**-4.14**	0.08	**-3.68**	0.10	0.52	0.33	1.22	0.37
	MO46	**-4.45**	0.02	**-4.15**	0.05	0.30	0.41	0.89	0.37
	WI08	**-3.20**	0.07	-2.25	0.17	0.80	0.24	**6.13**	0.03
	WI22	**-4.25**	0.04	**-4.32**	0.03	-0.07	0.48	4.52	0.12
	WI31	**-4.78**	0.03	**-4.49**	0.04	-0.22	0.44	3.17	0.22
	WI36	-1.96	0.18	-1.12	0.27	0.72	0.30	1.18	0.34

	WI99	-2.18	0.22	-0.53	0.40	1.64	0.23	3.48	0.15
	Subtotal	-2.5±1.6		-1.8±1.8		0.68±0.79		2.2±2.4	
Southeast	AL03	-0.18	0.48	**2.64**	0.09	2.82	0.18	1.02	0.36
	FL05	-0.58	0.37	-1.07	0.24	-0.21	0.43	-1.02	0.36
	FL11	-1.23	0.24	-1.28	0.22	-0.17	0.44	0.29	0.47
	FL34	-0.02	0.49	-1.24	0.22	-0.88	0.13	**9.57**	<0.01
	GA09	1.83	0.15	0.20	0.45	**-1.63**	0.07	**-7.96**	0.02
	GA40	-1.92	0.22	0.62	0.38	**2.61**	0.10	**7.27**	0.01
	MS22	1.29	0.26	-0.29	0.45	**-1.58**	0.07	-1.70	0.33
	NC08	-1.86	0.13	0.95	0.27	**2.78**	0.02	**-5.08**	0.07
	NC42	**-4.76**	0.02	0.01	0.50	**4.77**	<0.01	**-7.11**	0.02
	SC05	-0.07	0.49	**3.46**	0.02	**3.52**	0.04	-2.50	0.25
	SC19	**-3.76**	0.03	-1.79	0.16	**1.97**	0.08	1.48	0.33
	TN11	**-1.85**	0.08	-1.59	0.11	0.26	0.42	**-3.97**	0.06
	TX21	**4.96**	0.03	**6.04**	0.01	0.60	0.38	-3.12	0.19
	Subtotal	-0.63±2.5		0.51±2.3		1.1±2.1		-0.99±5.1	
West	CA75	**-11.61**	0.06	-6.61	0.14	11.36	0.26	**12.18**	0.01
	CO97	2.66	0.15	**4.46**	0.03	1.56	0.18	1.39	0.27
	CO99	**6.36**	0.01	**7.69**	<0.01	0.96	0.25	3.94	0.15
	NV02	**6.93**	0.06	**7.77**	0.04	0.83	0.23	-0.56	0.45
	WA18	-2.69	0.20	-1.88	0.27	0.07	0.48	1.73	0.30
	Subtotal	0.33±7.7		2.3±6.3		2.0±4.7		3.7±5.0	

[a] Trends of VWM Hg concentrations calculated in the BASE model simulation.

[b] Trends of precipitation observed at MDN sites.

[c] Significant trends ($p < 0.1$) are indicated in bold.

[d] Arithmetic mean and standard deviation.

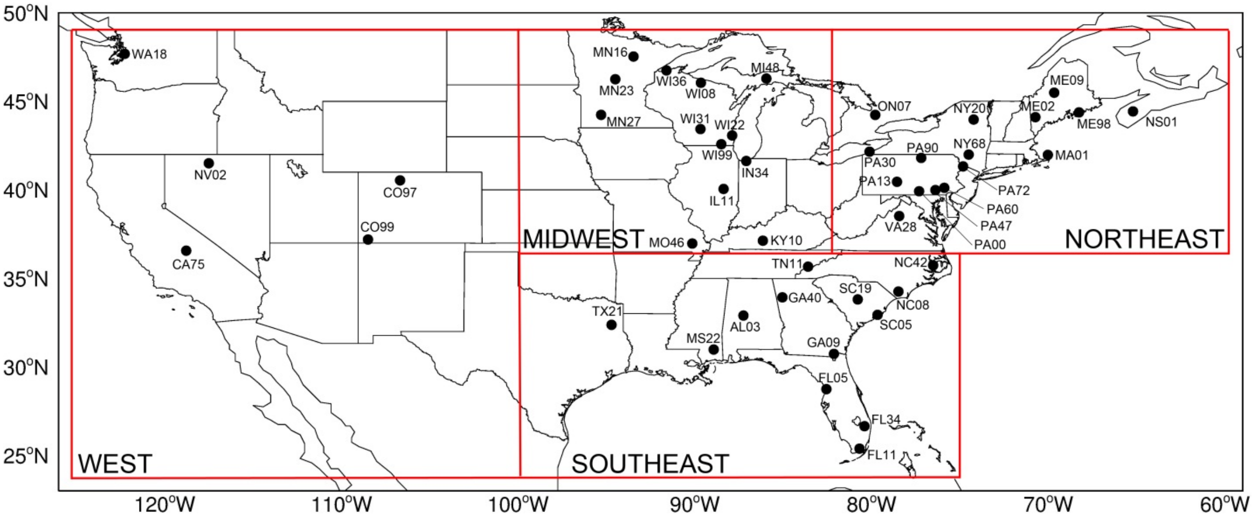

Figure A1.1: Map of the 47 Mercury Deposition Network (MDN) sites used in this study. The red rectangles define the boundaries of the four regions considered.

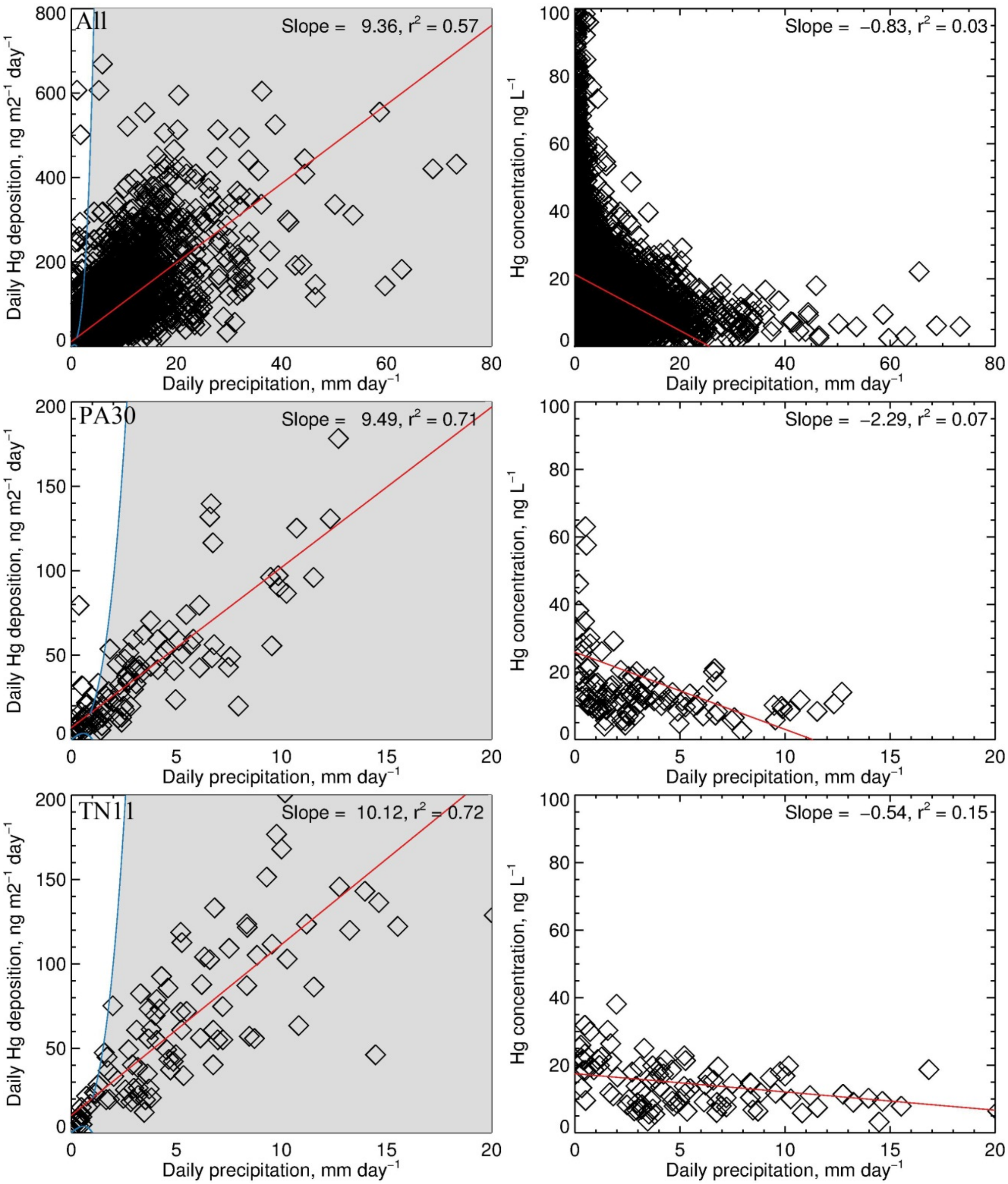

Figure A1.2: Correlation between observed summer time (JJA) weekly precipitation and Hg wet deposition flux (left column) and between precipitation and Hg concentrations in precipitated rain/snow for 2004-2010. Top panels: 47 MDN sites. Middle panels: PA30 site. Bottom panels: TN11 (bottom panels). The red line is a linear regression for all the points with slope and r^2 values shown in each panel. The shaded area indicates the regime where the Hg concentration in precipitation is less sensitive than Hg wet deposition flux to the change of precipitation depth.

Text A1.1 Sensitivity of different analytical variables to the change in precipitation

The sensitivity of Hg wet deposition flux (y) to precipitation depth (x) is defined as:

$$S_{\text{flux}} = \left|\frac{\frac{dy}{y}}{\frac{dx}{x}}\right| = \frac{x}{y}\left|\frac{dy}{dx}\right| = k\frac{x}{y} \tag{1}$$

where k is the slope of the regression line between y and x, as illustrated in the left panels of Figure A1.2. The sensitivity of Hg concentration in precipitation ($\frac{y}{x}$) to x can be written as:

$$S_{concentration} = \left|\frac{\frac{d\frac{y}{x}}{\frac{y}{x}}}{\frac{dx}{x}}\right| = \frac{1}{x^2}\left(\frac{x}{y}\left|\frac{dy}{dx}\right|\right) - \frac{1}{x^2} = \frac{1}{x^2}\left|S_{flux} - 1\right| \tag{2}$$

Therefore, $S_{\text{concentration}}$ would be less than S_{flux} if:

$$\frac{1}{x^2}\left|S_{flux} - 1\right| < S_{flux} \tag{3}$$

Combining Equations (1) and (3), we obtain:

$$kx^3 > |kx - y| \tag{4}$$

The regime satisfying equation (4) is shaded in grey on the left column of panels in Figure A1.2. Among all the data points, 86.4% belong to this regime. At PA30 and TN11, 85.7% and 90.4% of the points fall into this regime, respectively. This indicates less sensitivity for Hg concentration in precipitation to the variability of precipitation depth than Hg wet deposition.

Appendix B

APPENDIX FOR CHAPTER 4

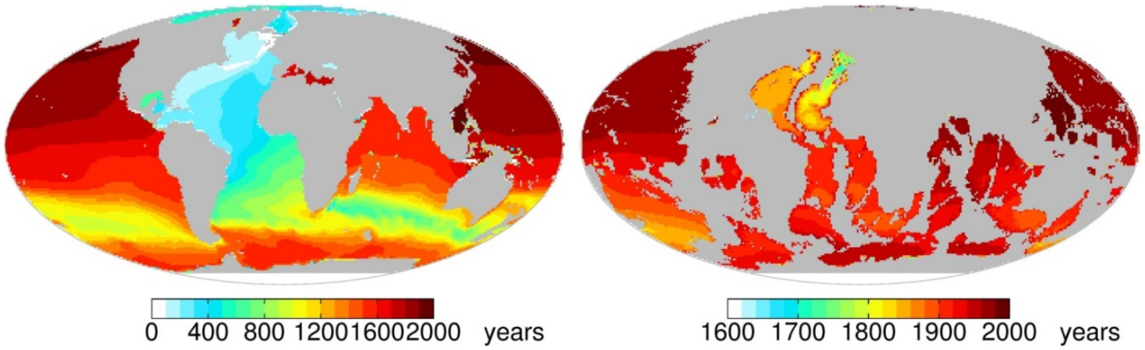

Figure A2.1: Modeled age of water mass at 1,000 m (left) and 4,000 m (right) depth

Appendix C

APPENDIX FOR CHAPTER 5

List of references for lake sediment, ice core, peat bog core profiles:

Asmund, G., and S. P. Nielsen (2000), Mercury in dated Greenland marine sediments. Science of the Total Environment 245: 61-72.

Biester, H., R. Bindler, A. Martinez-Cortizas, and D. R. Engstrom (2007), Modeling the past atmospheric deposition of mercury using natural archives. Environmental science & technology 41: 4851-4860.

Biester, H., R. Kilian, C. Franzen, C. Woda, A. Mangini, and H. F. Scholer (2002), Elevated mercury accumulation in a peat bog of the Magellanic Moorlands, Chile (53 degrees S) - an anthropogenic signal from the Southern Hemisphere. Earth and Planetary Science Letters 201: 609-620.

Bindler, R., I. Renberg, P. G. Appleby, N. J. Anderson, and N. L. Rose (2001), Mercury accumulation rates and spatial patterns in lake sediments from west Greenland: A coast to ice margin transect. Environmental science & technology 35: 1736-1741.

Cooke, C. A., P. H. Balcom, H. Biester, and A. P. Wolfe (2009), Over three millennia of mercury pollution in the Peruvian Andes. Proc Natl Acad Sci U S A 106: 8830-8834.

Drevnick, P. E., A. L. C. Shinneman, C. H. Lamborg, D. R. Engstrom, M. H. Bothner, and J. T. Oris (2009), Mercury Flux to Sediments of Lake Tahoe, California–Nevada. Water, Air, & Soil Pollution 210: 399-407.

Drevnick, P. E., H. Yang, C. H. Lamborg, and N. L. Rose (2012), Net atmospheric mercury deposition to Svalbard: Estimates from lacustrine sediments. Atmospheric Environment 59: 509-513.

Elbaz-Poulichet, F., L. Dezileau, R. Freydier, D. Cossa, and P. Sabatier (2011), A 3500-year record of Hg and Pb contamination in a mediterranean sedimentary archive (the Pierre Blanche Lagoon, France). Environ Sci Technol 45: 8642-8647.

Engstrom, D. R., and E. B. Swain (1997), Recent declines in atmospheric mercury deposition in the upper Midwest. Environmental science & technology 31: 960-967.

Fitzgerald, W. F., D. R. Engstrom, R. P. Mason, and E. A. Nater (1998), The case for atmospheric mercury contamination in remote areas. Environmental science & technology 32: 1-7.

Fitzgerald, W. F., D. R. Engstrom, C. H. Lamborg, C. M. Tseng, P. H. Balcom, and C. R. Hammerschmidt (2005), Modern and historic atmospheric mercury fluxes in northern Alaska: Global sources and Arctic depletion. Environmental science & technology 39: 557-568.

Guevara, S. R., M. Meili, A. Rizzo, R. Daga, and M. Arribere (2010), Sediment records of highly variable mercury inputs to mountain lakes in Patagonia during the past millennium. Atmospheric Chemistry and Physics 10: 3443-3453.

Jiang, S., X. Liu, and Q. Chen (2011), Distribution of total mercury and methylmercury in lake sediments in Arctic Ny-Alesund. Chemosphere 83: 1108-1116.

Kamman, N. C., and D. R. Engstrom (2002), Historical and present fluxes of mercury to Vermont and New Hampshire lakes inferred from Pb-210 dated sediment cores. Atmospheric Environment 36: 1599-1609.

Lacerda, L. D., M. G. Ribeiro, R. C. Cordeiro, A. Sifeddine, and B. Turcq (1999), Atmospheric mercury deposition over Brazil during the past 30,000 years. Environment and Biodiversity 51: 363-371.

Lamborg, C. H., W. F. Fitzgerald, A. W. H. Damman, J. M. Benoit, P. H. Balcom, and D. R. Engstrom (2002), Modern and historic atmospheric mercury fluxes in both hemispheres: Global and regional mercury cycling implications, Global Biogeochem. Cycles, 16, 1104, doi:10.1029/2001GB001847.

Landers, D. H., J. Ford, C. Gubala, M. Monetti, B. K. Lasorsa, and J. Martinson (1995), mercury in vegetation and lake-sediments from the us arctic. Water Air and Soil Pollution 80: 591-601.

Landers, D. H., C. Gubala, M. Verta, M. Lucotte, K. Johansson, T. Vlasova, and W. L. Lockhart (1998), Using lake sediment mercury flux ratios to evaluate the regional and continental dimensions of mercury deposition in arctic and boreal ecosystems. Atmospheric Environment 32: 919-928.

Landers, D.H., et al. (2008), The fate, transport, and ecological impacts of airborne contaminants in western national parks (USA). In: Christie, S. (Ed.), Western Airborne Contaminants Assessment Project Final Report, vol. 1 EPA/600/R-07/138.

Lindberg, S., R. Bullock, R. Ebinghaus, D. Engstrom, X. B. Feng, W. Fitzgerald, N. Pirrone, E. Prestbo, and C. Seigneur (2007), A synthesis of progress and uncertainties in attributing the sources of mercury in deposition. Ambio 36: 19-32.

Lockhart, W. L., P. Wilkinson, B. N. Billeck, R. V. Hunt, R. Wagemann, and G. J. Brunskill (1995), Current and historical inputs of mercury to high-latitude lakes in canada and to hudson-bay. Water Air and Soil Pollution 80: 603-610.

Lorey, P., and C. T. Driscoll (1999), Historical trends of mercury deposition in Adirondack lakes. Environmental science & technology 33: 718-722.

Mast, M. A., D. J. Manthorne, and D. A. Roth (2010), Historical deposition of mercury and selected trace elements to high-elevation National Parks in the Western U.S. inferred from lake-sediment cores. Atmospheric Environment 44: 2577-2586.

Muir, D. C. G., et al. (2009), Spatial Trends and Historical Deposition of Mercury in Eastern and Northern Canada Inferred from Lake Sediment Cores. Environmental science & technology 43: 4802-4809.

Paulson, A. J., and D. Norton (2007), Mercury Sedimentation in Lakes in Western Whatcom County, Washington, USA and its Relation to Local Industrial and Municipal Atmospheric Sources. Water, Air, and Soil Pollution 189: 5-19.

Roos-Barraclough, F., N. Givelet, A. K. Cheburkin, W. Shotyk, and S. A. Norton (2006), Use of Br and Se in peat to reconstruct the natural and anthropogenic fluxes of atmospheric Hg: A 10000-year record from Caribou Bog, Maine. Environmental science & technology 40: 3188-3194.

Roos-Barraclough, F., N. Givelet, A. Martinez-Cortizas, M. E. Goodsite, H. Biester, and W. Shotyk (2002), An analytical protocol for the determination of total mercury concentrations in solid peat samples. Science of the Total Environment 292: 129-139.

Ross-Barraclough, F., and W. Shotyk (2003), Millennial-scale records of atmospheric mercury deposition obtained from ombrotrophic and minerotrophic peatlands in the Swiss Jura Mountains. Environmental science & technology 37: 235-244.

Rossmann, R. (2010), Protocol to Reconstruct Historical Contaminant Loading to Large Lakes: The Lake Michigan Sediment Record of Mercury. Environmental science & technology 44: 935-940.

Sanders, R. D., K. H. Coale, G. A. Gill, A. H. Andrews, and M. Stephenson (2008), Recent increase in atmospheric deposition of mercury to California aquatic systems inferred from a 300-year geochronological assessment of lake sediments. Applied Geochemistry 23: 399-407.

Schuster, P. F., et al. (2002), Atmospheric mercury deposition during the last 270 years: A glacial ice core record of natural and anthropogenic sources. Environmental science & technology 36: 2303-2310.

Swain, E. B., D. R. Engstrom, M. E. Brigham, T. A. Henning, and P. L. Brezonik (1992), Increasing rates of atmospheric mercury deposition in midcontinental north-america. Science 257: 784-787.

Verta, M., K. Tolonen, and H. Simola (1989), History of heavy-metal pollution in finland as recorded by lake-sediments. Science of the Total Environment 87-8: 1-18.

Vo, A. T., M. S. Bank, J. P. Shine, and S. V. Edwards (2011), Temporal increase in organic mercury in an endangered pelagic seabird assessed by century-old museum specimens. Proc Natl Acad Sci U S A 108: 7466-7471.

Wang, X., H. Yang, P. Gong, X. Zhao, G. Wu, S. Turner, and T. Yao (2010), One century sedimentary records of polycyclic aromatic hydrocarbons, mercury and trace elements in the Qinghai Lake, Tibetan Plateau. Environ Pollut 158: 3065-3070.

Wu, Y. H., et al. (2008), The enrichment characteristics of mercury in the sediments of Dongjiu and Xijiu, Taihu lake catchment, in the past century. Science in China Series D-Earth Sciences 51: 848-854.

Yang, H. D., et al. (2010), Historical reconstruction of mercury pollution across the tibetan plateau using lake sediments. Environmental science & technology 44: 2918-2924.

Yang, H. D., D. R. Engstrom, and N. L. Rose (2010), Recent Changes in Atmospheric Mercury Deposition Recorded in the Sediments of Remote Equatorial Lakes in the Rwenzori Mountains, Uganda. Environmental science & technology 44: 6570-6575.

List of Reference for ocean profiles:

Cossa, D., M. H. Cotte-Krief, R. P. Mason, and J. Bretaudeau-Sanjuan (2004), Total mercury in the water column near the shelf edge of the European continental margin. Marine Chemistry 90: 21-29.

Cossa, D., et al. (2011), Mercury in the Southern Ocean. Geochimica et Cosmochimica Acta 75: 4037-4052.

Dalziel, J. A. (1992), Reactive mercury on the scotian shelf and in the adjacent northwest atlantic-ocean. Marine Chemistry 37: 171-178.

Hammerschmidt, C. R., and K. L. Bowman (2012), Vertical methylmercury distribution in the subtropical North Pacific Ocean. Marine Chemistry 132-133: 77-82.

Laurier, F. J. G., R. P. Mason, G. A. Gill, and L. Whalin (2004), Mercury distributions in the North Pacific Ocean - 20 years of observations. Marine Chemistry 90: 3-19.

Lawrence, A. L., and R. P. Mason (2001), Factors controlling the bioaccumulation of mercury and methylmercury by the estuarine amphipod Leptocheirus plumulosus. Environmental Pollution 111: 217-231.

Mason, R. P., and W. F. Fitzgerald (1993), The distribution and biogeochemical cycling of mercury in the equatorial pacific-ocean. Deep-Sea Research Part I-Oceanographic Research Papers 40: 1897-1924.

Mason, R. P., K. R. Rolfhus, and W. F. Fitzgerald (1998), Mercury in the North Atlantic. Marine Chemistry 61: 37-53.

Mason, R. P., and K. A. Sullivan (1999), The distribution and speciation of mercury in the South and equatorial Atlantic. Deep-Sea Research Part Ii-Topical Studies in Oceanography 46: 937-956.

Sunderland, E. M., D. P. Krabbenhoft, J. W. Moreau, S. A. Strode, and W. M. Landing (2009), Mercury sources, distribution, and bioavailability in the North Pacific Ocean: Insights from data and models, Glob. Biogeochem. Cycl., 23, GB2010, doi:10.1029/2008GB003425.

VITA

Yanxu Zhang was born and raised in Sichuan, China. He earned a Bachelor's degree in Environmental Science from Peking University in 2006. He continued his study at Peking University with Professor Shu Tao and earned a doctoral degree in Environmental Geochemistry in 2010. He joined the Department of Atmospheric Sciences at the University of Washington in 2009. Yanxu specializes in atmospheric chemistry modeling and biogeochemical cycle of critical pollutant and components in the environment.